High-density Flexible Neurophotonic Implants

Submitted in partial fulfillment of the requirements for

the degree of

Doctor of Philosophy

in

Electrical and Computer Engineering

Jay Warren Reddy

B.S., Electrical Engineering and Computer Science, University of California at Berkeley
B.S., Engineering Mathematics and Statistics, University of California at Berkeley

Carnegie Mellon University

Pittsburgh, PA

December 2021

Acknowledgments

The work in this thesis would not have been possible if not for the help of my family, friends, and colleagues. In particular, I would like to thank my thesis advisor, Maysamreza Chamanzar, for his guidance and support in completing the work described in this thesis. Additionally, I would like to thank the members of my committee: Alison Barth, Elias Towe, and Pulkit Grover.

The material in this thesis is based upon work supported in part by the National Science Foundation under Grant No. 1926804 and also by the National Institute of Neurological Disorders and Stroke of the National Institutes of Health under Award Number 1RF1NS113303. I also acknowledge support by the Carnegie Mellon University Ben Cook Presidential Graduate Fellowship, the Carnegie Mellon University Richard King Mellon Foundation Presidential Fellowship in the Life Sciences, the Axel Berny Presidential Graduate Fellowship, Philip and Marsha Dowd, and the Swartz Center for Entrepreneurship Innovation Commercialization Fellows program.

This page intentionally left blank

Contents

List of Tables

This page intentionally left blank

List of Figures

This page intentionally left blank

Abstract

From research to clinical neuroscience, high-resolution and minimally invasive neural interfaces are needed to study and treat brain function and dysfunction. Recently, optical techniques such as optogenetics and functional fluorescent imaging have enabled unprecedented throughput and specificity for interrogating neural circuits. However, the scattering and absorption of light in the brain tissue limits the resolution and depth of penetration of light-based methods. Therefore, implantable devices are used to deliver or collect light deep in the tissue with high spatial resolution. Currently, implantable optics are typically composed of rigid materials including silicon or silicon dioxide. These stiff materials have a significant mechanical mismatch with the soft brain tissue, triggering tissue damage and scar tissue formation over time. To alleviate these issues and enable minimally invasive chronic optical implants, they must be compact and flexible.

This thesis introduces two novel microfabricated device architectures to address this outstanding need in the field. The first, Parylene photonics, uses flexible biocompatible materials – Parylene C and polydimethylsiloxane (PDMS) – to form a novel photonic waveguide platform to passively guide light into or out of the tissue. The second, GaN-on-Parylene micro-light-emitting diodes (μLEDs), uses integrated light sources to generate light directly in the tissue. Due to the flexible polymer material composition and micrometer-scale structures implemented using a novel microfabrication process in both architectures, the devices can be made compact and flexible. In addition, recording electrodes for electrophysiology readout are monolithically integrated to allow for full read-write optogenetic stimulation and electrical recording capabilities in a flexible material platform.

I will discuss the design, simulation, fabrication, characterization, and biological demonstration of these novel devices. I present a complete course of work from concept to application for two separate solutions to an outstanding need in the neuroscience toolset, as well as a discussion of

their respective benefits and tradeoffs. In the first platform, Parylene photonics, I demonstrate through a simulation study that the refractive index contrast between Parylene C and PDMS is sufficient to confine and guide optical modes in compact, high-density waveguide routing. I developed a novel fabrication process to realize low-loss ($<$ 5 dB/cm @ 633 nm) photonic waveguides in a new Parylene C material platform with integrated 45-degree micromirrors for broadband out-of-plane input coupling and light delivery capabilities. The Parylene photonic waveguides were packaged and implanted in opsin-expressing mice to demonstrate optogenetic stimulation of neurons. In the second platform, GaN-on-Parylene μLEDs, I demonstrate a novel microfabrication process to create arrays of GaN μLEDs directly embedded in a Parylene C substrate. The proof-of-concept devices contain arrays of up to 32 GaN μLEDs as small as 22 μm x 22 μm. I developed a thermal and optical model of the system in the tissue via simulation studies to determine thermally safe stimulation paradigms using the novel device architecture. Finally, I use the GaN-on-Parylene μLEDs to perform optogenetic stimulation of opsin-expressing brain slices. In addition, the potentials of these platforms for realizing surface devices for electrocorticography (ECoG) recording and imaging will be discussed.

Chapter 1

Introduction

1.1 Thesis statement

This thesis demonstrates the design, simulation, fabrication, characterization, and proof-of-concept biological demonstration of flexible optoelectrical implantable neural interfaces based on GaN-on-Parylene micro-light-emitting diodes (μLEDs) and Parylene C/polydimethylsiloxane (PDMS) optical waveguides for brain recording and stimulation. Using a multipronged approach of theoretical design and simulation, innovation in microfabrication processes, design of customized characterization setups, and test and validation in real biological systems, I demonstrate the first ever fully flexible and ultracompact optoelectrical neural interface platforms for high-resolution interfacing with the brain for chronic full-duplex read/write access to neural circuits. This work addresses an outstanding need in fundamental and translational neuroscience and adds important functionalities to the neuroscience tool set.

1.2 Tools for Neuroscience Research

Neural interfaces with high-resolution read/write capabilities are used in neuroscience to elucidate the neural basis of brain function and dysfunction. Ultimately, this understanding can be used to design appropriate therapeutic interventions for neurological disorders. In general, there is a tradeoff between the invasiveness of such techniques and their resolution. For example, electroencephalograms (EEG) allows electrophysiology readout from the surface of the scalp without any implanted device, but the electric fields generated by neural activity are low-pass filtered as they propagate through the layers of the skull and scalp, resulting in poor spatial resolution [1]. Electrocorticography (ECoG) achieves higher spatial resolution, but requires an invasive surgical procedure so that recording electrodes can be placed directly on the surface of the brain cortex. This way, the recording electrodes are placed closer to the electrically-active neurons. For the highest spatiotemporal resolution, penetrating neural probes include high aspect ratio shanks which pierce the brain tissue, allowing the device to be placed inside the neural tissue and enabling direct access to deep brain regions. This thesis is primarily concerned with technologies for penetrating neural probes.

High-resolution neural recording is needed to match the unprecedented scale and complexity of the brain. For example, a mouse brain has approximately 12 billion neurons, with the human brain having even more: 86 billion neurons [2]. In mice, neurons have an average density of more than 100,000 neurons/mm^3 [3]. Relatively low-resolution techniques such as functional magnetic resonance imaging (fMRI) have been successfully employed to localize different activities to specific brain regions [4]. On the other hand, low-throughput high-resolution recording techniques including Patch Clamp recording [5] and single-channel microwires have been used to elucidate the behavior of individual neural circuits including place and grid cells in the hippocampus [6] and the basal ganglia-thalamocortical circuit responsible for Parkinson's disease [7], among countless

others. However, there is an increasing need for high-resolution, high channel count neural interfaces to enable distributed, yet high-resolution recording from the brain tissue [8]. Over time, advances in microfabrication have increased the number of recording electrodes exponentially [9]. Overall, it is highly advantageous to stimulate and sample neuronal activity in the brain with high spatio-temporal resolution in multiple distinct regions simultaneously [10, 11]. This has been further accompanied by advances in algorithms and signal processing to analyze the signals recorded by the higher channel count neural interfaces [12]. Together, these have opened new routes for investigation in fundamental neuroscience.

In addition to the opportunities that have been enabled by increasing the recording site density, long-lasting neural interfaces open the way for new applications. For example, studying aging in neural circuits benefits from a stable chronic neural interface [13]. As neural interfaces make their way into humans in the form of neural prosthetics and brain-computer interfaces (BCIs), the requirement for chronic and minimally invasive implants becomes even more stringent. For example, cochlear implants and deep brain stimulators are expected to last the lifetime of the patient. Further, neural interfaces will need to be chronically durable while implanted in the body to address the emerging applications such as treatment of memory disorders, neuropsychiatric conditions, and chronic pain, among others [14]. Therefore, chronic neural interfaces are needed.

1.3 Optical Techniques in Brain-Computer Interfaces

Recently, the capabilities of neural interfaces have been expanded by new optical techniques. These methods can exceed the capabilities of traditional electrical stimulation and recording. For example, selective expression of optical agents and tags enables cell-type specificity. Furthermore, light focusing and steering enables higher resolution access to multiple targets within the neural tissue for higher spatial resolution. The great potential of optical stimulation and recording techniques call for efficient neural interfaces capable of light delivery and collection in brain tissue.

1.3.1 Optogenetics

Optogenetic stimulation is a powerful method for neural stimulation, requiring light delivery into the brain with high spatial resolution [15]. To effectively study the distributed and dynamic neural circuits of the brain requires technologies to manipulate neuronal activity with single-cell resolution simultaneously across different brain regions. In particular, optogenetics allows selective excitation or inhibition of specific cell types using light at different wavelengths [16, 17]. In addition to the cell-type specificity provided by viral or genetic targeting, it may also be desirable to stimulate or inhibit a subset of neurons which express the same opsin. Therefore, patterned, high-resolution light delivery into the tissue is required. Additionally, for closed-loop optogenetic experiments, recording electrodes must be integrated on an optical neural probe to enable simultaneous electrical recording and optical stimulation.

1.3.2 Applications of Optogenetics

Optogenetics provides a unique advantage compared to electrical stimulation by genetically targeting specific cell populations within the same region, and allowing selective inhibition. Since neurons do not naturally respond to light, only the subpopulation of cells in the stimulated region which express the opsin will respond to the optical stimulation. This capability enables studies that distinguish the role of specific cell types in neural circuits. For example, optogenetic techniques have been used to study the neural basis of sexual and aggressive behaviors in the amygdala, as well as the circuits governing Parkinson's and epilepsy, which could eventually enable new clinical interventions.

To understand neural circuits in the brain, optogenetics provides new tools to unravel neural circuit function, especially where multiple cell types with distinct circuit roles are intermingled. For example, it is understood that male sexual and aggressive behaviors are mediated via anatomically distinct regions of the hypothalamus: the medial preoptic nucleus (MPN) and ventrolateral part

of the ventromedial hypothalamus (VMHvl). A recent study [18] used optogenetic manipulation to identify the role of genetically-distinct estrogen receptor alpha-expressing (Esr1) cells in the posterior amygdala (PA) which project to these key regions in the hypothalamus: PA$^{Esr1+MPN}$ and PA$^{Esr1+VMHvl}$. Using independent optogenetic inhibition of each cell type, it was shown that PA$^{Esr1+MPN}$ cells were necessary for mating behavior, whereas PA$^{Esr1+VMHvl}$ inhibition reduced aggression and caused only minor deficits in sexual behavior [18]. Thus, optogenetic techniques have demonstrated that Esr1 cells in the PA are key mediators of sexual and aggressive behavior.

Recently, optogenetics has been applied to differentiate the origins of the direct and indirect motor pathways of the basal ganglia, which are thought to govern Parkinson's disease motor symptoms. These pathways originate from genetically-differentiated spiny projection neurons (SPNs) in the striatum, which can be optogenetically targeted via differences in the dopamine receptors (D1 vs D2) [19]. For example, the direct pathway can be activated by stimulating SPN-D1 neurons, while the indirect pathway can be activated via projections from SPN-D2 neurons in the striatum [19]. These neurons are genetically distinct and can be optogenetically targeted, but cannot be independently electrically stimulated since they are collocated in the striatum [19] and blunt electrical stimulation cannot discriminate these different pathways.

Deep brain stimulation (DBS) is a modern clinical intervention to alleviate the symptoms of Parkinson's disease using an implanted stimulating electrode. Optogenetic studies could be used to identify more specific targets for DBS, and minimize side effects from off-target stimulation. Optogenetic studies have recently revealed that DBS stimulation in the subthalamic nucleus (STN) does not relieve motor symptoms of Parkinson's via cells that originate in the STN, but via stimulation of axonal projections from cortical neurons through the STN [19]. Therefore, a potential DBS target is the origin of projections to the STN in the cortex [19]. Another recent optogenetic study has shown that the indirect pathway contains a subcircuit within the external globus pallidus (GPe) which can provide lasting relief of Parkinson's motor symptoms only when a

subset of cells (parvalbumin-expressing) are activated [20]. The results were later replicated using electrical stimulation, which could differentiate between the cell types using bursting stimulation due to synaptic differences between parvalbumin-expressing and lim-homeobox-6-expressing GPe neurons [21]. In this way, new targets for intervention and stimulation strategies identified using optogenetic studies in animal models could be translated to clinical DBS treatment. In addition to being useful in research, optogenetics could see future clinical adoption for optical deep-brain stimulation to increase the precision of clinical intervention [15].

Similarly, in the study of epilepsy, optogenetic targeting of specific neural populations has allowed the refinement of the mechanistic understanding of seizure development as well as potential targets for clinical intervention [22]. For example, optogenetic inhibition of interneurons including hippocampal pyramidal cells has been shown to stop or alleviate seizures [23, 24]. Furthermore, optogenetics can be used to induce seizures to study their origination [25].

1.3.3 Implantable Neural Probes for Optogenetic Stimulation

Optical scattering and absorption in tissue limits the depth and resolution achievable by conventional optical techniques based on external optics [26]. Therefore, non-invasive microscopy technique are limited to the superficial layers of the tissue. The amount of absorption and scattering depends on the type of tissue and wavelength of light, but is especially strong in the visible range of the optical spectrum. Therefore, techniques such as two-photon microscopy use near-infrared wavelengths to access deep layers of tissue, up to a few millimeters deep [27]. However, there is a need to access deeper regions of the tissue to investigate diseases such as Parkinson's that involve deep brain structures such as the basal ganglia nuclei. Optical implants can collect and deliver light in the tissue without suffering from the effects of scattering and absorption in the tissue. These implants consist of one or more optical channels - referred to

as "optrodes". Furthermore, traditional bulky microscopes are not suitable for experiments in free-roaming animal subjects, which require miniaturized technologies that can be carried without encumbering the animal.

1.3.3.1 Active Versus Passive Optical Neural Probes

Recently, optoelectronic probes using either active integrated micro-light-emitting diodes (μLEDs) or passive optical waveguides have been introduced to enable light delivery in deep tissue [28, 29, 30, 31, 32, 33, 34, 35]. Probes based on μLED arrays can potentially provide a higher device density for individual optical output ports, at the expense of heat generated in the tissue. Waveguide-based optical neural probes are completely passive, minimizing concerns of heat generation on the tissue. However, they are limited in density because each waveguide needs to be independently routed through the shank. Moreover, packaging of commercially-available light sources at the backend further limits the number of independently addressable channels for waveguide probes. Therefore, active and passive neurophotonic implants have inherent advantages and tradeoffs that will influence the choice of one over the other for specific applications.

1.3.3.2 Passive Photonic Implants

Neural probes based on passive photonic waveguides deliver light from external light sources into the brain tissue. Photonic waveguides are optical structures which utilize the refractive index contrast between a high refractive index core surrounded by a low refractive index cladding to confine and guide light. Traditionally, these structures have been formed using rigid materials such as SiO_2 and SiN [36, 37, 38]. A fully-flexible integrated photonic platform suitable for chronic implantation requires careful material choice of flexible and biocompatible materials to form the waveguide core and cladding. A modified fiber drawing process using polymer materials can be used to make flexible passive photonic implants [39]. Another approach is to use microfabrication to pattern integrated photonic waveguides in planar layers. Many polymer photonic materials have been demonstrated in the literature, including Polycarbonate, SU-8, PDMS, Ormocers, EpoCore,

and Cytop. However, in some cases these polymers have been fabricated on rigid substrates, rendering the resulting device rigid [40, 41]. Only recently have fully-flexible integrated photonic platforms begun to emerge, including Polymeric Opto-Electro-Mechanical Systems (POEMS) [42] and flexible multifunctional fibers [43, 44].

An inherent limitation of passive photonic neural implants is that they require a connection to a separate light source in order to provide light. Different approaches to backend packaging of optical neural probes have been explored, including bonding to optical fibers through butt-coupling [40], or using grating couplers from the surface of the waveguides [45]. Fiber bonding would require bonding many fibers in order to scale up the number of device channels. Another approach has been to use a single fiber bundle combined with a digital micromirror device or scanning mirror galvanometer to modulate the input to multiple input facets without having to align and bond individual fibers [36]. However, all of these techniques would require a rigid tethered fiber or fiber bundle to connect to external light sources, which would become cumbersome and inhibit experiments on free-roaming animals. To alleviate the need for a tethered fiber connection, light sources can be directly bonded to the waveguide input, including packaged laser diodes [29] and flip-chip bonded bare laser diodes using direct butt-coupling [30, 42] or through a gradient-index (GRIN) lens to boost the coupling efficiency [46]. This way, the light sources are integrated on the neural probe headstage to obviate the need for an external fiber tether and a benchtop laser source.

Waveguide output ports can also be designed to illuminate specific localized volumes of the brain tissue. In end-firing waveguides, light is emitted directly from the output facet along the direction of the waveguide. To increase the spatial resolution of optical stimulation and incorporate multiple output ports on a single shank, an out-of-plane illumination profile is desired. This configuration reduces the overlap of the output beam profiles along the same shank. For the integration of

collocated electrical recording capability, out-of-plane beam profiles additionally prevent direct illumination of surface recording electrodes, which reduces the photoelectric artifact [38]. In previous work, grating couplers have been used to achieve out-of-plane illumination [38, 47].

1.3.3.3 Active Photonic Implants

Rather than delivering light from external light sources into the tissue, active light sources can be integrated onto the penetrating probe shank and directly inserted into the brain to generate light in-situ. For Channelrhodopsin (ChR2), GaN μLEDs are commonly used in a range of wavelengths from 450-470 nm. Although GaN is traditionally grown on sapphire substrates, it can be grown directly on a Si substrate, albeit with lower efficiency, which can be micromachined into a neural probe with integrated optical stimulation capabilities [48]. Another method to integrate active photonic functionalities into neural probes have been to attach off-the-shelf LEDs to flexible substrates. The microfabricated flexible shanks incorporate bondpads and electrical interconnects, which are used to power the μLEDs. However, commercially-available LEDs are relatively large (220 μm × 270 μm × 50 μm) [49], resulting in a large optical implant, although such devices have seen other uses, including in Cochlear Implants [50].

Alternatively, custom-fabricated μLED chips have been lithographically defined directly on a sapphire substrate, then released via a laser liftoff (LLO) process. Released GaN chips fabricated via this method can be significantly smaller than what is commercially available (e.g., 50 μm × 50 μm × 6.45 μm). The chips are then transferred to a microfabricated flexible substrate via serial flip-chip bonding [51, 52]. More recently, a wafer-scale μLED transfer process has been developed for cochlear implants to transfer entire arrays of μLEDs to flexible substrates in a single step [53, 54]. Such processes greatly increase the scalability and throughput of the packaging process. However, these existing techniques have significant limitations. After the flip-chip bonding process, the electrical contacts must be encapsulated to protect the devices from the biological environment, which precludes the inclusion of recording electrodes on the same device.

1.3.3.4 Tradeoffs of Passive and Active Photonic Implants

Active neurophotonics based on μLEDs have been demonstrated with high density and number of light sources. In general, routing of the electrical interconnects to power μLEDs is less stringent than routing passive optical waveguides since the electrical traces can be made very small and densely routed with sharp bends and vias for multiple routing layers. Photonic waveguides, on the other hand, are subject to losses due to tight bends and corners. Additionally, at the backend, electrical interconnect technology using wirebonds or zero insertion force (ZIF) connectors facilitates high-throughput electrical packaging. On the other hand, traditional photonic interconnects are typically bulkier and require precise alignment. Therefore, from a practical standpoint, high-density arrays of μLEDs can be more easily implemented. On the other hand, the limited efficiency of the μLEDs ($< 1\%$ [48]) means that heat conduction in the tissue can be a concern. To avoid tissue heating, the μLEDs must typically be operated at limited powers and in a pulsed configuration [48]. Therefore, existing active photonic neural probes can achieve higher density, at the expense of limited operating ranges to avoid damage to the tissue. Waveguide-based passive probes, on the other hand, promise safe operation, but are currently limited to fewer light sources per probe due to difficulties of interconnects and routing.

1.3.4 Functional Imaging

From biological science to clinical practice, optical methods for imaging tissue are the gold-standard for non-invasive interaction [55, 56, 57]. Exogenous or endogenous optical tags, such as fluorophores, can be used as labels or detectors in the tissue. In neuroscience, calcium imaging enables functional optical recording of neural activity. However, due to limitations of scattering and absorption, implantable and endoscopic imaging technologies are needed to enable such techniques in deep tissue. To enable free-roaming animal experiments, miniaturized technologies such as miniscopes and optical fiber bundles have been used for implantable imaging devices.

Furthermore, these techniques can be combined with optogenetics for closed-loop all-optical manipulation of neural circuits [58]. However, miniscopes require a large GRIN lens which can be several millimeters in diameter, and optical fiber bundles are typically large as well (diameter $\tilde{2}50$ µm) [59, 60]. These large implantable imagers cause severe damage to the tissue. Therefore, there is an outstanding need for minimally-invasive implants for functional imaging of deep brain regions.

1.3.5 Flexible Devices for Chronic Implants

Neural implants, especially those composed of rigid materials, can damage the brain tissue. Typically, penetrating neural probes are designed in the shape of a long, high aspect ratio shank needle in order to minimize the probe cross-section and resulting tissue displacement, which is the cause of acute tissue damage during implantation [61]. Over time, the performance of neural implants degrades due to the foreign body response (FBR) [62]. This tissue response, which is a combination of inflammation and astro-glial scarring, is triggered by a mismatch between the mechanics of the implanted device and the surrounding neural tissue [63, 64]. Over time, the buildup of scar tissue around the implantation site degrades the signal-to-noise ratio of electrophysiology recording [65]. Ultimately, this poses a limitation to the lifetime of the implants.

Stiffer, more rigid devices are shown to trigger a more severe response from the tissue [63, 66, 67]. This depends on the size, material density, and cantilever stiffness of the implantable device [63, 66, 67]. When the probe is anchored to the skull, this effect is exacerbated by brain micromotions [68, 69] which can be caused by heartbeat, respiration, and head movements [68, 70, 71].

To understand the neural basis of brain function and dysfunction, it is essential to perform chronic experiments over a long period of time. For electrical recording, flexible polymer devices have been shown to reduce damage to the brain tissue, and thus enable longer term neural recording [72]. An equivalent flexible optical platform is desired to enable chronic optical interrogation of neural circuits.

1.3.6 Probe Mechanics

The rigidity and stiffness of a neural probe is a function of its shape as well as the Young's modulus of the materials [73]. This is typically represented by a cantilever model anchored to the skull on one end [67]. The stiffness varies linearly with the Young's modulus of the constituent materials. The most common materials in integrated photonics are rigid dielectrics and semiconductors such as silicon, silicon nitride, or silicon dioxide [74]. Compared to common microfabrication materials, biocompatible polymers including Parylene C and PDMS have orders of magnitude lower Young's moduli, closer to most biological tissues (Table 1.1). Therefore, these materials have been prioritized to create less damaging neural implants. Histology studies have shown that polymer probes cause reduced FBR compared to rigid probes [72].

The cantilever stiffness of the device along the x-direction (k_x) and y-direction (k_y) can be obtained from the following equations, where b is the width of the cantilever, h is the thickness of the cantilever, L is the length, and E is the Young's modulus.

$$k_x = \frac{Ebh^3}{4L^3} \tag{1.1}$$

$$k_y = \frac{Ehb^3}{4L^3} \tag{1.2}$$

Material	Young's Modulus, E (GPa)
Silicon [77]	130-170
Silicon Nitride [78]	280-290
Parylene C [79]	1.5 - 4
PDMS [80]	1.32×10^{-3}
Brain Tissue [81]	$(1.389 - 1.895) \times 10^{-6}$
Skin [82]	$(6 - 22) \times 10^{-6}$
Muscle [82]	$(2\text{-}12) \times 10^{-6}$

Table 1.1: Young's Moduli of Common Materials

Reducing the width and thickness of the neural probe cross-section makes the device more flexible. Thus, even for rigid materials, devices can be made flexible by reducing the cross-section [75]. Even if flexible polymer substrates are used, electrophysiology readout requires routing metallic traces, typically made of rigid metals (i.e., Pt). In addition to reducing the cross-sectional size of these embedded traces, the device can be made more flexible using serpentine wiring patterns [76].

For optical access to tissue, large single-channel light guides, including quartz optical fibers and polymer silicone light guides [83, 84] have been used. However, these devices are typically large, which causes acute tissue damage and mitigates the flexibility benefits of the polymer materials. Therefore, a compact device composed of flexible polymers is preferred.

1.3.7 Flexible Probe Implantation

Although flexible neural implants cause less chronic damage to the tissue, they pose difficulties to implantation since they may lack the rigidity to penetrate the brain tissue. In order to be successfully implanted, the neural probe must not buckle under the insertion force [73]. The buckling force for a typical neural probe with a rectangular shank depends on the Young's modulus and geometry of the implant. The buckling force, F, depends on b, the probe width, h, the probe

thickness, L, the probe length, E, the Young's modulus, and K, the effective length factor that varies from 0.5 to 2 during multiple stages of implantation depending on the probe boundary conditions at the top and bottom ends of the probe, can be written [85]:

$$F = \frac{\pi^2 E b h^3}{12(KL)^2}. \tag{1.3}$$

If the buckling force F is less than the force necessary to penetrate the brain tissue, the probe will buckle and fold rather than entering the tissue during implantation. Therefore, the same strategies that make the probe more flexible, such as reducing the probe width and thickness, or using materials with lower Young's moduli, inherently render the resulting device more prone to buckling due to implantation.

To overcome the difficulty of implantation, techniques have been developed to stiffen flexible neural probes during the implantation process. These include using rigid shuttles [86], insertion guides [87], bioresorbable stiffeners [88, 89], pressurized fluidic channels [90], a PEG brace [85] or a dissolvable scaffold [91]. Although these techniques were primarily developed for implantation of flexible electrical neural probes, they can also in principle be adopted for any flexible device, including optical implants.

1.3.8 Conclusion

Based on the outstanding need for flexible optical implants, this thesis demonstrates two new photonic architectures to address this need in the neuroscience tool set. First, I develop a passive photonic waveguide platform based on the flexible biocompatible material Parylene C as the core. Second, I develop an active photonic µLED platform based on GaN µLEDs embedded in a flexible Parylene C substrate. The design, simulation, fabrication, characterization and demonstration for optogenetic stimulation of these two optical platforms are discussed in the following chapters.

1.4 Thesis Contributions

Individual contributions that were developed as part of this thesis include:

1. Optical mode simulation of Parylene C and PDMS as a photonic material platform to determine modal confinement and crosstalk.

2. Optical mode simulation of Parylene photonic waveguides formed by an etchless process of polymer deposition in a silicon mold.

3. Development of a microfabrication process to implement Parylene C and PDMS optical waveguides integrated with micromirrors for out-of-plane illumination and recording electrodes for electrophysiology recording, as well as a release process to create fully-flexible polymer devices.

4. Characterization of the propagation and bend loss characteristics of Parylene photonics, as well as output beam profiles of integrated micromirrors and electrochemical impedance of integrated recording electrodes.

5. In vivo demonstration of optogenetic stimulation of neurons using Parylene photonic waveguides to deliver light.

6. Development of a microfabrication process to implement arrays of GaN μLEDs and electrical interconnects on a flexible Parylene C substrate.

7. Electrical and optical characterization of GaN-on-Parylene μLED neural probes.

8. Thermal and optical modeling of heat and light spread in brain tissue from GaN μLEDs to determine thermally-safe stimulation paradigms.

9. Ex vivo demonstration of optogenetic stimulation of neurons using GaN-on-Parylene μLEDs to deliver light.

Chapter 2

Parylene Photonics

2.1 Introduction

This chapter discusses the concept of Parylene photonics, a novel integrated photonic platform to realize compact, biocompatible, and fully flexible polymer-based optical waveguide arrays that can deliver light efficiently into tissue in a minimally invasive way. Parylene photonic waveguides are realized entirely in a flexible, biocompatible material platform composed of Parylene C and PDMS polymers.

This passive architecture addresses the outstanding need for implantable optical neural interfaces for deep-tissue light delivery. Since the material platform is composed of mechanically compliant polymer materials, the resulting integrated photonic devices are flexible (Fig. 2.1) to reduce the tissue damage during chronic implantation. Furthermore, this integrated photonic platform may find future uses in other application domains which would benefit from the mechanical flexibility, including soft robotic sensors, wearable devices, and board-to-board optical interconnects.

Portions of this chapter are adapted, with permission, from the author's prior work in [92]

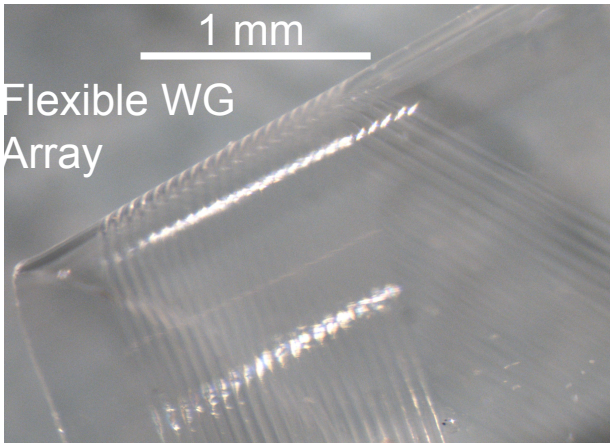

Figure 2.1: A released, flexible array of Parylene photonic waveguides.

2.2 Parylene Photonics Architecture

2.2.1 Parylene Optical Properties

The Parylene photonic waveguide architecture is composed of flexible, biocompatible polymers: Parylene C and PDMS. Parylene C is chosen as the waveguide core material due to its high refractive index (n = 1.639) and high transparency to visible wavelengths [93]. Compared to Parylene C, PDMS has a lower refractive index (n = 1.4) and is used as the waveguide cladding. PDMS is also optically transparent in the visible range and has demonstrated strong resistance to degradation in a biological environment [94, 95]. These materials provide a large index contrast (Δn = 0.239) to confine and guide an optical mode. A large index contrast causes the electric field of the optical mode to be primarily contained in the core, with less of the optical power propagating in the evanescent tail region in the waveguide cladding. As a result, high index contrast improves mode confinement and results in a small bend loss. A cross-sectional schematic of the waveguide structure on the wafer is shown in Fig. 2.2. Both Parylene C and PDMS are used in FDA-approved medical implants [96, 97] and are also widely used in research as well as

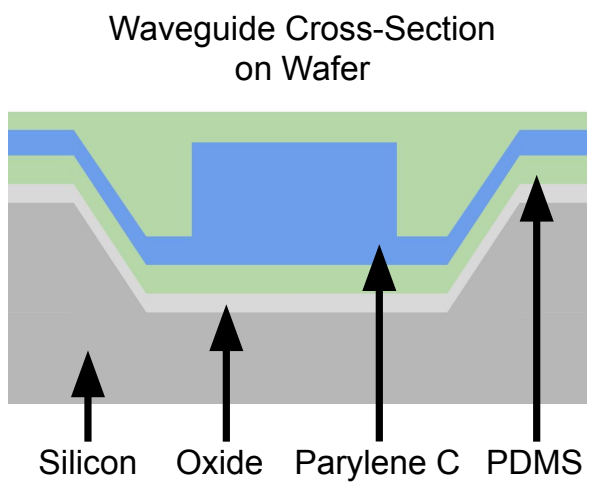

Figure 2.2: Schematic of the waveguide transverse cross-section on the wafer.

clinical applications [98]. With a proven history of biosafety in humans, Parylene C and PDMS form a compelling basis for an integrated photonic biointerface material platform with translational potential for medical applications.

2.2.2 Waveguide Operating Principles

The operating principle of a photonic waveguide is that confined optical modes guide light along the length of the waveguide. The optical modes can be determined by solving the Wave Equation:

$$\nabla^2 \vec{\mathbf{E}} = \frac{1}{c^2} \frac{\partial^2 \vec{\mathbf{E}}}{\partial t^2} \tag{2.1}$$

subject to the boundary conditions [99] to find the electric field profile of light in the structure. In a source-free medium, the boundary conditions at the interface of the core and the cladding are that the normal component of the electric displacement and the tangential component of the electric field are continuous across the waveguide boundaries, where the refractive index changes.

The refractive index pattern of the waveguide cross-section shapes the optical mode that is able to satisfy these constraints. For light propagating along the z direction in the waveguide at a fixed angular frequency ω, the electric field of an optical mode can be written:

$$\vec{E}(x, y, t) = Re\{\vec{E}_0(x, y)e^{i(\omega t - \beta z)}\}, \tag{2.2}$$

where $\vec{E}_0(x, y)$ is a vector field of the mode profile, and β is the modal propagation constant, defined as

$$\beta = n_{eff}\frac{2\pi}{\lambda}, \tag{2.3}$$

where n_{eff} is the effective index of the confined mode and λ is the wavelength of the light in vacuum. Compared to the core and cladding material, $n_{core} > n_{eff} > n_{cladding}$. The electric field mode profile of a 1 µm x 1 µm Parylene C waveguide surrounded by PDMS cladding is shown in Figure 2.3. This mode has an effective index of 1.488 at $\lambda = 460$ nm. The mode profiles and propagation constants are determined using a commercial numerical solver (Lumerical Mode Solutions, Ansys Inc).

2.2.3 Scaling Waveguide Size and Crosstalk

A key property of any integrated photonic platform is its potential for size scaling and dense integration. An arbitrarily small waveguide will support at least one guided mode as long as the core refractive index is larger than the cladding refractive index. However, such a waveguide may not be practically useful, since as the waveguide becomes smaller the effective index becomes closer to the cladding index and more of the optical power propagates outside the core region in the evanescent tail of the mode. The evanescent field can interact with surrounding materials resulting in absorption or scattering losses, or coupling into another waveguide structure. When

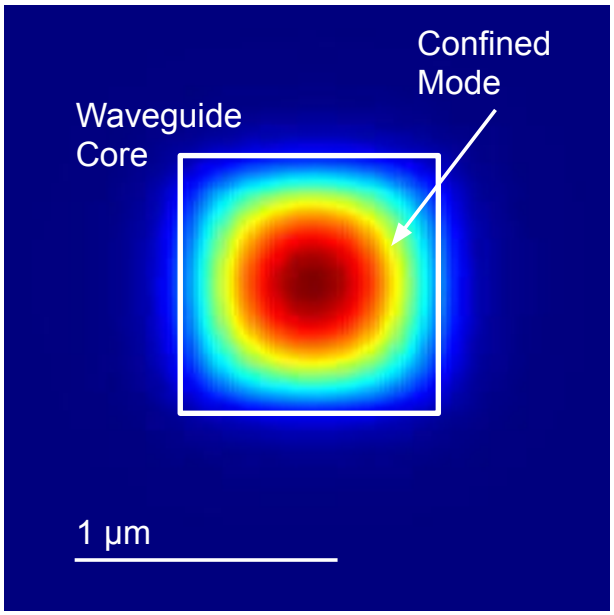

Figure 2.3: Mode field profile of the fundamental TE mode of a 1 µm × 1 µm Parylene photonic waveguide at $\lambda = 460$ nm, with an effective index of 1.488. The waveguide cladding is formed by PDMS (n = 1.4), which fills the full simulation region (2 µm x 2 µm). A perfectly matched layer boundary is used. Simulation is performed using the finite difference eigenmode solver of Lumerical Mode Solutions 2018b.

two waveguides are routed close together, the overlap in the evanescent fields of the waveguides allows power coupling between the adjacent waveguides. Therefore, densely integrated waveguide arrays are vulnerable to crosstalk between adjacent channels due to evanescent field coupling. Aside from the practical considerations of fabrication for small structures, a photonic material platform will have a practical density limit based on the physics of modal confinement defined by the index contrast. If waveguides are made too small and placed too closely together, optical power will couple from one waveguide to the next so that they will no longer function as independent optical channels.

To demonstrate the potential of Parylene photonics for dense system integration, a simulation study is performed using an eigenmode expansion (EME) solver (Lumerical MODE Solutions 2018b, Lumerical Inc., USA). Two parallel 1 µm x 1 µm waveguides with 1 µm gap between them are simulated over a propagation length of 5 cm (Fig. 2.4a). Input optical power in the "input waveguide" is normalized to 1 and the proportion of optical power in the adjacent "probe waveguide" is measured. Over the 5 cm propagation length, increasing power is observed in the probe waveguide due to evanescent field coupling (Fig. 2.4b). Over a 5 cm length, a total crosstalk of -32.86 dB is observed (Fig. 2.5).

This result indicates that Parylene photonics can be used to realize highly compact integrated photonic waveguides based on the high index contrast between the core and cladding materials. Although a sufficiently high-resolution fabrication process would need to be implemented to practically realize such small waveguides, the physics of the material platform itself would support size scaling for high-density interconnects with minimal crosstalk.

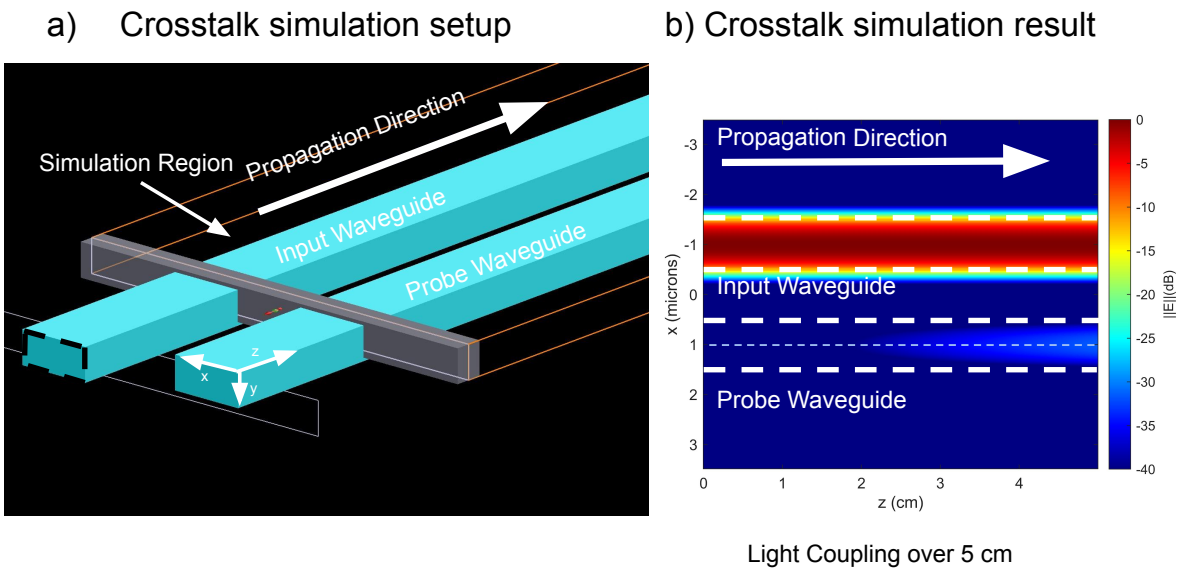

Figure 2.4: a) Schematic of two parallel waveguides for crosstalk analysis. The input waveguide (left) is powered while the probe waveguide (right) is monitored over a propagation length of 5 cm. b) Electric field profile of the parallel waveguide structure over a 5 cm propagation distance. Light coupling into the probe waveguide is observed. This result demonstrates that if a high-resolution fabrication process can be developed, then in principle, the high index contrast between Parylene C and PDMS support dense routing.

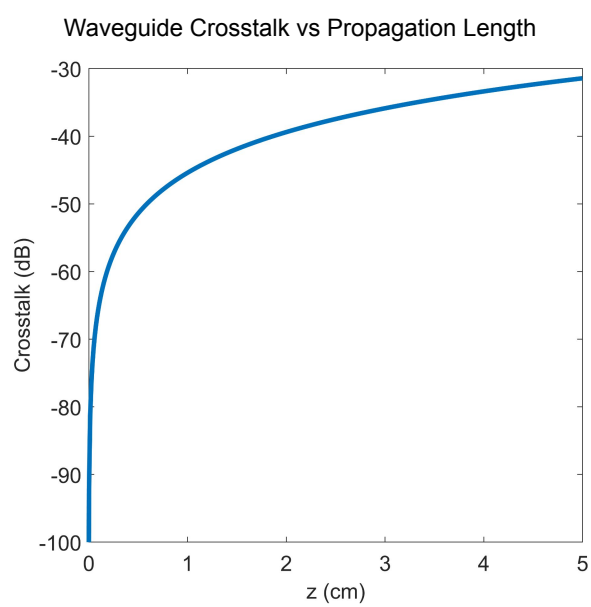

Figure 2.5: Plot of crosstalk in the probe waveguide vs propagation length in decibels (dB).

2.3 Parylene photonic Neural Probes

One specific application of Parylene photonics is to address the need for a compact, flexible, biocompatible photonic platform to deliver light into brain tissue with high spatial resolution for optogenetic stimulation.

2.3.1 Device Concept

An array of Parylene photonics waveguides in the shape of an implantable neural probe can be designed to deliver light from external light sources deep into the tissue (Fig. 2.6). Light is coupled into the waveguide from light sources at the backend of the probe, which would remain outside of the brain. Since it is outside of the tissue, the backend can be made relatively large to allow external connections to light sources or control circuitry. The probe has a long flexible shank that is implanted into the tissue, which contains waveguides to deliver light from the probe backend to a target depth. To minimize damage to the surrounding tissue, the shank should be thin and narrow. Ultimately, the shank width is determined by the waveguide pitch and the total number of channels.

Most optical waveguides and fibers operate in an end-firing configuration (Fig. 2.7a), where the output light is directed along the axis of the waveguide. The end-firing design produces an in-plane beam profile which illuminates a large region of the probe surface and limits the number of non-overlapping output ports that can be arranged on a shank. By contrast, an out-of-plane illumination profile minimizes the illumination volume overlap between adjacent optical channels, enabling high spatial resolution illumination patterns along the probe shank (Fig. 2.7b). For bidirectional neural probes which use recording electrodes to record electrophysiology activity of surrounding neurons, an out-of-plane beam profile also avoids direct illumination of recording electrode sites, reducing the severity of photoelectric artifacts [38]. In prior work, side-firing waveguides have been used to allow high-resolution light delivery along the probe shank [36].

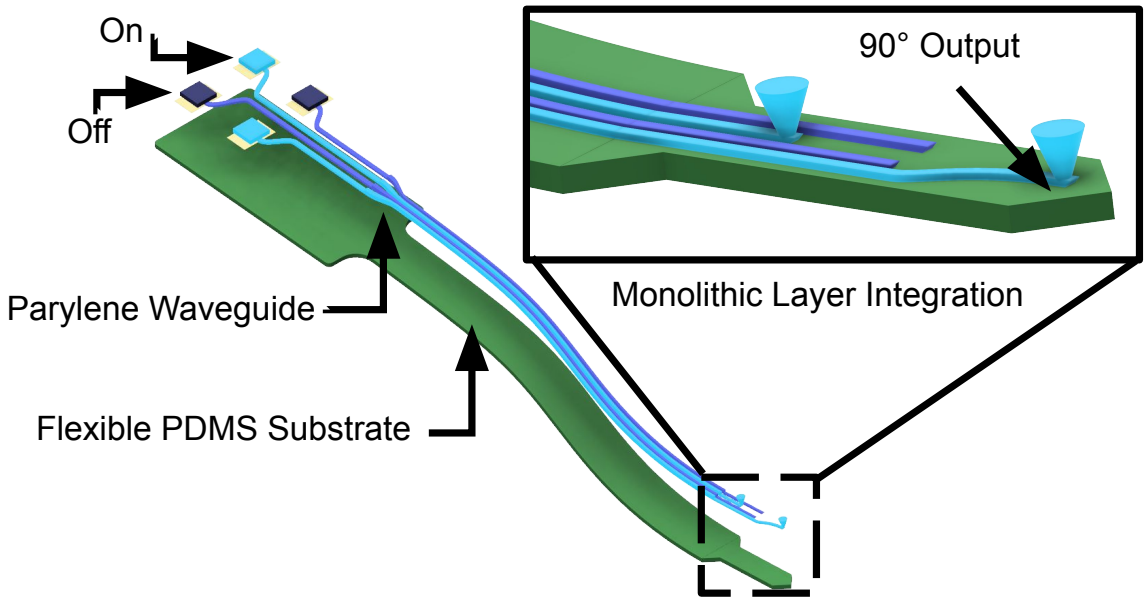

Figure 2.6: Schematic diagram of the Parylene C/PDMS optical waveguide neural probe. The inset image shows the monolithically-integrated device capable of out-of-plane light delivery.

However, in order to make use of integrated recording electrodes on the probe shank, out-of-plane illumination profiles from the top surface are preferred to enable collocated stimulation and recording volumes with surface electrode arrays.

Although Parylene photonics has the potential to be used in many biomedical applications, in this thesis I focus specifically on neural stimulation using optogenetics. Depending on the purpose of the desired experiment, different input/output port arrangements or probe geometries may be desired. The broader Parylene photonics architecture can be used to create many instantiations of neural probe designs, depending on the needs of a specific application area. For example, output ports may be spaced along the length of the probe shank to stimulate different regions of tissue (i.e., layers of cortex) or placed in a dense grid for interrogation of neural circuits in a small area.

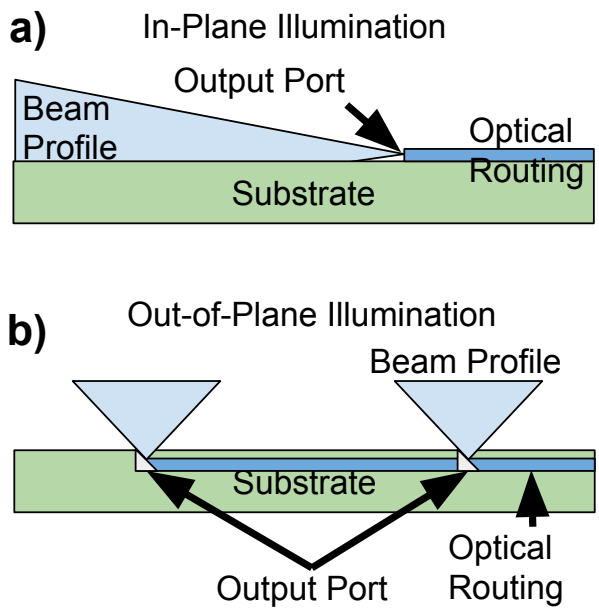

Figure 2.7: a) Schematic of the traditional in-plane illumination from an end-firing waveguide, where waveguide illumination is along the probe shank, limiting the spatial resolution. b) Schematic of the out-of-plane illumination in our design, where the waveguide output is oriented perpendicular to the probe shank, allowing for higher spatial resolution.

2.3.2 Micromirrors for Input/Output Coupling

A unique feature of the Parylene photonic waveguides for neural applications is the integration of micromirrors to redirect light at 90-degrees into or out of the plane of the waveguide. At the input/output ports of the Parylene photonic waveguides, 45-degree micromirrors can be monolithically integrated to enable broadband input/output coupling of light. In this thesis, I use a mold-based approach that first uses anisotropic etching to form a 45-degree silicon surface, which is used as a mirror mold (Fig. 2.8). Then, subsequent conformal deposition of polymers Parylene C and PDMS take on the precisely-defined topography of the silicon substrate. The fabrication details and characterization of these mirror structures will be presented in detail in the subsequent chapter. These monolithically embedded micromirror structures are capable of 90-degree out-of-plane input/output light coupling (Fig. 2.9). As output ports, these micromirrors enable out-of-plane illumination normal to the surface of the implantable probe.

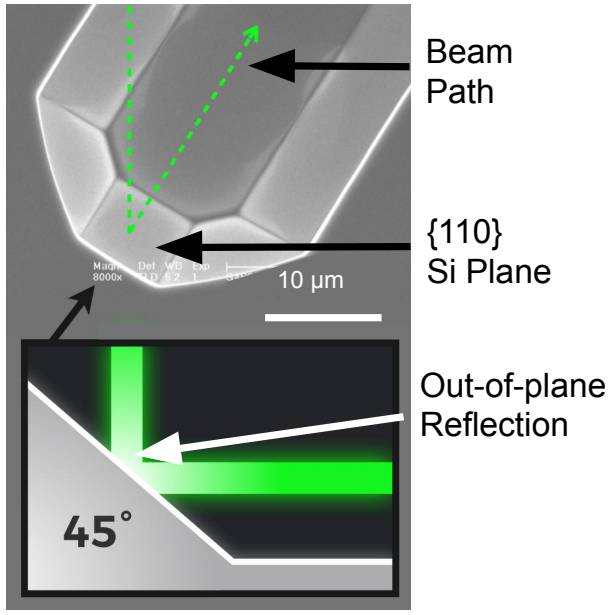

Figure 2.8: Scanning electron microscope (SEM) micrograph of a Si trench etched using KOH with the {110} plane indicated, which acts as the mold for the micromirror port, as shown in the cross-sectional schematic diagram.

2.3.3 Power Requirements for Optogenetic Stimulation

In order to successfully stimulate neurons, the complete optical system needs to have sufficiently low loss so that enough optical power reaches the neural tissue. The generally accepted threshold for optogenetic stimulation in 1 mW/mm^2 [100], although in practice, optogenetic stimulation has been demonstrated with significantly less power density, as low as 0.01 mW/mm^2 [101]. The system design must account for the losses which are incurred between the light source and the target neural tissue in order to ensure that sufficient power is delivered to evoke neural activity.

There are multiple sources of loss including the coupling efficiency, η, propagation loss, scattering and absorption in the tissue, and geometric spreading in the tissue (Fig. 2.10). First, the coupling efficiency determines the amount of optical power, P that is coupled from the light source into the waveguide, P_0.

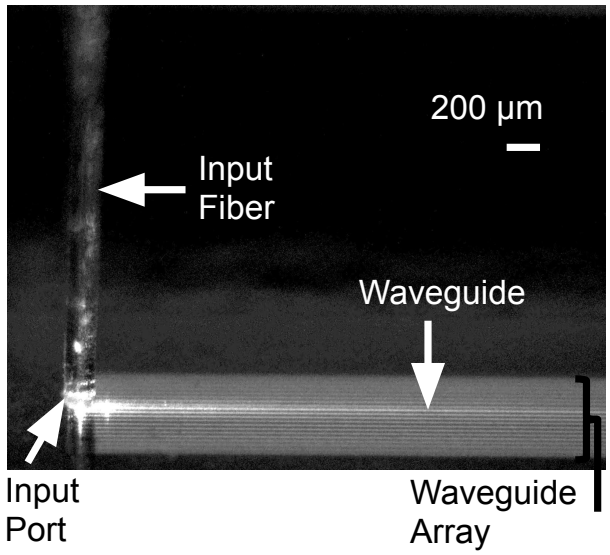

Figure 2.9: Out-of-plane input coupling from an optical fiber into a Parylene C waveguide using the 45° micromirror at the input port. Adjacent waveguides appear bright due to the brightfield illumination and reflections from the bright beam spot of the input fiber. Only a single waveguide is excited, as seen by the bright line of outscattered light in the center of the array. Fiber alignment was performed using a precision micromanipulator (PatchStar, Scientifica, UK)

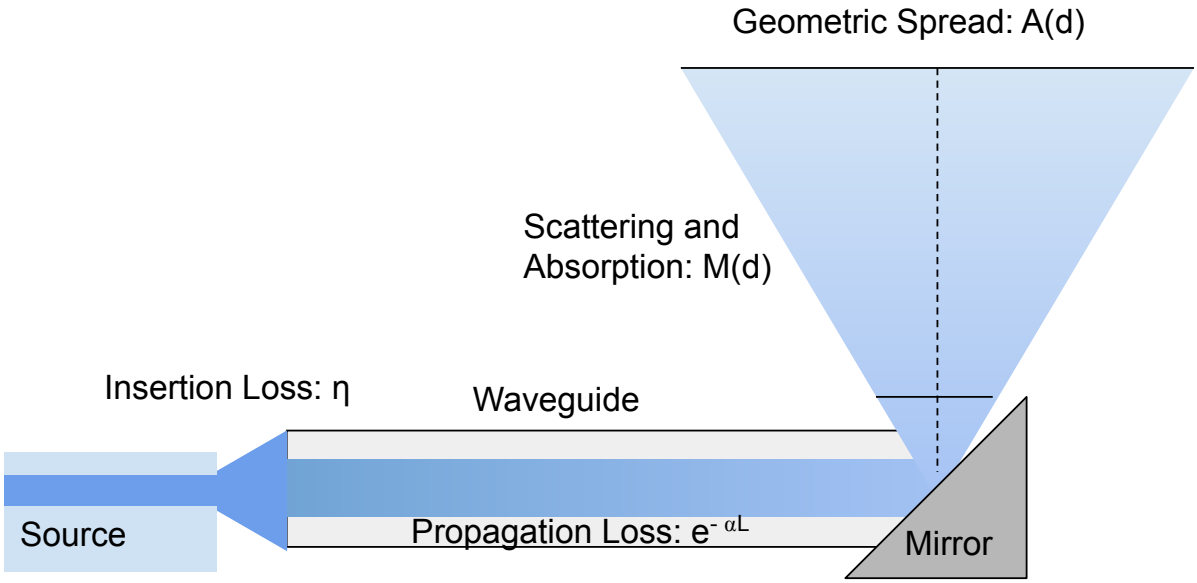

Figure 2.10: Schematic illustration of sources of loss in a waveguide system as light is coupled into a photonic waveguide, guided to a target location, and delivered into the tissue.

$$P_0 = \eta P \tag{2.4}$$

Once light is coupled into the waveguide, it is attenuated by propagation loss resulting from the scattering and absorption of light in the waveguide core. The power at the output of the waveguide, P_{out} is a function of the length of the waveguide, L, as well as the propagation loss constant, α.

$$P_{out} = P_0 e^{-\alpha L} \tag{2.5}$$

Once light is emitted from the output port, it is further attenuated due to scattering and absorption in the tissue, and also the geometric spreading of light [100]. If the light is emitted with a divergence angle of θ from the tip of the waveguide and propagates a distance d, then the light would be spread across the surface area of a spherical section.

$$A(d) = 2\pi d^2(1 - \cos\theta/2) \tag{2.6}$$

$$M(d) = \frac{b}{a\sinh(bSd) + b\cosh(bSd)}, \tag{2.7}$$

$$a = 1 + K/S, \tag{2.8}$$

$$b = \sqrt{a^2 - 1}, \tag{2.9}$$

The attenuation of light is approximately given by $M(d)$ according to the Kubelka-Munk scattering model [100] where S is the scattering coefficient and K is the absorption coefficient of tissue.

Thus, the final power density inequality to satisfy the stimulation of opsins can be written as:

$$\eta P e^{-\alpha L} M(d)/A(d) \geq 1\text{mW/mm}^2 \tag{2.10}$$

From this formula, we can gain basic intuitions about the design requirements for each component of the waveguide system. First and foremost, there is a quadratic decay of the light intensity in the tissue due to the geometric divergence of the beam in the tissue $(A(d))$, and a further exponential decay due to the scattering and absorption of light in the tissue $(M(d))$. If the neuron is closer, the attenuation due to the beam divergence, scattering, and absorption is reduced. Let's consider the case of the power requirements to stimulate neural tissue 200 µm away from the output port. Assuming S=19.96 mm^{-1} [102], and K=0.14 mm^{-1}[103] at a wavelength of $\lambda = 450nm$, M(200 µm)= 0.189, so more than 80% of the light would be lost due to scattering and absorption in the tissue before it reaches the target at a depth of 200 µm. Additionally, with a beam divergence of 15 degrees, there would be an additional geometric attenuation of A(d)= 0.0085 mm^2. Thus, in order to stimulate a neuron which is 200 µm from the output port with 1 mW/mm^2 intensity would require at least 45 µW of power to be delivered.

Therefore, the optical neural probe must be designed such that the output power satisfies:

$$\eta P e^{-\alpha L} \geq 45\mu\text{W} \tag{2.11}$$

Although it may seem that since the relationship is linear, any coupling efficiency η and propagation loss α can be overcome by an arbitrarily high input power P, this is only feasible up to a point. In general, single-mode fiber lasers are mainly available at powers $<$ 100 mW.

Multimode fiber lasers are available at higher power, but may not be able to efficiently couple to the waveguide input due to the large aperture ($>$ 50 - 100 µm diameter). Compact integrated diode laser sources have even lower powers on the order of 5 mW. Higher power laser sources require more complex coupling schemes involving free space optics or multimode input fibers. Therefore, there is a practical total system loss of 33 dB in a configuration using an external laser source, or 20 dB with an integrated laser diode source.

This optical system loss budget motivates the reduction of propagation loss for the photonic waveguides in order to enable longer waveguides to deliver light more deeply into the brain tissue. A typical length for a neural probe in mice is 6-9 mm long [104], whereas for primates, larger devices up to 5 cm in length may be needed [105]. Therefore, to be feasible for large-brain animals, a propagation loss of $<$ 5 dB/cm, combined with an insertion loss of $<$ 8 dB would be desired.

2.4 Conclusion

Parylene C and PDMS are excellent materials for a biocompatible photonic material platform due to their high index contrast and biocompatibility, as evidenced by its prior use in neural probe applications [106]. Here, for the first time, I have discussed a detailed simulation study of the properties of this novel material platform for integrated photonics. I have shown that the high index contrast of Parylene C and PDMS enables realization of compact optical waveguides for dense routing of light in arrays with pitches as small as 2 µm. Additionally, I have presented the design considerations for light delivery in tissue for optogenetics.

The takeaways from these simulations are that widely-used materials Parylene C and PDMS also have a refractive index contrast that can be used to form integrated photonic waveguides. Although the index contrast is not as large as silicon photonics, it is sufficient to enable micron-scale waveguide routing. Therefore, the material platform is promising for applications such as neural probes which must be compact and flexible.

This page intentionally left blank

Chapter 3

Optical Waveguide Microfabrication

3.1 Introduction

This chapter discusses a novel microfabrication process that was developed and optimized to realize high-performance Parylene photonic waveguides. This microfabrication process involves optical lithography to define waveguide structures at the micron scale. Furthermore, the use of photolithography to pattern device geometry allows for device layers to be defined in any arbitrary in-plane shape. This approach gives great flexibility for waveguide routing so that input/output ports can be placed in customized arrangements. Fabrication is performed at the wafer scale, so each wafer can contain hundreds of devices which are processed in parallel, making the entire process extremely scalable.

The process consists of 3 main steps. First, a precisely defined mold is patterned in the silicon substrate to create highly smooth 45-degree surfaces for micromirrors. Second, the waveguide cladding and core layers composed of PDMS and Parylene C are deposited onto the mold and patterned to form the waveguide. Third, the polymer waveguides are released from the mold to form flexible devices.

Portions of this chapter are adapted, with permission, from the author's prior work in [92]

3.2 Preparing the Silicon Mold

Fabrication is performed according to the fabrication process flow shown in Figure 3.2. The process begins with a 4 in Si wafer (n 100) with a 1 µm thermal oxide layer on the surface. The thermal oxide was lithographically patterned and etched using reactive ion etching (RIE) (Step 1 in Table 3.1) to form a hardmask for the silicon substrate. Wet etching in potassium hydroxide (KOH) mixed with Triton X-100 Surfactant (Step 2 in Table 3.1) was used to expose the 45-degree (110) Si Plane [107]. Wet etching was performed to a depth of 6 microns, verified via profilometry (Fig. 3.2a). After etching Si, the oxide hardmask was removed via 49% HF immersion for 2 minutes.

To target the (110) crystal plane of Si, which intersects the top plane of the waveguide at 45 degrees, the mask features should be oriented at 45 degrees to the (100) plane, which is indicated by the wafer main flat [108]. The 45-degree angle topography of the Si substrate forms the micromirror surface. Although KOH etching along the crystal planes of Si allows for precisely angled 45-degree sidewalls as shown in Figure 2.8, these planes can create sharp intersections between planes. In the context of optical waveguides, sharp bends tend to create optical loss due to scattering. However, the addition of the surfactant creates smooth surfaces as the orientation of the sidewall changes, allowing for bent structures as shown in Figure 3.1.

Subsequently, 300 nm of conformal oxide is deposited on the patterned Si surface using a plasma enhanced chemical vapor deposition (PECVD) process (Step 3 in Table 3.1). This material will be used later in the process as a sacrificial layer to protect the polymer devices during release from the Si mold (Fig. 3.2b).

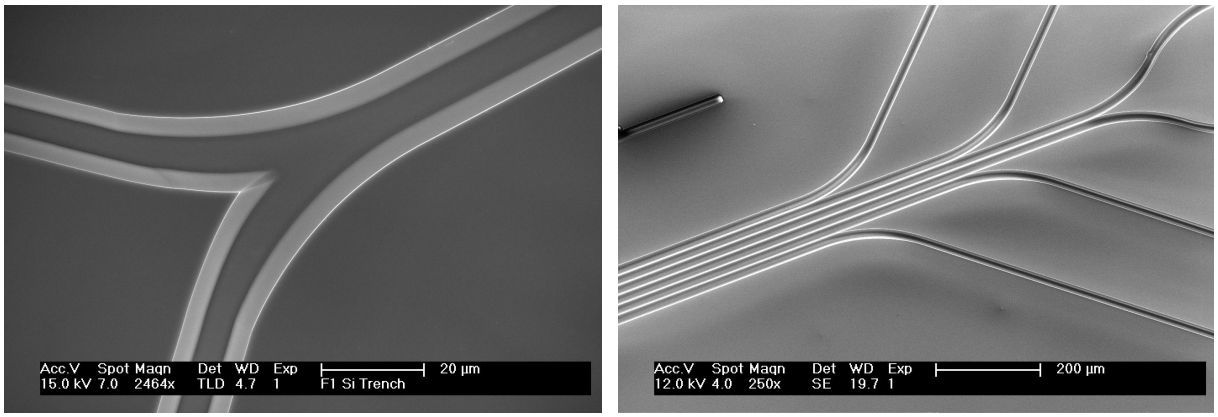

Figure 3.1: Fabrication of bent trench structures in Si using anisotropic KOH etching with the addition of surfactants to smooth the sidewall angle transitions.

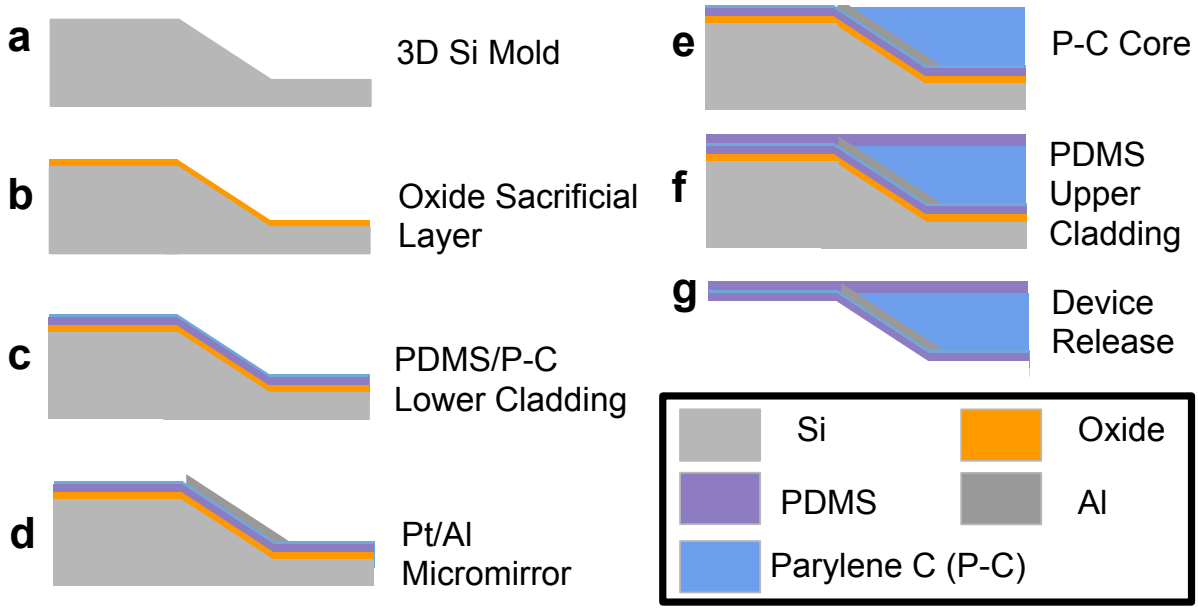

Figure 3.2: Fabrication process steps to realize Parylene photonic waveguides

3.3 Spin-coating PDMS Lower Cladding

3.3.1 Optimized Spin-coating Process

To form the lower cladding for the waveguide structure, a 1 µm PDMS layer was spin-coated on the silicon mold. Hexane was used to dilute the PDMS solution prior to spin-coating to reduce the viscosity of the solution and create a thin layer [109]. The process steps are as follows: The PDMS (Sylgard 184, Dow Corning Corp, USA) was thoroughly mixed (10:1 base:primer ratio by weight), filtered through a 0.2 µm membrane filter to remove any particulates, and diluted to 1:10 PDMS:Hexane by volume. The solution was spin-coated for 60s at 2000 rpm, with no spread step and a very high ramp speed (30 krpm/s setpoint). Finally, wafers were baked in a 1 Torr vacuum oven for 2 hours at 100 °C to cure the thin-film and remove the solvent. To verify the thickness of PDMS to be 1 µm, PDMS was mechanically removed from a portion of the wafer using a razor blade, and the step height of the thin-film was measured using a surface profilometer (P-15 Stylus Profiler, KLA Tencor, USA).

3.3.2 Spin-Coating Process Optimization

PDMS spin-coating is not perfectly conformal and is highly sensitive to the trench topography as well as the spin parameters. The final coating thickness is primarily determined by the steady-state achieved between the centrifugal force from the rotating substrate and the surface tension of the coated material. The evaporation rate of the solvent also plays an effect, causing the remaining polymer to gel on the surface of the wafer after a certain point [110, 111]. However, when a highly volatile solvent is used, the solvent rapidly evaporates during the first few seconds of the spin cycle, which becomes a dominant effect on the coating [112]. In the PDMS preparation

used here, the spin-coated film was empirically found to depend heavily on the initial spread step and ramp speed of the system, possibly due to the high solvent concentration of the preparation and high volatility of Hexane.

3D optical profilometry measurements (Zygo NV7000, AMETEK, USA) of the wafer surface were used to analyze the conformality of PDMS coating in the Si trenches. In order to optically profile the transparent PDMS surface, the samples were prepared by sputter deposition of 40 nm Al film to form a reflective surface for imaging. Samples with a 5 µm Si trench depth were prepared according to the previous steps of the fabrication process.

First, a sample was prepared with a 6s 500 rpm spread cycle, followed by a 60s 2000 rpm spin cycle with a 500 rpm/s ramp rate for each step. The surface profile of the thin-film coated over the Si trench is shown in the top panel of Figure 3.3. Samples coated with these parameters showed severe defects. First, the PDMS filled and partially planarized the trenches. From the 5 µm original trench depth, the depth after coating was reduced to 2.36 µm, more than 50% infill. Notably, the surface quality was also poor and significantly rough, with a measured root-mean-square (RMS) surface roughness of 110 nm. By removing the spread cycle and increasing the ramp speed to the spin coater maximum (nominally 30 krpm/s), the conformality of the coating is significantly improved (Fig. 3.3, lower panel). The trench infill is avoided with this method and the depth is now measured as 5.4 µm. The measured depth of the trench is actually increased after the coating due to the formation of a small edge bead around the upper edge of the trench. However, since this is beyond the region where the waveguide core and micromirror are located, it is unlikely to affect the device functionality.

The surface roughness was also seen to improve via the elimination of the spin coating spread step and increasing of the ramp speed. The relationship between the ramp speed and the resulting PDMS surface roughness is shown in Figure 3.4. Increasing the ramp rate to a nominal 30 krpm/s decreased the surface roughness from 110 nm RMS in the case of a 500 rpm/s ramp and 6s

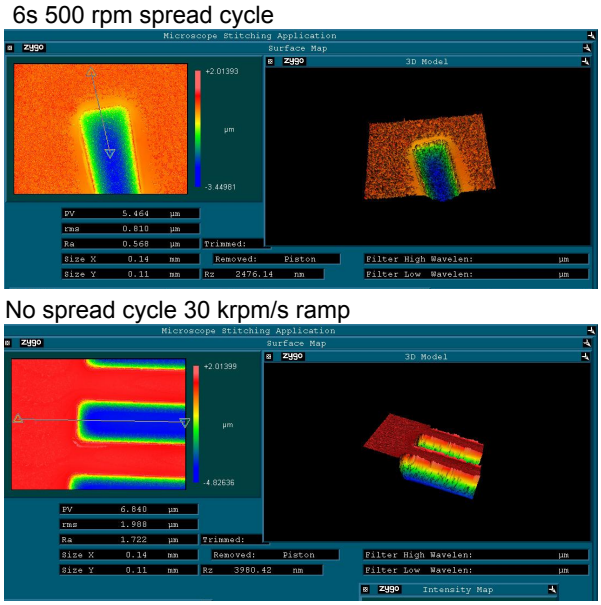

Figure 3.3: 3D optical profilometry measurements showing the topography of PDMS spin coated over a 5 µm Si trench mold under two spin-coating conditions.

500 rpm spread cycle to 40 nm RMS. Notably, in this figure, the ramp rate denotes the machine setpoint. The configuration of the machine did not allow the actual ramp rate to be measured in-situ. At such a high ramp rate, it is likely that the real acceleration is much lower than the rated number.

The PDMS spin-coating process is not perfectly conformal and is affected by the waveguide trench topography. The spin-coating parameters and size of the trench must be optimized to achieve the desired thickness at the bottom of the trench. 3D profilometry measurements show that multiple trenches of the same width routed in parallel tend to achieve uniform infill (Fig. 3.5). Notably, due to the topography of the trench structures, raised edge beads can be observed in the regions between the trenches. Here, the edge bead effect is more severe than in the parallel structures depicted in Figure 3.3 due to pockets formed where the waveguide trenches converge. However, the PDMS infill varies depending on the trench width (Fig. 3.5). Multiple waveguides can be routed through a wide common trench. However, when multiple thin trenches conform to

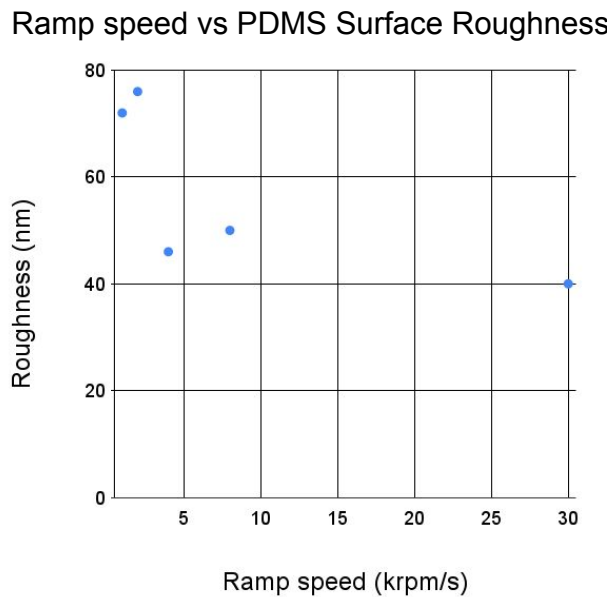

Figure 3.4: Relationship between ramp speed during spin coating and resulting roughness of PDMS thin-film.

a wider shared trench, there is a transition in infill between the two regions due to the difference in how the PDMS is spin-coated in the two regions. This should be taken into account when designing waveguide structures, since such a transition could cause a sharp bend in the waveguide core, which can cause optical power loss. Therefore, if the shared trench design is employed, the trench should remain a uniform width across its length.

Evidently, the conformality of the coating of the cladding material, PDMS, puts limitations on the shapes and arrangements of trench structures which can be practically envisioned using this technique. Since the Si mold is removed before the end of the fabrication process, it is possible to design structures with trenches that are much wider than necessary, without impacting the final device dimensions. One could imagine that instead of etching a narrow trench to contain the waveguides, a wide "valley" structure could be etched to contain all of the waveguide routing, shown schematically in Figure 3.6. Furthermore, instead of terminating the waveguides at the edges of the recessed region, small mesa structures could be formed to define the micromirror surfaces. Such an

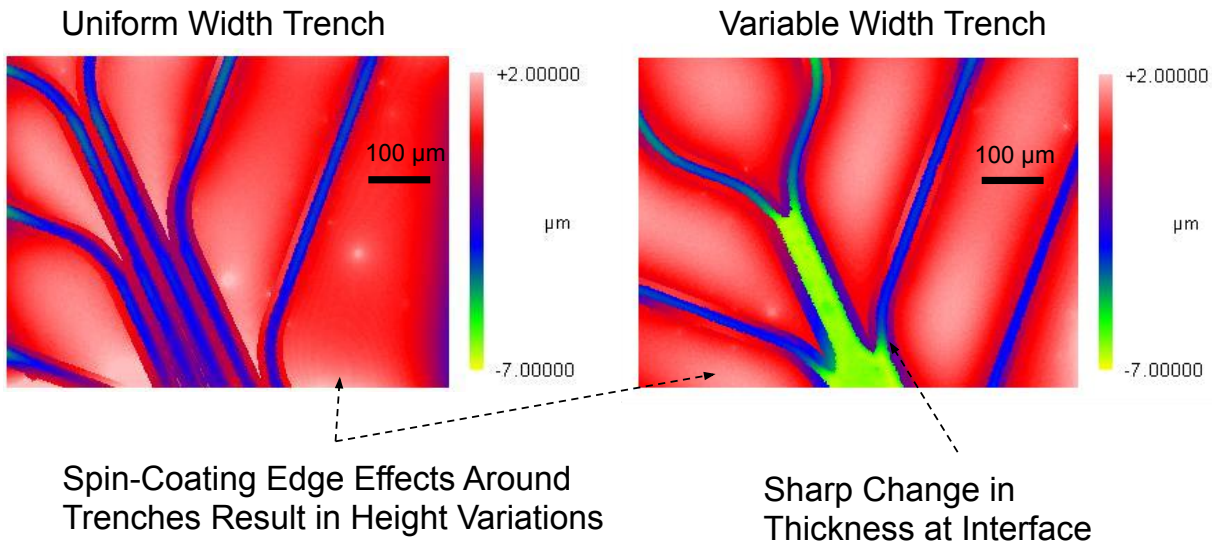

Figure 3.5: 3D optical profilometry measurement showing the topography of PDMS spin coated over Si trench molds with uniform and variable trench widths.

approach would alleviate the PDMS infill inherent to the trench waveguide design. Alternatively, further process optimization could be pursued in order to increase the conformality of PDMS, or alternative deposition strategies such as spray coating could be employed to produce a more conformal surface [113].

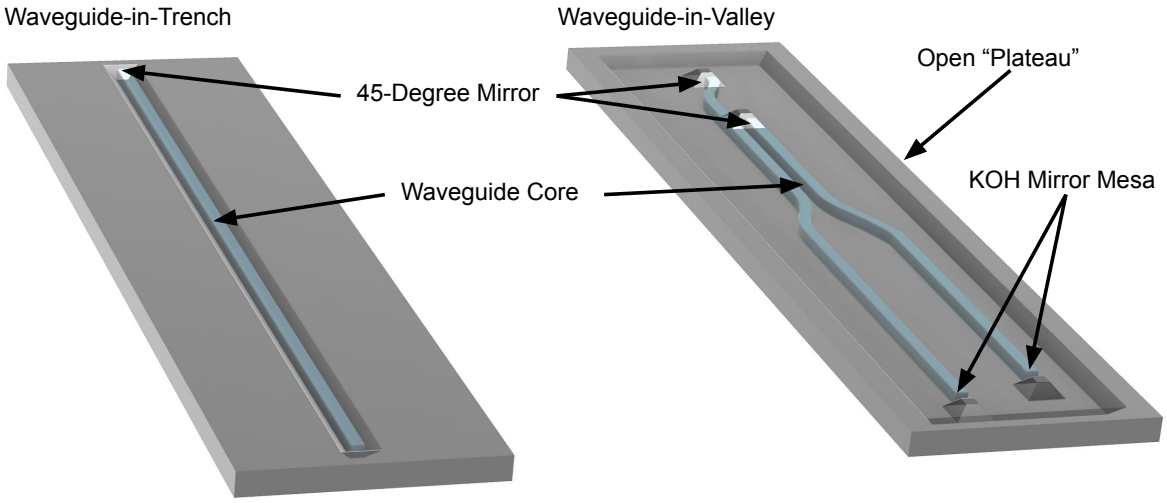

Figure 3.6: Schematic diagram showing how multiple waveguides can be routed in arbitrary configurations in a large open "valley" design in order to avoid the infill effects of PDMS in a narrow trench.

3.4 Metal Micromirrors

The next step of the process forms a highly reflective metal surface for the micromirrors. First, a thin (300 nm) Parylene C film is deposited on the PDMS to serve as an adhesion layer for photoresist and enable optical lithography (Fig. 3.2c, Step 4 in Table 3.1). This step is necessary due to the low surface energy of PDMS, which precludes directly spin-coating photoresist on the surface for lithography [114]. The Parylene C is deposited on the surface of PDMS via chemical vapor deposition, the adhesion between the two materials is strong [115]. The metal micromirror was then formed via electron beam evaporation of 5 nm Pt and 100 nm Al films (Steps 5,6 in Table 3.1) and lift-off using AZ 4210 photoresist. The thin Pt layer aids adhesion to Parylene C [116], while Al makes an ideal mirror surface for high reflectance across the visible range [117]. Alternatively, Au can also be used as an input mirror material (Fig. 3.9a) for red-shifted wavelengths. Lift-off was performed via acetone soaking, followed by pulsed (5-10 s)

sonication (Fig. 3.2d). The RMS surface roughness of the Al micromirrors was measured via optical profilometer (Zygo NV7000, AMETEK, USA) to be 49.3 nm with a standard deviation of 3.7 nm from mirror to mirror (N = 10).

In addition to the underlying material properties of the material, the reflectivity of the surface is also determined by the surface roughness compared to the wavelength of the light. A simple model [118] to describe the effect of surface roughness on the reflectivity of a surface is given by

$$R_s = R_0 e^{-\frac{(4\pi\sigma)^2}{\lambda^2}}, \tag{3.1}$$

where R_s is the specular reflection coefficient, R_0 is the reflectivity of the material, σ is the RMS surface roughness of the material, and λ is the wavelength of reflected light. Based on the measured surface roughness of our mirrors, we expect only 38% of the reflection to be specular in the case of $\lambda = 633$ nm, which reduces further to 15% for $\lambda = 450$ nm.

Although the surface roughness of the mirrors could be further improved during the fabrication process to increase the amount of specular reflection, diffuse reflection should also be coupled into the waveguide due to the high numerical aperture, although it may be coupled into higher-order modes which have higher propagation loss.

3.5 Waveguide Core Etching and Smoothing

The core of the waveguide is formed by depositing and patterning a layer of Parylene C. Parylene was deposited to an initial thickness of 3.5 µm using chemical vapor deposition (CVD). Due to the low selectivity of photoresist to Parylene C etching, a hardmask layer of 40-nm sputtered chromium is used (Step 7 in Table 3.1). The shape of the waveguide is lithographically defined and patterned in the hard mask layer by wet etching of Cr (Cr 1020 Etchant, Microchem GmbH, DE).

The patterns in the hardmask were then transferred to Parylene C via oxygen plasma RIE (Fig. 3.2, Step 8 in Table 3.1). Significant overetch (40%) is used to ensure that Parylene is completely removed from all regions of the wafer. The PDMS lower cladding acts as an etch stop layer since PDMS is not effectively etched by oxygen plasma alone [119]. Parylene C removal is verified via reflectometer measurements. Then, the Cr hardmask is stripped by immersion in Cr etchant.

3.5.1 Conformal Coating to Reduce Propagation Loss due to Surface Roughness

Propagation loss in photonic waveguides not only stems from the material properties (i.e. absorption), but also the quality of the fabrication. For example, optical scattering due to sidewall roughness from etching causes increased propagation loss. The propagation loss of Parylene photonic waveguides (λ = 532 nm) are reported in Fig. 3.7 for different waveguide widths. Comparing the losses of 15 μm waveguides to 30 μm waveguides, the average propagation loss is decreased from 40.1 dB/cm to 28.9 dB/cm for the wider waveguide (black circle dots in Fig. 3.7). This effect is likely due to the optical mode becoming more confined within the waveguide core, reducing the intensity of the interaction with the sidewall. However, this propagation loss is prohibitively high to practically deliver light into the tissue for optogenetics. Scanning Electron Micrographs (SEMs) of the waveguides reveal a very rough sidewall of Parylene C after etching in oxygen plasma (Fig. 3.8a) [121]. This surface roughness is responsible for high scattering losses in untreated waveguide structures.

Propagation losses in waveguides are the result of three main factors: 1) Material absorption, 2) Scattering due to material inhomogeneities and 3) Scattering due to sidewall roughness. The sharp increase in the propagation loss when decreasing the waveguide width suggests that the

[0]Portions of this section are adapted, with permission, from the author's work in [120]

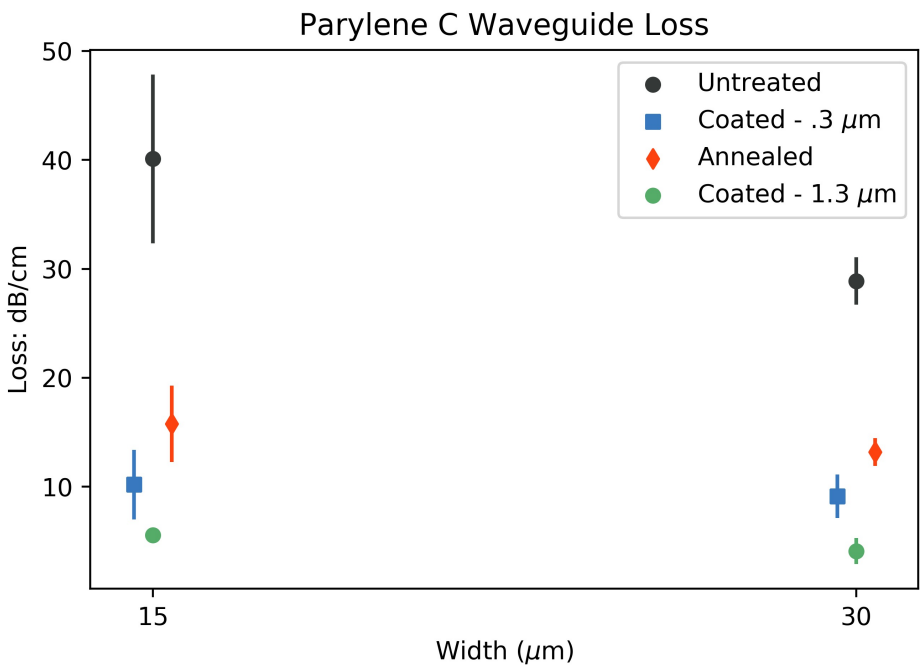

Figure 3.7: Waveguide propagation loss measured using the scattering method for four different cases: directly after fabrication and also under three different treatment methods (recoating-300 nm, recoating-300 nm and annealing, and recoating-1.3 µm) for two waveguide widths: 15 and 30 µm.

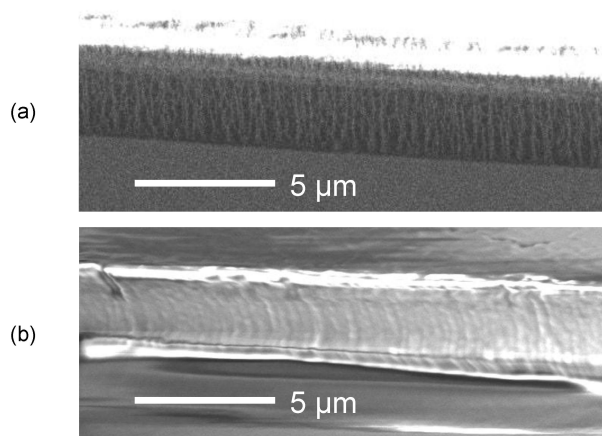

Figure 3.8: Scanning electron microscope (SEM) images showing a) characteristically rough Parylene C sidewall after etching and b) reduced sidewall roughness after additional 300 nm Parylene C deposition.

sidewall scattering is the primary source of loss due to the increased mode exposure to sidewalls. I tested two treatments to reduce the propagation losses of the Parylene photonics waveguides by addressing sidewall scattering:

1. Smoothing the sidewall with a conformal layer of Parylene C: Due to the conformal deposition process of Parylene C, I hypothesized that depositing a thin additional layer would fill the gaps in the sidewalls and effectively low-pass filter the roughness. The SEM images show that the sidewalls were smoothed after this treatment (Fig. 3.8b). The propagation loss was significantly reduced in all cases (Fig. 3.7). For example, in the case of the 15 μm waveguides, 300 nm of additional Parylene C decreased the average propagation loss from 40.1 to 9.2 dB/cm. An additional, identical sample was produced and coated with a 1.3 μm of Parylene C. This resulted in an even more dramatic loss reduction, to 4.1 dB/cm in the case of the 30 μm waveguides. Thus, conformal coating can effectively smoothen the sidewall and reduce the propagation loss, and the effect depends on the thickness of the material that is used.

2. Annealing at 300 °C in N_2 atmosphere: Previous work has shown that annealing Parylene C can increase crystallinity and improve adhesion between Parylene-Parylene interfaces by causing entangling of polymer chains at the interface [122]. I hypothesized that annealing could also benefit the waveguide performance by reducing Parylene C defects, or modifying the interface between the Parylene C core and smoothing layer. I performed annealing in a vacuum oven (Hotpack 633) in N_2 atmosphere at 300 °C for 3 hours. However, the propagation losses increased after the annealing treatment (Fig. 3.7 and Table 5.1). There could be several reasons for this change: the effects of annealing on the optical properties of Parylene C have not been studied, so the treatment may increase the optical absorption in the waveguide core. Alternatively, the annealing could modify the properties of the interface between the Parylene C core and the smoothing layer in a way that increases scattering or reduces modal confinement.

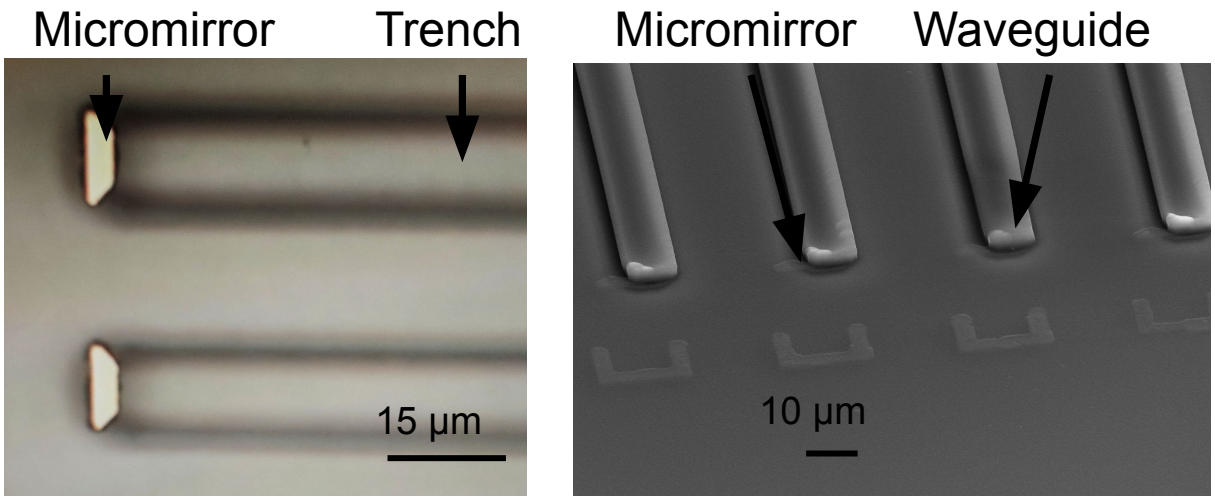

Figure 3.9: a) Microscope image of metal Au micromirror patterned via lift-off at the waveguide input/output port. b) Scanning electron microscope (SEM) image of waveguide core in waveguide trench.

The post-fabrication smoothing method described here, which uses the conformal deposition of Parylene C to effectively low-pass filter the sidewall roughness of the Parylene photonic waveguides, is able to dramatically reduce the propagation loss from > 30 dB/cm to < 5 dB/cm. By thickening the smoothing layer that is applied, even smoother sidewalls and therefore lower levels of loss may be achieved, although this process would have the additional effect of increasing the size of the waveguide cross-section, and thus decreasing the routing density that can be achieved with these waveguides. The three sequential Parylene C layers, i.e., the thin (300 nm) layer on PDMS substrate, the waveguide layer (3.5 µm), and the conformal coating on the top (1.3 µm) form the waveguide core with a total thickness of approximately 5 µm. Nevertheless, this treatment provides a route to the practical realization of Parylene photonic devices. A more systematic study of the influence of annealing on the optical properties of Parylene C waveguides and its interplay with the smoothing layer would be required to optimize these techniques.

The source of the sidewall roughness is, in part, due to the roughness of the metal hardmask. Switching from a Cr to an Al hardmask resulted in smoother sidewalls directly after the etch (Fig. 3.9b), and < 10 dB/cm propagation losses even without the smoothing layer. Therefore, further optimization of the masking and etching steps themselves may be pursued in the future to obviate the need for a smoothing step. Finally, the optical upper cladding of 1 µm PDMS was spin-coated (Fig. 3.2f).

3.6 Release Process

To release the device, first the device outline is etched: a 100 nm sputtered Al hardmask was deposited and lithographically patterned (AZ 4210) and wet etched (Al Etchant Type-A, Microchem GmbH, DE) to expose the outline of the device. (Step 9 in Table 3). PDMS cladding was etched and arrays were singulated using RIE (Step 10 in Table 3.1). Finally, the Al hardmask was stripped in Type A Al etchant. To release the devices, first the wafer was diced into individual chips, each containing 6-8 probes. On each chip, the silicon substrate was thinned down to 100 µm using backside grinding. Then, a laser cutter (ProtoLaser U4, LPKF) was used to cut the device outlines and singulate interleaved pairs of probes (Fig. 3.10a). The probe pairs were then mounted facedown to a glass slide using Crystalbond, and the Si backends of each device were protected using photoresist (AZ4110). The Si backing of the probe shanks was removed via an etching step in XeF_2 (Xactix e2). The sacrificial oxide layer protects the backside of the waveguide array from overetch of the XeF_2. Once Si was removed, the devices were soaked in Acetone overnight to release the chips from the glass slide. Then, the sacrificial layer was stripped in Buffered Hydrofluoric acid (BHF), resulting in a released, flexible waveguide array connected to a rigid Si backend (Fig. 3.2g, 3.10b). Devices are thoroughly rinsed in deionized water after release to avoid contamination of biological tissues by process chemicals.

Process Step	Tool	Parameters	Rate
1) Thermal Oxide Etch	PlasmaTherm 790 RIE	Gas: 22.5 SCCMs CHF_3	55 nm/min
2) Anisotropic Si Etch	Wet Bench	Concentration: 2M KOH, 60 ppm Triton X-100 Temperature: 90 °C Agitation: 210 rpm stirring	280 nm/min
3) PECVD Oxide Deposition	Trion Orion II PECVD	Temperature: 375 °C Pressure: 900 mTorr Gas: 75 SCCMs N_2O Gas: 70 SCCMs SiH_4	60 nm/min
4) Parylene Deposition	SCS Labcoter-2	Furnace Temperature: 690 °C Chamber Gauge Temperature: 135 °C Vaporizer Temperature: 175 °C Pressure: 35 mTorr	1g $\longrightarrow$ 300 nm 2g $\longrightarrow$ 1.3 µm 6.9g $\longrightarrow$ 3.5 µm
5) Pt Evaporation	Kurt J. Lesker PVD 75 E-Beam Evaporator	Pressure 3×10^{-7} Torr	3 Å/s
6) Au Evaporation	Kurt J. Lesker PVD 75 E-Beam Evaporator	Pressure 3×10^{-7} Torr	5 Å/s
7) Cr Sputtering	CVC Connexion Sputtering System	Pressure: 7 mTorr Pwer: 50 W RF Gas: 50 SCCMs Ar	10 nm/min
8) Parylene Etching	Trion Phantom II RIE	Gas: 14.0 SCCMs O_2 Pressure: 50 mTorr Power: 50 W RF	250 nm/min
9) Al Sputtering	Perkin Elmer 8L Sputtering System	Power: 100 W RF Pressure: 5 mT	30 nm/min
10) PDMS Etching	Trion Phantom II RIE	Pressure: 75 mT Gas: 30 SCCMs CF_4 Gas: 10 SCCMs O_2 Power: 200 W	200 nm/min
11) Si Etching	Trion Phantom II RIE	Pressure: 25 mTorr Power: 100 W Gase: 300 SCCMs SF_6	2.3 µm/min

Table 3.1: Process Parameters for Microfabrication Process

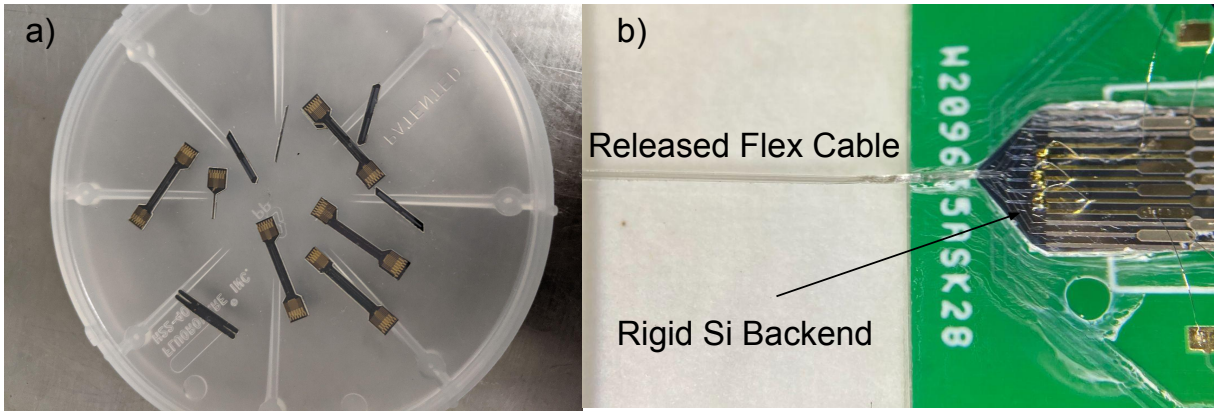

Figure 3.10: a) Parylene photonic waveguide neural probe chiplets on Si, singulated from a wafer via laser cutting. b) Released Parylene photonic waveguide neural probe. The flexible shank is released from the chiplet via XeF_2 etching, whereas the backend of the device is masked with photoresist to create a rigid region for bonding and handling.

3.7 Conclusion

In this chapter, I discussed a novel fabrication process for high-throughput, wafer-scale production of Parylene photonic waveguides with integrated micromirrors. The fabrication process has several novelties including the optimization of PDMS spin-coating for conformal deposition, use of Parylene C as an adhesion layer for Pt/Al micromirrors to overcome the low surface energy of PDMS, and the development of a novel technique using the conformal deposition of Parylene C to overcome propagation losses due to sidewall roughness.

Despite its low refractive index, PDMS has not been previously used as a substrate for integrated photonic waveguides. In general, PDMS is not compatible with photodefinable polymers, such as SU-8, due to the low surface energy of PDMS [114], which precludes spin-coating. These Parylene waveguides are the first to use PDMS as a substrate material. Other polymers with a lower refractive index than Parylene C and negligible optical absorption may also be explored as cladding for the Parylene C waveguides, and the presented fabrication process can be extended to realize similar waveguides in other polymer material platforms.

3. OPTICAL WAVEGUIDE MICROFABRICATION

The Parylene photonic waveguides discussed in this chapter serve as a practical platform for biophotonic applications. This opens the possibility to realize a new class of compact, flexible, biocompatible, all-polymer integrated photonics.

Chapter 4

Etchless Architectures Enabled by Mold-Based Fabrication

4.1 Introduction

One of the key challenges of integrated photonics is the development and optimization of the fabrication process to realize optical waveguides. This is particularly important to enable novel waveguide material platforms, including Parylene photonics. This chapter discusses novel waveguide architectures which can utilize the conformal deposition of polymers to create Parylene photonic waveguides in a mold. Usually, lithographic patterning and RIE etching are used to define the waveguide core in the shape of a ridge waveguide. Sidewall roughness due to fabrication process imperfections is a large contributor to propagation loss in photonic waveguides (See Chapter 3). For example, the performance of Parylene photonics is mainly limited by the etched sidewall roughness, which can be partially alleviated by depositing a conformal smoothing layer.

Portions of this chapter are adapted, with permission, from the author's work in [123]

4. ETCHLESS ARCHITECTURES ENABLED BY MOLD-BASED FABRICATION

Fabrication processes have been extensively developed and optimized to improve sidewall roughness due to etching [74, 115, 124]. An alternative approach would be to design a fabrication process such that etching is entirely avoided. Etchless fabrication of silicon photonic waveguides has been demonstrated [125, 126, 127], where a silicon waveguide core is isolated in a silicon-on-insulator thin-film using an oxidation process. In this method, the waveguide architecture is a ridge surrounded by SiO_2 from the sides. Similarly, etchless PDMS waveguides have been fabricated by using ultraviolet light exposure to locally increase the refractive index and form the waveguide core [128]. These techniques have enabled patterning the refractive index of a structure without an etching process that can introduce rough sidewalls. However, these techniques depend on the specific material properties and chemistry of silicon and PDMS. In this chapter, I demonstrate an etchless waveguide architecture that can be formed by material deposition in a trench mold without any subsequent processing steps.

There has also been work exploring the trench waveguide geometry using conformal deposition of the core material in a triangular or trapezoidal silicon mold to form the waveguide core [129, 130, 131, 132, 133]. These techniques have primarily explored triangular V-shaped trenches composed of traditional high-index contrast materials such as SiN and SiO_2. Additionally, these previous works exploit the thickening of polymer materials at the bottom of the trench. Previous work also employed silicon etching to form a smooth trough which was filled with optical epoxy (Emerson and Cuming 1269A) polymer via a casting and doctor blading process to form a waveguide core [134, 135]. All of these techniques fundamentally use a thicker region of high-index core material within the trench to confine and guide an optical mode. By contrast, the results presented here achieve 2D modal confinement without any thickening of the core to confine an optical mode.

Here, I show that a stratified material stack of continuous layers in a 3D mold can confine and guide an optical mode in 2D without any change in the waveguide core thickness or refractive index along the lateral direction. This structure is fundamentally different from conventional 2D

photonic waveguides, such as ridge waveguides or optical fibers, that confine light based on a boundary between waveguide core and cladding. It is also fundamentally different from traditional etchless waveguides that rely on a thickening of the waveguide core to create a rib waveguide. This novel waveguide structure confines light along the lateral direction based solely on bends in the waveguide cross-section (Fig. 4.1a). This design has unique performance characteristics compared to traditional ridge waveguides. A theoretically perfect ridge waveguide with no scattering or absorptive losses would suffer no propagation loss. On the other hand, the stratified trench geometry has an additional form of intrinsic loss, as light slowly leaks out of the bottom of the trench into the sidewalls. Through careful design of the structure, light can be effectively confined at the bottom horizontal segment of this stratified trench waveguide in 2D with low light leakage (Fig. 4.1b). The intrinsic leakage mechanism and design strategies to reduce this loss to practical levels are discussed in the following sections. Of course, like any other waveguide, practical limitations such as material absorption and surface roughness will add to the total propagation loss.

In my simulations, I assume that the materials are perfect and there is no material absorption. I also assume that the mold is perfect, and its surfaces do not have any roughness. In this way, scattering and absorptive losses are ignored and only the intrinsic leakage loss of the waveguide is characterized. I consider a thickness of the waveguide substrate and cladding of 1 µm to correspond to what I used in my Parylene photonics fabrication process, discussed in Chapter 3 and only vary the thickness of the waveguide core. The trench geometry is defined by four parameters: W, the width of the trench, D, the depth of the trench, Θ, the angle of the sidewall, and T, the thickness of the thin-film waveguide core layer (Fig. 4.2). For my analysis, I use a waveguide core material of Parylene C ($n = 1.639$), and PDMS as the waveguide cladding and substrate with ($n = 1.4$). The designs presented in this chapter provide etchless modal confinement (Fig.

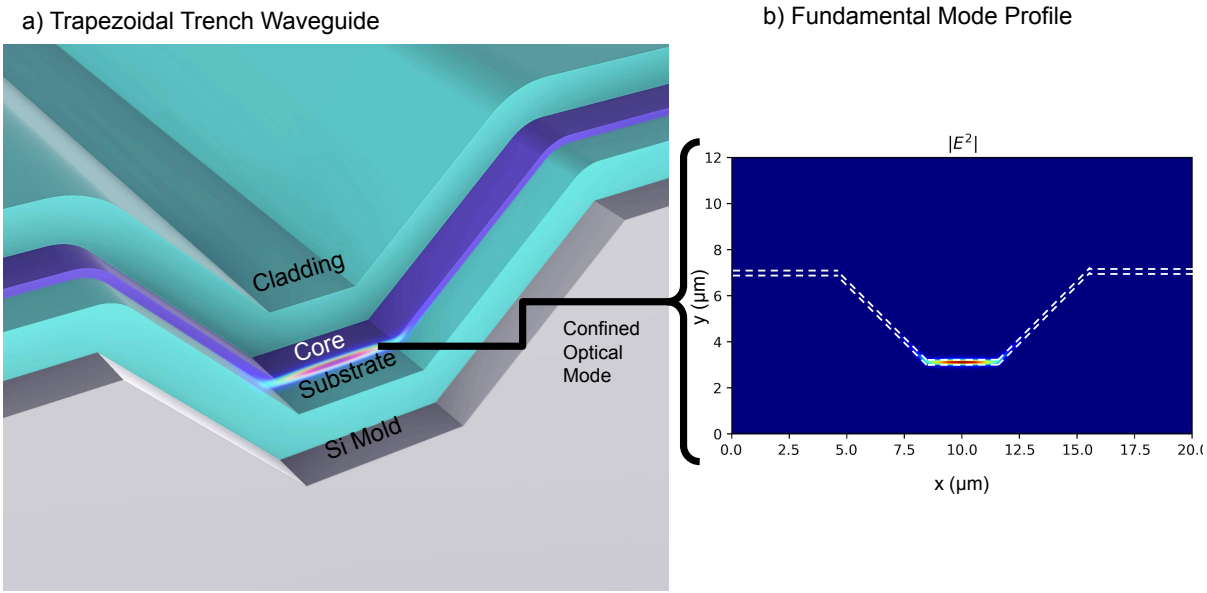

Figure 4.1: a) 3D model of the trapezoidal stratified trench waveguide cross-section b) Fundamental mode profile showing a confined optical mode at the bottom of the trench. The outline illustrates the shape of the waveguide core.

4.2) with a low intrinsic propagation loss of 0.139 dB/cm. All simulations are performed at the wavelength $\lambda = 470$ nm, which is of interest for optogenetic stimulation using channelrhodopsin2 (ChR2), a widely-used opsin.

This architecture has the potential to be useful for new polymer material platforms such as Parylene photonics, which lack optimized fabrication processes. This will help address the outstanding need for flexible and biocompatible integrated photonic devices[136, 137, 138]. The most common method of patterning polymers is to use O_2 plasma etching to break the polymer chain through oxidation and physical removal of reaction products[139, 140]. However, as discussed in the prior chapter, O_2 plasma etching process can result in very rough sidewalls, which contribute to a large propagation loss. The waveguide architecture presented here does not require etching the waveguide core, obviating the need to mitigate the issue of sidewall roughness through optimized fabrication techniques or smoothing treatments.

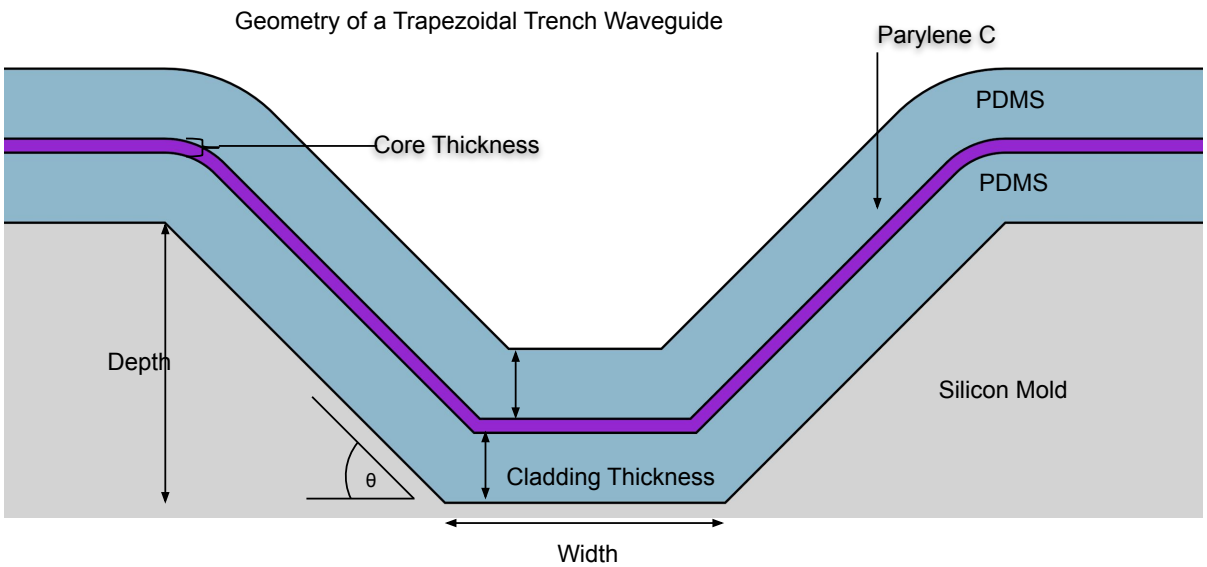

Figure 4.2: Schematic illustration of the mold-based waveguide cross-section and design parameters, depth (D), width (W), sidewall angle (Θ), core thickness (T), and cladding thickness (T_{Clad}) in trapezoidal stratified trench waveguide, where mode confinement is achieved via introducing corners into the waveguide. In this study, The cladding thickness is 1 µm for simplicity.

4.2 Etchless Mechanisms for 2D Light Confinement

Even when materials are modeled to be perfectly lossless, the presented etchless stratified trench waveguides have intrinsic losses due to light leakage from the bottom of the trench to the sidewalls. To explore design strategies to minimize this leakage loss, I consider a 90-degree rectangular stratified trench waveguide (Fig. 4.3). This structure can be approximated as the combination of multiple horizontal and vertical segments of slab waveguides. Although the waveguide thickness does not change, the corners of the waveguide structure divide it into individual sections composing the top, bottom, and sides of the channel. The modal structure of the 2D structure is more complicated than a combination of slab waveguide modes, but I use this simplification to illustrate the intuition of the waveguide behavior based on coupling of optical modes between the individual segments.

Considered independently, each segment of the structure can be analyzed as a slab waveguide. In this case, the modal structure of the horizontal segment at the bottom of the trench (segment A) and the horizontal segment on top (segment C) are identical. Since the polarization and propagation constants of the modes are the same, optical power can potentially couple between these two segments. The coupling of light from the bottom segment to the top horizontal segment would result in the leakage of light out of the center of the trench, the waveguide geometry must be designed so that there is sufficient gap between them to minimize the coupling.

Using a perturbation analysis method, the coupling between any two modes of the waveguide segments, e.g., modes m and n can be obtained as,

$$P_m(z) = P_{0n}\frac{\kappa^2}{\kappa^2+\delta^2}\sin^2\sqrt{\kappa^2+\delta^2 z}, \tag{4.1}$$

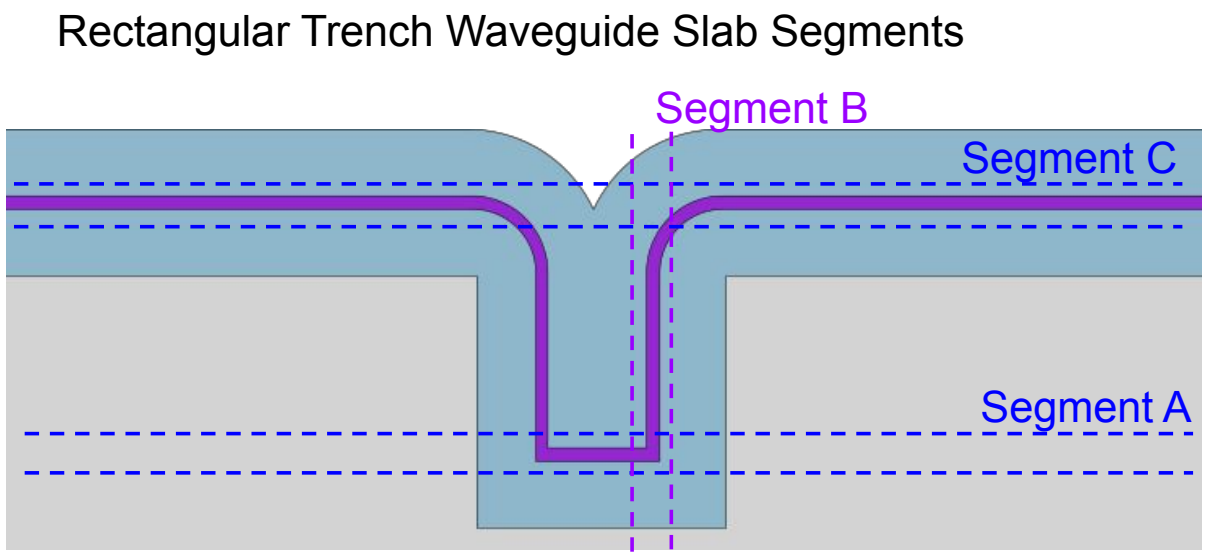

Figure 4.3: Schematic cross-section of the 90-degree rectangular stratified trench waveguide structure, showing how segments can be approximated as slab waveguides.

where $P_m(z)$ is the optical power coupled to mode m over a coupling length z and P_{0n} is the initial optical power in the bottom segment. The coupling coefficient, κ, and the phase mismatch between the two modes, 2δ, can be calculated as,

$$\kappa = \frac{\omega}{4}\epsilon_0 \iint \Delta n_n^2(x,y)\vec{E}_{0m}(x,y)\cdot\vec{E}^*_{0n}(x,y)dxdy, \tag{4.2}$$

and

$$2\delta = (\beta_m + \kappa_{mm})(\beta_n + \kappa_{nn}). \tag{4.3}$$

In these expressions, $\Delta n_n^2(x,y)$ is the refractive index perturbation caused by the top segment waveguide to the bottom segment waveguide. Also, κ_{mm} and κ_{nn} are small corrections to the propagation constants of each mode due to the dielectric perturbation of the other waveguide.

The increased power transfer between different segments of the waveguide structure as a function of geometrical parameters can be evaluated by either an increase in κ or decrease in δ. For example, the field strength of the confined slab fundamental mode of segment A at the bottom of the trench, $\vec{E}_{0A}$, exponentially decays outside of the core:

$$\lim_{c\to\infty} \vec{E}_{0A}(x,y) = 0 \tag{4.4}$$

.

Therefore, the coupling between the top and bottom segments decays by increasing the depth of the trench, D (Fig. 4.4a), because

$$\lim_{D\to\infty} \Delta n_A^2(x-D,y)\vec{E}_{0A}(x,y)\cdot\vec{E}^*_{0C}(x-D,y) = 0, \tag{4.5}$$

which leads to $\lim_{D\to\infty} = 0$. Therefore, deeper trenches are expected to exhibit less loss.

The coupling between the horizontal slab mode at the bottom of the trench and adjacent sidewall slab modes is another route for power leakage. Consider the TE_0 mode of the horizontal slab waveguide structure in segment A, which has only an E_x component. In the equivalent TE_0 mode in the 90-degree sidewall, segment B only has an E_y component (Fig. 4.4b), due to the rotated frame of reference:

$$\vec{E}_{0A}(x,y) = E_{x0A}(x,y)\mathbf{a_x} \tag{4.6}$$

$$\vec{E}_{0B}(x,y) = E_{y0B}(x,y)\mathbf{a_y} \tag{4.7}$$

Therefore, these two modes are orthogonal, i.e., $\vec{E}_{0A} \perp \vec{E}_{0B}$, which makes the coupling coefficient zero, since $\vec{E}_{0A}(x,y)\cdot\vec{E}^*_{0B} = 0$.

In the full 2D structure, unlike the slab mode equivalent approximation, pure TE modes do not have a perfect field polarization. For example, the TE-like mode of the bottom segment A, has a small E_y component. Therefore, in the 2D case, we would expect a small coupling between segments A and B.

Another potential optical leakage path is via coupling between the horizontal slab TE_0 mode at the bottom of the trench and the TM_0 mode of the vertical sidewall Fig. 4.4c. These modes have the same polarization, due to the 90-degree sidewall orientation. This creates a leakage pathway through the coupling of the optical mode of the bottom of the trench to the vertical sidewall and eventually to the top segment. This leakage path is primarily limited by the phase mismatch 2δ. In a 200 nm-thick slab waveguide, the phase mismatch between the TE_0 and TM_0 modes is significant: 0.56 μm^{-1}. However, as the thickness of the core becomes larger, the propagation constants converge as the modes become more confined in the core, reducing the phase mismatch. Thus, our model predicts increased coupling efficiency and power leakage from the bottom of the trench as the thickness of the waveguide increases. This behavior is contrary to a more traditional ridge waveguide structure, where increased core thickness typically increases the modal confinement. In the following sections, I will demonstrate that the intuitive prediction that reducing the thickness of the waveguide will reduce losses is corroborated by finite-difference eigenmode (FDE) simulation of the full 2D structure.

The fundamental mode of the 200 nm-thick 90-degree stratified trench waveguide computed using FDE simulation is shown in Fig. 4.5. Light is mainly confined in the bottom trench of the waveguide, and only a small amount of the power into the sidewalls and upper regions of the waveguide structure. The E_x and E_y fields confined to the horizontal and vertical sidewalls are shown in Fig. 4.6. The conditions to ensure effective confinement of light in the bottom segment A are (i) large enough depth of the trench to prevent direct coupling of the optical mode in the

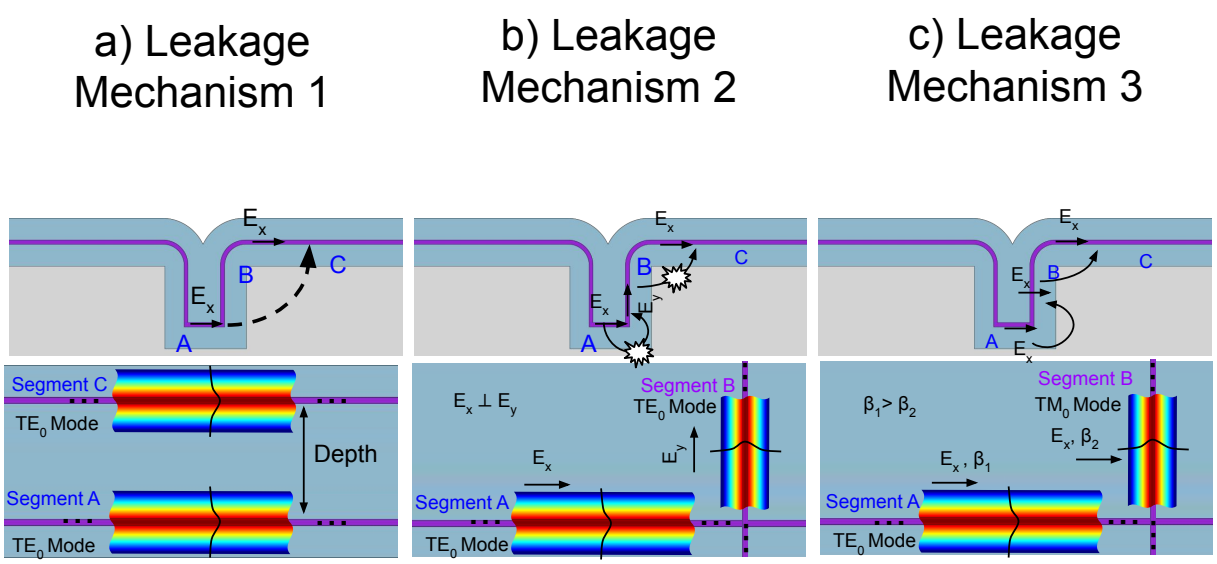

Figure 4.4: a) Juxtaposition of the segment A and segment C slab equivalents, showing the electric field decay outside of the core. b) Juxtaposition of the segment A and segment B slab equivalents, showing the perpendicular polarizations of the TE_0 modes. Inset images show the log-scale slab mode E-field intensity profile. c) Juxtaposition of the segment A and segment B slab equivalents, showing the β mismatch between the TE_0 and TM_0 modes of the two segments.

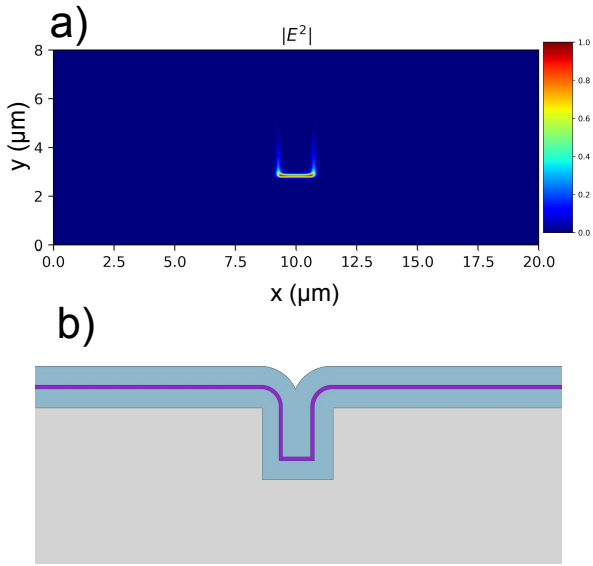

Figure 4.5: a) Fundamental mode of a 90-degree stratified trench waveguide. b) Schematic cross-section of the waveguide structure, showing the layers formed by conformal deposition into a rectangular mold. Due to the conformal deposition, the top corners are rounded.

bottom segment A to the top segment C; and (ii) small enough core thickness to prevent leakage through the coupling between the TE_0 mode of the bottom segment A and the TM_0 mode of the sidewall segment B.

The mechanism of the light confinement that was explained for the stratified trench waveguide with vertical sidewalls can be extended to other waveguides with angled sidewalls. The only difference is that when the sidewall segment B is not orthogonal to the bottom segment A, then the TE_0 optical mode of the bottom segment A would not be orthogonal to the TE_0 mode of the slanted sidewall segment B, thus creating a leakage pathway, which can be mitigated by minimizing the field overlap. Using this intuition, a waveguide structure can be designed which supports guided modes confined to the bottom of the trench without any core thickness variation along the width.

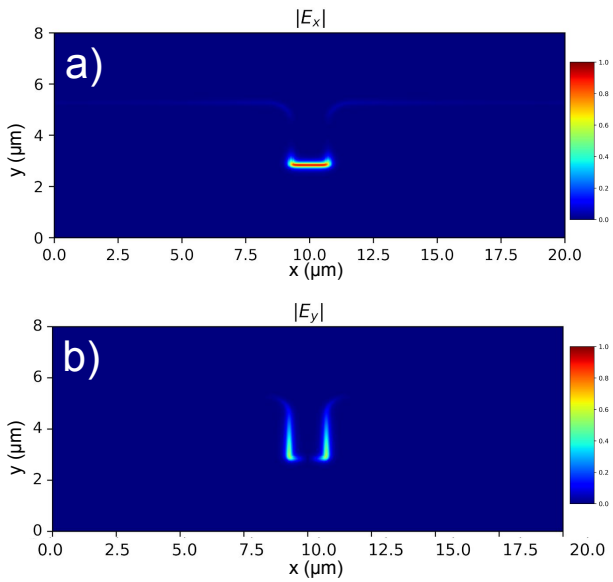

Figure 4.6: a) E_x component of the fundamental mode. The field is primarily contained in the horizontal segments. b) E_y component of the fundamental mode. The field is primarily contained in the vertical segments.

4.3 Low-loss Guided Modes in Trapezoidal Stratified Trench Waveguides

Here, I demonstrate a design for low intrinsic loss (0.139 dB/cm) guided modes in a trapezoidal stratified trench waveguide structure with 45-degree trench sidewalls. This design would be compatible with the KOH etching orientation used to define 45-degree angle mirrors in prior chapters. The mold geometry is formed by a 4 μm trench width and 4 μm trench depth, and 45-degree sidewalls. I then modeled conformal depositions of 1 μm PDMS substrate, 200 nm Parylene C core, and 1 μm PDMS cladding. These dimensions are chosen as a result of the parameter sweeps discussed in the following sections. FDE analysis shows the existence of several guided modes at the bottom segment of the stratified trench waveguide.

The fundamental confined mode of the optical waveguide is shown in Fig. 4.7a, which has an effective index of $n_{eff} = 1.52$. This mode is predominantly guided in the horizontal center section of the waveguide at the bottom of the trench (Fig. 4.7b). The magnitudes of the horizontal electric field component (E_x) and the vertical electric field (E_y) are shown in Fig. 4.8. Most of the guided mode power is concentrated in the E_x component of the electric field, which is mainly confined in the horizontal segment of the waveguide at the bottom of the trench. There is a comparatively weak E_y component, which is mainly confined in the diagonal sections of the waveguide core. The materials are modeled to be lossless, so the only loss mechanism is due to optical power leakage from the central waveguide trench into the sidewalls and out of the simulation domain. A perfectly matched-layer (PML) boundary condition [141] is used around the outer regions of the simulation domain to properly model the semi-infinite extension of the top horizontal sections of the waveguide. In this scheme, the calculated propagation loss is mainly due to the optical power leaking out of the waveguide and radiating into the PML. In this example, the intrinsic propagation loss due to the power leakage was measured to be 0.139 dB/cm for a 20 μm wide simulation domain. Since the power is being radiated from the waveguide, the measurement of power absorbed in the PML is independent of the placement of the boundary. This is contrary to the behavior of a traditional rib waveguide, which may also measure some propagation loss if the evanescent tail of the mode impinges on the PML, but would quickly decay to 0 as the PML is moved further from the core. For the 45-degree stratified trench waveguide, increasing the simulation domain to 32 μm wide only changed the propagation loss by 0.003 dB/cm, which further corroborates that we are measuring an intrinsic leakage of power from the structure, and this measurement is well converged (<10% variation from 16 μm wide to 32 μm wide simulation domain).

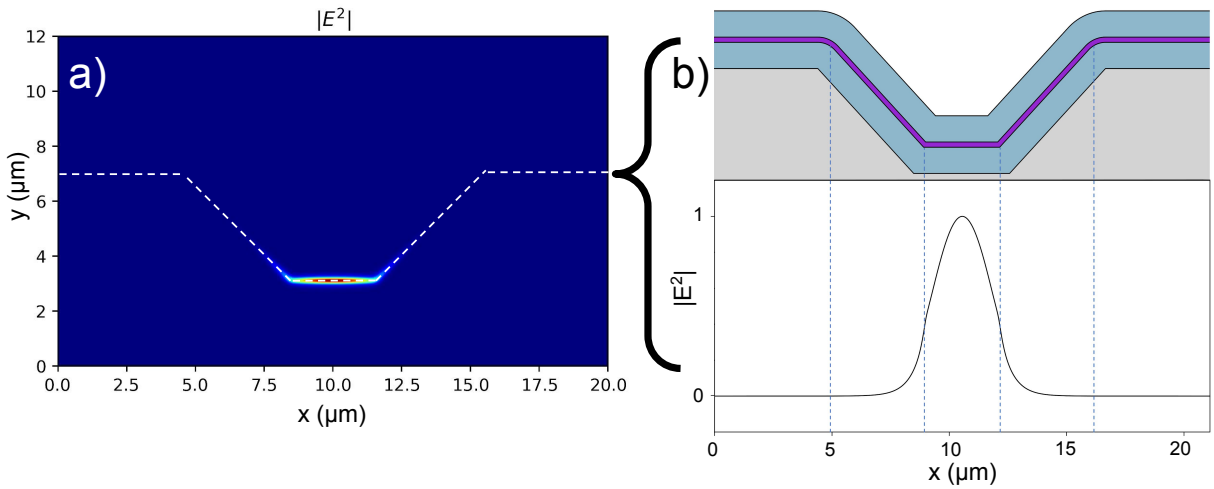

Figure 4.7: a) Fundamental mode of a 45-degree trapezoidal stratified trench waveguide. b) Line plot of electric field intensity across the mode cross-section with a schematic illustration of the waveguide geometry.

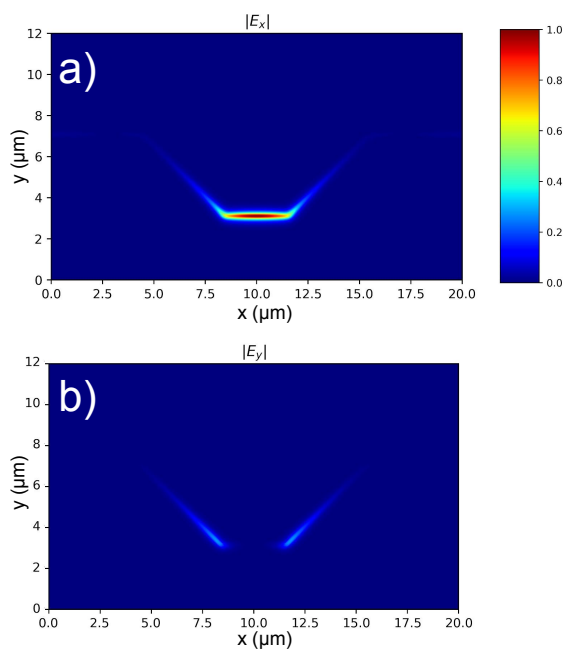

Figure 4.8: a) E_x component of the fundamental mode, which is allowed in both the horizontal slab region and the 45-degree sidewalls. b) E_y component of the fundamental mode is weaker in the horizontal slab regions.

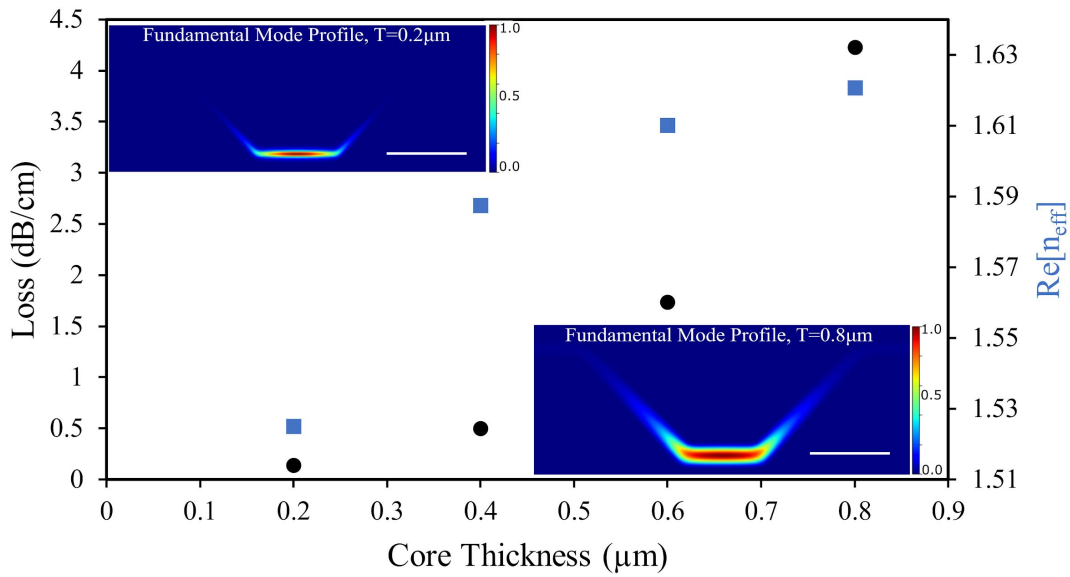

Figure 4.9: Fundamental TE mode loss and effective index vs core thickness (T). Inset images show the mode field profile. Scale bar indicates 4 μm.

4.3.1 The Effect of Waveguide Thickness

The modal structure and propagation loss of the stratified trench waveguide depends on the thickness of the core. Using the same size trench mold geometry (4 μm deep and 4 μm wide), I modeled the conformal deposition of a 1 μm PDMS substrate and a range of core thicknesses between 200 nm and 800 nm. The relationship between the core thickness, the propagation loss, and the effective index of the fundamental mode is shown in Fig. 4.9.

The relationship between confinement and core thickness for the waveguide structure is the opposite of traditional ridge or rib waveguides. Usually, a thicker core results in a higher level of confinement for the fundamental mode, i.e., less exposure to the cladding material and higher effective index. Instead, as the waveguide core thickness is increased in the trapezoidal stratified trench waveguides, the modal confinement is decreased, while at the same time, the effective index of the fundamental mode is increased, indicating that more of the modal field is propagating in the high-index slab region outside of the trench. As discussed in the previous section, by increasing

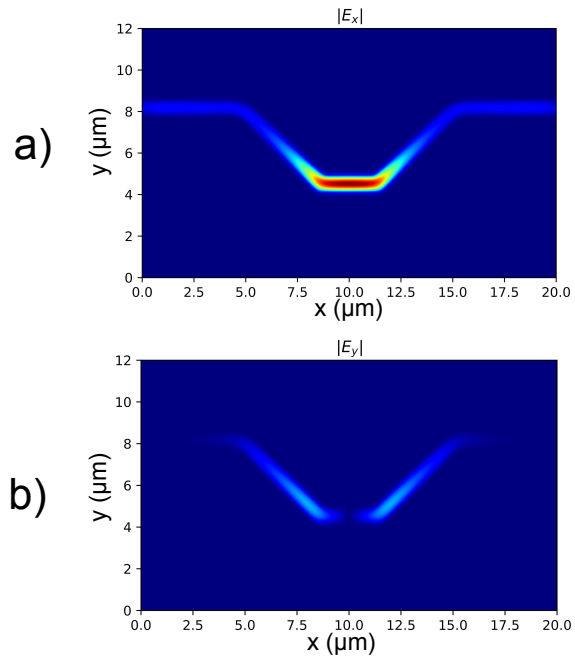

Figure 4.10: E_x and E_y components of 0.8 µm-thick waveguide structure, showing increased field overlap in the horizontal and diagonal segments.

the waveguide core thickness, the confined optical field in the bottom horizontal segment of the waveguide couples to the sidewall modes and leaks into the slab region outside of the trench (Fig. 4.10), thus increasing the propagation loss.

The fundamental mode losses increase drastically with increasing core thickness. At a thickness of 0.8 µm, the losses of the stratified trench waveguides due to leaky modes is 4.23 dB/cm, which is comparable to the Parylene C ridge waveguides with optimized smoothing techniques described in the previous chapter. This number only measures the intrinsic loss and does not consider additional fabrication imperfection. This simulation suggests that the thickness of the waveguide core should be minimized, and that the stratified trench waveguide conformal coating confinement strategy is not tenable beyond this thickness. Within this optimization range, 200 nm offers the best waveguide performance.

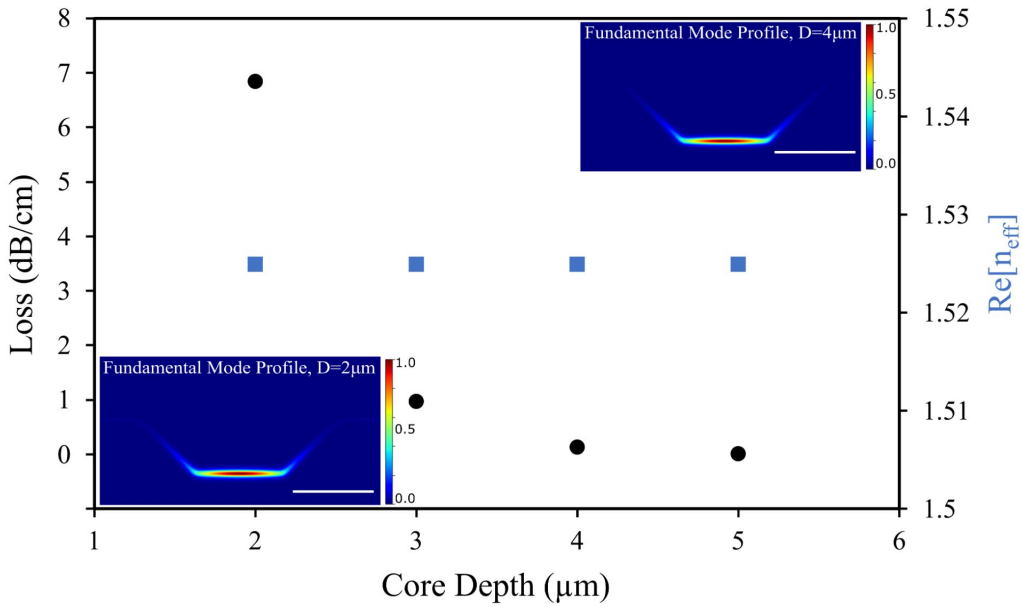

Figure 4.11: Fundamental TE mode loss and effective index vs trench depth (D). Inset images show the mode field profile. Scale bar indicates 4 μm.

4.3.2 The Effect of Trench Depth

The modal structure and propagation loss of the stratified trench waveguide also depends on the depth of the trench. I modeled the conformal deposition of identical layers (i.e., 1 μm PDMS substrate and 200 nm Parylene C core) into various trench molds with a width of 4 μm and varied depth (1 to 5 μm). The relationship between the trench depth, the propagation loss, and the effective index of the fundamental mode is shown in Fig. 4.11.

Increasing the depth of the trench significantly decreases the fundamental mode loss. At a depth of 4 μm, the losses of the stratified trench waveguides due to leaky modes is 0.139 dB/cm, which decreased further to 0.021 dB/cm at a depth of 5 μm. By contrast, the effective index of the fundamental TE mode does not significantly vary across the range of trench depths and is primarily determined by the core thickness.

These results show that the deeper trench geometries yield better modal confinement. Since the depth and width of the sidewall are related by the sidewall angle, deeper trenches inherently limit the routing density of waveguides. Therefore, there is a fundamental tradeoff between density and propagation loss. From a practical perspective, 0.139 dB/cm is sufficiently low that losses in a real system would likely be dominated by scattering and absorption due to material and fabrication imperfections. In principle, however, even lower intrinsic losses are possible by increasing the trench depth.

4.3.3 Waveguide Array Crosstalk

In a photonic platform, it is desirable to integrate several waveguides in an array with minimal crosstalk between them. While the optical mode is strongly confined in the bottom segment of the trapezoidal stratified trench waveguides, still a small fraction of the optical mode leaks to the top slab waveguide. Therefore, if multiple of such waveguides are densely integrated next to each other, there is a chance that light can be coupled between adjacent waveguides due to crosstalk. To quantify this crosstalk effect, I have simulated two adjacent optical waveguides as shown in Figure 4.12a. In this simulation, light is propagating in the fundamental mode of the "input waveguide", and the "probe waveguide" is monitored for the coupled optical power. The waveguide trenches are placed beside each other in our exemplar configuration. Each waveguide trench is 4 µm deep, which corresponds to a 4 µm wide sidewall due to the 45-degree angle, and 4 µm wide, resulting in a total waveguide pitch of 12 µm. At this spacing, we observe a negligible crosstalk of $<$ -60 dB over a coupling length of 5 cm (Fig. 4.12b).

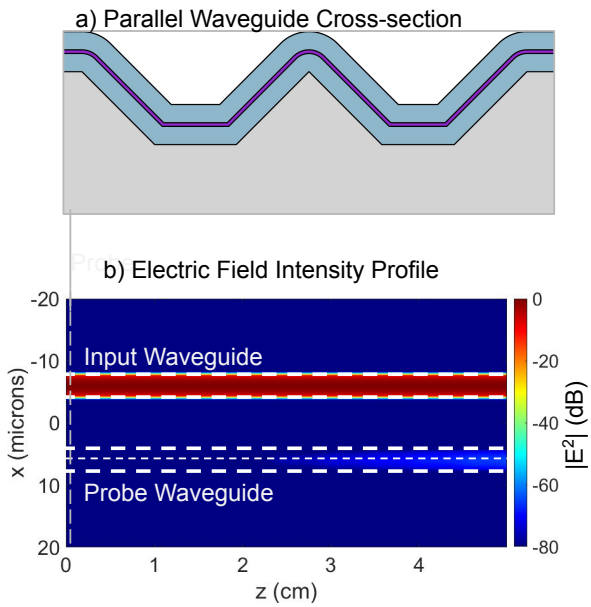

Figure 4.12: a) Schematic image of parallel waveguide cross-section. b) Crosstalk simulation, showing power coupled into the adjacent waveguide (top view).

4.4 Conclusion

In Chapter 3, I demonstrated that Parylene C and PDMS polymers can be used to realize Parylene photonic waveguides with low propagation losses of less than 5 dB/cm. The ridge waveguides discussed in Chapter 3 were realized by etching the outline of the Parylene C polymer waveguide core on a PDMS substrate. The primary loss mechanism in those waveguides was determined to be scattering due to sidewall roughness, and the low losses were only achieved through a highly optimized post-fabrication smoothing process. Here, I demonstrated a mold-based design which offers an alternative path to performance scaling, aside from simply optimizing the Parylene etching conditions. The etchless stratified trench geometry has inherent losses due to mode leakage out of the trench, but these losses can be made small by properly designing the waveguide geometry. These results indicate that a dense array of such etchless waveguides (12 µm pitch) can be designed with low inherent losses (e.g., 0.139 dB/cm), while promising to simplify the fabrication process. Of course, for any specific application, depending on the desired density

of the waveguide, the geometrical parameters of these etchless stratified trench waveguides can be optimized to minimize the intrinsic propagation loss, even beyond the numbers reported in this chapter.

Chapter 5

Characterization and Demonstration of Parylene Photonics

5.1 Introduction

This chapter shows that the performance characteristics of Parylene photonics are suitable for delivering light to the brain to stimulate neurons. A custom benchtop characterization setup was built to characterize the various unique features of Parylene photonics including: low propagation loss, 90-degree input/output micromirrors, and flexibility. The setup includes an input fiber which was used to couple optical power into the Parylene photonic waveguides, and a custom-built microscope system was used as a readout. The input fiber is mounted to a 3-axis XYZ robotic micromanipulator, while the output charge-coupled device (CCD) is mounted to a 5-axis XYZRΘ robotic positioning system. The output camera is able to pivot and perform axial scans (Θ, R movement) to capture the out-of-plane beam profile of the micromirrors.

Portions of this section are adapted, with permission, from the author's prior work in [92]

The custom design of the characterization setup compared to most integrated photonic measurement systems is motivated by the unique requirements of biological probes. Traditional photonic integrated circuits have input/output ports designed to integrate with standard chip-to-chip interconnects such as fiber array connectors. However, the output ports of a biophotonic device are typically sparse and irregularly spaced to match the target biology, rather than a standard photonic connector. This high variability in input/output port arrangements of biophotonic devices such as Parylene photonic neural probes motivates the design of a high-degree-of-freedom setup which can adapt to many device geometries and designs. Furthermore, the device operates in the visible range, unlike the majority of integrated photonic circuits which are designed to operate in near-infrared or telecom wavelengths. I therefore make use of widely-available visible range cameras in lieu of a single-point photodetector or fiber-based readout system so that rich high-resolution information can be captured about the spatial beam profile or evolution of the waveguide output intensity over the field of view. The design of the characterization system and results obtained from Parylene photonic waveguides using this system are discussed in the following sections.

5.2 Custom Characterization Setup

5.2.1 Hardware Setup

A custom characterization system was built to characterize the optical properties of the Parylene photonic waveguide arrays (Fig. 5.1. First, a micromanipulator (PatchStar, Scientifica) is used to align a single mode fiber (S405 XP, Thorlabs Inc, USA) to the input micromirror of the waveguide to couple light into the system. The FC/PC terminated input fiber can be connected to one of 3 fiber-coupled laser systems, providing an input wavelength of $\lambda = 450$, 532, or 633 nm. The fiber input-coupling stage is a high-precision (20 nm x,y,z step size) and high-stability (< 1 µm drift over 2 hours) micromanipulator. A CCD camera (EO-5012M, Edmund Optics) at

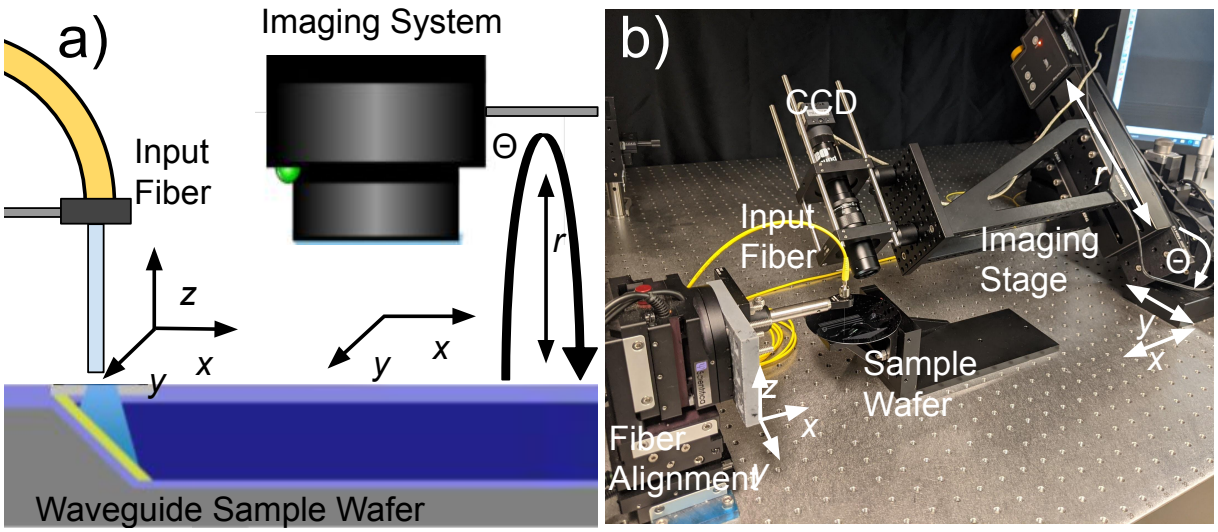

Figure 5.1: a) Schematic diagram consisting of an input fiber with 3-dimensional (x,y,z) motorized alignment capabilities, the waveguide sample wafer, and an output imaging system with 4-dimensional (x,y,r,Θ) motorized alignment capabilities. b) Annotated photograph of the characterization system schematically illustrated in a).

the output of the system was used to image the light from the Parylene photonic waveguides. The output camera can be moved in X,Y, or Z using 3 linear stages (NRT150, Thorlabs). The NRT150 stage has a rated absolute on-axis accuracy of 19.29 µm. The imaging system is mounted on a rotation stage (HDR50, Thorlabs) so that the waveguide could be imaged from any angle orthogonal to the propagation direction.

5.2.2 Custom Beam-Profiler

The system is able to measure the output beam profiles of the waveguides via 3 different methods:

1. By rotating the imaging platform in fixed increments about the axis of the waveguide and imaging the output port light intensity. To increase the dynamic range of the system, the imaging exposure time was scaled for each sample to avoid individual pixel saturation, and the pixel intensity values were then scaled by the exposure time.

2. By imaging the fluorescent profile in a block of Agar tissue phantom.

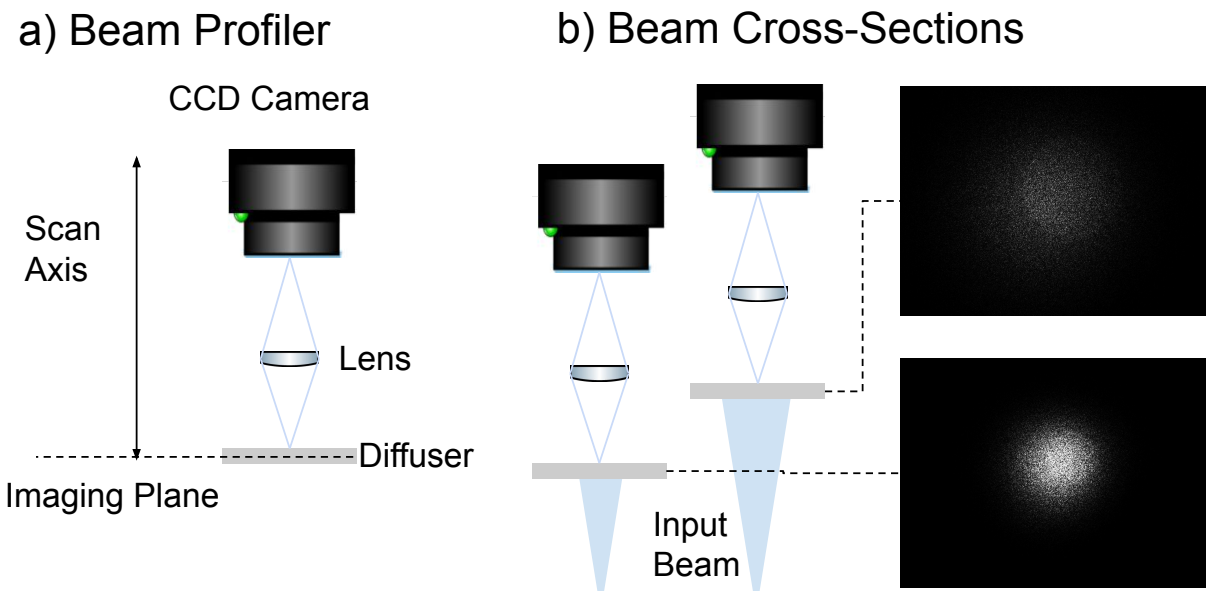

Figure 5.2: a) Schematic of the setup to measure the beam profile by imaging it onto a diffuser plate. b) Schematic of the scanning method to take beam cross-sections at various heights by moving the beam profiler along the output beam.

3. By imaging the beam profile onto a diffuser plate. The diffuser plate was scanned along the z-axis at 100 µm intervals, then the resulting profiles stitched together to reconstruct the axial beam profile. The system is shown schematically in figure 5.2. The measurement setup and a single beam cross-section are shown in Figure 5.3.

5.2.3 Assessing Propagation Loss

This section discusses the features and capabilities of the characterization setup to measure the propagation loss of the waveguides.

[0]Portions of this section are adapted, with permission, from the author's prior work in [142]

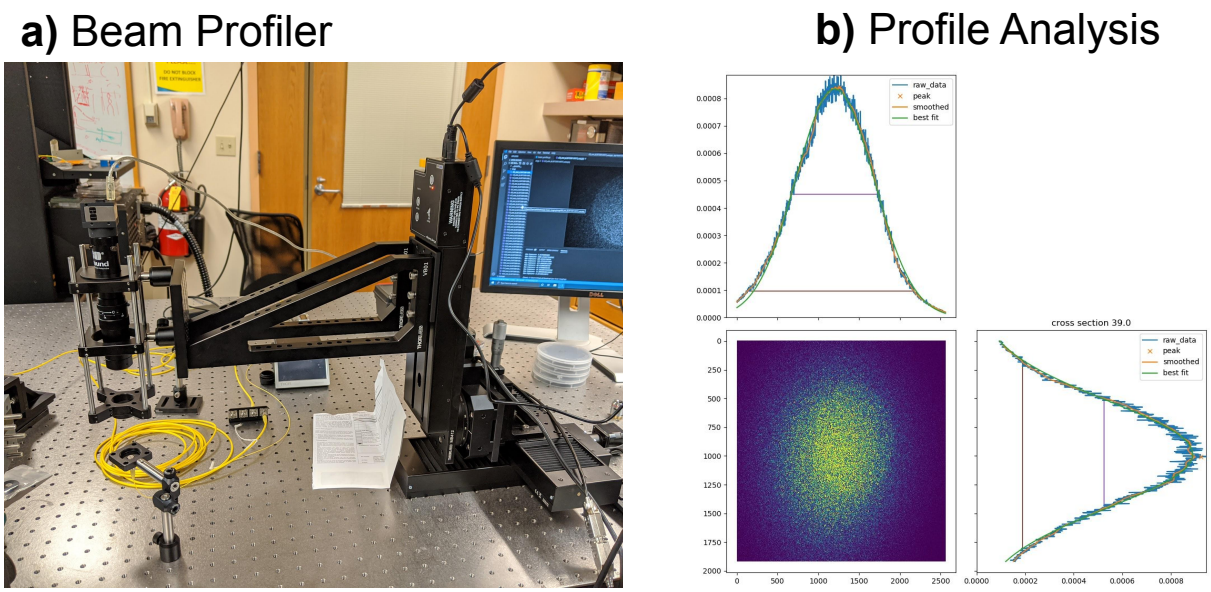

Figure 5.3: a) Beam profiling robot system b) Beam profile analysis (Gaussian fit) of single frame

5.2.3.1 Outscattered Light Measurement Technique

There are several ways to measure propagation loss in integrated photonic waveguides, including the cutback method [143] and the resonator Q fitting method [144]. However, the cutback method is destructive, and the resonator method requires the design and integration of microresonators to measure loss. A nondestructive, in-situ characterization scheme is desired.

The outscattered light method of loss measurement computes the propagation loss in the waveguide based on measurements of outscattered light intensity along the length of the waveguide. The optical power propagating in the waveguide decreases along the length according to the propagation loss. The intensity of light scattered out of the waveguide is proportional to the propagating optical power and the local defect density or sidewall roughness. Assuming that the surface roughness is uniform along the length of the waveguide, the intensity of the outscattered light decays with the same exponential loss coefficient as light propagating the waveguide. An exponential function is fit to the decaying intensity of the outscattered light to determine the

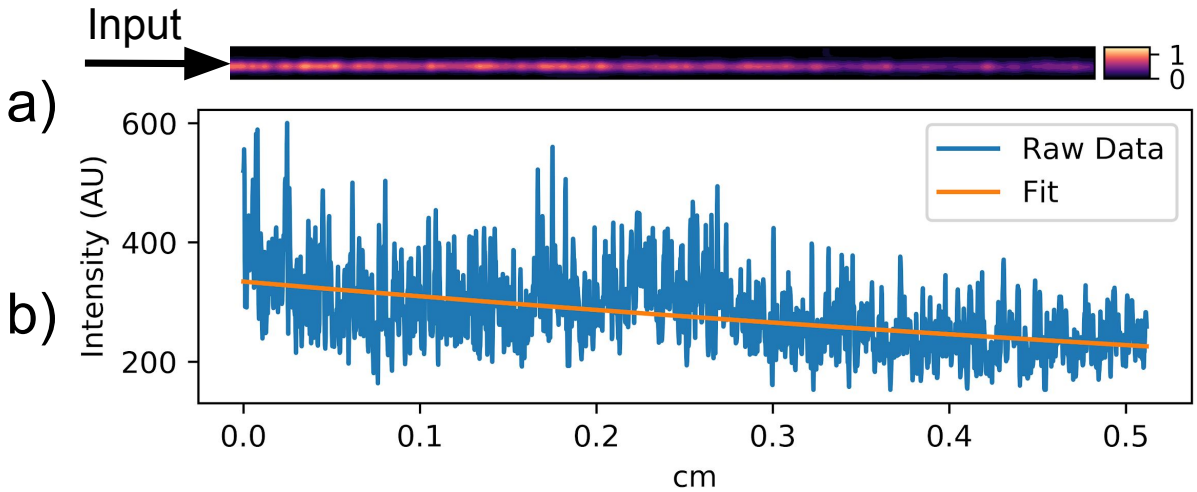

Figure 5.4: a) Scattering image captured from top of a 30 μm waveguide. Image contrast is enhanced by 100% in manuscript for visual clarity. b) The exponential fit to the scattering profile.

attenuation coefficient (Fig. 5.4). In this way, we can analyze the losses in a waveguide via imaging with a CCD camera. Since the devices studied in this thesis primarily operate in the visible range to stimulate visible-range opsins, the outscattered light could be measured with commercially available optics. This technique has previously been applied as an alternative to the cutback method for characterizing optical waveguide performance for neural probe applications [37, 145].

An image processing pipeline was developed to analyze the images captured by the characterization system. First, the waveguide is located in the image by denoising the image with a median filter, finding the brightest pixels in each column of the image, and fitting a line to those points (Fig. 5.5a). The Random Sample Consensus (RANSAC) algorithm is used to fit the line [146]. This fitting method was found to robustly handle images containing reflections and noise, as well as images where the waveguide trajectory does not span all columns of the image. The image is cropped to only the columns spanned by the waveguide, and the algorithm is run again to find the waveguide. This method prevents spurious fits by discarding the influence of irrelevant columns, which may contain reflections or noise.

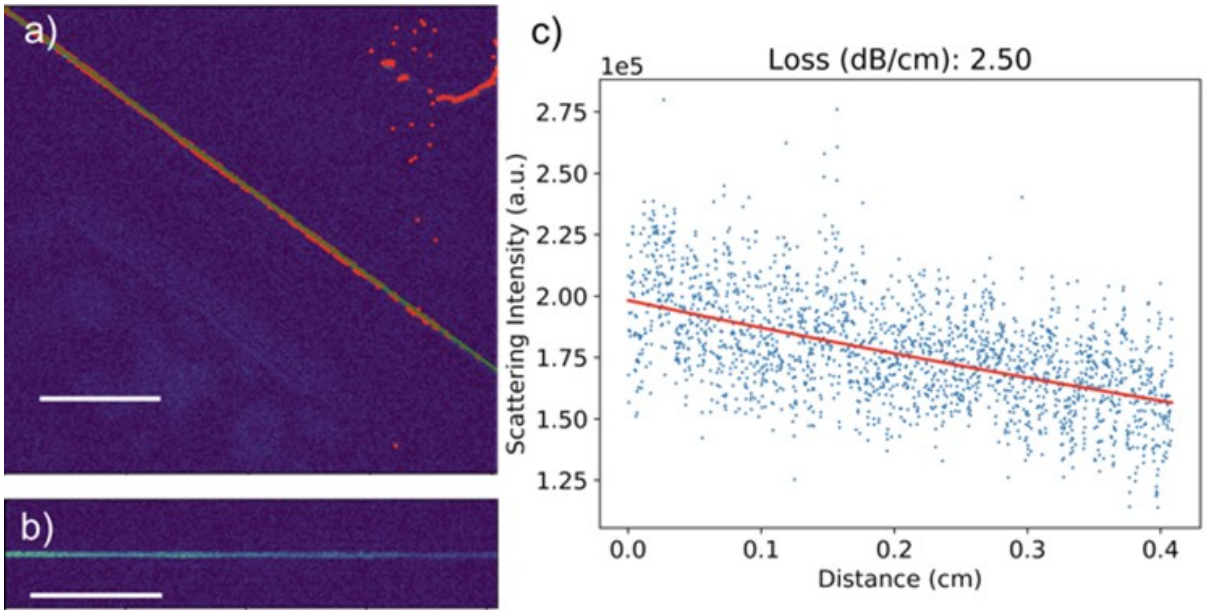

Figure 5.5: The scattering loss measured from a single image: a) identified path of waveguide (in green), superimposed on highest intensity rows for each column (in red) b) rotated and cropped image centered on waveguide path c) plot of scattering intensity vs distance. Scale bars indicate 1 mm.

The image is then rotated so that the waveguide is horizontal in the image and cropped to have a 500 px height, with 250 px on either side of the trajectory line (Fig. 5.5b). The pixel values in the image are vertically summed to obtain a scalar value of the intensity, and an exponential function is fit to obtain the propagation loss coefficient (Fig. 5.5c).

The intensity decay can be modeled as $I = I_0 e^{(-\alpha x)}$, where I is the light intensity at distance x from the input facet of the waveguide, I_0 is the initial light intensity, and α is the attenuation coefficient.

It should be noted that in large multimode waveguides, such as those measured here, light can propagate in multiple modes of the waveguide, which will experience different propagation losses. In general, lower-order modes are highly confined and experience less loss due to surface scattering compared to higher-order modes, which tend to experience higher propagation loss and are quickly attenuated. Power coupling between modes occurs due to perturbations in the

waveguide, such as imperfections due to surface roughness. Over a long propagation length, the modal power distribution will converge to a steady-state, and the overall waveguide loss will be a superposition of the losses of individual modes [147]. All measurements for waveguide loss and alignment are performed at least 1 cm from the input facet to allow the power distribution in the waveguide to reach steady-state.

5.2.4 Semi-Automated Functionality

5.2.4.1 Automated Image Collection and Stitching

To obtain a high-resolution image of the entire waveguide length, images of different waveguide segments are stitched together. The camera is automatically scanned in 1-mm increments along the axis of the waveguide, and individual images are captured at each position. Both the movement and image capture are automated, and the system is programmed with an offset between the fiber and camera to avoid collisions between the input fiber and the imaging system during movement.

Adjacent pairs of images are efficiently stitched by first identifying the waveguide trajectory of each image via the process described above. The two images are aligned along the waveguide trajectory to minimize the search space for the overlapping regions of the images. Then, the offset of each image along the waveguide trajectory is computed by minimizing the pixel error in the overlapping region. This process is repeated for each image captured during the scan to create a composite image. Figure 5.6 illustrates how a section of a stitched image was obtained from three adjacent original images. To measure the propagation loss of longer waveguides, a series of 20-30 images can be stitched to fit the loss over several cm of outscattered light data.

[0]Portions of this section are adapted, with permission, from the author's prior work in [142]

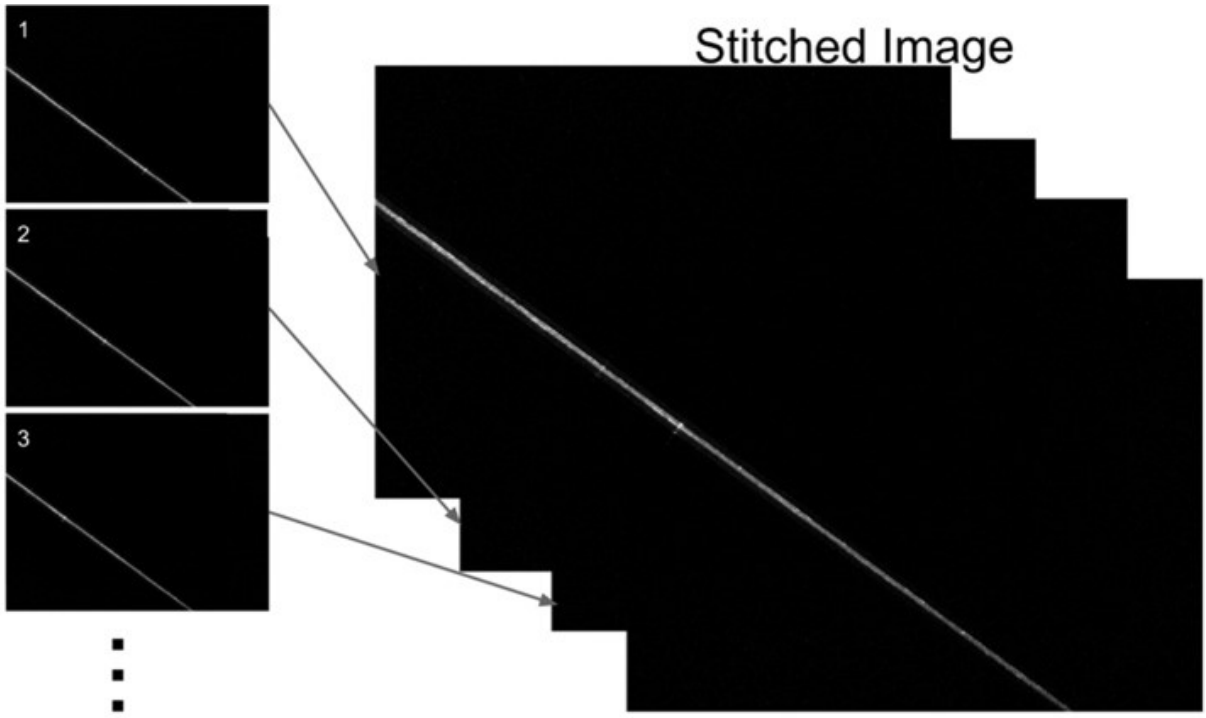

Figure 5.6: The effect of image stitching: The images on the left are original photos taken by the camera, and the image on the right is the combined image produced by the image stitching algorithm.

5.2.4.2 Automated Waveguide Input Coupling Optimization

The system is able to automatically optimize the fiber location at the waveguide input facet to maximize the coupling efficiency and facilitate rapid semi-automated measurements. First, the fiber tip is manually positioned just above the wafer surface after the sample is loaded. The characterization system can then automatically position the fiber at the optimal location in the plane of the wafer surface.

The fiber position is optimized within an initial search space. In a waveguide array, this initial search space cannot exceed the waveguide pitch, or the algorithm may converge to an adjacent waveguide rather than the target waveguide. For waveguide input ports with a 40 µm pitch, the search space is chosen to be a 20 µm by 20 µm square region.

The optimization algorithm iteratively narrows down this search space. In each step, the fiber is swept over a grid of points, and an image is taken at each point. The average brightness of the waveguide in each image is used to determine the optimal point in the grid, which is used as the new center point of the search during the next iteration using a smaller grid size.

Input coupling is performed in 3 iterations using a grid with (x, y) resolution of (2 µm, 2 µm). In the second and third rounds, points are spaced (0.4 µm, 0.5 µm) and (0.1 µm, 0.2 µm) apart.

Fig. 5.7 shows that if the automated alignment algorithm is run with a fixed grid resolution of (1 µm, 1 µm), it approaches the position with peak brightness value after a series of iterations. The brightness profile also indicates that achieving a resolution of 1 μm^2 around the peak corresponds to achieving a brightness value that is within 90% of the peak brightness value. This suggests that our algorithm, which attempts an even higher resolution of (0.1 µm, 0.2 µm), is suitable for aligning to within 90% of the peak brightness.

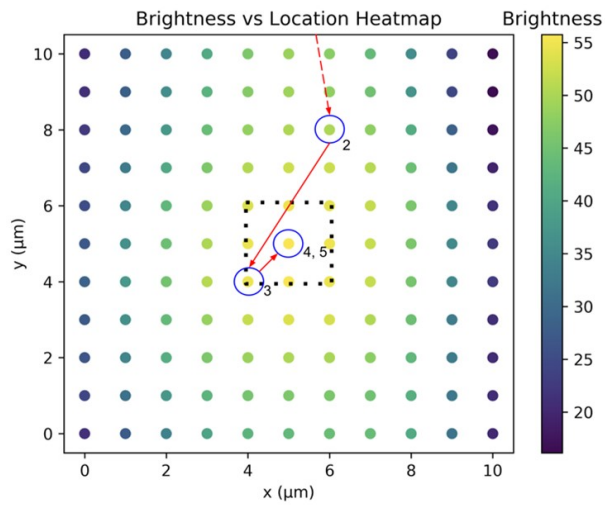

Figure 5.7: Fiber position convergence during 4 iterations of the algorithm, run with a fixed grid resolution of (1 µm, 1 µm). The starting position, at (5, 13), is out of range of the graph; the final positions of each subsequent iteration is labeled with a circle and a number (2 is the position one iteration after the start, 3 is the position 2 iterations after, and so on). The arrows show the transition from iteration to iteration. The dotted box is the target 1 μm^2 region.

5.3 Propagation Loss

The waveguide propagation loss was measured at various wavelengths of interest ($\lambda = 450, 532, 633, 680$ nm) by imaging the scattered light along the length of the waveguide using the method detailed above. The average loss values for 30 µm-wide waveguides are shown in the table below 5.1.

Table 5.1: Waveguide Probe Loss for Optogenetics Wavelengths

Wavelength λ (nm)	Propagation Loss α (dB/cm)
450	6.1 ± 1.4
532	4.9 ± 1.2
633	4.1 ± 0.8
680	3.2 ± 1.7

5.4 Bend Loss

Parylene photonics is envisioned as a flexible photonic architecture that can freely flex with the tissue to avoid exerting strain on the tissue (Fig. 5.8a). To operate reliably in vivo, the bends induced by tissue motion should not significantly impact the delivered optical power at the output port. However, bending of optical waveguides results in radiation of confined optical modes before light reaches the output facet. This section discusses the measurement of bend loss in Parylene photonic waveguides.

5.4.1 Measurement Setup

To characterize the overall bend loss, we experimentally measured the bend loss at different radii of curvature using a custom-designed jig (Fig. 5.8b). This jig has two parts. The first part is a 3D printed V-groove to hold the input fiber in place, and the second part is a precisely machined cylindrical rod to form the bend geometry. We used a series of different rods with different diameters to study the effect of bend loss at different bending radii.

A single Parylene photonic waveguide array was sequentially wrapped around rods of different radii (0.3 mm – 5 mm) to measure the bend loss. In all cases, the bend angle was 90 degrees. The transmitted output power was measured by imaging the output port onto a CCD camera. To minimize errors due to variations in input coupling conditions, we optimized and maximized the coupling from the input optical fiber by measuring the transmission of the straight waveguide and then permanently affixed the fiber to the input facet using an epoxy to maintain a consistent input coupling. We repeated the experiments four times, each time sweeping the range of bend radii, to ensure the repeatability of the results and characterize the measurement error at different radii (Fig. 5.9).

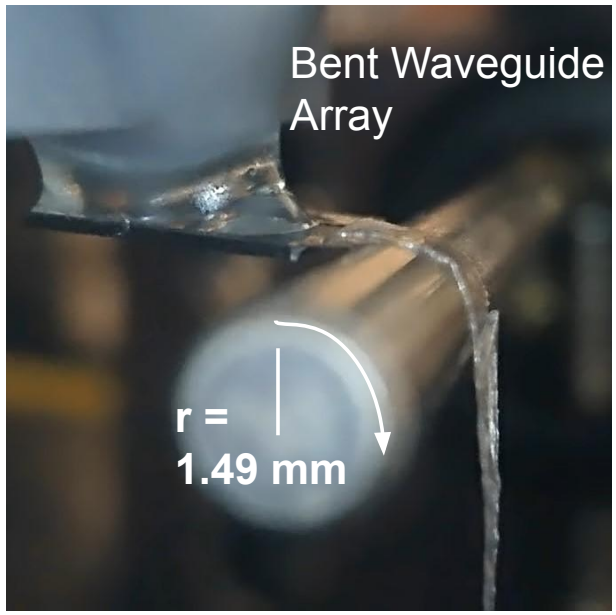

Figure 5.8: The flexible waveguide array, bent over a custom jig to measure the bend loss (radius = 1.49 mm).

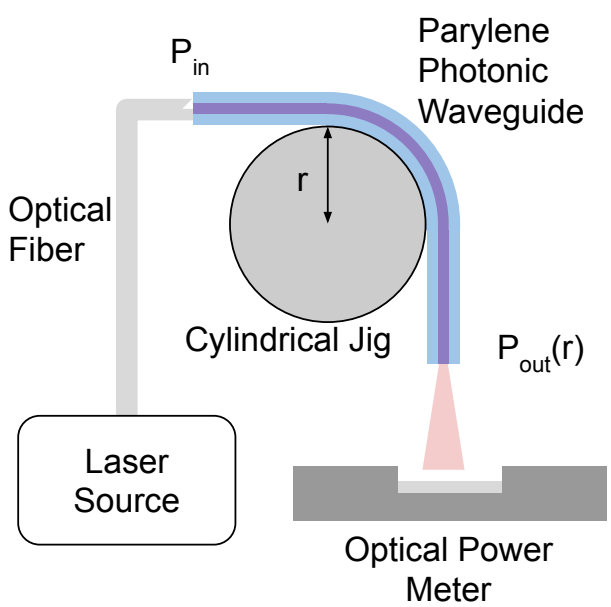

Figure 5.9: Schematic of the setup to measure the attenuation due to bend loss of a Parylene photonic waveguide around a bend radius r.

5.4.2 Results

The experimental bend loss measurement results are presented in Fig. 5.10, showing negligible bend losses for millimeter-scale bends, i.e., more than 95% of maximum output intensity even at a bend radius of 1.5 mm. For bend radii smaller than 1 mm, the variance in measurements is larger compared to the measurements at larger radii of curvature. This is caused by experimental challenges in wrapping the probe smoothly around rods at such small radii. We suspect that loops or creases formed in the probe shank during these tight bends, reducing the measurement accuracy. Therefore, the presented flexible waveguides preserve their performance through millimeter-scale bends in the probe shank. Bends of this size (1.5 mm – 5 mm) are likely to occur during implantation and routing of the flexible shank in the body. Our bend loss measurement results suggest that the output optical power will be minimally affected by flexing in the tissue after implantation.

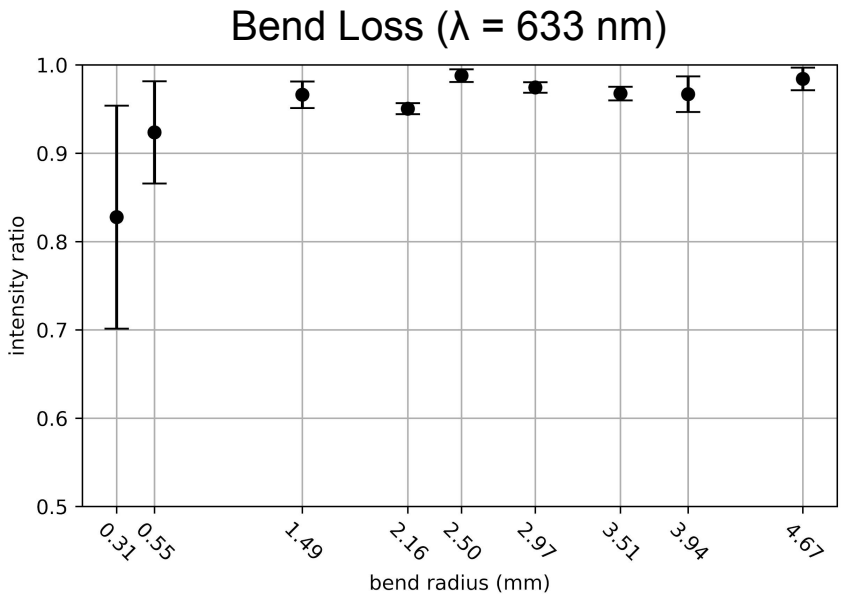

Figure 5.10: Waveguide bend loss measurements of the relative output intensity (normalized to the output intensity from a straight waveguide) through a 90° bend of various radii. Low waveguide bend losses are demonstrated with a high intensity ratio (more than 95%) at millimeter-scale bends. The number of measurements for each data point was n = 4. The error bars denote the standard deviation.

5.5 Beam Profile

In addition to enabling broadband vertical input coupling, the 45° output micromirrors are capable of localized broadband illumination normal to the probe surface. The output beam profile was qualitatively and quantitatively measured via 3 methods, described in the following sections.

5.5.1 Beam Profiling Method 1: Agar Tissue Phantom

To characterize the output beam profile, a CCD camera was aligned to the output port of a Parylene waveguide in an array, and input coupling was adjusted to maximize the light intensity at the output port (Fig. 5.11). Subsequently, to image the beam profile, a block of fluorescent tissue phantom (0.6% Agar mixed with 10 ppm AlexaFluor 532) was aligned above the output

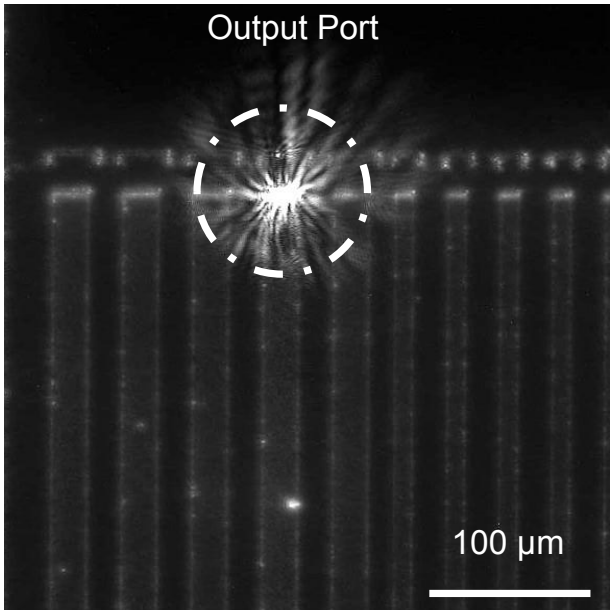

Figure 5.11: A brightfield image of the waveguide array (top view), featuring an illuminated output port.

port with a micromanipulator and imaged from the side (Fig. 5.12). The resulting fluorescent emission profile is shown in Fig. 5.12, with isointensity contours superimposed on the image to show the spatial decay of the light intensity.

5.5.2 Beam Profiling Method 2: Measurement by Rotating Sensor

The output beam profile reflected by the micromirror was quantitatively measured by imaging the output light intensity at multiple angles (Fig. 5.13). Characterization of a 30 µm × 5 µm micromirror output port at $\lambda = 532$ nm shows a directional beam profile. The $1/e^2$ beam width is 13° orthogonal to the surface of the probe (Fig. 5.14). This localized illumination profile allows for multiple output ports to be independently spaced along the probe surface for targeted light delivery.

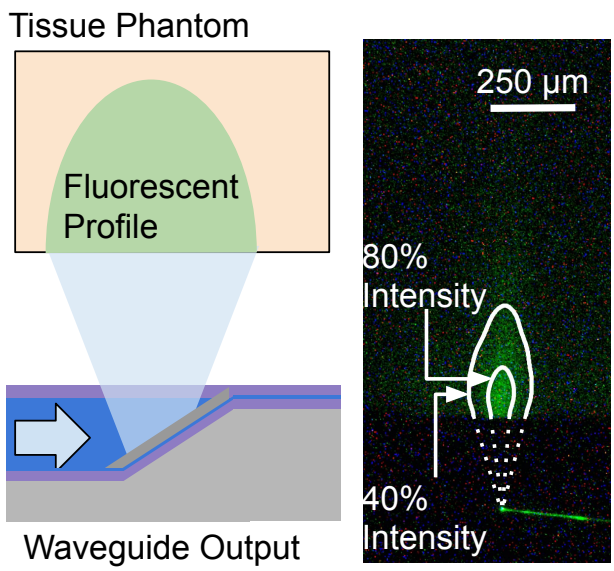

Figure 5.12: (left) Schematic illustration of the fluorescent beam imaging experimental setup. (right) Out-of-plane beam profile imaged in a fluorescent tissue phantom with labeled isointensity contours.

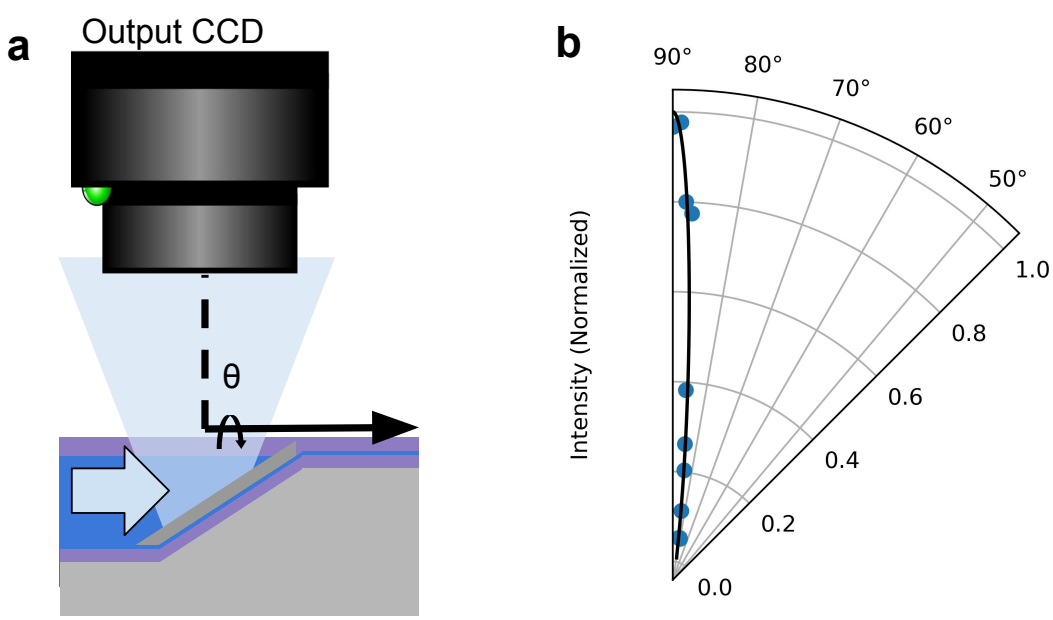

Figure 5.13: a) Schematic of the beam profile characterization system. b) Radial beam profile, showing a peak intensity at 90°, with rapid off-axis decay.

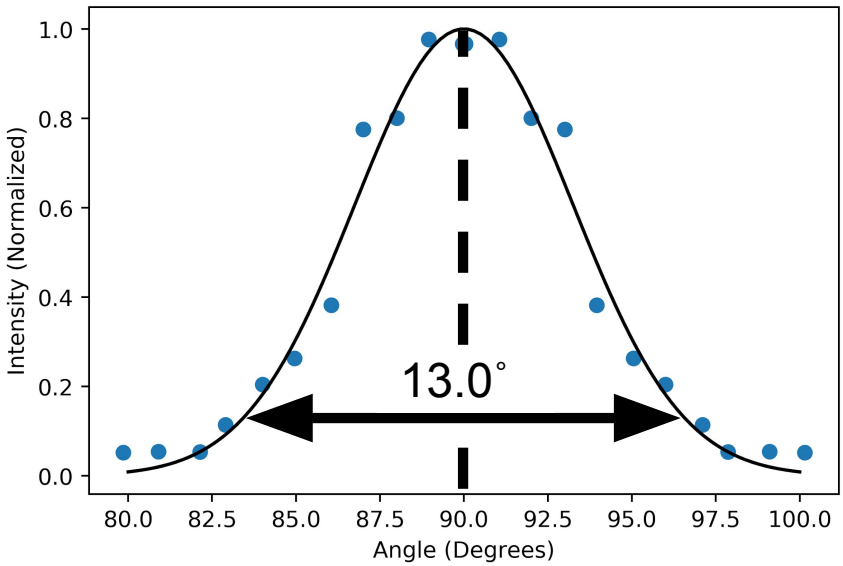

Figure 5.14: Gaussian curve fit to the radial beam profile, showing a beam divergence of 13° ($1/e^2$ beam width)

5.5.3 Beam Profiling Method 3: Measurement by Axial Scanning

The reconstructed beam profile produced with the diffuser beam profiler, shown in Fig. 5.15 for a 3.5 µm x 10 µm waveguide, illustrates the narrow out-of-plane beam profile. The beam profile is also anisotropic: the $1/e^2$ divergence angle in the YZ plane, corresponding to the wider 10 µm facet of the waveguide, is 5.45°, whereas the narrower 3.5 µm XZ direction shows a wider beam divergence of 18.98°.

This narrow out-of-plane beam profile is helpful in the context of optogenetic stimulation because it allows localized light delivery in the tissue. End-firing neural probes illuminate tissue along the axis of the probe, which limits the resolution along the direction of the shank. Since recording electrodes are typically integrated along the probe shank, this means that the stimulation volume would overlap with the recording volumes of several electrodes. Therefore, the out-of-plane beam profile would allow for high-resolution collocated stimulation and recording. In addition to the advantages of an out-of-plane beam profile, the narrow beam divergence means that each

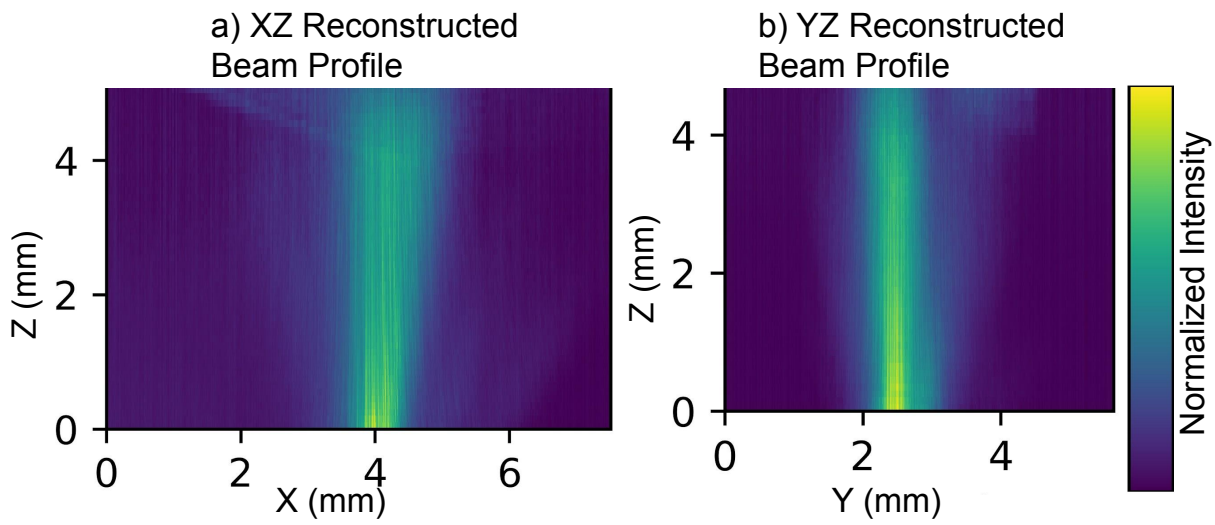

Figure 5.15: Reconstructed beam profile of a) the XZ plane and b) the YZ plane of a 3.5 µm x 10 µm Parylene photonic waveguide

individual output port is more selective in the volume of the tissue that it illuminates. A narrow beam profile enables closely-packed optical stimulators with non-overlapping stimulation volumes for high-resolution interrogation. The ability of light to be focused and steered, as opposed to electrical currents which are immediately dispersed in a conductive medium, is one of the key advantages of optogenetic stimulation over electrical stimulation.

5.6 Device Packaging with Integrated VCSEL Sources

In addition to the capabilities of the Parylene photonic waveguides, the development of Parylene photonics into an implantable biocompatible device requires compact packaging techniques to attach to light sources. Characterization is performed using a fiber-tethered benchtop laser as a light source. However, this is not suitable for a chronic or free-roaming experiment since the large laser would encumber an animal during experiments. Furthermore, a fiber tether may snag or

break if it is left permanently attached to an animal. This section discusses a method of attaching compact vertical-cavity surface emitting laser (VCSEL) diodes to the waveguide input for a highly compact method of packaging with light sources.

VCSEL sources are chosen since they emit an out-of-plane emission profile which can be coupled to the input micromirror of the waveguide by placing the VCSEL on the surface above the micromirror. This simplifies the three-dimensional alignment required in edge coupling to a planar, two-dimensional solution of aligning to the input port on the wafer surface. Bare VCSEL chips are compact (220 µm x 220 µm) and lightweight (0.5 mg), enabling a small backend form factor. The bare die VCSEL chip (Vixar 0680M-0000-X002, Osram, Munich, Germany) emits light at 680 nm, suitable for stimulating red-shifted opsins such as Chrimson. The VCSEL is bonded to the waveguide surface using anisotropic conductive film (ACF).

5.6.1 Bonding Process

ACF film (CP34531-18AK, Dexerials Corporation, Tokyo, Japan) is placed over the input micromirror. The VCSEL chip is then aligned to the input facet using a commercial flip-chip bonding tool (M9A, BE Semiconductor Industries N.V. (Besi), The Netherlands). Once aligned, the ACF is cured (120 °C, 15 minutes) to fix the VCSEL in place. The p-contact and n-contact of the diode are electrically connected to an external PCB using an Al wirebond (Model 7476D, West Bond, Anaheim, CA) (Fig. 5.16).

5.6.2 Coupling Efficiency and Limitations

Light delivery through the waveguide system relies on sufficient end-to-end power transmission, despite losses incurred along the way. Losses are categorized as either insertion or propagation losses, with propagation losses following an exponential decay along the length of the waveguide. Insertion losses produce a difference between total VCSEL emitted power and P_{in} seen by the waveguide, either due to the packaging process or the modal structure of the waveguide.

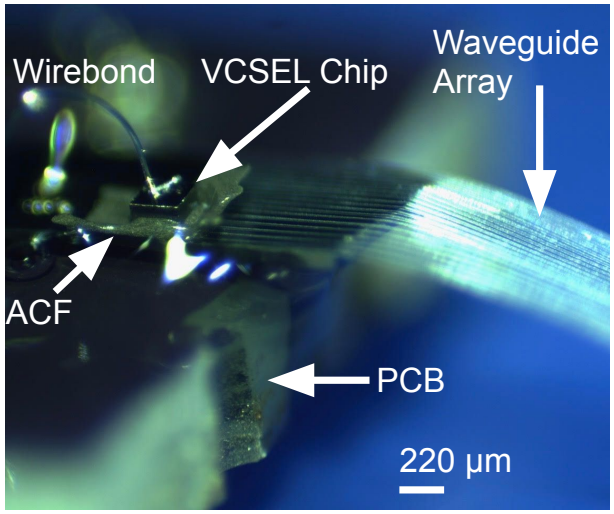

Figure 5.16: A vertical cavity surface emitting laser (VCSEL) chip bonded to the input port of a flexible Parylene waveguide using anisotropic conductive film (ACF)

Measurements were performed on n=5 waveguide samples fabricated on the same wafer. The optical power emitted by the VCSEL chip and the waveguide probe were measured using an optical power meter (PM100D, Thorlabs, Newton, NJ). The average output power from each waveguide was measured to be 67 nW, while the emission power of the VCSEL was measured to be 5 mW, corresponding to a total system loss of 48.7 dB.

The waveguide platform itself was low-loss: a fundamental propagation loss of 3.2 dB/cm (σ = 1.74 dB/cm) was measured at a wavelength of 680 nm across 5 different samples (n = 5). Furthermore, a transmission measurement of the ACF film yielded an average transmission of 70.22% (σ = 1.27%) across the range of optogenetics wavelengths.

This proof-of-concept demonstration presents several opportunities for optimization. The output power is measured to be 67 nW at the output facet. Although optogenetic stimulation has been shown with as low as 60 nW [48], the power emitted by this device is very close to the minimum threshold, so it is not likely to be feasible without further improving the loss. Shorter

probes reduce the total optical loss in the waveguide; at 1.3 cm our probe is longer than is required for mice, since deep brain regions such as the basal ganglia are only several millimeters into the brain [148]. Most of the optical loss is due to the surface area mismatch between the VCSEL emission mesa and waveguide input port (3300 μm^2 versus 150 μm^2). A larger input facet with a taper along the waveguide can match the size of the VCSEL output facet while allowing high-density routing in the probe shank. We can leverage adiabatic waveguide tapers for optimizing mode conversion to significantly improve end-to-end power transmission [149]. Further, microlenses are commonly used to focus and couple from VCSEL sources [150, 151].

5.7 Butt-Coupling Optical Fibers

To overcome the limitation in input coupling efficiency presented by the VCSEL bonding approach, an alternative technique to couple directly to the waveguide using butt-coupling was developed. First, the waveguide was diced orthogonally to the direction of the waveguide array to expose the end facet and bypass the input micromirror. Then, an input fiber was aligned to the edge of the chip along the axis of the waveguide (Fig. 5.17). Using this technique, the output power of the waveguide array was 15 µW with an input optical power of 15 mW from the optical fiber. Therefore, the system loss was $\tilde{3}$0 db, an increase of 18.7 dB compared to the VCSEL coupling method.

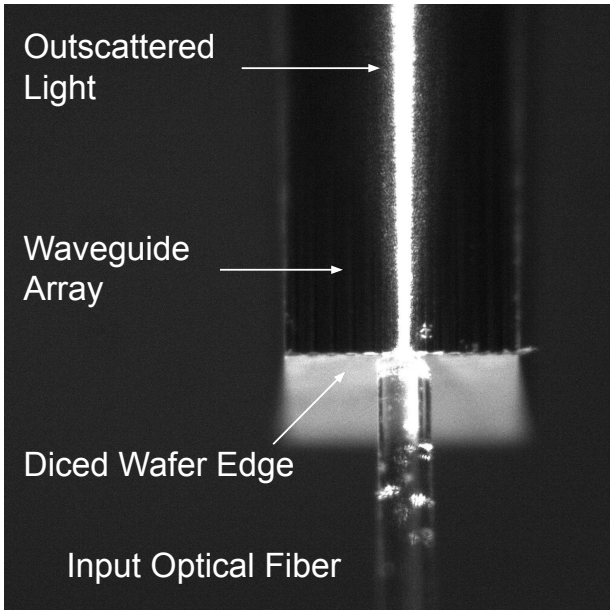

Figure 5.17: Input coupling to a Parylene photonic waveguide via butt-coupling to an optical fiber.

5.8 Discussion

The embedded micromirror input/output port is a unique feature of the Parylene photonic platform. The micromirrors are broadband, unlike traditional out-of-plane illumination mechanisms such as grating couplers, which are highly wavelength dependent. Using the micromirrors, light at multiple wavelengths can be coupled to the waveguides. In the context of neural probes, different optogenetics wavelengths can be used to switch between stimulation and inhibition, or to perform cell-type specific targeting. This material platform is the first to enable such high-resolution, broadband, out-of-plane light delivery in a fully compliant and biocompatible platform.

To realize high-spatial resolution stimulation with multiple output ports, light sources must be integrated in an efficient and compact way to the frontend of the device. I have demonstrated that this is possible, in principle, using flip-chip bonding of VCSEL sources. However, currently, the insertion losses with this method are prohibitively high for practical use (~30 dB). This is mainly limited by the input-port mismatch between the input micromirror and the VCSEL source.

Mass-produced visible-wavelength VCSELs are poorly suited to this application because of their large aperture (80 µm), which is a poor match to the input micromirror, resulting in poor coupling efficiency. Additionally, although the micromirror can be made arbitrarily large along the x-direction to make a wider input port, the width of the mirror along the y-direction is limited by the depth of the KOH etch and waveguide thickness. Therefore, it is only practical to achieve a micromirror width of 5 µm. Thus, the aperture mismatch is a large limiting factor for coupling efficiency. However, this is not a limitation of the underlying VCSEL technology. Custom output apertures as small as 3 µm are commercially available.

Another fundamental limitation of the current approach is that VCSELs must be individually flip-chip bonded onto the device backend. This means that the assembly complexity increases with the number of light sources, so arbitrarily high numbers are not permitted. A possible solution to this issue is the custom fabrication of VCSEL arrays, with apertures spaced to match the waveguide input ports. This way, many independent devices can be bonded in a single flip-chip step.

Finally, another option is to bond a single laser diode chip or optical fiber, and to include integrated photonic switches in the Parylene photonics platform itself. This has recently been demonstrated for multichannel optical neural probes built in silicon nitride [152]. In general, integrated routing and switching capabilities would remove the need for multiple external light sources. Furthermore, although active integrated photonics are well studied in mature material platforms such as silicon nitride, similar capabilities would need to be carefully designed and studied for the Parylene material platform. In contrast to silicon nitride, the thermo-optic and electro-optic properties of Parylene, which are fundamental to the operation of such photonic switches, have not been rigorously studied.

5.9 Conclusion

Here, I have shown that Parylene photonics has excellent propagation and bend loss characteristics to be able to deliver sufficient power for optogenetic stimulation. The strong dependence of the losses on the sidewall quality shows that future process optimization and size scaling are possible with optimized etching techniques. Although very compact and efficient integrated photonic circuits can be implemented, the density and efficiency of input coupling are major bottlenecks to the practical use.

This page intentionally left blank

Chapter 6

Parylene Photonics for In Vivo Implants with Optical Functionality

6.1 Introduction

This chapter discusses the practical demonstration of the Parylene photonic waveguides for efficient light delivery for in vivo optogenetic stimulation of neural tissue in transgenic mice. I show that the end-to-end system losses are low enough to enable practical stimulation of neurons. Implantation techniques to allow the flexible Parylene photonic waveguides to penetrate into the brain tissue are demonstrated. Optogenetic stimulation of mice expressing red-shifted opsins, i.e. ReaChr, using Parylene photonic waveguides are also shown. The evoked activity in response to optical stimulation is recorded using electrophysiology techniques. The electrophysiology data collected from these experiments are analyzed and spike-sorted using a custom software system that I have developed. Lastly, the feasibility of monolithically integrating recording electrodes with Parylene photonic waveguides in a fully-flexible device is shown.

Portions of this chapter are adapted, with permission, from the author's prior work in [92]

6.2 Implantation of Flexible Parylene Photonic Waveguides

Although flexible neural probes are beneficial for the long-term biocompatibility of the neural interface Chapter 1), at the time of implantation, this means that the probes will buckle on the surface of the tissue during unaided insertion. Due to high mechanical compliance of the devices, they lack the rigidity to penetrate the tissue. Various implantation techniques including temporarily increasing the neural probe rigidity using bioresorbable stiffeners during implantation [153], implanting the probe alongside a rigid insertion shuttle [154], and using mechanical guides to stabilize the probe at the tissue surface [87] have been developed in the literature to address this challenge of flexible probe implantation. In principle, Parylene photonic waveguide neural probes are compatible with the wide range of techniques that have been developed for the implantation of flexible polymer neural probe implants. For proof-of-concept demonstration, I have adopted a technique whereby the flexible Parylene C-based neural probe can be bonded to a rigid tungsten shuttle using bioresorbable polyethylene-glycol (PEG) for implantation [155]. After implantation with the rigid shuttle, the PEG dissolves in the tissue. PEG is biocompatible and safe to the tissue upon resorption [156]. Then, the tungsten shuttle can be retracted, leaving the compliant neural implant freely-floating in the tissue.

The procedure to attach the tungsten probe is as follows: A 125 µm diameter tungsten wire (Midwestern Tungsten Service) was cut to 2 cm length using wire cutters. Then, the tungsten wire was affixed to the back of the neural probe printed circuit board using mounting putty (FUN-TAK, Loctite). The tungsten wire mounting was manually adjusted so that the shank was parallel to the base of the neural probe and oriented along the implantation axis. Before attachment, the neural probe shank is separate from the tungsten shank (Fig. 6.1a), and the neural probe shank has a tendency to curl due to the highly flexible substrate and residual stress of the layers that constitute the neural probe. The probe was attached to the shuttle via immersion and withdrawal

of the tungsten shuttle and neural probe in 5% PEG solution at room temperature. When the probe was inserted into the PEG solution, the flexible Parylene C probe would have a tendency to float on the surface due to the water surface tension and would sometimes need to be manually submerged using a fine-tipped paintbrush. To form an initial connection between the probe and the shuttle, the fine-tipped paintbrush was used to press the base of the neural probe against the shuttle. After initial contact, the two pieces were pinned together by the surface tension of the water around the shuttle and probe. In the case of Parylene probes with high amounts of spontaneous curling, multiple attempts to form an initial attachment between the probe and tungsten shuttle were sometimes necessary. Although this was not seen in any of the probes tested here, it is possible that sufficiently high curling in the probe may render attachment using this technique infeasible. Therefore, it is important to minimize the residual stress in the neural probe layers during the microfabrication process so that the resulting devices are nearly stress-neutral. Stress-neutral devices are not only beneficial for implantation, but also for ease of handling and to minimize tissue damage once implanted. After the initial attachment was made, the neural probe and tungsten shuttle were retracted slowly at a rate of 200 μm/s. As the device is retracted, the two devices are pulled together by the surface tension of the liquid solution. Once the probe is retracted, the solution dries, leaving a thin coating of PEG to anchor the two devices together (Fig. 6.1b,c).

After implantation, the PEG quickly dissolves in the Agar tissue phantom. The dissolution of PEG was monitored via impedance measurements of the electrode-Agar interface after insertion. The electrode impedance decreased rapidly over the first 5 minutes after insertion, indicating PEG dissolution from the electrode sites. After 15-20 minutes, the electrode impedance stabilized, indicating complete removal of PEG from the recording sites 6.3. This result demonstrates that for stable recordings, 15-20 minutes should be allowed after implantation while PEG dissolves.

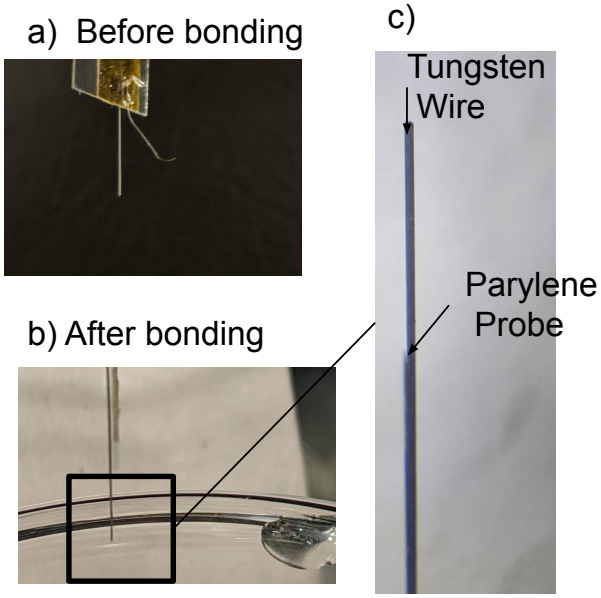

Figure 6.1: Images of flexible probe attachment to a tungsten shuttle using PEG. a) Before bonding, the neural probe shank is separated from the tungsten shuttle. b) Flexible Parylene C neural probe attached to the tungsten shuttle via PEG dip-coating. c) Microscope image of the Parylene probe laminated to the Tungsten wire.

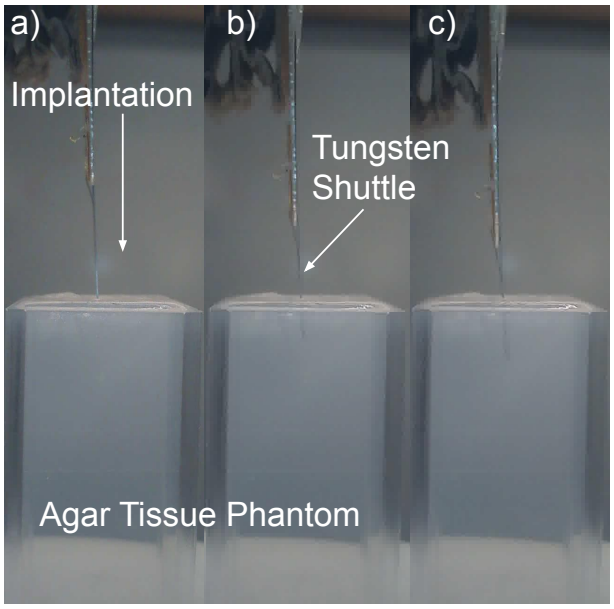

Figure 6.2: A series of photos showing Parylene probe implantation a) 0 mm b) 2.5 mm c) 3.8 mm deep into an Agar tissue phantom using a tungsten shuttle.

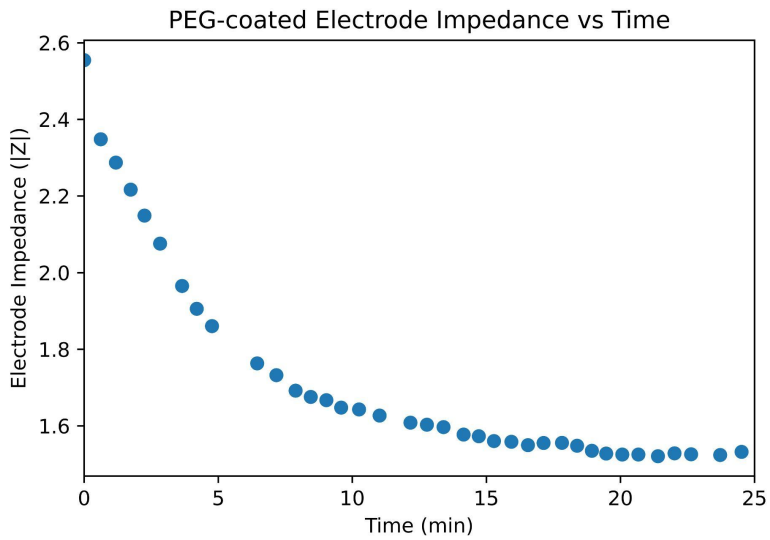

Figure 6.3: Plot of magnitude of electrode impedance (at 1 kHz) of a Parylene microelectrode array implanted into an Agar tissue phantom using PEG attachment to a tungsten shuttle. The electrode impedance rapidly decreases during the initial implantation, before stabilizing after 15-20 minutes, indicating the dissolution of PEG from the recording sites.

6.3 Adding Optical Functionality to Electrical Neural Probes using Parylene Photonics

Not only can Parylene photonic waveguides be used as stand-alone light delivery tools, but they can also be laminated on existing neural probes to provide *add-on* functionality. This is possible due to the very thin (7 µm) planar construction of Parylene photonics. In this section, I describe a method of attaching Parylene photonic waveguides to a commercial Si neural probe to add optical functionality. The hybrid devices are then used for simultaneous optogenetic stimulation and electrical recording in vivo. Here, I use the bioresorbable material PEG to bond Parylene photonic waveguides to a commercial Si neural probe. After dissolution, the Parylene photonic waveguides would detach from the Si neural probe if it were retracted or moved, so the attachment technique

only works for a single implantation. If a permanent attachment is desired, the same technique could be used along with a permanent bonding method, as long as the electrodes can be protected during the coating process so that they aren't insulated by the bonding material.

To the best of my knowledge, this is the first time that PEG dip coating has been used to attach flexible optrodes to a commercial Si neural probe, which would also serve as a functional rigid shuttle. A Cambridge Neurotech 64 channel single-shank H2 electrode array was used as a rigid shuttle for implantation. Using the same method of attachment as the tungsten wire, the flexible Parylene C neural probe could be attached to the rigid Si shank, as shown in Figure 6.4. This way, the optical stimulation capabilities of the Parylene probe augment the recording electrodes of the commercial Si neural probe during acute experiments.

However, when the Parylene photonic neural probes are laminated to the surface of the silicon recording electrodes, the closest electrodes are physically blocked by the Parylene photonic waveguide array. As a result, only the electrodes further away are exposed and can record, and there is a distance (200 µm) between the optical output port and recording electrode in this configuration, as shown in Figure 6.4. In this configuration, the illuminated volume does not coincide with the recording region. To overcome this limitation, the Parylene photonic waveguides were converted to end-firing configuration by using dicing to terminate the waveguide array. This resulted in a blunt tip of the Parylene photonic neural probe (Fig. 6.5).

A blunt tip can impede easy penetration of the Parylene probe into the tissue. This may cause additional tissue damage, or cause the Parylene probe to delaminate from the Si shuttle during implantation. To alleviate the concerns of a blunt tip, the waveguide was mounted on a dual-shank silicon probe to add further rigidity and stability for implantation. Since the array is end-firing, the region of tissue interrogated by the recording electrode arrays are directly illuminated, allowing for collocated stimulation and recording of neurons in the hybrid rigid-flex optrode configuration. Attaching the probe in the manner shown in Fig. 6.5 results in a very large probe cross-section

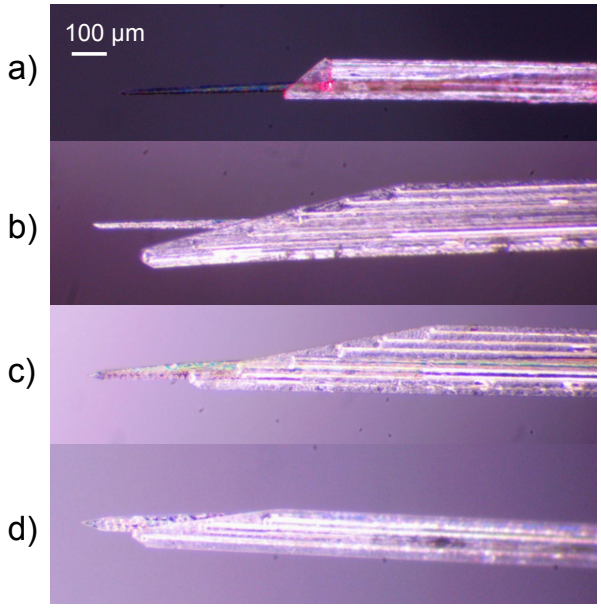

Figure 6.4: Photos of Parylene photonic neural probes attached to a 64 channel Cambridge Neurotech H2 probe via PEG dip coating. a) 2-channel Parylene photonic waveguide optrode attached to H2 probe with one output port illuminated. b) 6-channel Parylene photonic waveguide optrode attached to an H2 probe. The probe is aligned to the center, which results in a concave profile between the two tips, since the Parylene photonic waveguide probe is significantly wider. c) 6-channel Parylene photonic waveguide optrode from b) attached to an H2 neural probe. The Parylene photonic waveguide probe is mounted offset from the H2 shank so that the tips are aligned for a narrower insertion profile. d) 3-channel Parylene photonic waveguide optrode attached to an H2 probe.

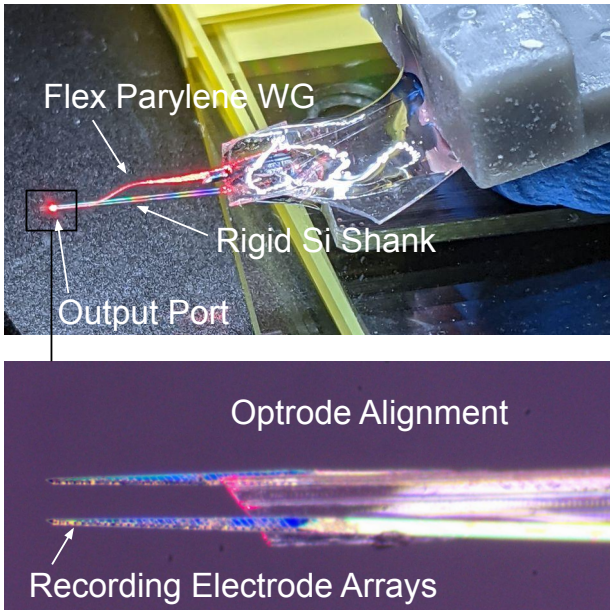

Figure 6.5: An end-firing Parylene photonic waveguide array attached to a dual-shank 64 channel Cambridge Neurotech recording electrode via PEG dip-coating.

which would be more damaging to the tissue. However, this is not a fundamental limitation of the Parylene photonic platform, which I have already shown can be made in arbitrary shapes using high-resolution lithography, and can, in principle, integrate high-yield recording electrodes with additional fabrication optimization. Similarly, the Parylene photonic waveguide probe could be specifically designed to be laminated onto a rigid Si probe to augment its capabilities. For example, holes could be etched into the Parylene photonic neural probe to match the location of recording electrodes on the Si probe so that the Parylene photonic waveguides do not block the recording electrodes of the commercial probe. Moreover, the result shown here is a simplified proof-of-concept demonstration of the optical stimulation capabilities of Parylene photonics, namely that it is capable of delivering sufficient light into the tissue to stimulate opsin-expressing neurons.

6.4 Input Coupling From an Optical Fiber

To provide optical input power to the waveguide from a fiber-coupled laser source for optogenetic experiments, the input fiber is bonded to the waveguide input using an optical epoxy. During characterization, the input coupling is achieved using a precision micromanipulator to align the input fiber to the waveguide input facet. The alignment during optical characterization is performed on a highly stable vibration isolation table and is sensitive to any movement in the system. During implantation, the probe is mechanically lowered into the mouse brain tissue. Furthermore, the system is prone to slight movement, even in a head-fixed setting, due to mouse respiration and heartbeat. Therefore, a robust and stable method to bond the fiber to the input port permanently is needed. To form a stable input coupling condition for the optical fiber during implantation, I bonded the fiber to the input port using an optical epoxy, as described below.

First, a single mode optical fiber is fixed to a custom-designed 3D printed fixture with a V-groove using a drop of UV-curable epoxy (Norland Optical Adhesive 61, Norland Products Inc).The sample is then spot cured for 30 s under a UV laser to form an initial mechanical bond and then cured for 1 hour under a UV lamp to strengthen the bond.

The fixture is attached to a precision micromanipulator (PatchStar, Scientifica Inc, UK, Fig. 6.6a). For top-side coupling through the micromirror, the fixture is mounted so that the fiber points down (Fig. 6.6d). For butt-coupling to a waveguide chip, the fiber is mounted at 90-degrees so that it is facing in the plane of the waveguide (Fig. 6.6b). A drop of UV-curable optical epoxy is placed on the waveguide array backend, covering the input facet. The fiber is then dipped into the UV epoxy drop and aligned to the input facet using the 3D micromanipulator to optimize the light intensity at the output. Once optimal coupling is achieved, the UV epoxy is spot cured with a UV laser for 30 s to form an initial bond (Fig. 6.6c). The fiber alone is not strong enough to support the waveguide and risks breaking during handling. Additional optical epoxy is applied to

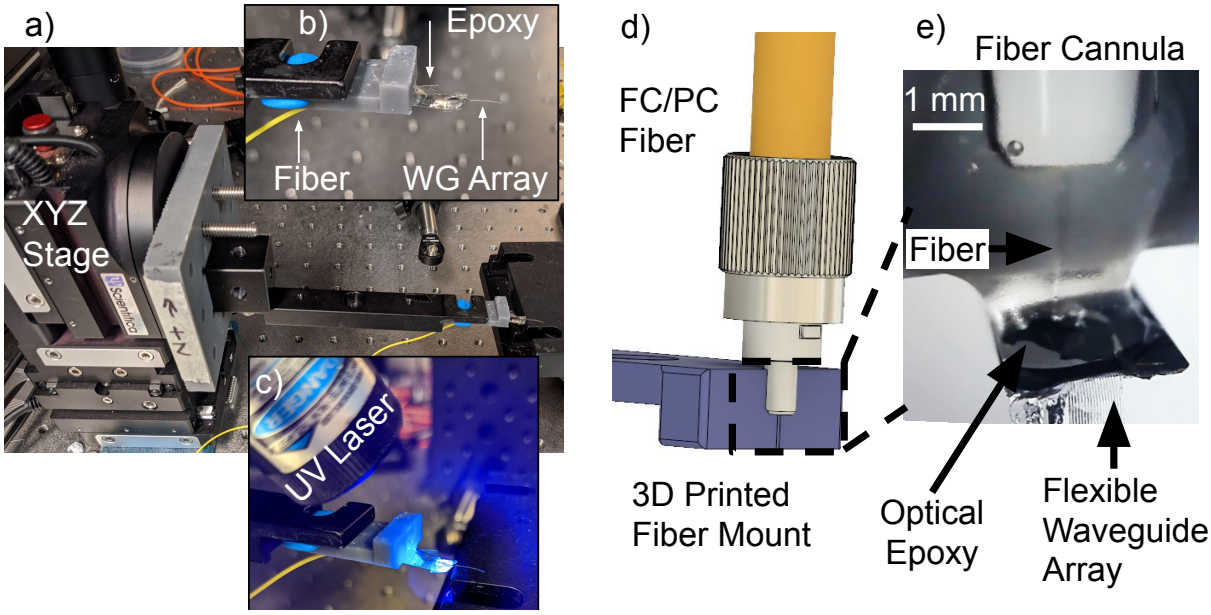

Figure 6.6: a) Fiber probe mounted to precision Scientifica XYZ stage for bonding. The probe rests on a platform while the fiber is aligned to the input facet and secured using optical epoxy. b) Optical epoxy bonding of an optical fiber to a Parylene waveguide array. c) Curing optical epoxy bond with a UV (405 nm) laser. d) Schematic of a fiber-bonding 3D printed mount for out-of-plane fiber coupling b) Optical fiber bonded to the input micromirrors at 90-degrees for out-of-plane input coupling to a flexible Parylene waveguide.

the fiber-waveguide interface to form a mechanically stable bridge from the 3D printed fixture to the waveguide backend (Fig. 6.6e). This epoxy is spot cured using the same method, then the entire assembly is left to cure for 1 hour under a UV lamp. The assembly is detached from the micromanipulator and handled using the 3D printed fixture. The assembly is then baked in an oven overnight at 80°C to fully cure the epoxy.

Here, I have demonstrated bonding of a single fiber to the waveguide input facet. Although the fiber core and cladding are small (125 µm diameter), serial bonding of individual fibers must take into account the prohibitive size of the fiber ferrule and sleeve, which is typically 2.5 mm. This limits the size and density of light source coupling at the device input. Scaling the bonding process to many channels will require commercially available photonic chip coupler arrays which

are now available at channel pitches from 127 µm to 20 µm pitch, e.g, PLC Connections, USA. Alternatively, directly bonding compact laser diode chips such as VCSELs could provide a route to high channel count Parylene photonics (Chapter 5).

6.5 Experimental Design and Methods

Now that I have discussed the preparation of Parylene photonic neural probe for implantation via permanently bonding a light source at the input and attaching to a rigid Si neural probe for implantation and simultaneous electrophysiology recording, I will discuss an experiment to demonstrate Parylene photonics in vivo. Parylene photonic neural probes were implanted in Layer 5 of a mouse motor cortex to stimulate neural tissue that expresses ReaChr, a red-shifted opsin that can be excited at λ= 633 nm. The details of the transgenic animal breeding, surgery, optical stimulation and electrophysiology recording will be discussed in the following sections. An overview of the optogenetic stimulation experiment is shown in Figure 6.7.

6.5.1 ReaChr Expression in Mice

ReaChR opsin [157] was expressed in excitatory neurons of the mouse brain tissue using transgenic mouse lines. All experiments involving animals were performed in accordance with the Institutional Animal Care and Use Committee guidelines. The use of animals and all procedures were approved by the Carnegie Mellon University's Institutional Animal Care and Use Committee. Animals were maintained on a 12 h light-dark cycle with free access to food and water. Homozygous Emx1-Cre mice (Stock no. 005628, Jackson Laboratory, Bar Harbor, ME) were crossed with heterozygous Ai136(TITL-ReaChR-YFP)-D (Stock no. 030216, Jackson Laboratory), and the resulting Emx1-Cre;Ai136D offspring (heterozygous for both transgenes) were used for experiments. A high level of opsin expression was achieved in these mice, verified through fluorescence imaging of the yellow fluorescent protein (YFP) fluorescent tag in mouse brain slices (Fig. 6.8).

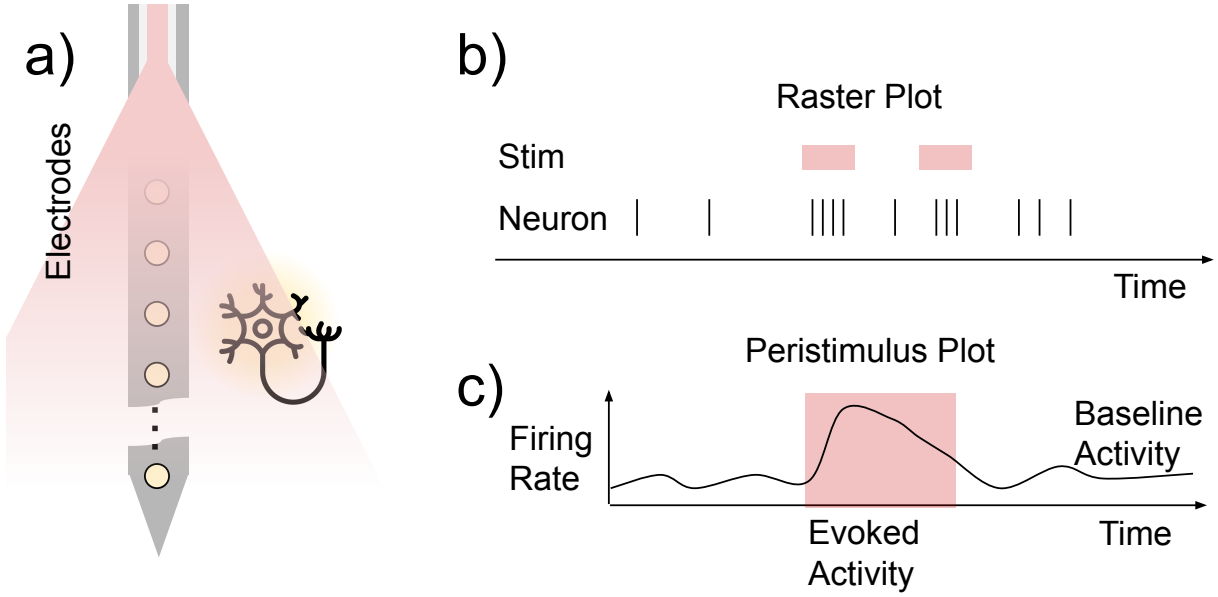

Figure 6.7: Schematic overview of optogenetic stimulation experiment a) waveguide neural probe stimulates activity in nearby neurons while simultaneously performing electrophysiology recording. b) Optical stimulus drives time-locked neural activity. c) A peristimulus plot showing cumulative activity across many stimulus trials. During the stimulation period, the average firing rate is increased above the baseline activity.

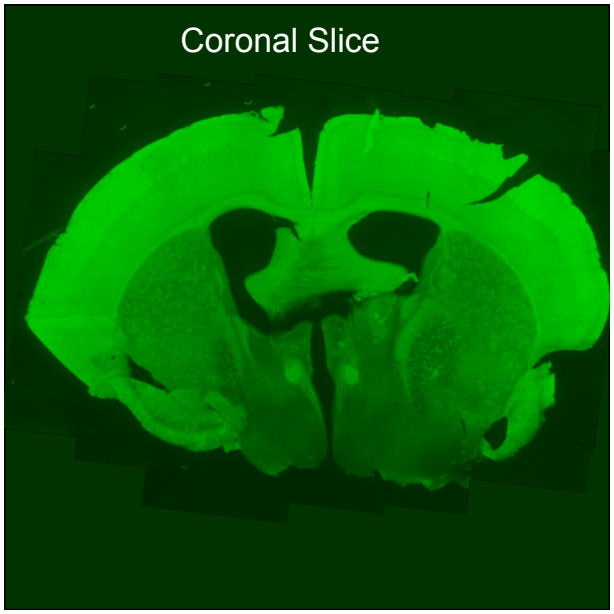

Figure 6.8: Fluorescence image of yellow fluorescent protein (YFP) fluorophore co-expressed with ReaChr in a coronal brain slice, indicating widespread expressing in Emx1-Cre;Ai136D mice used for optogentics experiments.

6.5.2 In Vivo Electrophysiology Rig

In vivo validation of the Parylene photonic neural probes was performed in the electrophysiology rig shown in Figure 6.9. The Cambridge neurotech 64 channel probe was connected to two 32-channel Intan RHD2132 Headstages, which were recorded on a host computer via an Intan RHD2000 Acquisition board. The Parylene photonic waveguides were bonded to an external optical fiber, which was connected to a ThorLabs LP633-SF50 pigtailed laser diode ($\lambda = 633$ nm), powered by a ThorLabs CLD1010 Laser Diode Driver. An external signal generator was used to modulate the laser diode for pulsed light delivery, while the signals were temporally synchronized to the Intan recording system via a TTL pulse. Experiments were performed in a grounded Faraday cage to reduce electrical interference. During the experiment, the Intan amplifier reference and ground were connected to both the Faraday cage ground and a ground screw placed in the mouse's skull.

6.5.3 Surgery

The mouse is head-fixed in a Neurostar robotic stereotax. All procedures were approved by Carnegie Mellon University Institutional Animal Care and Use Committee (IACUC; protocol -AR202100003). 4-6 weeks old Emx1-Cre; Ai136D mice were used for recording neuronal activity. Briefly, mice were anesthetized with isoflurane (3% induction, 1–2% maintenance) and placed on a feedback-controlled heating blanket maintained at 36°C (Kent Scientific, Torrington, CT) mounted on a stereotaxic frame (Neurostar, Tubingen-Germany). An incision was made in the skin and craniotomy was performed by drilling a 1 mm diameter hole in the right hemisphere with the coordinates of AP +1 mm and ML +1.5 mm with respect to bregma, targeting the motor cortex region. A screw hole was made near the lambda region to provide reference ground to the recording probe. Following the craniotomy, the optoelectronic probe (Fig. 6.5) was inserted at the target site at the depth of DV -1.1 mm. Recording electrodes extend 500 microns from the

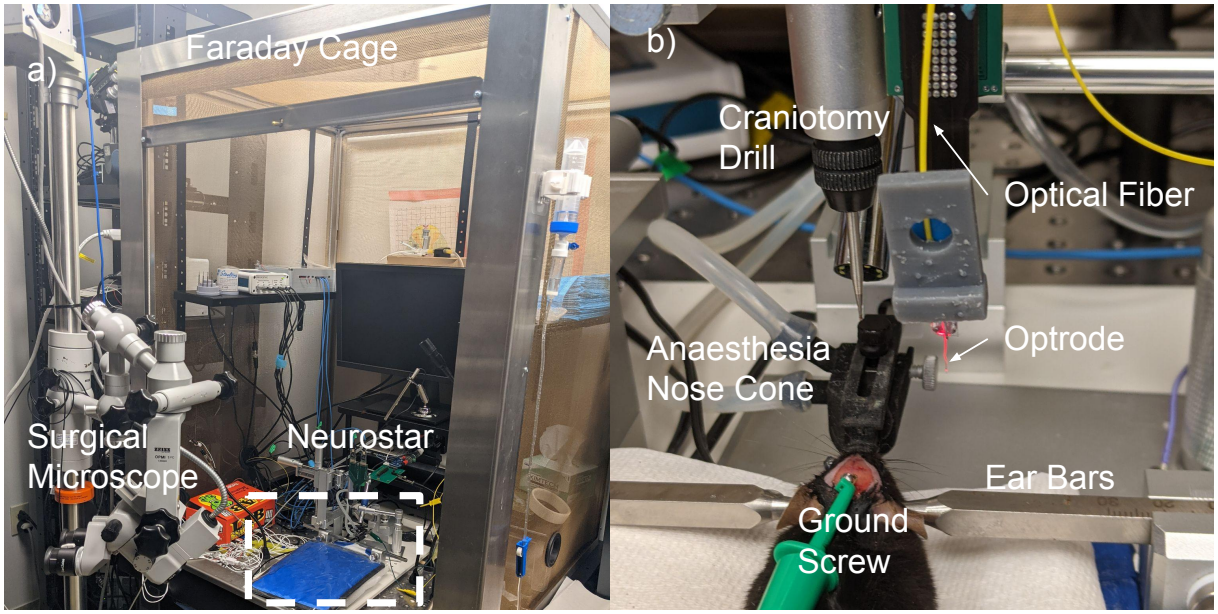

Figure 6.9: a) Electrophysiology rig for in vivo optogenetic stimulation experiments, showing surgical microscope, Neurostar robotic stereotax, and Faraday cage. The area in the rig where the mouse is placed during experiments is highlighted by a dashed white box. b) Close-up image of an anesthetized mouse in the in vivo rig to perform optogenetic stimulation experiments. The mouse's head is fixed in place by the ear bars, and isofluorane anesthesia is delivered through the nose cone. The fiber-coupled Parylene photonic waveguide optrode is illuminated to visualize the light delivery.

tip of the neural probe, spanning a depth of -0.6 to -1.1 mm. This implantation depth was chosen to target Layer 5 of motor cortex at a depth of -0.8 mm. Following insertion, 10 min of recovery time was allowed to acclimatize the tissue to the external material of the probe before starting optical stimulation.

6.5.4 Experimental Procedure

Optical stimulation was delivered as 40 ms pulses (3 second inter-stimulus interval) with a power of 45 µW at 633 nm. Simultaneous electrophysiology recording was performed via the 64 channel Cambridge Neurotech electrode array at a 30 kS/s sampling rate.

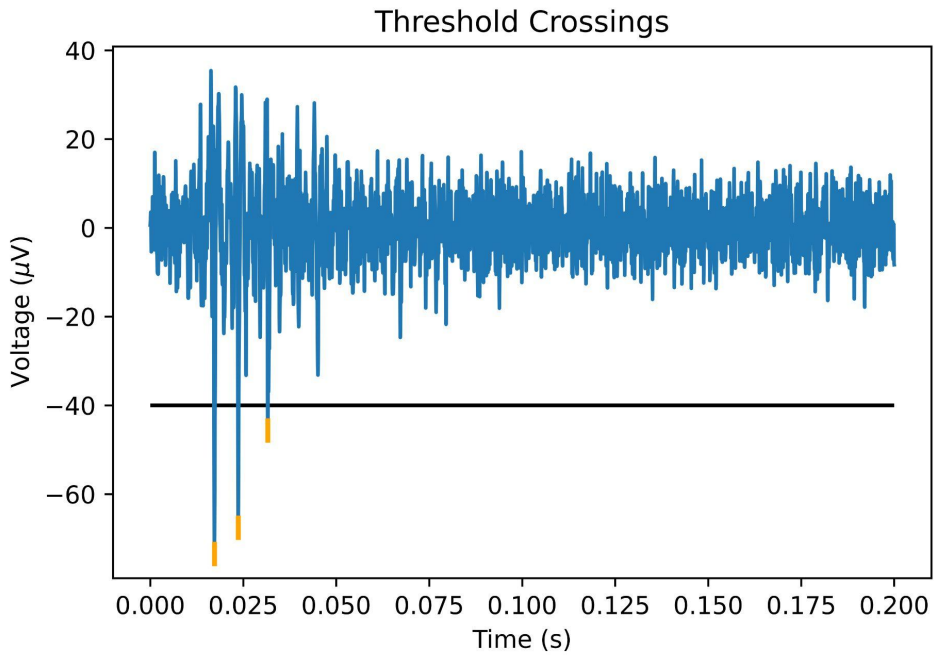

Figure 6.10: A voltage trace from a single recording electrode filtered from 500 Hz - 5000 Hz with a 60 Hz notch filter. Optogenetic stimulation is applied from T=0 to T= 40 ms.

6.5.5 Optically-Evoked Neural Activity

A voltage trace from a single recording electrode channel, bandpass filtered from 500-5000 Hz with a 60 Hz notch filter, is shown in Figure 6.10. Putative neural action potentials can be identified as large deviations from the baseline noise of the signal. Neural spikes identified with a threshold of -40 μV are indicated with orange markers. This threshold was chosen to be distinct from the noise floor of the recording (10-12 μV RMS). Using simple thresholding, three spikes are identified during the stimulation pulse, as shown in Figure 6.10.

The recorded spikes were accumulated across 45 trials to create a peristimulus histogram of spike timings, as shown in Figure 6.11. While low baseline activity can be seen outside of the optogenetic stimulation interval (indicated by red shading), there is a marked increase in neural activity during the stimulation interval, indicating that the Parylene photonic waveguides are able

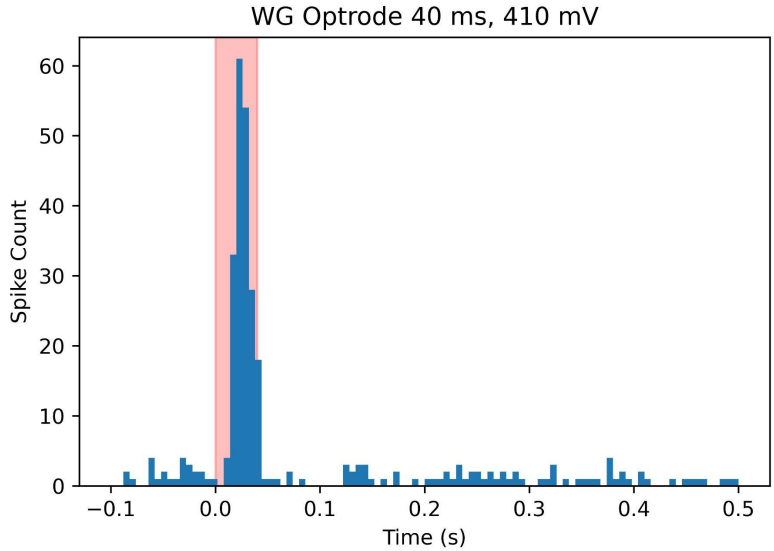

Figure 6.11: Peristimulus histogram over 45 trials, showing a histogram of threshold crossings on a single channel with respect to the timing of light deliver for optogenetic stimulation (red shading).

to deliver sufficient optical power to elicit a neural response. Notably, there are a few milliseconds of delay between the onset of the optical stimulus and the increase in neural firing rate, which is attributed to the time constants of the ReaChr ion channels [157].

6.6 Spike Sorting and Data Analysis

In addition to the raw thresholding discussed in the previous section, machine learning and signal processing techniques, collectively called "spike sorting" can be used to more accurately detect neural signals in time-domain recordings, such as those shown in Figure 6.10. These techniques are also able to detect differences between the waveforms of individual neurons in the tissue, allowing spikes to be classified as originating from individual neurons. This data takes the time-domain trace data and transforms it to the "unit" domain, where individual events and

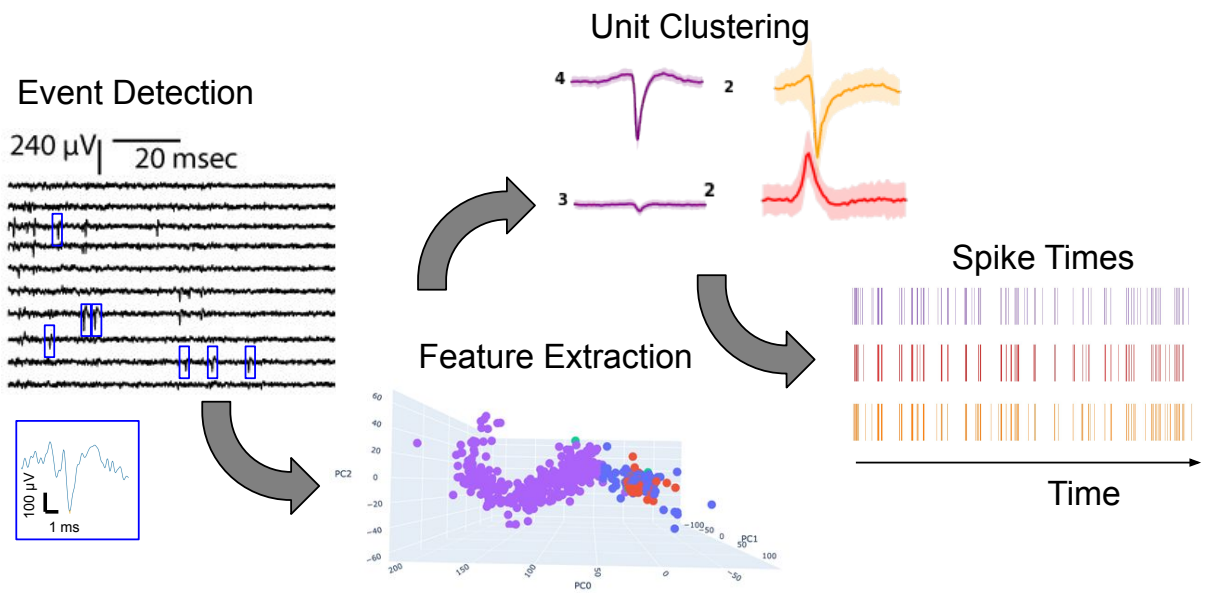

Figure 6.12: Schematic diagram of the spike sorting process where data is processed to associate events with units via event detection, feature extraction, and clustering to find units and their associated spike times.

spike times can be associated with a specific neural unit, as shown in Figure 6.12. For the work completed in this thesis, I have developed a custom software system for neural data analysis, which uses state-of-the-art spike sorting algorithms.

6.6.1 Steps of Spike Sorting

Spike sorting is typically performed via a software pipeline in 4 key steps:

1. Data Preprocessing - During this step, the biological signal is filtered to remove irrelevant (i.e. non-spike) waveforms and eliminate external interference. This is done through a combination of time-domain and frequency domain processing techniques. In the frequency domain, raw data is bandpass filtered to the 'spikes band', which is the frequency band that contains most of the information for neuronal spikes [158]. Outside of this band, the ratio of spike signal compared to other biological signals such as local field potentials (LFPs), or background noise is much lower.

Therefore, band-limited signals in the spikes band (typically 500-5000 Hz) possess an overall higher signal-to-noise ratio for spiking activity. Notch filters at 60 Hz and harmonics are also used to suppress interference from power-line noise and external electronics.

In addition to frequency-domain techniques, time-domain artifacts, such as those caused by electronic switching artifacts or animal muscle artifacts are removed through common median referencing (CMR). This technique references the recording of each individual recording electrode to the median signal of all of the channels. This way, time-domain artifacts which are detected on all channels are removed.

2. Event Detection - Discrete events that can be considered for spike sorting are detected in the raw time-domain signal via simple thresholding of the filtered voltage trace of each channel. An example is shown in figure 6.10. To avoid accidental inclusion of noise as events, the threshold is typically set in terms of a multiple of the standard deviations of the signal, modeled as a zero-mean Gaussian process (i.e. $\sqrt{\sum_{i \in n} |x_i|^2/n}$). Here, I use an event detection threshold of 5 standard deviations. Each event is stored as a snapshot of the electrophysiology behavior at the given time across all of the channels. Here, I choose a snapshot window of 1 ms before the threshold crossing and 2 ms after the crossing (3 ms duration). Therefore, a single event can be represented as a matrix of voltage samples of size: (duration $\times$ sampling rate, number of channels). For the 64 channel probe used here at a sampling rate of 30 kS/s, this matrix is (90, 64), or a 5760-dimensional vector.

3. Dimensionality Reduction - The raw data events can have extremely high dimensionality for high sampling rate and high channel-count data (e.g., 5760 here). This is a problem from a data-analysis perspective. As the dimensionality of a vector space increases, distance metrics, which are used to measure the similarity between two points, become less useful. All points begin to look uniformly distant from all others [159]. Therefore, techniques such as spike sorting which attempt to group events based on similarity become less effective. To alleviate this problem, I use

principal component analysis (PCA) to reduce the dimensionality of the event vectors. Per-channel PCA is performed amongst all of the events, and the event is represented by the 3 largest principal components for each channel, reducing the dimensionality of the event vectors to 192.

4. Clustering - To identify groups of events which are likely to be spikes from a specific neuron, the event vectors are clustered in the PCA space. Traditional techniques for clustering in spike sorting include k-means clustering and Gaussian mixture models. However, both of these techniques have a drawback that the number of clusters must be specified at the outset. Typically, this results in an iterative approach to spike sorting where the data is sorted and inspected and then the user decides whether more or fewer clusters might be needed. This human-in-the-loop process is time-consuming and additionally requires a high degree of expertise in interpreting the electrophysiology data. Recently, a fully automated approach to spike sorting, MountainSort, has been developed [158]. This technique automatically decides to split or merge clusters based on marginal distribution of the data along the first principal component for the clusters of interest. Thus, the optimal number of clusters can be found without any human intervention, making this algorithm ideal for high-throughput automated data analysis. This algorithm is adopted for the analysis described in this thesis.

After raw neural data has been run through the pipeline, the result is a series of events with labels corresponding to their cluster number. Each cluster, also called a "unit" is a putative neuron. However, some manual curation is usually still required at the end of the process since the algorithm will sometimes form a unit composed of artifacts or noise events, which should be excluded from further analysis.

6.6.2 Custom Spike Sorting Software Platform

To enable the scalable use of the spike sorting algorithm, a custom in-house cloud-based software pipeline for neural signal processing was developed. The system was developed around the open source SpikeInterface software library [160], using the MountainSort4 algorithm for spike sorting. The system was developed to alleviate the problems of computing and sharing spike sorting results for large neural signal datasets collected for the experiments discussed in the thesis.

A cloud processing system was developed based on the Google Colab platform. Data storage in the cloud for read/write access from the Google Colab infrastructure was implemented using the Google Drive filesystem as a cache. Custom user interfaces for specific data visualization and data analysis were implemented in Python using interactive Jupyter notebooks on Google Colab. This infrastructure allowed the manipulation of large datasets in a web browser, while all analysis and storage was executed remotely on cloud-based infrastructure.

Analysis was performed in several steps: data preprocessing, spike sorting, statistical analysis, and visualization. For large datasets, each of these operations could be computationally expensive. To avoid redundant computation, the results of each step were cached in the filesystem and loaded when available or dynamically computed (Fig. 6.13). This way, once a certain dataset was preprocessed using bandpass and notch filtering at specific frequencies, spike sorting with multiple parameters could be performed in multiple sessions without recomputing the filtered data. Alternatively, analyzing results with new filtering parameters would be computed for the first time, then stored and dynamically loaded as needed. This infrastructure allowed for quickly comparing results between datasets, or processing parameters. Additionally, since the data and analysis infrastructure resides in the cloud, results could be quickly accessed and shared amongst teams of researchers working in collaboration.

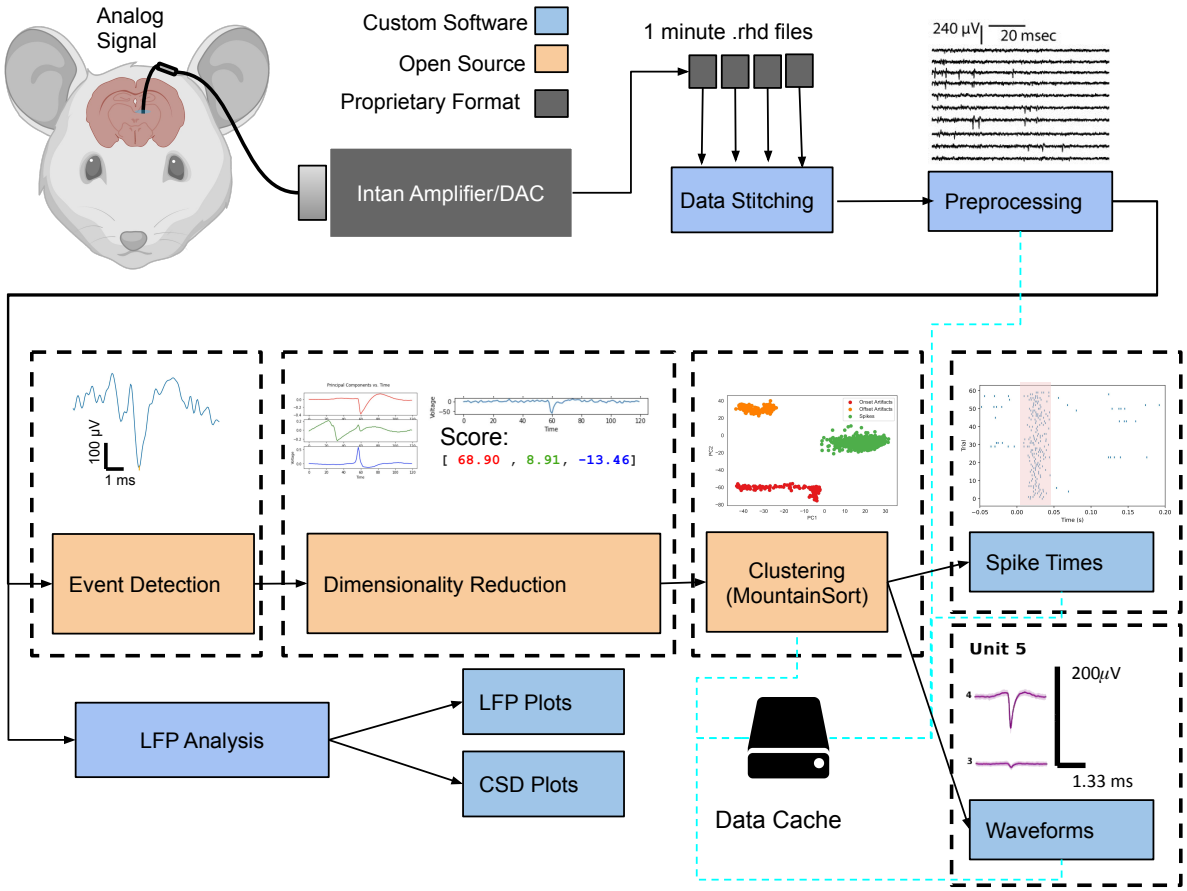

Figure 6.13: Schematic diagram of the different stages and capabilities of the in-house neural signal processing pipeline. Custom, open source, and proprietary software components are color-coded. Representative plots showing the data format at different stages of the processing are shown above the corresponding schematic block, grouped by a dashed line boundary. Light blue dashed line indicate stages of the pipeline where the data are cached, allowing for the results to be loaded on-demand rather than recomputed.

This software system allowed for easy remote collaboration between teams of researchers. A team of undergraduate students worked to implement visualizations and preprocessing steps in accordance with the evolving neural signal processing needs of the lab. Furthermore, the user-friendly Python notebooks allowed non-programmer users to analyze data and generate visualizations with minimal local hardware resources and without needing to modify the source code.

All results presented in the following sections were produced via this system.

6.6.3 Results

Spike sorting resulted in identifying 23 distinct neural units in the recorded dataset. Unit waveforms are detected on multiple adjacent electrodes in the vicinity of the neuron. A single example waveform is shown in figure 6.14. Example waveforms for several of the units are shown in Figure 6.15. Additionally, peristimulus histograms show the response of each cell during and immediately after optical stimulation 6.16 The peristimulus histogram for "spontaneous" units do not show any excitation during the stimulus interval, whereas "evoked" units show clear excitability by the optical stimulus. Therefore, it appears that the optical stimulus of the probe is selective to only certain cells in the recording volume. It is possible that not all cells in the vicinity of the probe are expressing the ReaChR opsin. Alternatively, some of the cells may be too far from the output port of the waveguide to be optogenetically stimulated with the emitted optical power. As light is dispersed and scattered in the tissue, it will lack the intensity to stimulate neurons that are located further away.

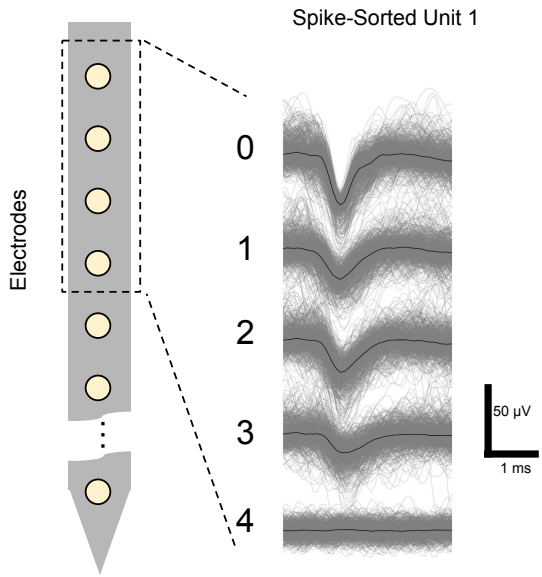

Figure 6.14: A single example unit waveform plotted. The waveform is plotted for each channel on which it is detected, indicated by the schematic diagram of a probe. The average waveform is denoted by a thick black line. Individual events are overlaid in thin gray lines.

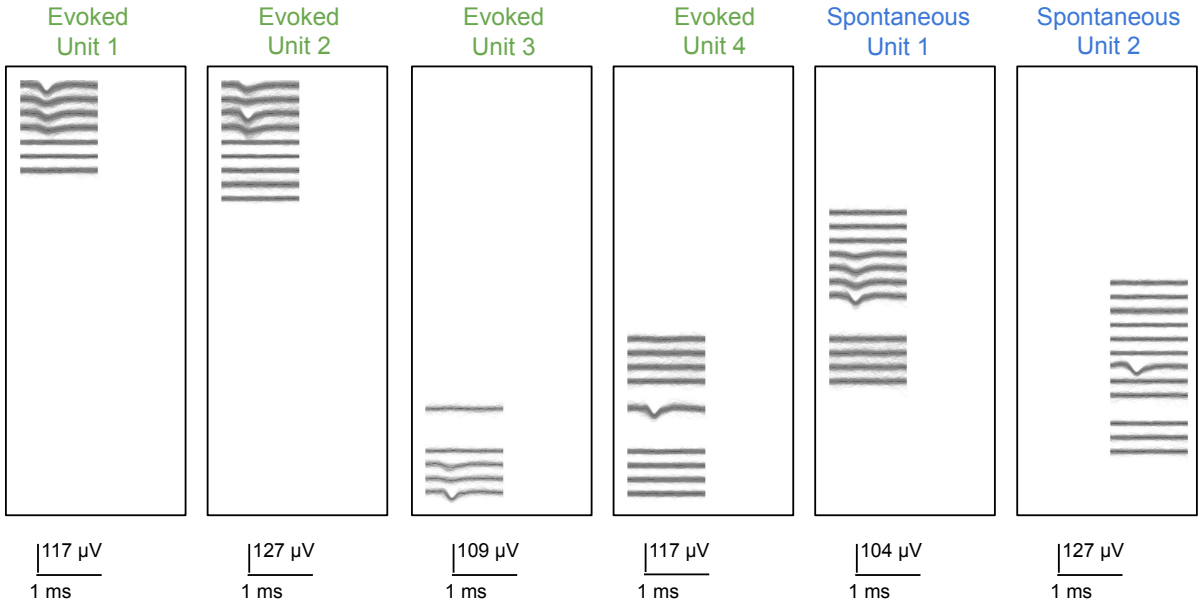

Figure 6.15: Example unit waveforms detected via spike sorting. The waveform is plotted for each channel based on the channel location on the probe shank, denoted by a black rectangle. The waveform is plotted for all electrodes in a 150 µm radius of the peak waveform for each unit.

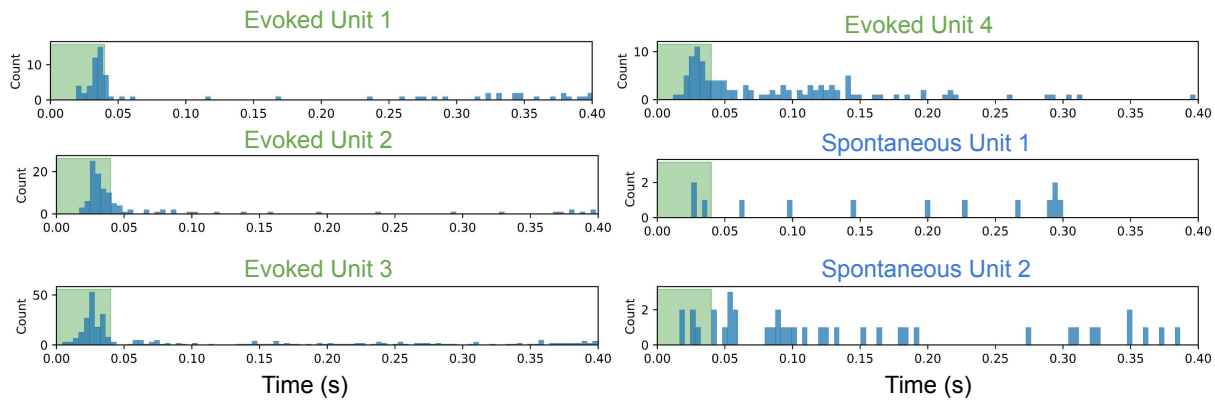

Figure 6.16: A peristimulus histogram is shown for each unit across a 400 ms interval, including a 40 ms stimulation. The period of optogenetic stimulation is denoted by green shading. Units with evoked activity show increased firing during the stimulus interval, but return to baseline firing rates immediately following stimulation. On the other hand, spontaneous units do not show any increase in firing probability during the period of optogenetic stimulation.

6.7 Integrated Recording Electrodes for Read/Write Neural Probes

For the intended application of read/write bidirectional neural interfaces in this thesis, the optical capabilities must be designed to accommodate the monolithic integration of recording electrodes to facilitate electrophysiology recording as a readout mechanism. Recording electrodes are usually formed via exposed metal sites connected by traces embedded in polymer insulation [1, 105]. These can be routed over the Parylene photonic waveguides in a separate planar layer, deposited subsequently in the microfabrication process. In this section, I discuss additional process steps which can be combined with the Parylene photonic waveguide fabrication process discussed in Chapter 3 to create monolithically integrated recording electrodes.

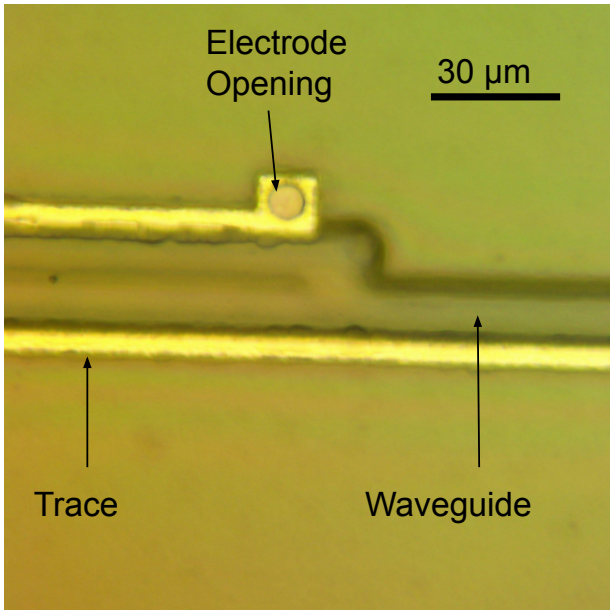

Figure 6.17: Microscope image of lithographically-defined traces and etched electrode openings monolithically integrated with Parylene photonic waveguides.

6.7.1 Recording Electrode Fabrication

A 5-µm thick layer of Parylene C was then deposited (SCS Labcoter-2) to form the lower trace insulation. Metal traces were deposited (5 nm Pt, 100 nm Au, 5 nm Pt) using an electron beam evaporation process (Kurt J. Lesker PVD 75). Platinum serves as an adhesion layer to Parylene C, whereas gold is used as the core conductor since it is a soft and highly conductive metal. The metal layer was lifted off using photoresist (AZ 4210). A second layer of Parylene C was deposited to a thickness of 5 µm as the upper trace insulation. A 100 nm-thick Al hardmask was deposited via sputtering (CVC Connexion Sputtering System), and patterned using lithography and wet etching (Al Etchant Type-A, Microchem GmbH, DE). The recording electrode sites (Fig. 6.17) were exposed using O_2 plasma etching (Trion Phantom II RIE). After etching, the Al hardmask was stripped.

6.7.2 Modal Confinement from Metal Traces

One concern of combining electrical and optical functionalities on the same platform is the interaction of the optical waveguide modes with electrical traces, which will decrease the delivered optical power due to absorption losses in the metal. Commonly used metals such as Au, Pt, Ti, and Al exhibit large absorption coefficients in the visible range of the optical spectrum [161]. Electrical traces can be routed along the length of the device, parallel to the optical waveguides. Therefore, any significant interaction between the guided optical mode and metal traces would cause significant attenuation of light after traversing the full probe length. The electrical traces are vertically spaced from the photonic layer by the PDMS cladding (Fig. 6.18a). To study the optical propagation loss due to the electrical traces, finite difference eigenmode (FDE) simulations of the waveguide geometry (30 µm x 5 µm) with a thin sheet of metal (200 nm of Pt) situated over the cladding were performed. A target PDMS thickness of 1 µm was chosen for the study.

The Parylene photonic waveguide with dimensions of 30 µm x 5 µm is multimode in the visible range. Since each mode profile has a different intensity distribution inside and around the waveguide core, the modes experience different levels of attenuation from the presence of the metal sheet. However, when such a multimode waveguide is excited by an external light source (i.e., a laser), optical power is preferentially coupled to lower order modes, due to the larger overlap between the typical Gaussian mode profile of the light source and the optical mode profiles of the lower order modes. Optical losses caused by the interactions with the Pt layer were modeled for the lowest 30 modes and were found to be less than 3×10^{-10} dB/cm for the fundamental mode (Fig. 6.18b), and less than 5×10^{-8} dB/cm for each of the remaining simulated modes (Fig. 6.18c). These results demonstrate that 1 µm of PDMS cladding is sufficiently thick to insulate the waveguide modes from interaction with additional metal layers.

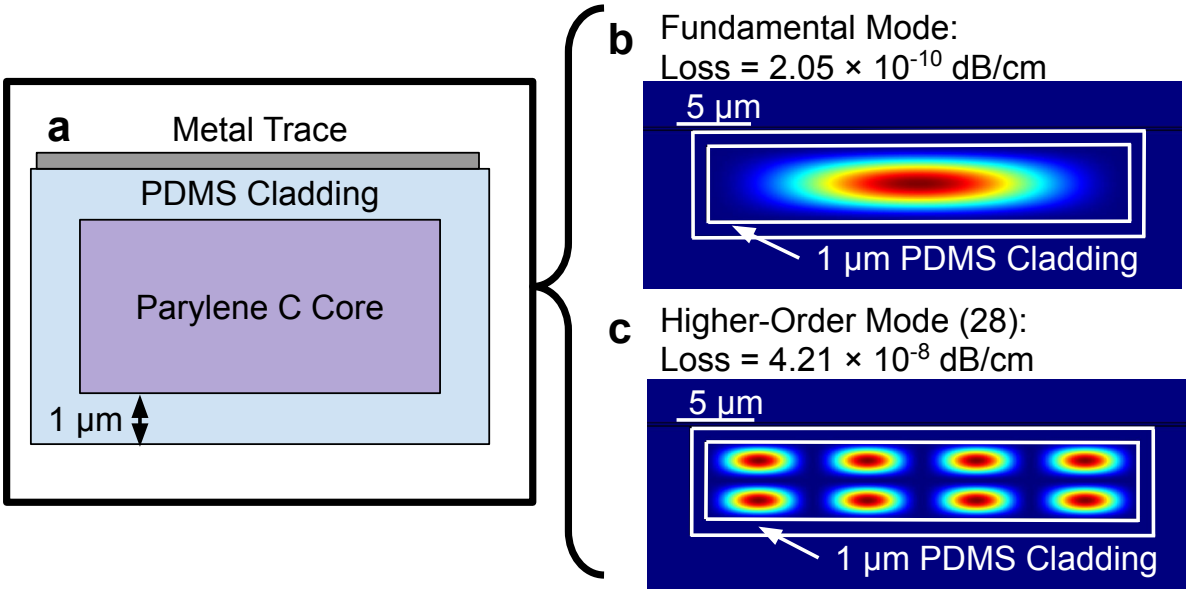

Figure 6.18: a) Schematic cross-section of the device shank, with a metal trace over the waveguide core on top of the cladding. Modal analysis of the waveguide in the presence of the metal traces. Here, due to minimal interaction with the metal layer, both the b) fundamental mode and c) higher-order modes show negligible losses

6.7.3 EIS and Characterization

The electrochemical interface of the integrated recording electrodes were characterized using Electrochemical Impedance Spectroscopy (EIS) measurements in 1X phosphate buffered saline solution in a 3-electrode potentiostatic configuration. Measurements were performed using a potentiostat/galvanostat (PSGSTAT202N, Metrohm Autolab). A silver/silver chloride (Ag/AgCl) reference electrode (MF-2052, BASI Inc.) and a platinum wire counter electrode (MW-1032, BASI Inc.) were used.

PEDOT:PSS was electroplated to reduce the channel impedances, which increases the signal-to-noise ratio of electrophysiology recordings. The electroplating solution was prepared as follows: 20 ml deionized water was combined with 120 mg polysodium styrene sulfonate (pss) in a test tube and mixed thoroughly with a stirring rod at 1500 rpm for 30 minutes. 12 µL of 2,3-ethylenedioxythiophene (EDOT) was added with a micropipette and the solution was stirred

at 1500 rpm for 1 hour. The solution was covered and refrigerated for 24 hours prior to use. The solution was then brought to room temperature before electroplating. Electroplating was performed via chrono amperometry with a 3 electrode configuration. Deposition was performed at 0.8 V while the applied current was monitored. The deposition was stopped once the current plateaued, indicating that PEDOT:PSS had formed a new electrochemical interface, typically 200-400 s. After PEDOT:PSS coating, the electrode impedance is reduced from 4.4 MOhm at 1 kHz to 77.6 kOhm at 1 kHz.

6.8 Conclusion

In this chapter, I have demonstrated that Parylene photonic waveguides can deliver sufficient power into the tissue to optogenetically stimulate neural activity. Additionally, I have demonstrated a process flow for monolithically integrating recording electrodes onto the probe shank, collocated with the Parylene photonic waveguides. In the future, this approach will allow for high-density optical stimulation and neural recording with a single flexible device. The major outstanding challenge for the practical application of Parylene photonics is the efficient coupling of light at the input port. The easiest way to couple light into the waveguide is butt-coupling with an optical fiber. However, this approach does not scale easily to many channels. Even using a fiber array connector, the resulting backend would be bulky due to the large number of fiber tethers. I have shown that miniature VCSEL laser sources can be packaged at the waveguide input port. However, the large size mismatch between the VCSEL and waveguide input mirror aperture leads to prohibitively low coupling efficiency. This can be resolved in future work through the use of custom VCSEL sources which can match the size of the waveguide input, or by using an alternative input coupling technique such as grating couplers combined with adiabatic tapers to form a large input port for the waveguide. Nevertheless, this thesis provides a proof-of-concept demonstration of the fundamental capabilities of the Parylene photonic platform for flexible biocompatible photonics.

Chapter 7

Active Implants - μLEDs

7.1 Introduction

In this chapter, I discuss the design, fabrication, characterization, and testing of μLEDs using gallium nitride (GaN) grown on a silicon wafer, monolithically integrated and encapsulated in a flexible polymer substrate that includes embedded electrical interconnects. Compared to passive photonic neural interfaces including Parylene photonics, which deliver light from external light sources into the tissue, μLEDs generate light in the tissue itself. Without the need to connect to an integrated light source, μLED neural probes obviate the need for bulky and alignment-sensitive optical connections at the backend. μLED traces only require backend electrical connections to external power supplies, which allows for the use of simpler and more established electrical packaging techniques, such as wirebonding.

In this chapter, I demonstrate that high-density arrays of up to 32 light sources can be achieved with this approach. However, light generation inside the tissue creates excess heat that is dissipated into the tissue from the embedded μLEDs. Therefore, tissue heating needs to be analyzed and managed.

Portions of this chapter are adapted, with permission, from the author's prior work in [162]

The polymer and electrical interconnects are realized on top of the wafer during the fabrication process to encapsulate linear or 2D arrays of GaN μLEDs. The monolithic flexible stack is then released from the silicon substrate at the end of the fabrication process. I demonstrate wafer-scale, high-throughput microfabrication processes to implement μLED neural probes, consisting of monolithically integrated arrays of GaN μLEDs and recording electrodes on a flexible Parylene C polymer substrate. Although GaN-based LEDs grown on silicon substrates typically have a low emission efficiency compared to similar devices fabricated on sapphire substrates, the fabrication process is scalable and is based on commonly-used microfabrication techniques on silicon. This process allows for a dense integration of optical stimulation and electrical recording functionalities on a unified platform for realizing high-resolution, minimally invasive neural interfaces.

7.2 LED Arrays in Parylene Substrate

The GaN-on-Parylene optoelectronic neural probe architecture is designed to allow simultaneous optical and electrical access to the brain, while the flexible substrate minimizes tethering forces and tissue damage inherent to rigid implantable devices. A schematic of a penetrating neural probe implemented in the architecture is shown in Figure 7.1. The probe backend, which is designed to remain outside the tissue, contains an array of bonding pads to interface with external control and signal processing electronic circuits. The implantable portion of the probe frontend consists of a flexible strain-relief cable which routes a dense array of electrical interconnects and an interface region containing collocated μLEDs and recording electrodes. Each layer is lithographically defined, allowing for customizable layouts of the electrodes and μLEDs along the probe shank. Arbitrary sizes and shapes of lithographically-defined GaN μLEDs can be realized. Therefore, different specific instantiations can be envisioned from a sparse array of optical stimulators along the length to record and stimulate different layers of the cortex, or dense arrays for high-resolution interrogation of a specific region of the tissue.

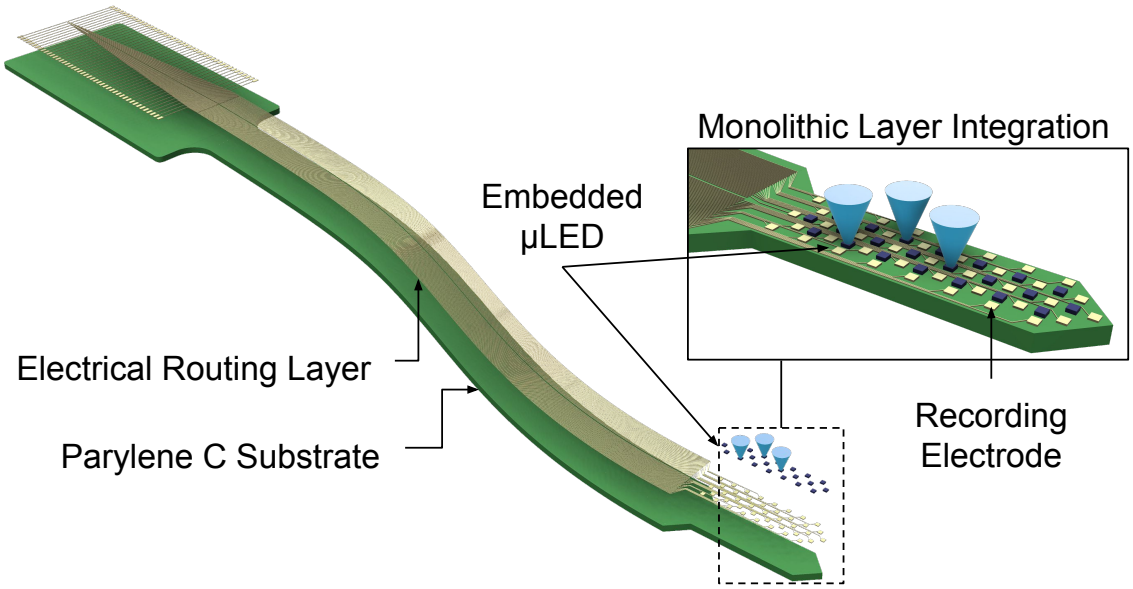

Figure 7.1: Schematic of a µLED neural interface with a high-density array of optical stimulators and recording electrodes monolithically integrated in the active region. Electrical traces are routed to the probe backend through the flexible Parylene C polymer insulation.

The cross-section of the GaN LED mesas is shown in figure 7.2. The LED mesas are encapsulated in Parylene C on the top and sides. On the bottom of the structure, insulating undoped GaN and (Al,Ga)N covers the bottom surface. Parylene C and undoped GaN are optically transparent at optogenetics wavelengths (i.e., $\lambda = 445$ nm). Therefore, light generated in the GaN mesa can be emitted from both sides. Therefore, GaN-on-Parylene can be used to realize double-sided LED neural probes, which is a unique feature compared to LEDs realized on opaque substrates.

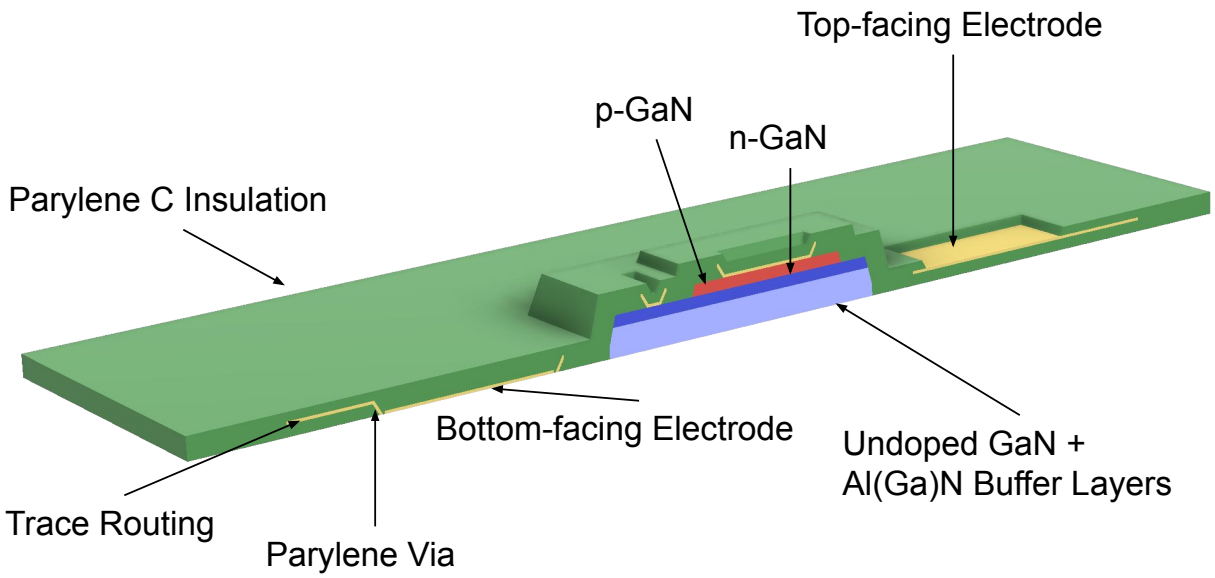

Figure 7.2: Schematic of monolithically integrated architecture for μLED optical stimulators and recording electrodes in a Parylene C polymer substrate.

7.3 Microfabrication Process - μLEDs

I have optimized a scalable, wafer-level fabrication process for high-throughput manufacturing of optoelectronic neural probes using the GaN-on-Parylene architecture. Fabrication is performed on commercially available GaN-on-Si epitaxial wafers (Suzhou Innovo Semicondocutor Co., China). The substrate is a 2-inch, 1.5-mm thick Si (111) wafer. The epitaxial layer structure consists of 900 nm of an (Al,Ga)N buffer layer on top of silicon, 400 nm of an undoped GaN, 3200 nm of an n-type doped GaN layer, a 250 nm active region comprised of multiple quantum wells, and a 150 nm p-type doped GaN layer. The fabrication process is schematically illustrated in Fig. 7.3. The steps of the fabrication process are detailed in the following sections.

7.3.1 GaN Mesa Fabrication

First, the GaN μLED mesas are patterned in the epitaxial layers of the GaN-on-Si wafer. Metal p-type contacts (17 nm Ni/150 nm Au) are deposited on the top p-type GaN layer of the device structure using an electron beam evaporator (Kurt J. Lesker PVD 75) and patterned via lift-off (Fig. 7.3b). The p-type GaN mesa is then patterned into the epitaxial layers of the wafer using an inductively-coupled plasma reactive-ion etching (ICP RIE) process (PlasmaTherm Versaline) in chlorine gas chemistry (Fig. 7.3c). A timed etch was used to pattern p-type GaN layer and stop at the n-type layer. N-type metal contacts (17 nm Ni/ 150 nm Au) are then deposited on the exposed n-type GaN layer using an electron beam evaporation and patterned via lift-off (Fig. 7.3c). The n-type layer is then patterned and etched to form the μLED mesa structure. The n-type GaN and (Al,Ga)N layers are completely etched to reveal the underlying Si substrate (Fig. 7.3d) using the chlorine ICP RIE process (PlasmaTherm Versaline). Due to the poor selectivity of photoresist to the chlorine etch chemistry, a thick layer of photoresist was used (10 μm, AZ4620). During the etching process, the backside of the wafer was cooled by the chuck and the etching was cycled in 2-minute intervals to prevent substrate heating.

7.3.2 Parylene Vias and Metal Interconnects

To insulate the mesa structures, a 300-nm film of SiO_2 was conformally deposited using a plasma-enhanced chemical vapor deposition (PECVD) method in a Trion Orion II PECVD machine (Fig. 7.3e). The SiO_2 was then selectively removed from the μLED contacts and the probe outline using a CHF_3 RIE process (PlasmaTherm 790 RIE).

If backside electrodes are desired, the SiO_2 layer should also be removed from the regions where the electrode surface will be deposited. This way, the backside electrodes will be exposed at the end of the process when the wafer is released. The SiO_2 under the flexible cable is purposefully left in place and serves as an etch-stop layer during the release process.

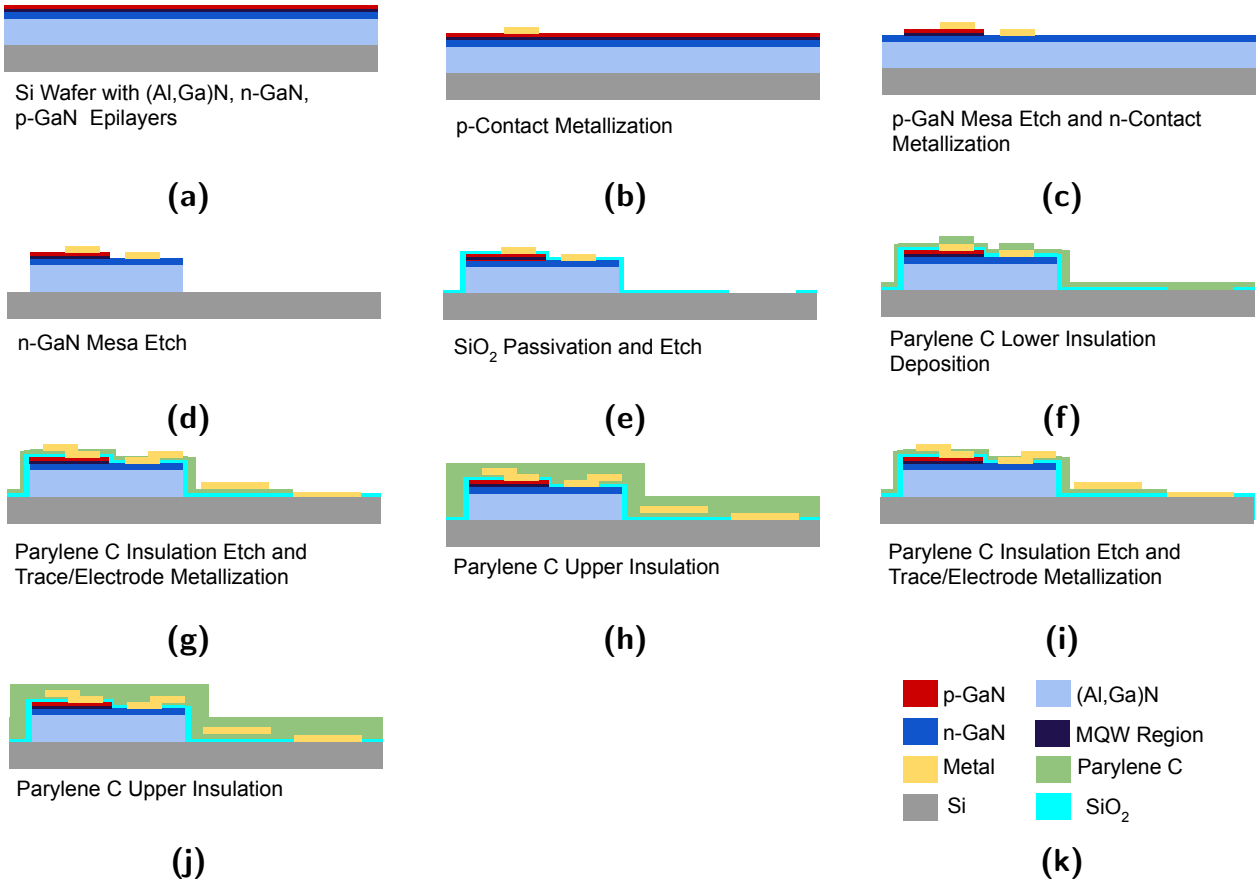

Figure 7.3: Schematic process flow for a µLED neural probe

A 5-µm thick layer of Parylene C was then deposited (SCS Labcoter-2) to form the neural probe substrate and lower trace insulation. An adhesion promoter (A174 Silane) was applied prior to the deposition of Parylene C to prevent its premature delamination during processing (Fig. 7.3f).

The Parylene C layer is conformal and covers the entire wafer surface. To form electrical connection to the p-type and n-type ohmic contacts of the µLEDs and backside recording electrodes, vias are etched through the Parylene C insulation. To form the vias, a thick photoresist mask was spin-coated on the Parylene C surface (8 µm) and deliberately under-exposed during lithography to form a slanted sidewall profile. The vias are etched in oxygen plasma RIE (Trion Phantom II), which creates sloped sidewalls in the Parylene C layer (Fig. 7.3g). The average sidewall angle to by

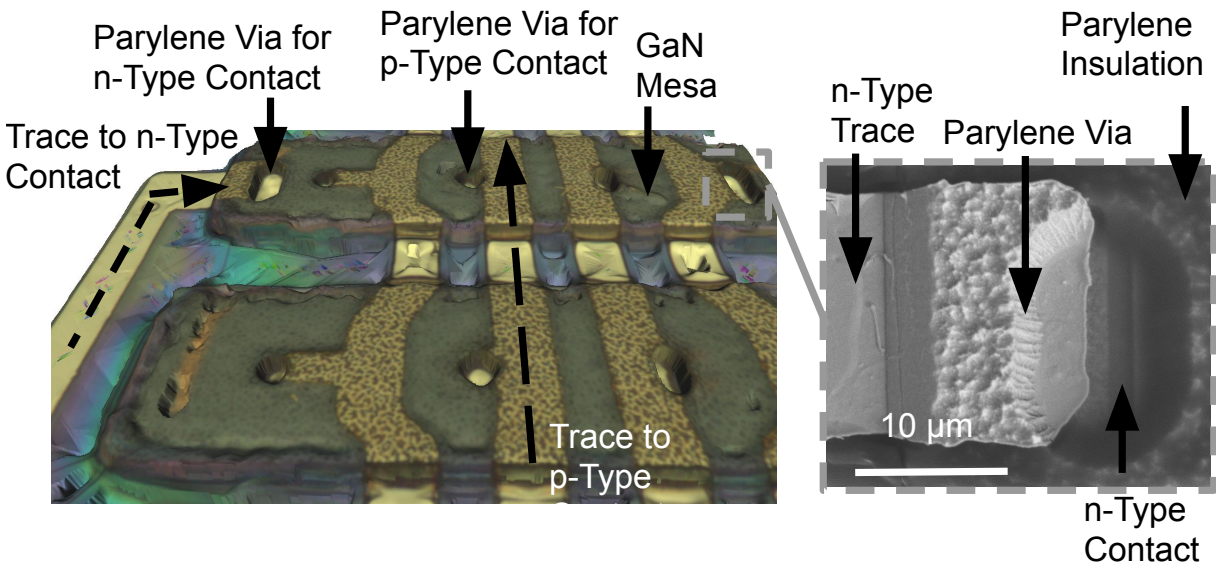

Figure 7.4: (Left) Reconstructed 3D microscope image (InfiniteFocus, Alicona Imaging GmbH) of µLED mesa topography and interconnects (Right) SEM image of Parylene via interconnect.

70.3° using a combination of step-height measurement and top-down SEM. Electrical connection was established through the via using electron beam evaporation (Kurt J. Lesker PVD 75) and lift-off of a thick metal layer (15 nm Pt, 400 nm Au, 15 nm Pt). Platinum is used as an adhesion layer to Parylene C because it features biocompatibility and low electrochemical impedance as a recording electrode [163]. LOR 5B is used as a lift-off resist to aid the patterning of such a thick metal stack. LOR 5B resist requires a 180°C bake step, which conflicts with the low temperature processing requirements of Parylene C (160°C glass transition temperature). However, Parylene C can withstand temperatures as high as 300 °C in a nitrogen or vacuum environment [122]. Therefore, the LOR 5B resist was baked in a nitrogen oven to protect the Parylene C. The mesa topography and metal interconnects are shown in Figure 7.4. An upper insulation of 5 µm Parylene C was deposited on the wafer surface (Fig. 7.3h) to complete the device encapsulation.

This optoelectronic neural probe platform features monolithic integration of μLEDs on a flexible Parylene C substrate. The wafer-level fabrication process introduced in this paper greatly increases the process scalability compared to serial packaging processes such as flip-chip bonding. Unlike manual assembly processes, which are limited by the alignment accuracy of the available device bonders and increased fabrication time with the number of devices, lithographic definition of the electrical and photonic devices in this design results in much higher precision, allowing for high-throughput realization of an arbitrary number of devices in parallel.

7.4 Routing Considerations for μLED scaling

To enable high-density optogenetic stimulation in the tissue, it is desirable to maximize the number of μLED stimulators that can be incorporated into the neural probe. There is an inherent tradeoff between the number of channels that can be integrated in the neural probe shank and the size of the resultant device. Compact devices are desired to minimize implantation damage to tissue and maximize the device flexibility. However, each electrical trace requires additional routing space in the probe shank, increasing the size. If each μLED trace is routed separately, then the size probe shank will scale linearly with the number of traces. The minimum width is determined by the number of traces to be routed n_t and the trace pitch p (Eq. 7.1).

$$W = p \times n_t. \tag{7.1}$$

Here, I have used a conservative 10 μm trace pitch for ease of fabrication across the via topography. However, traces as small as 300 nm [121] have been demonstrated on Parylene C substrates. In principle, lithographic scaling is possible using deep-UV or electron-beam lithography [164, 165]. These processes would increase the device density at the expense of additional process complexity. Furthermore, size scaling would eventually become limited by the trace resistance. As traces become narrower, the cross-sectional area decreases and the resistivity

increases. An increased trace resistance would lead to increased power dissipation in the traces themselves to provide current to the μLEDs. For recording electrodes, increased resistance in the traces causes an increase in the amount of thermal noise, which would decrease the signal-to-noise ratio for electrophysiology recording. Therefore, scaling is only practical to a point through improved lithography resolution. Here, I am going to demonstrate that the monolithic fabrication process of GaN-on-Parylene allows for routing designs that reduce the number of total traces which are required and enable a massive scaling of the number of μLEDs which can be integrated in a single neural probe shank.

In any routing scheme, each μLED requires a p-type and an n-type ohmic contact trace. If each contact trace is routed individually (Fig. 7.5 (left)), the total probe width is

$$W = p \times 2N, \tag{7.2}$$

where N is the number of μLED devices. In such a scheme, a probe shank with 200 traces would support a maximum of 100 μLED devices. This scheme can be improved through use of a shared common n-type contact in linear arrays (Fig. 7.5 (center)), thus reducing the width of the shank to

$$W = p \times (N + 1), \tag{7.3}$$

since each μLED now requires only one trace for each contact to the p-type layer, and all devices share a common trace for the n-type contact. In this shared n-type contact scheme, a probe shank that can accommodate 200 traces would support a maximum of 199 μLEDs.

To allow for a massive scaling of the number of μLED devices per probe shank the traces for the p-type and the n-type contacts can be shared among μLEDs in an individually-addressable grid (Fig. 7.5 (right)). Such a scheme would reduce the required probe in a square array width to

$$W = p \times 2\sqrt{N}. \tag{7.4}$$

In general, the number of traces required is equal to the product of the number of rows and columns in the grid. This design offers a quadratic increase in the number of devices that can be accommodated compared to linear routing schemes. For example, 200 traces would support 10,000 μLEDs. However, this routing scheme can't be implemented in a single routing layer. Perpendicular traces defined in a single layer would cross each other and cause short-circuits. The fabrication process can be modified to include additional routing layers, but this would further complicate the process by adding additional lift-off and insulation steps, which would increase cost and reduce device yield.

Monolithic device fabrication can circumvent this limitation by taking advantage of the lithographic definition of the GaN mesa to achieve 2D routing with a single trace layer. Since the p-type and n-type GaN layers are patterned in separate lithographic steps, they can be defined in arbitrary shapes. Here, I define the individual p-type mesas in a rectangular grid, and n-type mesas in horizontal strips along the axis of the grid. The routing of each n-type "row" of the grid is accomplished by the n-type contacts on the GaN mesa itself (Fig. 7.5 (right)). Electrical traces running in vertical "columns" join the p-type contacts vertically. The n-type layer is separated from the electrical traces by SiO_2 and Parylene C passivation, providing two separate layers for routing without additional processing steps. This architecture is only possible when the GaN mesas and neural probe cable routing are monolithically integrated, since it requires that the shape of the GaN μLED structures accommodate the trace routing.

As a proof-of-concept of this architecture and routing scheme, I have demonstrated dense 2D arrays with a pitch of 60 μm in the y-axis and 40 μm in the x-axis. Individual GaN μLEDs have an active area of 22 μm × 22 μm. Although two-dimensional indexing of μLEDs in this manner

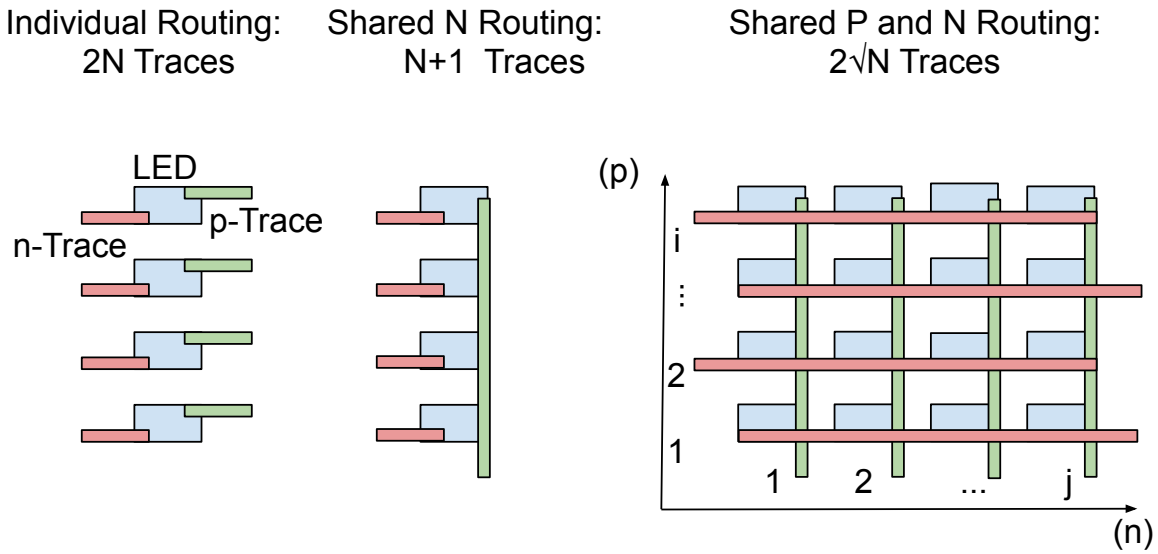

Figure 7.5: (Left) Trace routing scheme when each μLED has a dedicated electrical trace for the p-type and n-type contacts, resulting in 2N total traces. (Center) Trace routing scheme where a linear array of μLEDs share n-type contacts, resulting in $N + 1$ total traces. (Right) Trace routing scheme where a 2D array of μLEDs share traces for p-type and n-type contacts, resulting in only $2\sqrt{N}$ traces. This routing scheme cannot be achieved in a single routing layer, as trace intersections will short the p-type and n-type traces.

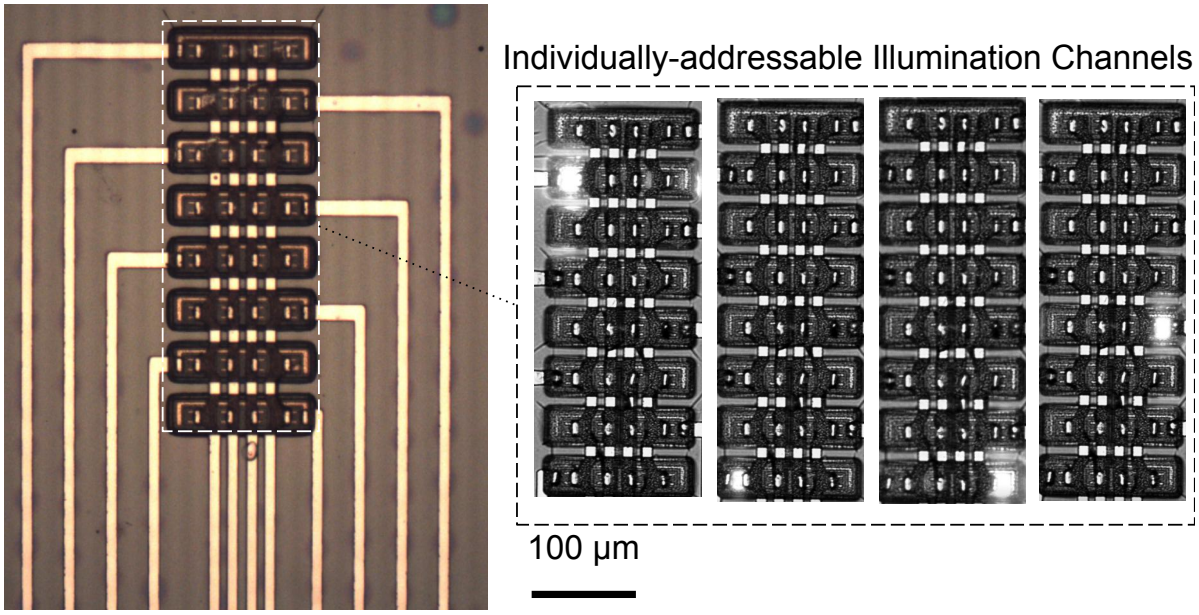

Figure 7.6: Microscope image of a 2D LED array with multiplexed routing scheme. Inset images show illumination of individual LEDs in the array.

has been previously suggested by Goßler et al. [166], these devices are the first active photonic neural probes to utilize a full 2D implementation of the shared-contact routing scheme (Fig. 7.6). The enabling feature is the monolithic fabrication process, which allows fabrication of the n-type mesa in horizontal strips to access μLEDs in each row. This removes the need for a separate layer of traces to make horizontal connections in a 2D routing scheme.

Each μLED can be individually indexed in the array and activated by sourcing current to the trace corresponding to the μLED's p-type contact while grounding the trace corresponding to the n-type contact. Additionally, entire rows of μLEDs can be simultaneously activated by sourcing power to a single p-type trace to select the row, and grounding all the n-type traces. However, this indexing scheme does not allow for arbitrary sets of μLEDs in the array to be activated at the same time. Each LED device can be indexed in the array by the trace number for the p-type and n-type contacts: (p, n). Multiple devices may be powered simultaneously by connecting multiple p-type and n-type contacts. In this scheme, only specific sets of devices can be simultaneously

powered. For example, devices $(1, 1)$ and $(2, 2)$ may not be powered without activating devices $(1, 2)$ and $(2, 1)$. The set of indexed devices is the cartesian product of the sets of active p-type and n-type contacts. In this scheme, entire rows of μLEDs may be powered simultaneously.

Although arbitrary patterns of simultaneous illumination are not possible, arbitrary patterns of simultaneous neural stimulation can be achieved through time-division multiplexing. The temporal response of ion channels, which mediates the generation and propagation of action potentials, is generally on the order of milliseconds (kHz); the light sources in this platform, on the other hand, can be modulated at frequency rates in the range of MHz [167]. This means time-division multiplexing on these timescales would be indistinguishable to a neuron from continuous illumination. This way, one may generate arbitrary patterns of neural stimulation by rapidly time-division multiplexing sets of μLEDs. Using this method, the average delivered power to neural tissue is reduced since it is split between various μLEDs, providing an ultimate limit to the number of simultaneous optical stimulation sites that can be achieved. Additional research into the behavior of these devices at short pulse durations is needed to ascertain the total number of simultaneous active light sources that could ultimately be possible.

7.5 Conclusion

This neural probe platform is the first to monolithically integrate GaN μLEDs and recording electrodes on a flexible polymer substrate using a process that can be achieved in standard microfabrication facilities. This architecture allows manufacturing of extremely high density of μLEDs in 2D arrays. Since each device layer is lithographically defined in the fabrication process, I am able to use the n-type GaN mesa as an additional routing layer to create a 2D grid without multiple layers of metal traces. This novel routing scheme enables realization of ultra-compact, high-density, optoelectronic neural probes with correspondingly compact shanks and cables. The overall scheme enables arbitrary patterns of neuronal stimulation. Furthermore, through an optimized

wafer-scale fabrication process and post-fabrication packaging, we can achieve a high-throughput manufacturing process to produce many of these neural probes. Arbitrary patterns of optical stimulation can be generated using these optoelectrodes. The collocation of recording electrodes and μLEDs enables simultaneous electrophysiology recording and optogenetic stimulation of the brain to study individual neural circuits with high spatio-temporal resolution.

Chapter 8

Characterization and Demonstration of Active μLED Arrays

8.1 Introduction

This chapter discusses optical characterization of GaN-on-Parylene μLED arrays and applications for optogenetic stimulation of neurons. Optical measurements are performed in the same setup discussed in section 5. Based on the characterized efficiency and beam profile of the μLEDs, a thermal and optical model is developed to analyze patterns of optical stimulation and heat spread in tissue. Based on these models, thermally-safe stimulation patterns are designed. The μLEDs are then demonstrated for ex vivo optogenetic stimulation of Channelrhodopsin-expressing brain slices in a patch clamp electrophysiology rig. Finally, incorporation of monolithically-integrated recording electrodes for read/write neuroscience experiments is discussed.

Portions of this chapter are adapted, with permission, from the author's prior work in [162]

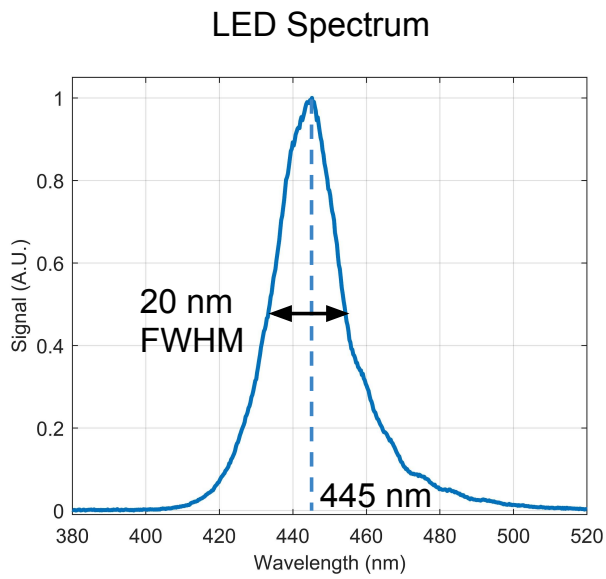

Figure 8.1: Emission spectrum of μLED, with peak at $\lambda = 445$ nm, with a narrow spectral bandwidth of 20 nm

8.2 LEDs Optical Characterization

The μLED neural probe was designed to stimulate commonly used channelrhodopsin variants that have peak absorption at $\lambda = 450$ nm. The μLED emission peak is at $\lambda = 445$ nm, with a narrow spectral bandwidth of 20 nm, full-width-at-half-maximum (FWHM) (Fig. 8.1). Optical device characterization was performed using a fiber spectrometer (Flame-S, OceanOptics) with an integrating sphere.

The optical power and wall-plug efficiency for individual (22 μm × 22 μm) μLEDs were measured using a calibrated power meter from the top and bottom surfaces of the device across a range of drive currents (Fig. 8.3). The device was powered using a probe station connected to a sourcemeter (Fig. 8.2). The peak wall plug efficiency of 6.5% is typical for GaN LEDs grown on silicon substrate [48]. The peak efficiency drive current of 8.5 μA corresponds to 540 nW of optical power from the top surface of the probe and 1.3 μW of optical power from the bottom surface. The different intensity between top and bottom is due to the reflection of emitted light

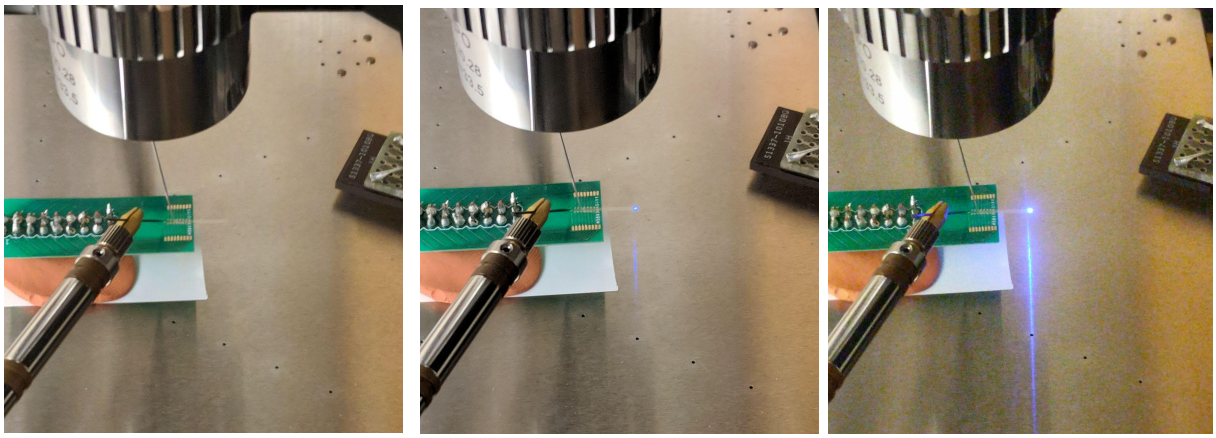

Figure 8.2: Images of µLED measurement setup on a probe station during various phases of an IV measurement sweep.

from the frontside U-shaped metal contacts, and fresnel reflections as light is reflected from the various epitaxial layers above and below the multiple quantum well (MQW) region. The IV characteristics of the µLEDs shows a turn-on voltage of 2.5V 8.4, which is typical for blue GaN LEDs [48].

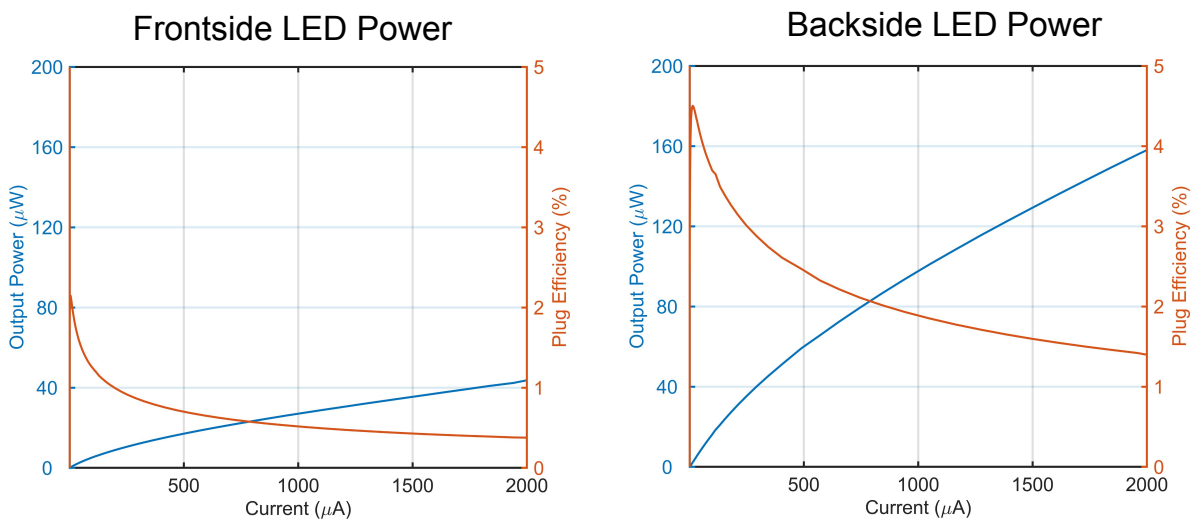

Figure 8.3: (left) Frontside and (right) Backside μLED power and efficiency vs. drive current. Backside emission is approximately 4 times higher due to reflection from the frontside metal contacts. Total efficiency of the μLED structure for a given current is the sum of the frontside and backside efficiencies. Peak efficiency is therefore 6.5%.

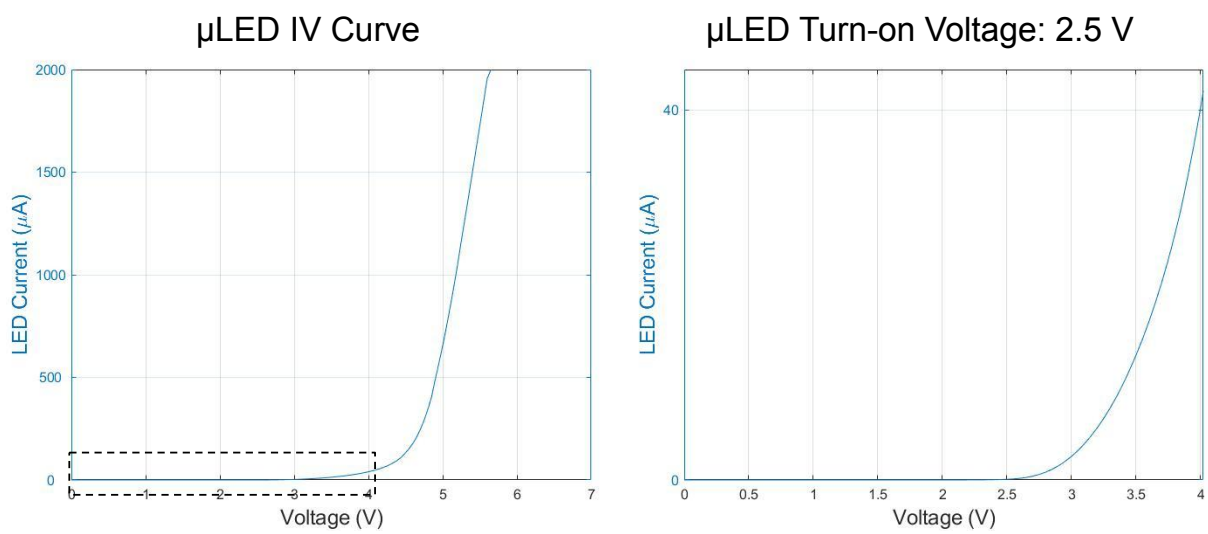

Figure 8.4: IV curve of GaN μLEDs showing a turn-on voltage of 2.5V.

8.3 Ex Vivo Demonstration

In this section, I discuss the demonstration of μLED neural probes for optogenetic stimulation of Channelrhodopsin-expressing neurons in mouse brain slices. Details of the experimental setup, brain slice preparation, stimulation paradigm, and data analysis will be discussed in the following sections.

8.3.1 Ex Vivo Setup

A custom patch clamp electrophysiology setup was built to demonstrate proof-of-concept ex vivo validation of GaN-on-Parylene μLEDs for optogenetic stimulation. A custom recording chamber was built around a μLED probe wafer, which formed the bottom of the chamber (Fig. 8.5). This way, the brain slice can be placed directly on top of the μLED array, and the top surface of the brain slice is accessible for patch clamp recording. The Si wafer provides a mechanically robust substrate for the bottom of the recording chamber.

The walls of the recording chamber were constructed using laser-cut acrylic sheets. The design consists of 3 layers: 1. a piece designed to attach to a standard patch clamp electrophysiology rig. 2. A sheet cut in the shape of the outline of the μLED chip, so that the two will slot together to form a solid surface as the base of the recording chamber. 3. A sheet with a 2 cm diameter hole cut in the center to form the walls of the recording chamber. The three pieces were glued together with superglue along with the μLED chip to form the recording chamber (Fig. 8.6a). After leak-testing the chamber and using additional superglue to fill any gaps, the custom recording chamber was placed on an electrophysiology rig (Fig. 8.6b) and filled with recirculating oxygenated artificial cerebrospinal fluid (ACSF) for ex vivo experiments.

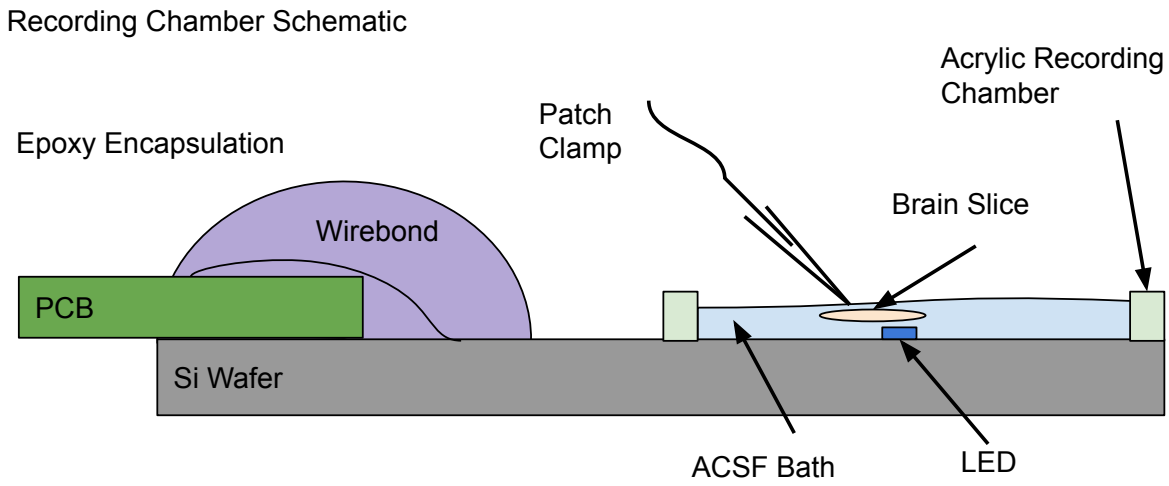

Figure 8.5: Schematic diagram of the design of the ex vivo experiment for optogenetic stimulation using μLED neural probes. A custom ex vivo recording chamber capable of holding artificial cerebrospinal fluid (ACSF) is built on the surface of the μLED wafer before release, allowing for a live brain slice to be placed on top of the μLED array. Patch clamp electrophysiology recording is performed from the top surface of the brain slice.

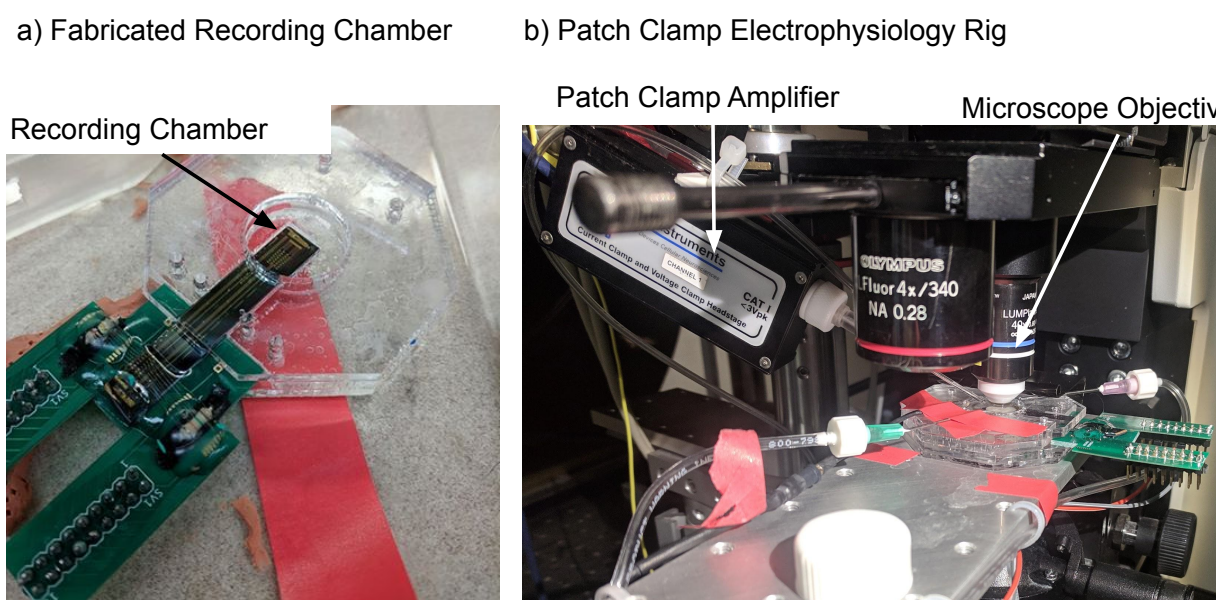

Figure 8.6: a) Custom acrylic recording chamber built around a packaged μLED chip. b) Custom recording chamber placed in electrophysiology rig.

8.3.2 Brain Slice Preparation

Brain slices for optogenetic stimulation were obtained from p22 sst-cre/Ai32 ChR2-expressing mice (Sst-Cre, stock: 013044; Ai32(RCL-ChR2(H134R)/YFP), stock: 024109; Jackson Laboratory; Bar Harbor, ME). A VT1200S vibrating blade microtome (Leica Biosystems Inc., Buffalo Grove, IL) was used to cut 350 µm thick coronal slices in ice-cold ACSF containing (in mM): 119 NaCl, 2.5 KCl, 1.3 $MgSO_4$, 2.5 $CaCl_2$, 1 NaH_2PO_4, 26.2 $NaHCO_3$, 11 glucose. Before the experiment, brain slices were allowed to recover for at least 45 minutes in room temperature ACSF under continuous oxygenation (95% O_2 5% CO_2). Experiments were performed a maximum of 6 hours after slicing.

8.3.3 Electrophysiology

Juxtacellular and whole cell current clamp recordings were performed using an Axon Instruments MultiClamp 700B microelectrode amplifier (San Jose, USA) and a borosilicate glass electrode (6-10 MΩ). Visually-guided electrode positioning and cell patching were performed under an Olympus BX43 Light Microscope (Tokyo, Japan). Neocortical ChR2-yellow fluorescent protein (YFP) expressing somatostatin interneurons were targeted using a fluorescein isothicyanate dye filter set (Olympus-Lifescience, Center Valley, PA). Targeted recordings were carried out using fluorescence signal from a YFP-tagged channelrhodopsin genetically expressed in the target cells. Cell targeting and electrophysiology recording were performed from the top surface of the brain slice. The brain slice recording chamber was perfused with modified ACSF composed of 119 mM NaCl, 5 mM KCl, 0.5 mM $MgSO_4$, 1 mM $CaCl_2$, 1 mM NaH_2PO_4, 26.2 mM $NaHCO_3$, 11 mM glucose. Optogenetic stimulation was performed using a 5 pulse train of blue light stimulation (10 ms duration, 80 ms interstimulus interval) from either the Gan-on-Parylene µLED arrays or through the microscope objective.

8.3.4 Neural Data Analysis

Neural data were acquired using custom-written IgorPRO software. Notch filters were applied at 60 Hz harmonics to remove electronic power line interference. Additionally, the data were spectrally limited to the spikes band via a 400 Hz to 5 kHz bandpass filter. Postprocessing was performed using Python 3.7.2 and Scipy 1.2.1.

8.3.5 Neuronal Spikes and Synaptic Network Activation Elicited by μLED Illumination

As a proof-of-concept demonstration of μLEDs for optogenetic stimulation of channelrhodopsin-expressing neurons, acute ex vivo experiments were carried out in brain slices in the custom experimental setup detailed in prior sections. GaN-on-Parylene μLED arrays were used to deliver light from the bottom of the brain slice for optogenetic stimulation, while simultaneous electrophysiology readout was performed via patch clamp from the top of the brain slice. Somatostatin-expressing (SST) inhibitory neurons were genetically targeted for this experiment since they typically rest at depolarized potentials [168], which would reduce the stimulation threshold to drive spiking. ChR2-expressing cells located near the μLED array were targeted for recording (Fig. 8.7).

Delivery of the optical stimulus pulse train (5 pulses, 10 ms pulse duration, 80 ms inter-pulse interval) from the μLEDs was correlated with an increase in the firing activity of the recorded neurons (Fig. 8.8, top trace), demonstrating optically-evoked activity. Control experiments were performed using full-field illumination (wavelength of 470 nm) using the same stimulus paradigm through the 40x objective of the rig microscope (Fig. 8.8, bottom trace). Notably, the full-field optical stimulation delivered through the rig microscope showed increased spiking activity in the target cell. This effect is likely due to more widespread opsin recruitment in neurites of the target cell resulting from wide-area illumination of the rig microscope compared to the targeted

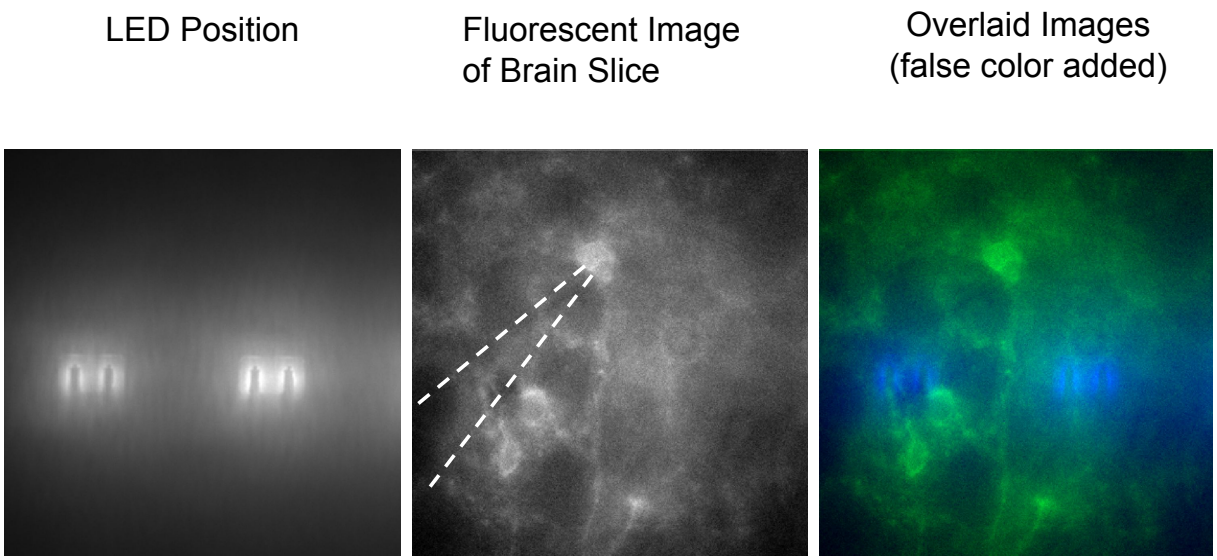

Figure 8.7: left: Activation of μLED array embedded beneath recording chamber prior to slice positioning. center: Targeted recordings from fluorescent ChR2-expressing somatostatin (SST) interneurons above array. right: overlay. (Scale = 22 μm).

stimulation volume of the μLEDs. Notably, in the case of the μLEDs, there is a large onset and offset stimulation artifact present for each optical pulse. The artifacts are caused by the proximity between the recording electrode and the μLED source, which allows electromagnetic fields from the large currents switched to activate the μLEDs to be coupled to the recording electrode. The waveforms of onset and offset artifacts were visually distinct from neuronal spikes, and were manually excluded from the analysis. This experiment demonstrates that the μLEDs are sufficiently powerful to directly stimulate ChR2-expressing neurons.

To demonstrate network-level effects of optogenetic stimulation, whole-cell current clamp recordings were carried out in neocortical pyramidal neurons. μLED stimulation resulted in SST-mediated inhibition of spontaneous pyramidal neurons firing (Fig. 8.9, top trace). This inhibitory effect is due to the selective expression of ChR2 opsins in inhibitory cells in the SST x Ai32 mice. Control experiments were again performed using wide-field illumination from the rig microscope (Fig. 8.9, bottom trace), which also resulted in a pause in spiking. As opposed to the

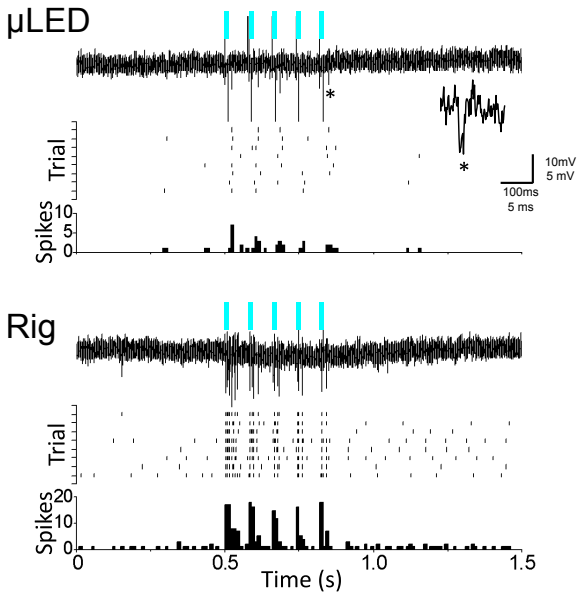

Figure 8.8: Top: Juxtacellular recording showing LED activation (blue bars) of channelrhodopsin-expressing somatostatin (SST) interneuron, multi-trial spike raster plots from the same neuron aligned to μLED activation, and peri-stimulus spike time histograms (PSTH) from the above. *Shown as inset, single μLED evoked spike. Bottom: As in top panel, but with full-field LED activation of SST interneuron

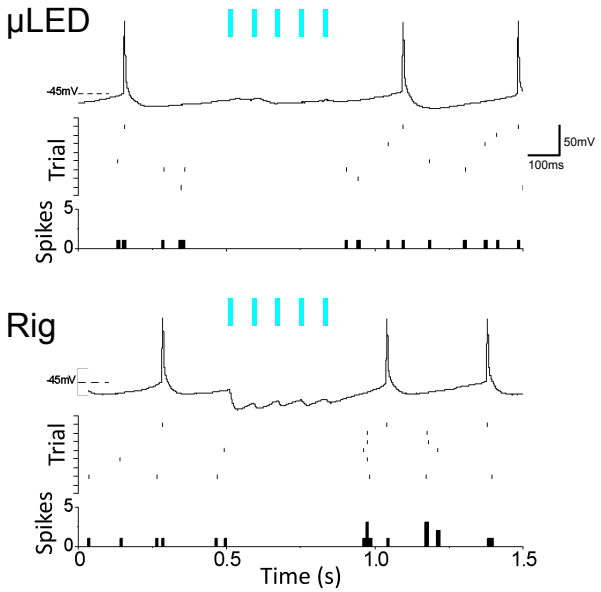

Figure 8.9: Top: As in Fig. 8.8, but for whole-cell current clamp recording of neocortical pyramidal neuron showing feedforward inhibition during µLED activation of somatostatin (SST) interneurons, with suppression of spontaneous pyramidal neuron firing activity. Bottom: As in top panel, but using full-field LED activation. Inhibitory postsynaptic potentials (IPSPs) are larger than with µLED activation and visible as inward currents.

effect of light delivery using µLEDs, full-field illumination showed distinct inhibitory post-synaptic potentials following stimulation. This effect is likely due to broader recruitment of SST inhibitory interneurons, which provide inhibitory input to the recorded cell. This result demonstrates that not only are the individual SST neurons activated via optogenetic stimulation with µLEDs, but that the wider inhibitory network effects of these cells can be optically activated.

For high-throughput experiments, neural spikes can be robustly distinguished from the onset and offset artifacts using automated spike sorting techniques. Signals were filtered from 300-5000 Hz and clustered using a Gaussian Mixture Model with N=3 clusters specified. The detected unit waveforms are shown in (Fig. 8.10a). In principal component space, the clusters were clearly distinct (Fig. 8.10b), allowing highly accurate automated classification.

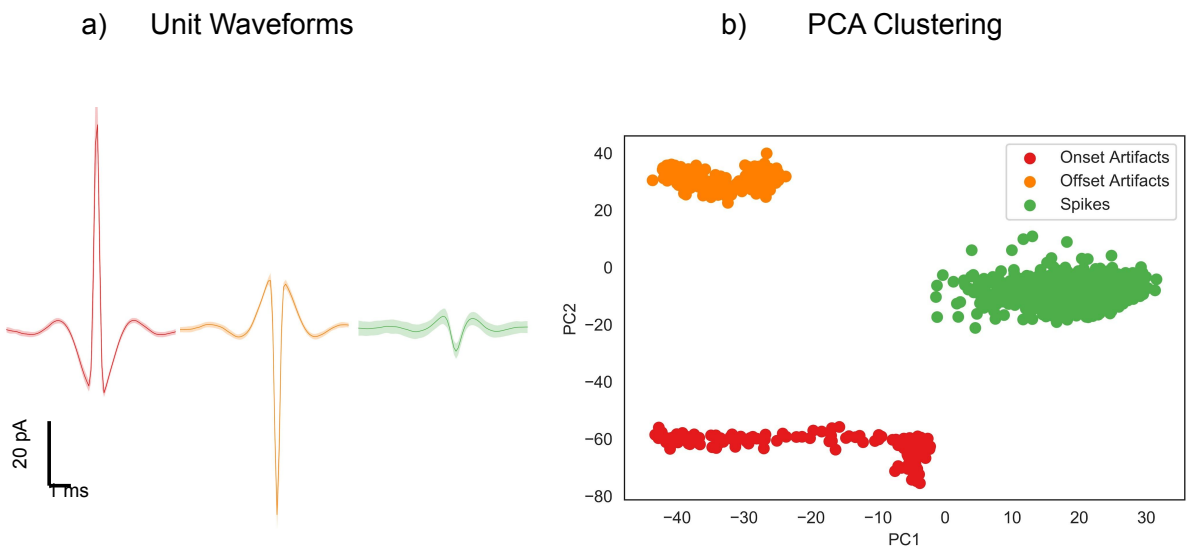

Figure 8.10: Spike sorted extracellular recording during optogenetic stimulation using μLED neural probes showing a) Spike-sorted unit waveforms and b) Principal component analysis (PCA) clustering of spikes (green) and artifacts (red, orange).

8.4 Thermal and Optical Modeling and Simulation

A design consideration for the use of implantable μLEDs probes is tissue heating during operation. The conversion efficiency from electrical to optical power of the devices demonstrated here is low (6.5% peak efficiency), typical of GaN grown on a Si substrate. Therefore, the majority of the device power ($> 90\%$) is dissipated as heat into the tissue surrounding the tissue. To avoid tissue damage due to heating, it is important to identify safe operating powers and stimulation paradigms for practical use [48, 169]. Here, I present a thermal model of the tissue heating to predict safe operating powers for the μLED probes, as well as an optical model to predict the illumination volume in the tissue resulting from a given power.

8.4.1 Thermal Model

In this section, I discuss the application of the Pennes bio-heat transfer model to model μLED neural probe heating in the tissue, and perform finite element method simulations in COMSOL Multiphysics (COMSOL Inc.). The Pennes bio-heat model describes heat transfer in a biological tissue. This is a modification of the standard heat equation, whereby in a homogeneous medium, the temperature flows over time according to the second derivative of the temperature across the medium, scaled by k, the thermal conductivity, ρ, the density, and C_p, the specific heat capacity of the medium.

$$\rho C_p \frac{\partial T}{\partial t} = k \nabla^2 T \tag{8.1}$$

The Pennes bioheat model adds two additional terms to model the processes of the tissue:

$$\rho C_p \frac{\partial T}{\partial t} = k \nabla^2 T + \rho_b C_b w_b (T - T_b) + Q_m \tag{8.2}$$

First, it is assumed that heat is generated in the tissue due to metabolism, modeled by Q_m. Rather than heat transfer in the tissue purely by conduction, it is assumed that heat spread is additionally aided by blood perfusion of the tissue, modeled by the second term,

$$\rho_b C_b w_b (T - T_b), \tag{8.3}$$

where ρ_b is the blood density, C_b is the specific heat capacity of the blood, w_b is the blood perfusion rate, and T_b is the blood temperature. Thus, the blood is assumed to act as an additional heat source or sink to equilibrate the tissue temperature. Notably, this model incorporates several

Material	k (W/(m*K))	ρ (kg/m^3)	C_p (J/(kg*K))
Brain Tissue [169]	0.6	1057	3600
GaN [169]	200	6150	485
Parylene	0.084	1110	712
Gold	317	19300	129

Table 8.1: Material Properties for Thermal Simulations

simplifying assumptions, including the homogenous distribution of metabolic processes and uniform, isotropic blood perfusion in the tissue, that the blood perfusion is anisotropic, and that the blood temperature remains constant.

To model the device in the tissue, the probe geometry was modeled using dimensions from the photomask design files and layer thicknesses measured during the fabrication process. The GaN μLED mesas, metal traces, and Parylene insulation were included in the model. The relevant material properties are listed in Table 8.1. Blood perfusion rate, density, and heat capacity are taken from [48].

Thermal simulations show the effects of local heating in the μLED structure on the surrounding tissue. The front- and backsides of the probe experience different local heating due to the difference in thermal conductivity of the Parylene insulation on the top surface and the GaN mesa on the bottom. Figure 8.11 shows the heating profile at the μLED/tissue interface. The tissue in contact with the GaN mesa experiences significantly more heating than the upper Parylene interface. Due to the higher thermal conductivity of the GaN mesa and traces compared to Parylene and surrounding tissue, heat spreads preferentially throughout the GaN mesa structure and through traces to the adjacent mesas.

To simulate worst-case heating performance, I performed analysis on the μLED mesa at the tip of the neural probe, which has only one adjacent mesa. The temperature of Parylene/Tissue and GaN/Tissue interfaces on front- and backside of the probe, directly over the center of the active μLED, were monitored in a time-dependent study (Figure 8.12). To remain below the

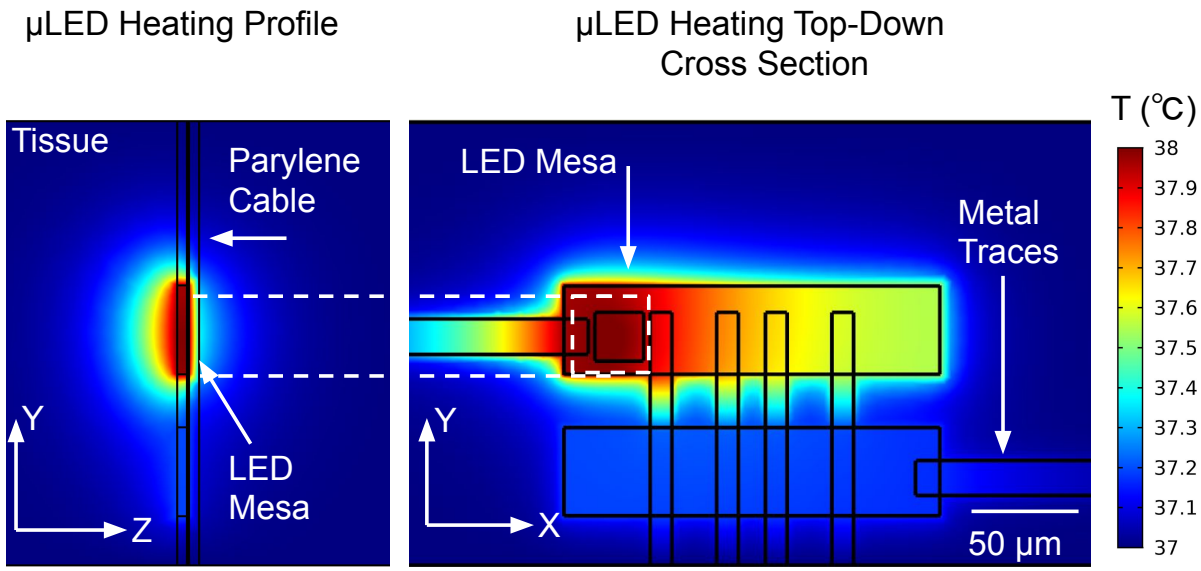

Figure 8.11: (left) Profile of simulated tissue heating using Pennes bio-heat model at 90 µA of µLED drive current. Due to the difference in thermal conductivity between GaN and Parylene C, front- and backside of the probe experience different amounts of tissue heating. (right) Top-down cross-section of heat spread in µLED device structure at 90 µA of µLED drive current. Thermal conduction in GaN mesa and along metal traces can be observed.

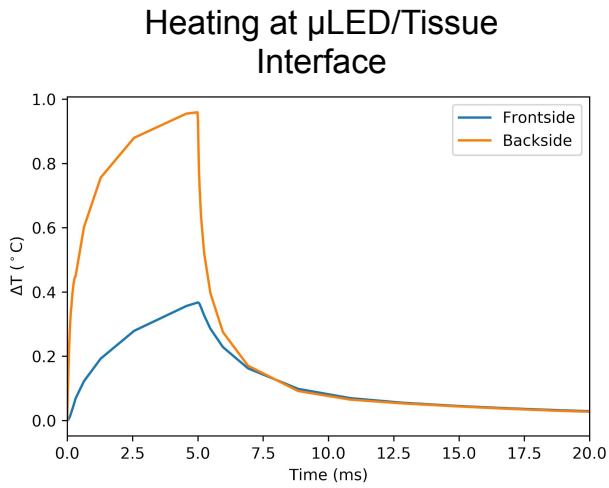

Figure 8.12: Tissue heating plot at front- and backside probe/tissue interfaces for 5-ms, 90-μA pulse.

standard safety limit of 1 °C temperature increase in tissue, a 5 ms pulse of 90 μA was found to be the limit. This drive current corresponds to a frontside optical power of 4.82 μW and a backside power of 14.3 μW. The heat is quickly dissipated in the tissue, and after 10 ms following stimulation offset, the temperature in the surrounding area is less than 0.05 °C above ambient temperature (37 °C).

8.4.2 Optical Model

To enable high-resolution interrogation of individual neural circuits, dense two-dimensional arrays of GaN μLEDs may be individually modulated to create independent stimulation voxels in tissue. Analytical and Monte Carlo methods have been developed to describe light scattering in tissue [170, 171], with the latter being necessary to accurately model light penetration beyond 200 μm, as light enters the multiple scattering regime [102].

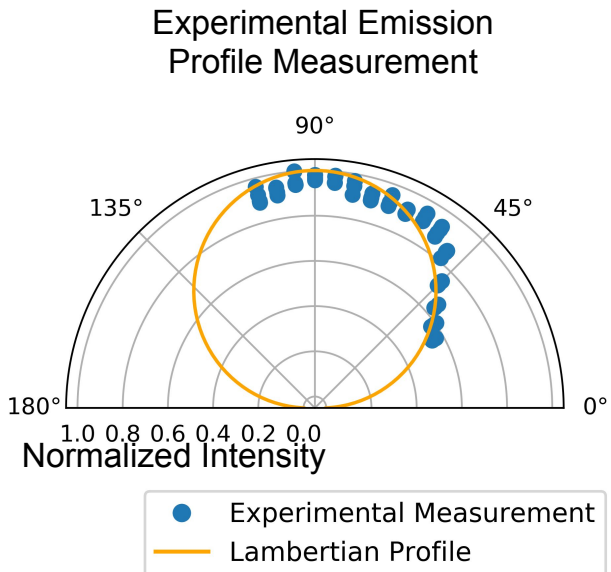

Figure 8.13: Experimental measurement of directional µLED intensity profile and comparison to ideal Lambertian source.

I experimentally measured the relative light intensity from multiple angles using a low-NA microscope (NA = 0.10) equipped with a CCD camera on a rotating stage to obtain the µLED emission profile (Fig. 8.13). The measured emission profile closely resembled an analytical Lambertian profile. Therefore, modeling of light spread in the tissue discussed in subsequent sections assumes a Lambertian emission from the µLED.

To describe the high-spatial resolution achievable near the device, I developed an analytical model of the µLEDs illumination volume in absorbing and scattering media to understand the illumination volume in tissue. This model adapts an analytical description of optical fiber illumination to the Lambertian profile of an LED [100]. The irradiance at a point $(I(r,z))$ in a cylindrical coordinate system centered on the µLED source can be described by a transmission term $(T(r,z))$ and the initial intensity (I_0):

$$I(r,z) = T(r,z)I_0. \tag{8.4}$$

The transmission term is described as the product of independent attenuation effects in tissue:

$$T(r,z) = L(r,z)G(r,z)M(r,z), \tag{8.5}$$

where L describes the Lambertian distribution of the μLED, G describes the spherical geometric expansion of the light sphere from the emission point, and M models the scattering and absorption of light according to the Kubelka-Monk theory of light propagation in diffuse scattering media.

The Lambertian distribution models the intensity profile of a source in terms of the angle, θ from the central axis:

$$L(\theta) = \frac{\cos(\theta)}{2\pi}. \tag{8.6}$$

In the cylindrical coordinate system, this becomes

$$L(r,z) = \frac{1}{2\pi\sqrt{(\frac{r}{z})^2 + 1}}. \tag{8.7}$$

This intensity distribution is mapped across a spherical surface which expands as light propagates through tissue, giving an additional geometric attenuation G of

$$G(r,z) = \frac{1}{\pi d^2}, \tag{8.8}$$

$$d = \frac{r^2 + z^2}{z}. \tag{8.9}$$

Finally, the attenuation of light due to scattering and absorbing media can be described by M as:

$$M(r,z) = \frac{b}{a\sinh(bS\sqrt{r^2+z^2}) + b\cosh(bS\sqrt{r^2+z^2})}, \tag{8.10}$$

$$a = 1 + K/S, \tag{8.11}$$

$$b = \sqrt{a^2 - 1}, \tag{8.12}$$

according to the Kubelka-Monk model. Here, S is the scattering coefficient and K is the absorption coefficient of tissue. I adopt values from previously reported measurements at 450 nm, which is the closest wavelength to the measured emission wavelength (445 nm). The model parameters are $\mu_s = 19.96\text{mm}^{-1}$ [102], and $\mu_a = 0.14\text{mm}^{-1}$ [103].

This model allows for the rapid estimation of penetration depth and light spread for a given optical power. A plot of optical power density spread for 4.8 µW of emitted optical power, which corresponds to the frontside emission at the maximum thermally-safe (less than 1 °C) tissue heating threshold, is shown in Figure 8.14. A penetration depth of approximately 40 µm for 0.1 mW/mm^2 optical power density is observed, with a lateral spread of less than 20 µm. Thus, the stimulation volumes of adjacent high-density µLEDs are independent at this distance.

During chronic implantation, glial encapsulation and reduced local neuron density can hinder the effectiveness of a neural probe, requiring greater depth of penetration to reach healthy cells. Greater depth of penetration can be achieved by increasing the µLED power up to 200 µW. Figure 8.15 shows the spatial intensity decay of light from the µLED at several ranges of operating power predicted by my model. To stimulate further from the device, multiple µLEDs may be operated as one larger LED to achieve greater overall optical power and penetration depth (Fig. 8.16). With

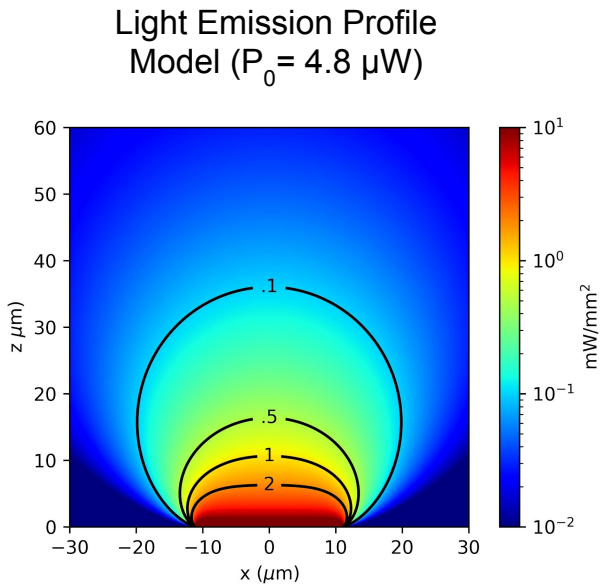

Figure 8.14: Analytical model of light intensity in tissue from a Lambertian source with 4.8 μW of optical power.

the presented thermal and optical model, 5-ms pulses lead to the emission of 4.82 μW of optical power from the probe frontside and 14.3 μW from the probe backside, while inducing less than 1 °C temperature increase in surrounding tissue.

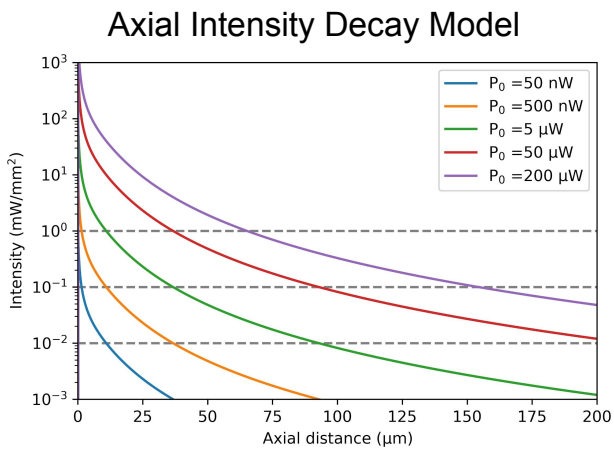

Figure 8.15: Analytical model of axial intensity profile in tissue for various optical powers.

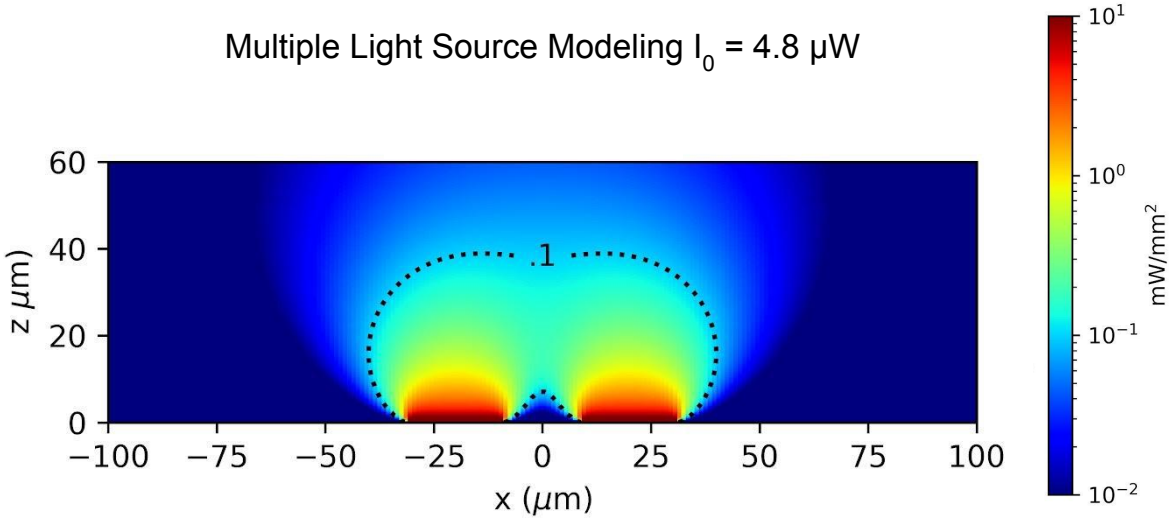

Figure 8.16: Illumination profile resulting from simultaneously powering two adjacent μLED sources.

8.5 Microfabrication and Metrology - Electrodes and Release

To enable closed-loop experiments, where neural activity may be monitored and stimulated at the same time, the optoelectronic neural probe platform features collocated recording electrodes and light sources. Recording electrodes and associated interconnects are realized on the same layer as the metal traces for powering the μLEDs. The traces and interconnects are insulated with a second layer of Parylene C. The recording electrodes are then exposed by etching the Parylene C layer covering the electrode sites. The monolithic fabrication process and lithographic patterning of features in each layer of the neural probe enable us to create customizable recording electrode arrangements. In this design, recording electrodes may be fabricated either on the front- or backside of the probe, allowing for directional recording from both sides (Fig. 7.2). This capability, along with the bidirectional light emission from individual μLEDs, is a unique feature of this design that maximizes the yield of neural recording from volumes of neural tissue on both sides of the probe. An example of a released optoelectronic neural probe is shown in Figure 8.17 with the active region near the tip of the flexible probe cable.

8.5.1 Frontside and Backside Recording Electrodes

Before the metallization step (Fig. 7.3f), backside recording electrodes are defined by patterning and etching the lower Parylene C insulation layer to create a via all the way to the surface of the Si substrate. The backside electrodes are exposed after the device is released from the silicon substrate.

To expose the frontside recording electrodes and bond-pads, the top layer of the Parylene C must be etched. To singulate the neural probe, the top and bottom layers of the Parylene C (which have a total thickness of 10 μm) need to be patterned and etched around the outline of

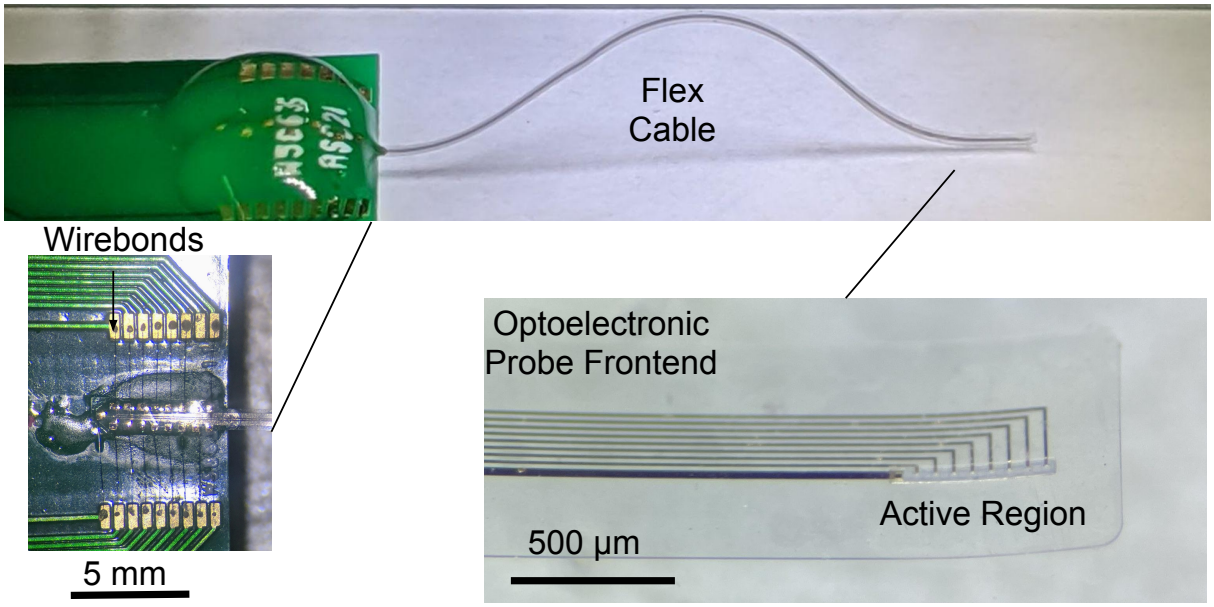

Figure 8.17: Microscope images of microfabricated GaN-on-Parylene neural probes

the device. To pattern such a thick layer of Parylene C, I used a 100-nm chromium (Cr) hardmask. The thin-film stress in the Cr hardmask layer can sometimes result in the formation of cracks in the Parylene C film. To alleviate this issue, a customized sputtering process (CVC Connexion) was carefully optimized for the deposition of the Cr hardmask layer in order to minimize the thin-film stress by adjusting the chamber pressure during the deposition. I found that cracking of the Parylene C was eliminated when the Cr thin-film stress was less than 1 GPa. The optimized deposition process yielded a final stress of 600 MPa, providing a safe margin for achieving crack-free Parylene C films. I patterned the Cr hardmask using wet etching (Cr 1020 Etchant, Microchem GmbH). Parylene C was then etched using oxygen plasma (Trion Phantom II). At an etch depth of 5 µm, the bond-pads and frontside electrodes are exposed. The etch is continued to a depth of 10 µm in order to define the probe outline through the top and bottom layers of Parylene C. Over-etching of the electrode and bond-pad sites removes Parylene residue from the surface. The

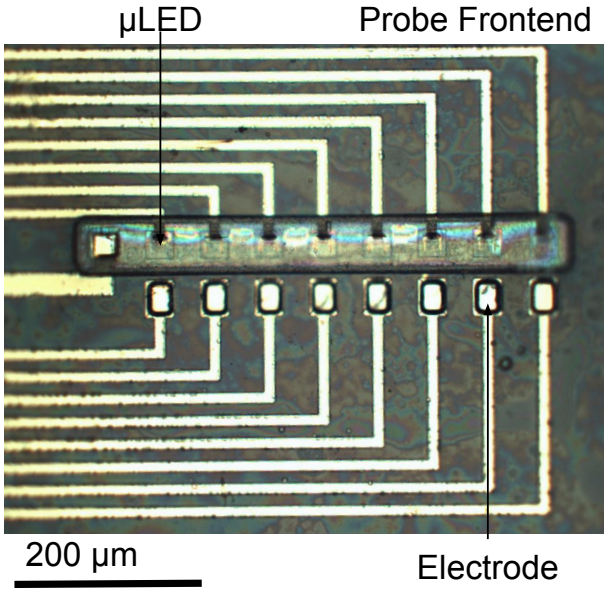

Figure 8.18: Microscope image of monolithically integrated neural interface active region with collocated μLED optical stimulators and recording electrode arrays.

Cr hardmask is stripped away using a wet etch step in Cr etchant (Cr 1020 Etchant, Microchem GmbH). Following this step, the optoelectronic probes are finally realized on the wafer (Fig. 7.3jAi).

As an example, a linear array of μLEDs with a pitch of 60 μm and 30 μm × 30 μm active area is shown in Figure 8.18. Two-dimensional arrays with any desired arrangement of light sources and recording electrodes can also be designed in this platform.

8.5.2 Release Process

To release the flexible devices from the Si substrate, the wafer is first ground down from the backside to a thickness of about 100 μm from its initial thickness of 1.5 mm (Grinding Dicing Services, Inc. San Jose, CA). The remaining silicon is then isotropically etched using XeF_2. The wafer is first mounted on a quartz carrier substrate upside-down using a CrystalBond adhesive and then etched using XeF_2 (Xactix e2) from the backside. The Parylene C cable is protected by the 300-nm SiO_2 passivation layer. Once the Si layer is completely removed, the bottom-facing

electrodes are exposed. Finally, the probes may be released from the carrier wafer by dissolving the CrystalBond adhesive by soaking the samples for 4 hours in Acetone (Fig. 7.3j). The SiO_2 sacrificial layer along the probe cable is removed by dipping the backend into a buffered 49% HF acid solution, leaving only the flexible Parylene C cable.

8.5.3 Packaging

The released optoelectrodes are packaged with a printed circuit board (PCB) adaptor that connects with a recording head-stage to a commercial neural recording amplifier (Intan Inc.) through Omnetics connectors. The PCB adaptor also connects with custom-designed electronic control circuitry for driving individual μLEDs. This electronic control circuitry utilizes a switching network of commercial metal-oxide-semiconductor field-effect transistors to route current to the appropriate traces. A commercial Kiethley 2401 Sourcemeter, (Kiethley Instruments) with a precise (±100 nA) current control capability, was used as a current source to prevent accidental breakdown of the μLEDs.

To package the released optoelectronic probes with the PCB adaptor, I developed a die attach technique using Epotek 301 epoxy to affix the flexible probes to the adapter PCB. Electrical connections to the bond-pads on the backend of the flexible polymer substrate to the PCB were then made using an aluminum wedge-bonder.

Once released, the μLED probe is supported by a flexible Parylene C substrate, which can significantly help with reducing the foreign body response in tissue. However, flexible neural interfaces incur difficulty during implantation since they lack the rigidity to penetrate brain tissue. The flexible neural interfaces need to be temporarily stiffened so that they can be feasibly implanted. This can be carried out by coating the probes with bioresorbable materials such as polyethylene glycol or silk or by attaching them to a stiff shuttle for implantation [68].

8.5.4 Recording Electrode Characterization

The electrodes were characterized using electrochemical impedance spectroscopy (EIS). Measurements were performed in a 3-electrode configuration in potentiostatic mode (PSGSTAT202N, Metrohm Autolab) in a phosphate-buffered saline (PBS) solution. The electrochemical impedance of the electrode was characterized from 0.1 Hz to 10 kHz with a sinusoidal signal whose peak amplitude was 50 mV at an open circuit potential configuration. A silver/silver chloride (Ag/AgCl) reference electrode (MF-2052, BASI Inc.) and a platinum wire counter electrode (MW-1032, BASI Inc.) were used.

Front- and backside electrodes (25 μm × 35 μm) were fabricated alongside the GaN μLEDs in this architecture. The frontside electrode performance is shown in Figure 8.19, while the backside electrode performance is shown in Figure 8.20. Both electrodes exhibit a similar electrochemical impedance of ≈1.0 MΩ at 1 kHz, which is typical for electrodes of this size and suitable for neural recording [172, 173]. The ability to record from both sides of the probe shank, along with the bidirectional emission of the μLED is a unique feature of this design that enables stimulation and recording from a much larger volume compared to the usual single-sided probes.

The transparency of Parylene C combined with the process-enabled light emission from both facets of the GaN μLEDs, makes it possible to use light in the tissue from the frontside as well as the backside of the device. This new feature means that having only frontside recording electrodes may be inadequate for recording signatures originating from the entire stimulated volume. The design of this platform allows the integration of backside recording electrodes for simultaneous recording and stimulation from both sides of the probe. The emission profiles from the top and bottom surfaces in this device are asymmetric due to reflections from the metal contacts of the top surface. Symmetric emission profiles could be achieved using thin or transparent contact materials such as indium tin oxide [174].

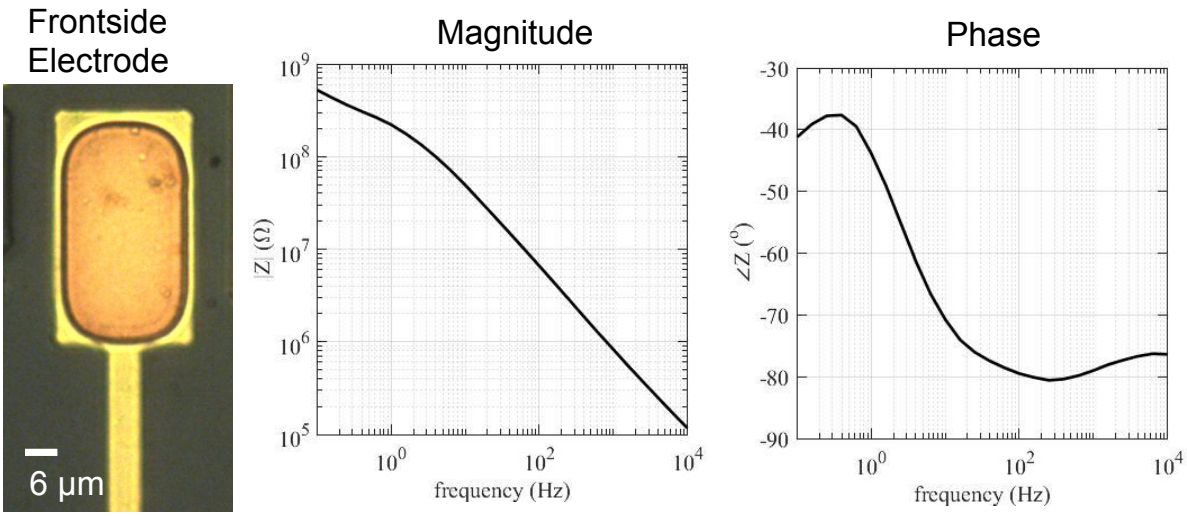

Figure 8.19: Microscope image of the recording electrode surface and electrochemical impedance spectroscopy measurements of the electrochemical impedance.

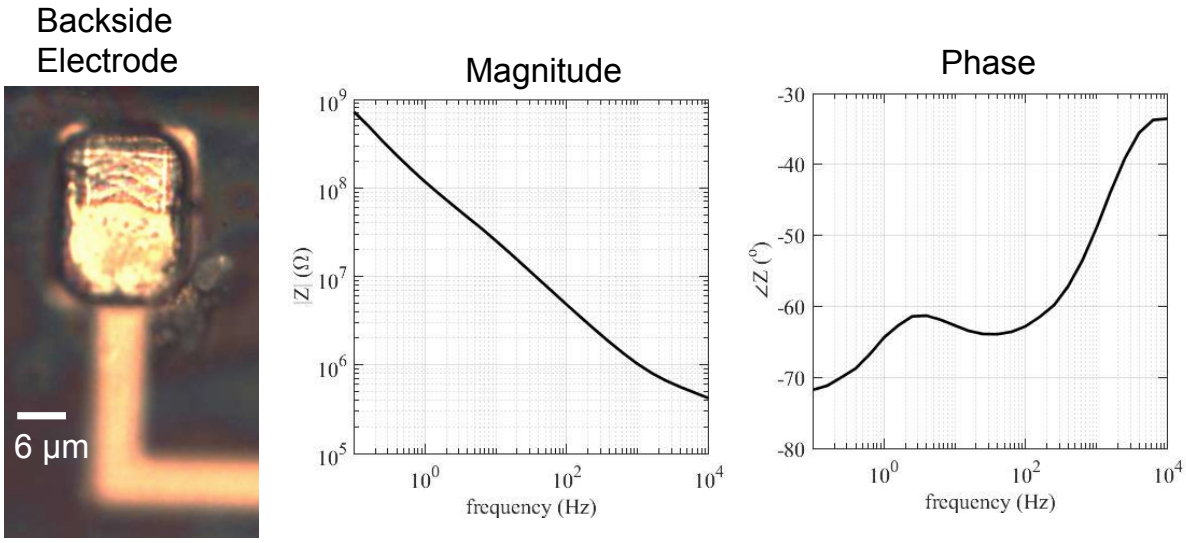

Figure 8.20: Microscope image of the recording electrode surface and electrochemical impedance spectroscopy measurements of the electrochemical impedance.

Electrodes on both sides exhibit electrochemical impedances suitable for neural recording. Electrodes are implemented in separate fabrication steps, etching the top Parylene insulation layer to expose the frontside electrodes, and deposition of the metal films for the electrodes through Parylene vias on the silicon substrate surface, which is eventually etched off during the release process to expose the backside electrodes. These fabrication differences are believed to be responsible for the different phase characteristics of the impedance of the front- and backside electrodes, either because of Parylene C or silicon debris that remains on the surface or a surface modification of the electrode from exposure to the etching gasses.

8.6 Discussion

Here, the shank of the demonstration device is very large (570 μm active region), which would be highly damaging during in vivo implantation despite the flexibility of the substrate. This is primarily limited by the conservative trace pitch (16 μm). As previously discussed, the overall size of the device is determined by the lithography resolution and number of required traces. The 2D routing scheme allows for a significant reduction in the number of traces, and can be combined with high-resolution lithography to create extremely compact, high-density devices.

The following sections discuss some considerations for identifying appropriate uses of the μLED architecture developed in this thesis.

8.6.1 Tissue Heating Due to μLED Versus Electrical Stimulation

As I discussed earlier (Chapter 1), optical stimulation provides cell type selectivity as opposed to blunt electrical stimulation that cannot discriminate between different types of neurons. In terms of safety, these two methods of stimulation have specific limitations to avoid thermally damaging the tissue. In general, the cause of heating from electrical stimulation in the tissue is Joule heating due to the electrical resistance of the brain tissue as electrical current is applied.

Optical stimulation also causes inherent heating in the tissue due to optical absorption. However, in the case of the μLEDs presented here, the heating effect of optical absorption is minimal compared to the heating in the device due to the low conversion efficiency of the μLEDs (<6%).

A recent study has analyzed deep brain stimulation (DBS) heating in the tissue using the Pennes BioHeat model, which I have also used to analyze the effects of μLED heating [175]. Using commercial DBS electrode designs at maximum stimulation intensity (10 V, 210 ms) would result in a peak temperature increase of 0.8 °C in the tissue surrounding the electrode. This peak heating is comparable to the 1.0 °C generated by the μLED stimulation paradigm developed in this thesis, corresponding to the in vivo tissue heating safety limit.

Evidently, the DBS electrode can maintain a much longer stimulus interval for the same amount of heating (210 ms for DBS [175] vs 5 ms for μLEDs [162]). In each case, the stimulus duration is chosen so that the total amount of heating is comparable, corresponding to the safety limit of the tissue. The efficiency of power delivery into the tissue is almost 100% for DBS electrodes since the conductivity of the traces of the electrode is very high compared to the tissue (0.35 S/m - tissue, 9.4 × 106 S/m - platinum) resulting in negligible heating in the device itself - the vast majority of the power is transmitted to the tissue. On the other hand, the relatively low efficiency of the μLEDs (<6%) means that the majority of the power delivered to the device is dissipated as heat rather than light for optogenetic stimulation. Additionally, the DBS electrode is significantly larger (1.27 mm diameter [175]) compared to the μLED (22-micron width [162]), so the little heat generated in the device is spread over a larger area. The size of the device determines the amount of power that can be safely dissipated into the tissue. To first order, the local heating of a system is given by

$$\Delta T = \Delta Q / C, \tag{8.13}$$

where Q is the heat added to the system and C is the heat capacity of the system. The larger the device, the larger the volume of tissue that it interfaces with, increasing the thermal capacity of the system and allowing it to absorb more thermal energy for the same change in temperature. Therefore, the large discrepancy between the maximum stimulus intervals that are possible with each device is primarily due to the low efficiency of the μLEDs, and also the significantly larger size of the DBS electrodes.

8.6.2 Photon Sensitivity of Neurons and the Effect of Source Efficiency

In this chapter, I developed a model to show the attenuation of light emitted from an LED source due to geometric beam spreading, scattering, and absorption in the tissue, which predicts the light intensity (in mW/mm^2) in the illumination volume of the LED. But what light intensity is required to stimulate a neuron? A widely-used conservative estimate is 1 mW/mm^2 [162], but the actual number varies according to the duration of the stimulus, the efficiency of the opsin at the stimulating wavelength, and the expression level of the opsin [176]. Theoretical modeling of ChR2-expressing neurons found a rheobase irradiance level of 0.3 mW/mm^2 at the neuron surface, assuming a ChR2 expression of 130 molecules/μm^2 [100]. Assuming a soma diameter of 20 μm, each cell would require an illumination via 94.2 pW directly at the neuron surface, corresponding to a photon flux of 2.1 × 108 photons/s (wavelength of 450 nm). However, the utilization of this photon flux is low based on the cross-sectional area of an opsin molecule (1.2 x 10-8 μm^2), and expression level (130 molecules/μm^2), only 1.56×10^{-4}% of the neuron surface is photoactive, so the total number of photons actually absorbed to depolarize a cell is quite low (n = 327/s). Currently, however, there is no practical way to direct photons to the exact locations of the opsin molecules where they are needed, so wide-area illumination is required. Furthermore, additional photons are lost due to scattering, absorption, and beam spreading en-route to the target neuron, which is why relatively high optical power is required from the light source (on the order of μW).

I would like to note that this theoretical model predicts quite a large irradiance level to activate neurons (0.3 mW/mm^2), whereas activation with lower irradiances (0.015 mW/mm^2) and low power (60 nW) has been experimentally demonstrated [177, 178]. The most likely explanation for this discrepancy is that there is higher opsin expression ($>$130/µm^2), leading to higher utilization of the available light.

Currently, the amount of optical power that can be emitted from a µLED is limited by the low wall-plug efficiency, which leads to a large amount of the power ($>$93% in this thesis) being dissipated as heat in the tissue. However, optimized manufacturing processes have realized GaN-on-Silicon LEDs with significantly higher efficiency. The methods include the design of stress-compensating buffer layers to reduce the lattice mismatch between GaN and Si to achieve $>$57% wall plug efficiency [179], and the design of via-like electrodes to improve current spreading efficiency in the LED structure and achieve wall-plug efficiency $>$63% [180]. This efficiency is more than 10X the efficiency of the LEDs demonstrated here, so neural probes implemented in this process could be operated at 10X higher power with a similar heat profile. In the future, if a light source with near-100% efficiency can be developed, then the only limitation to the amount of delivered optical power would be heating via optical absorption in the tissue, which is insignificant at the optical powers discussed here [100]. Additionally, heating due to optical absorption is inherently broadly spread throughout the tissue since the attenuation coefficient is on the order of mm: 7.37 mm^{-1} [100], whereas heating due to light source inefficiency is concentrated at the LED mesa, leading to higher local heating.

The required power also depends on the distance between healthy neurons and the optical stimulator after implantation. Acute and chronic damage to tissue by the neural implant reduces neuron density around the implantation site. Although the flexible platform presented here is intended to reduce chronic damage, a "dead zone" around the implant is unavoidable. In this case, higher optical power will be necessary to stimulate neurons, inducing more local heating. However,

heating above 1°C is not a concern in dead tissue. Thus, a higher power stimulation paradigm, where sufficient optical power extends beyond the "dead zone", but heating above 1°C is localized, can be envisioned. Since the extent of tissue damage around the neural probe is difficult to predict, the stimulation paradigm for the probe will need to be calibrated after implantation by slowly increasing optical power until robust evoked activity is observed. I showed that these μLEDs, individually driven at 625 μA can stimulate neurons that express channelrhodopsin through a 350-μm thick mouse brain slice.

8.6.3 Size Limitations for μLEDs

There are two potential limitations to the size of μLEDs that could be realized on a neural probe. The first is the fabrication challenges to realize smaller μLEDs. The second is the utility of dense arrays of LEDs for optogenetic stimulation.

As LEDs get smaller, fabrication imperfections play a larger role in the device's performance. For example, a smaller rectangular LED mesa increases the sidewall perimeter to mesa area ratio of the device, which leads to increased electron-hole recombination at sidewall defects caused by fabrication imperfections, mainly due to the dry etching process [181]. Recently, optimized etching techniques for GaN LEDs have been able to alleviate the size-dependent efficiency decrease down to an LED size of 6 microns [182].

Even if extremely high-density arrays of μLEDs can be fabricated, there is also a practical limitation to the useful density of neurons in the tissue. To be practically useful for high-density stimulation, there must be a meaningful difference for neurons in the vicinity when one of two adjacent LEDs are illuminated (Fig 8.21). For example, LEDs 1 and 2 have significant overlap from the perspective of Neuron 1, whereas Neuron 2 sees a large difference in the stimulation

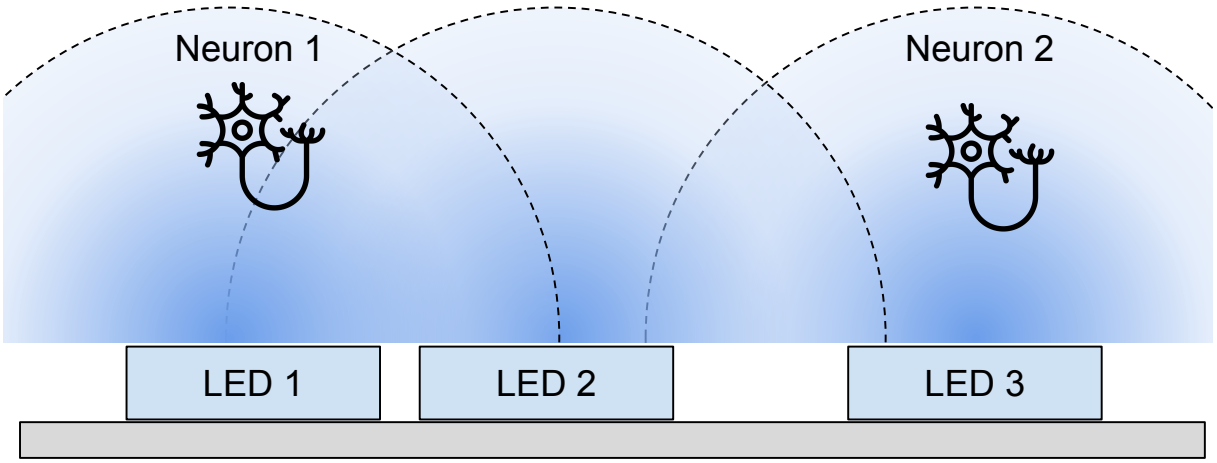

Figure 8.21: Overlapping stimulation profiles of adjacent LEDs. LEDs 1 and 2 have significant overlap from the perspective of Neuron 1, whereas Neuron 2 sees a large difference in the stimulation profiles of LED 3 and LED 2.

profiles of LED 3 and LED 2. Evidently, this is a function of the distance of the neuron from the LED, since neurons which are further away are less able to 'resolve' the difference between two adjacent LEDs.

Two adjacent LEDs when operating at equal power P_0 will illuminate the volume of the tissue around them with power density PD_1 and PD_2, which each decay as a function of the position where the power density is measured and the distance from each LED. We can assume the two LEDs are distinct if a neuron located directly above one of the LEDs observes a significant difference (i.e. $>$ 3 dB) between PD_1, originating from the first LED and PD_2, originating from the second (Fig. 8.22). I employ several simplifying assumptions in this model. I use the Kubelka-Munk scattering approximation. I assume that the width of the LEDs is equal to half of the pitch (p), and that two LEDs are distinct for a neuron if there is a 3 dB difference between PD_1 and PD_2. Using this model, I can find the minimum pitch for which two LEDs are distinct from the viewpoint of a neuron at a certain vertical distance (d_N) above the first LED.

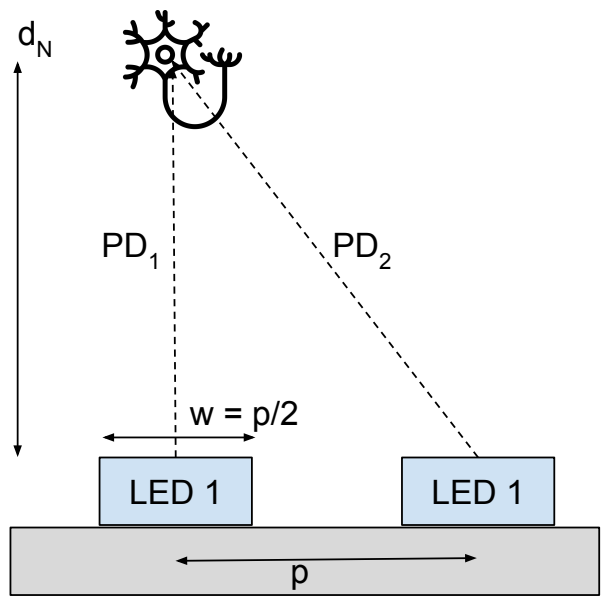

Figure 8.22: The power density (PD) that a neuron observes from two separate LEDs with a pitch, p, is a function of the distance to the neuron, d_N.

Evaluating this problem using the analytical model developed in the thesis yields the relationship between the minimum distinguishable pitch between adjacent LEDs p, and the distance to the neuron, d_N, as illustrated in Figure 8.23.

Therefore, different LED densities may be justified depending on the average inter-neuron distance (d_{N-N}), which depends on the animal model and brain region. From the cell density, we can calculate the average inter-neuron distance. Since the average inter-neuron distance gives the expected distance to the nearest neuron, I take this as d_N in my calculation to determine the minimum useful LED pitch. This way, we are assuming the nearest target neurons are a distance d_N away from the LEDs, where d_N is equal to the inter-neuron distance ($d_N = d_{N-N}$). The neuron densities, average inter-neuron distance, and corresponding minimum LED pitch for different regions of a mouse brain are shown in Table 8.2. This calculation gives an upper limit for the

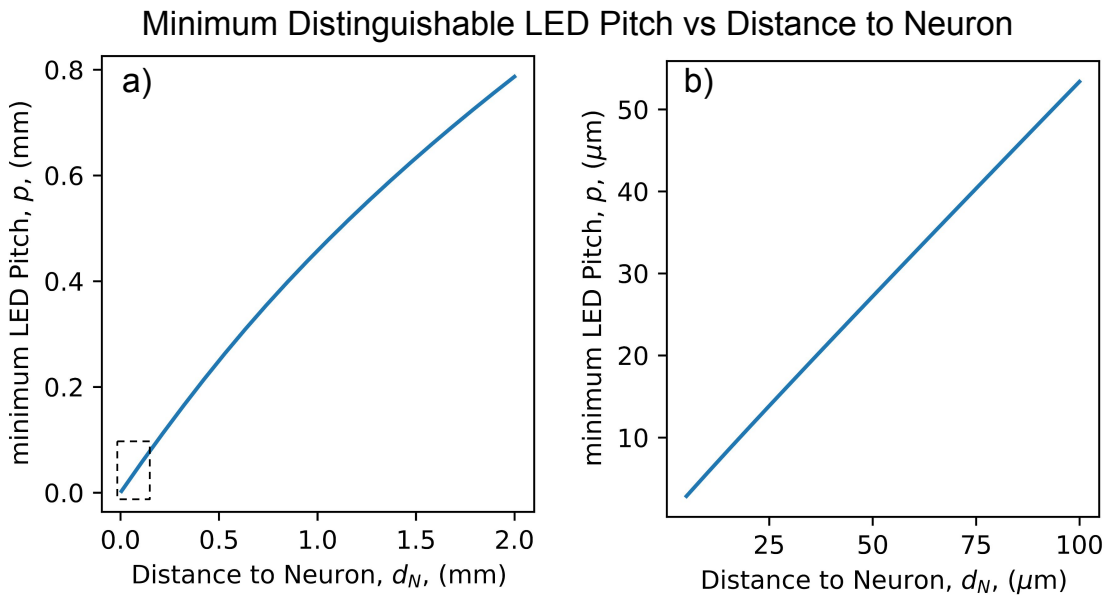

Figure 8.23: The relationship between the minimum 3 dB-distinguishable pitch between adjacent LEDs, p, and the distance to the neuron, d_N for a) 0-2 mm and b) 0-100 µm

Brain Region	Cell density (#/mm^3) [3]	Average Inter-neuron distance (µm), d_N	Corresponding minimum LED pitch (µm), p @($d_N = d_{N-N}$)
Cortex (General)	92,000	22.15	12.3
Visual Cortex	164,000	18.27	10.2
Dorsal CA1	307,000	14.82	8.3
Dentate Gyrus	501,000	12.59	7.1

Table 8.2: Minimum LED Pitch Corresponding to Neuron Density in Mouse Brain Regions

useful density of LEDs on a device. Of course, if the target neurons are further than the average inter-neuron distance away, adjacent LEDs in the high-density array will become redundant, and therefore the minimum LED pitch should be designed to be larger than this limit (Figure 8.23).

These results show that even higher density micro-LED arrays beyond the 40-micron pitch shown in this thesis may be useful in the future for single-cell interrogation in certain high-density brain regions.

8.7 Conclusion

In this chapter, I demonstrated that μLED neural probes fabricated using the GaN-on-Parylene fabrication process from the previous chapter are suitable for optogenetic stimulation of ChR2-expressing neurons. However, due to the low conversion efficiency of the μLEDs (<6%) the stimulation parameters must be carefully chosen so as not to cause thermal damage to the tissue. I developed thermal and optical models of the device operation to inform the thermally-safe application of the μLEDs. In the future, these models can be used to determine the maximum μLED density for specific applications in different brain regions or to inform new stimulation parameters as higher efficiency GaN-on-Si becomes commercially available [179, 180].

Chapter 9

Future Directions and Conclusion

In this thesis, I demonstrated novel penetrating optoelectrical neural probes based on waveguides and μLEDs. In this chapter, I will discuss follow-on applications including surface neural interfaces and imaging, as well as other potential future directions for this work.

9.1 Surface μLEDs Integrated with Artificial Dura

As discussed in the previous chapter, thermal limitations and concerns about tissue heating pose limitations to the use cases of penetrating μLED neural probes. This problem is exacerbated by the use of flexible polymer materials such as Parylene C compared to their rigid Si-based counterparts, which can use the thermally-conductive Si shank itself as a heat sink to reduce the tissue heating. In a flexible polymer-based neural probe architecture, heat is not efficiently conducted by the substrate and mainly deposited into the tissue, requiring that the light source be operated at a limited power or duration in order to avoid thermal damaging of the biological tissue. In the future, improving the efficiency of μLED substrates may help alleviate this constraint by reducing the amount of heat produced in the tissue.

Another potential solution to the problem of heat generation in the tissue for μLED platform is the inclusion of heat-sinking layers. In general, this is difficult to achieve in a penetrating neural probe without increasing the stiffness of the device, due to the low typical thermal conductivity of polymer materials compared to electric conductors such as metals or semiconductors. The application of μLEDs is not limited to designing penetrating neural probes. These light sources can also be used to implement surface neural interfaces.

The application of the GaN-on-Parylene platform to surface optical stimulation paradigms would provide an alternative route for chronic optical interfacing with the brain. An external device is inherently less damaging to the tissue since it does not displace or cut the tissue due to implantation. Electrocorticography (ECoG) devices have long been used to record electrophysiology via an array of recording electrodes on the surface of the brain. These devices are commonly implemented in flexible substrates so that the arrays can conform to the surface of the brain. Recently, there has been interest in performing simultaneous optogentic stimulation in combination with ECoG recording [183]. To date, these techniques usually consist of optical stimulation using an external microscope system through a transparent ECoG substrate.

Optically-transparent artificial duras have been shown to provide chronic optical ports to the brain for external microscope systems over the course of several months [184]. During the craniotomy surgical procedure to give access to the surface of the cortex, the native dura is replaced with the transparent artificial dura. The artificial dura is a passive PDMS molded device which replaces the native dura to help prevent infection and maintain intracranial pressure. These devices are chronically stable for 3 to 9 months after implantation, until a growth of neomembrane (connective tissue rich with capillary network on the cortical surface) is observed, which subsequently limits optical access to the brain [185, 186, 187, 188]. This neomembrane then needs to be surgically removed to regain optical access. The flexible GaN-on-Parylene architecture could be used to augment these passive artificial duras with high-resolution arrays of surface

μLED stimulators. Such a design would leverage the known stability of the artificial dura platform for chronic optical access, while significantly miniaturizing the bulky external optical microscope setups that are currently used in such experiments [184]. This would ultimately allow for more naturalistic experimental paradigms on free-roaming subjects.

To enable simultaneous electrophysiology readout from the surface of the cortex, it is desirable to place an ECoG array underneath the artificial dura, on the surface of the cortex. However, when the artificial dura is heterogeneously combined with ECoG recording in acute or chronic configurations, tissue growth is significantly accelerated (to 8 days) [184]. The root causes of the accelerated tissue growth are: i) For acute configuration, each time the ECoG array needs to be placed on the surface of the brain, the artificial dura needs to be removed, accelerating the tissue growth via manipulation and exposure to air. ii) For chronic configuration, where an ECoG array was placed on top of the brain and covered by the artificial dura, accelerated neomembrane growth occurs between the smart dura and the ECoG array. The neomembrane growth encapsulated the array and obstructed light penetration to the brain [189]. In addition, the ECoG interconnects were routed through the side of the artificial dura, opening a path for infection. The modular architecture of EcoG integrated with artificial dura is problematic and accelerates the growth of the neomembrane.

To address these issues, monolithic integration of recording electrodes and μLED optical stimulators to form a multimodal structure could combine the benefits of high-density flexible ECoG arrays and chronically stable artificial dura in a unified monolithically fabricated functional device. The density of device integration that I have demonstrated in this thesis (optrode/electrode pitch = 40 μm), would represent orders of magnitude improvement for recording and optical stimulation of cortical tissue in comparison to the current state of the art ECoG technology [183, 186, 190, 191]. The artificial dura would not simply be a passive artificial port; instead, it would contain integrated functional recording elements for seamless chronic electrophysiology recording as part of its

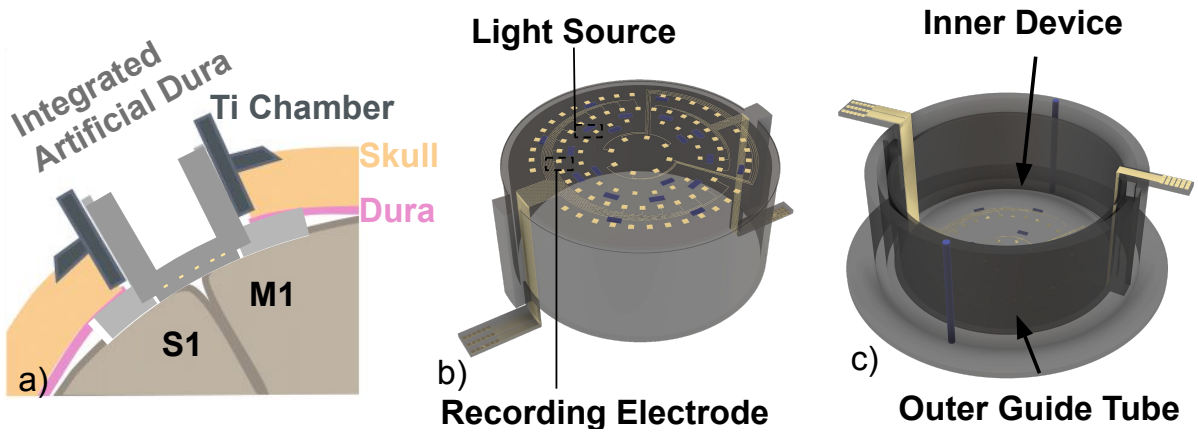

Figure 9.1: a) Schematic of conceptual integrated functional artificial dura for surface interfacing with the brain. b) Integrated smart dura with recording electrodes and GaN µLEDs. c) Integrated smart dura with optoelectronic inset in external guide tube.

structure. Moreover, integrated µLEDs in the structure of the device would enable high-density simultaneous optogenetic stimulation as well as electrophysiology recording in cortical tissue in a standalone device that would not need external optics (microscopes or optical fibers) for optogenetic stimulation. Such a high-density optoelectrical neural interface, shown conceptually in (Fig. 9.1) would be an important addition to the neuroscience tool set for closed-loop neuromodulation.

9.2 Parylene Photonic Endoscopic Imager

An intriguing application of passive neurophotonics, including Parylene photonics, is to utilize the bidirectional capabilities of the waveguides to collect light in addition to delivering it for optogenetics. To demonstrate the feasibility of Parylene photonics for fluorescent imaging, I designed, fabricated, and characterized a prototype Parylene photonic microimager featuring a 2D array of 25 pixels. The imager is implemented using an array of flexible Parylene photonic waveguides. With the integration of 90-degree input/output micromirrors, the waveguide array imager is capable of light collection and readout from the surface, unlike traditional end-firing fiber bundle endoscope and GRIN lenses [193, 194].

[0]Portions of this section are adapted, with permission, from the author's prior work in [192]

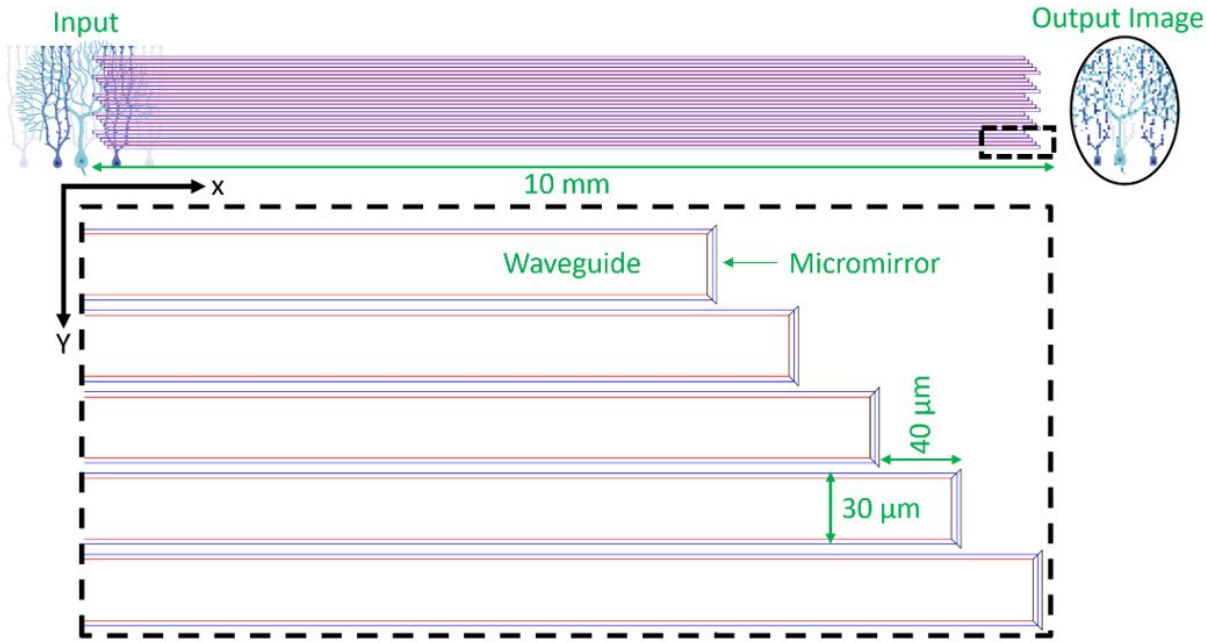

Figure 9.2: Schematic diagram of the waveguide array microimager.

9.2.1 Design of Parylene Photonic Imagers

The design of the waveguide array microimager is shown in Fig. 9.2. The imager input pixels form a 200 µm × 1000 µm input region that is relayed to a symmetric output region by a long (1 cm) waveguide array. A 2D arrangement of 25 waveguide channels form individual pixels of the waveguide array microimager in the input and output regions. The input port to each waveguide is a 5 µm × 30 µm micromirror. These input ports are staggered to accommodate routing of individual waveguide channels.

9.2.2 Methods

9.2.2.1 Characterization Setup

To analyze the response of the Parylene photonic waveguide array imager, an optical fiber (P1-460Y-FC, ThorLabs) connected to a fiber-coupled laser source (LP633-SF50, ThorLabs) at λ = 633 nm was moved over the imager input port array while the output port array was imaged

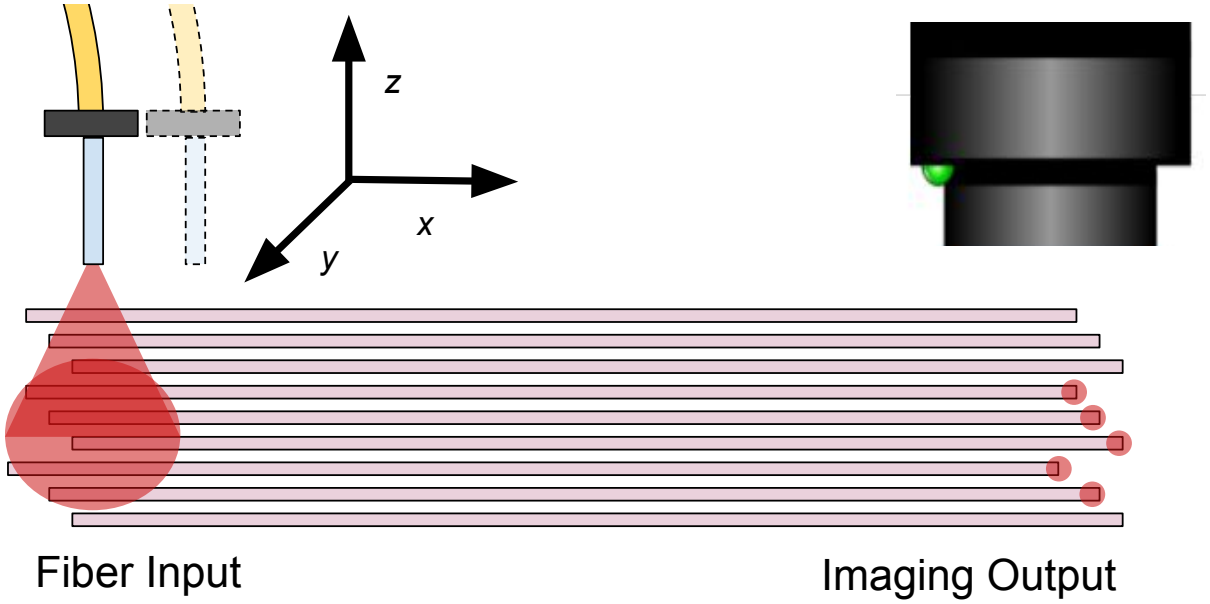

Figure 9.3: Imager characterization: A fiber is moved over the input port array while the output is detected through a CCD camera.

onto a CCD camera (EO-5012M, Edmund Optics) through a zoom lens (600i, Edmund Optics). The fiber position was controlled by a precision XYZ motorized micromanipulator (Patchstar, Scientifica). The exposure time of each image was automatically adjusted to keep the CCD camera sensor under saturation and maximize the dynamic range. A schematic diagram of the characterization setup is shown in Figure 9.3. An example of the raw image captured from the output of the waveguide array resulting from an optical fiber placed at 2 cm from the input array is shown in figure 9.4a. The methods to process the images captured using this technique are discussed in subsequent sections.

9.2.2.2 Data Analysis

Images captured by the CCD camera were analyzed using Python 3.8 and OpenCV 4.5.1. An example image of the waveguide imager array output when all output ports are illuminated from a fiber located 2 cm from the input array is shown in figure 9.4a. Individual output ports were detected by thresholding and circular regions of interest (ROIs) were defined around each

identified output port. The CCD camera position was fixed during the entire experiment so that the position of each output port within the image did not change from image to image, and the same ROIs were used for all images. The relative intensity of each waveguide was measured by summing the pixel intensities within each circular ROI, each with a 25 µm radius. Pixel intensities between different images were scaled by the exposure time from the image capture,

$$I_{scaled} = I_{raw}/t_{exp}. \tag{9.1}$$

A 5×5 matrix of waveguide output intensities was processed for each input condition (Figure 9.4b). Marginal distributions of the fiber intensity over the x- and y-axis were calculated by summing over the other axis:

$$I(x) = \Sigma_y I(x, y), \tag{9.2}$$

$$I(y) = \Sigma_x I(x, y). \tag{9.3}$$

The input fiber position along the x- and y-axis were estimated as the center of mass of the marginal intensity distributions:

$$\hat{x} = \frac{\Sigma_x x I(x)}{\Sigma_x I(x)}, \tag{9.4}$$

$$\hat{y} = \frac{\Sigma_y y I(y)}{\Sigma_y I(y)}. \tag{9.5}$$

To estimate the noise of the center of mass estimate, a third-degree polynomial was fit to the data. The residual error of the polynomial model was used as a measure of the noise of the system, and the standard deviation (σ) of the noise was calculated. The peak sensitivity was defined as

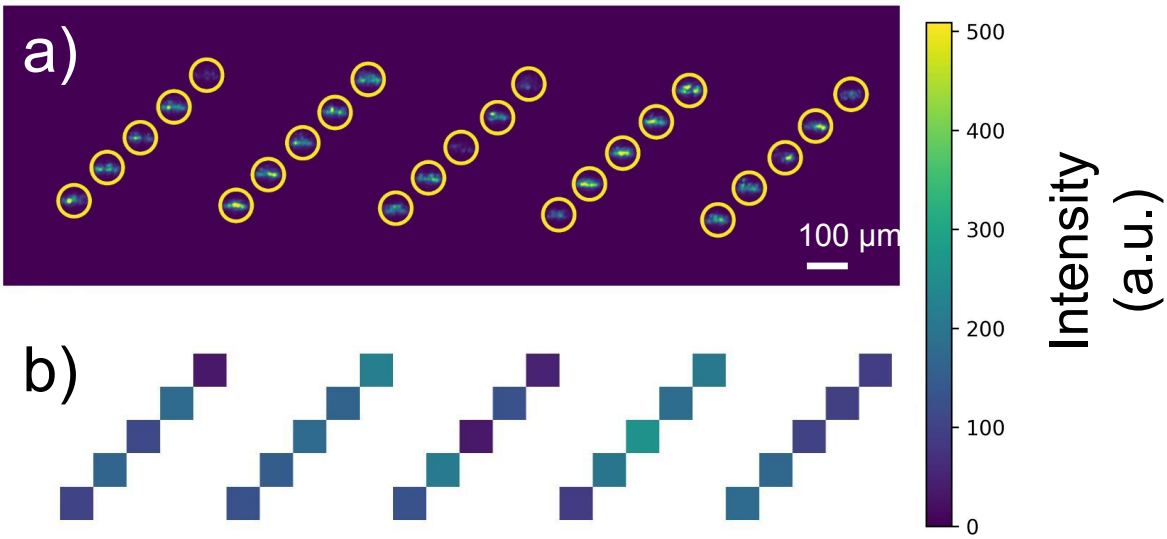

Figure 9.4: a) A raw image of the waveguide array output captured by the CCD camera. Individual waveguide regions of interest are circled. Illumination is provided by an optical fiber source located 2 cm from the array input. b) Analyzed waveguide array imager matrix showing pixel intensities.

$$\text{sensitivity} = \max\left(\frac{\partial \hat{x}}{\partial x}\right). \tag{9.6}$$

Then, the limit of detection (LOD) for a 95% confidence interval of the light source position is calculated as

$$\text{LOD} = \frac{4\sigma}{\text{sensitivity}}. \tag{9.7}$$

9.2.3 Spatial Resolution

9.2.3.1 Axis Sweeps

The response of the waveguide array imager to optical fiber movements along the x-, y-, and z-axes were measured. First, the fiber was positioned above the center of the waveguide array input and the intensity was measured as the fiber was withdrawn along the z-axis (Fig. 9.5a).

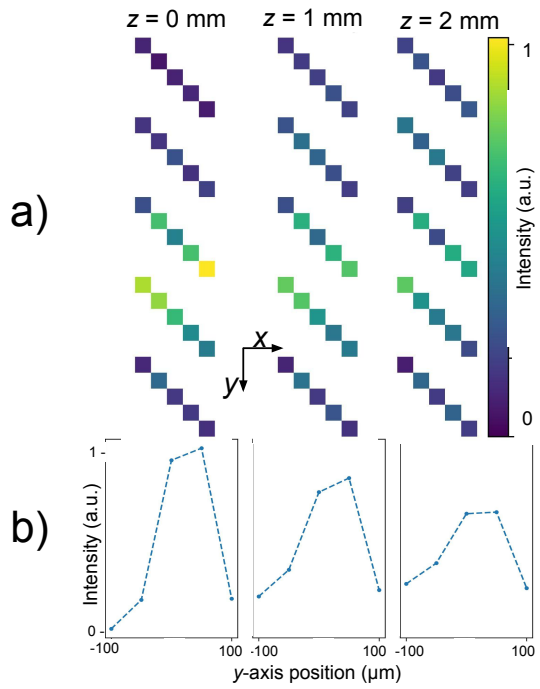

Figure 9.5: a) Waveguide array imager response to a fiber sweep along the z-axis. b) y-axis marginal intensity distribution showing the Gaussian beam profile of the fiber. The beam is attenuated and spread as the fiber is moved further from the input port.

The marginal intensity distribution along the y-axis (Fig. 9.5b) shows the downsampled 5-pixel reconstruction of the Gaussian beam profile of the fiber. As the fiber is moved farther from the waveguide array imager along the z-direction, the intensity of the fiber output beam is attenuated, and the beam width is increased as the beam diverges.

Next, the waveguide array imager response was measured as the fiber was swept along the y-axis (Fig. 9.6). Although the peak intensity of the fiber beam should not change as it is moved in the imaging plane, the imager output shows different peak intensities depending on the location, due to the different sensitivities of individual pixels from fabrication variation.

Lastly, the waveguide array imager response along the x-axis was measured (Fig. 9.7). The x-axis pixel spacing (40 μm pitch) is smaller than the spacing along the y-axis (200 μm pitch). As a result, the fiber beam profile is sampled over a smaller interval and the edge-to-edge variation of

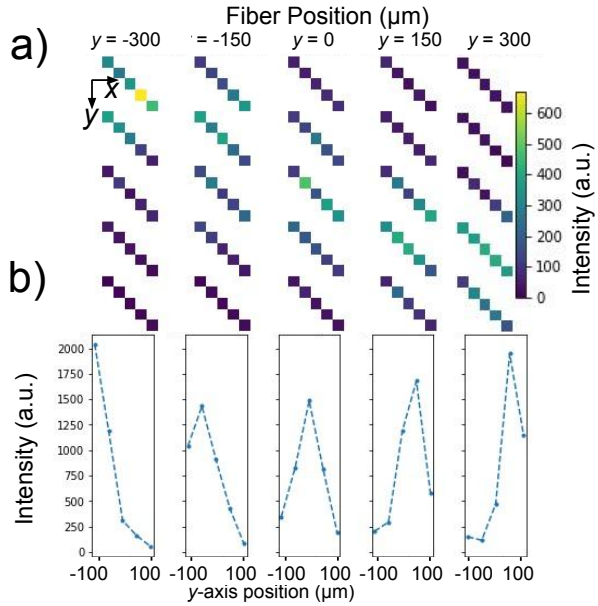

Figure 9.6: a) Waveguide array imager response to a fiber sweep along the y-axis. b) y-axis marginal intensity distribution, showing the Gaussian beam profile of the fiber. The center of the intensity distribution moves as the waveguide is swept in the y-direction.

the underlying signal is reduced. The fiber distribution looks flatter overall along the x-axis, and variations in pixel intensity become more prominent, since there is less variation in the underlying signal.

9.2.3.2 Localization Accuracy

Ultimately, the purpose of an imager as opposed to a photometer is to capture spatial information about light sources in a scene. To demonstrate this capability for the waveguide array microimager, the optical fiber light source position in the xy plane was localized based on the imager readout. I estimated the center of mass of the x and y marginal intensity distributions to estimate the fiber position in x and y. Figure 9.8 shows that the center of mass of the intensity distribution directly tracks the x and y position of the fiber across the imager. Both estimates saturate as the fiber position exceeds the limits of the imager (+/- 100 μm in x, +/-500 μm in y) (Fig. 7). As the fiber beam location extends beyond the edge of the imager array, the center of mass estimate does not receive information beyond the extents of the imager. Therefore, the

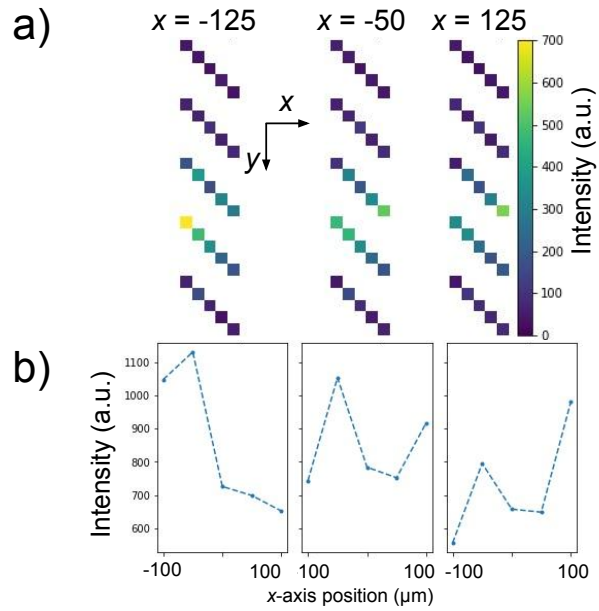

Figure 9.7: a) Waveguide array imager response to a fiber sweep along the x-axis. b) x-axis marginal intensity distribution, showing the Gaussian beam profile of the fiber. The center of the intensity distribution moves as the waveguide is swept in the x-direction.

sensitivity of the imager to a change in fiber location is reduced near the edges of the imager array. Based on the peak sensitivity at the center of the array, I calculate an LOD of the waveguide array imager is 17.04 μm along the x-axis and 30.07 μm along the y-axis.

9.2.4 Discussion

These results demonstrate that a 5×5 array of Parylene photonic waveguides can be used for imaging. The accuracy of the waveguide array was characterized by imaging an input optical fiber.

It should be noted that some waveguide outputs are dimmer than others. The waveguide-to-waveguide variability stems from the fabrication imperfections and results in distortion of the input image. These variations can be accounted for by calibrating the individual waveguides before imaging. Two feasible calibration procedures would be to either measure the response of each waveguide pixel to a uniform light source, or sequentially illuminate each waveguide pixel and measure the output intensity.

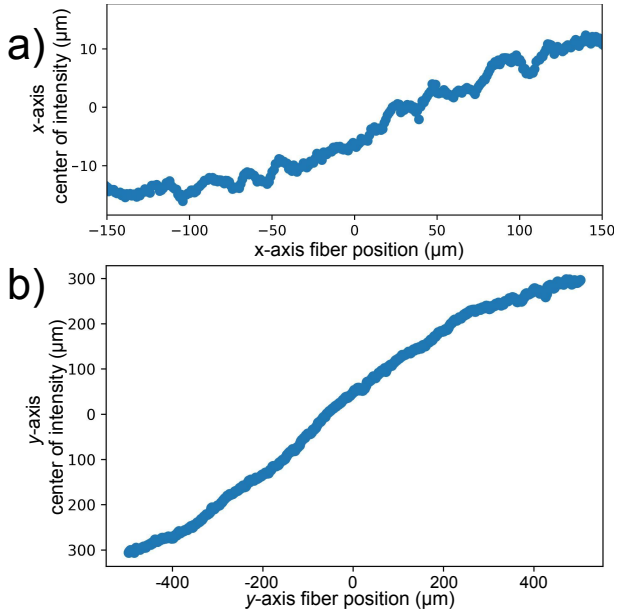

Figure 9.8: a) Fiber position localization via center of intensity along the x-axis. b) Fiber position localization via center of intensity along the y-axis.

Here, the proof-of-concept imager had only 25 waveguide pixels. However, the waveguide routing uses a very conservative pitch of 40 µm. Parylene photonic waveguides have been demonstrated with sizes as small as 10 µm [8], so simple lithographic scaling will allow a moderate increase to at least 100 waveguide imager pixels. The single-layer routing of the current imager design requires a linear increase in routing space for each pixel, which puts a fundamental limit on the number of pixels and the maximum pixel density. Scaling beyond a few hundred pixels in the waveguide imager array will require additional planer routing layers, or photonic switches to form an integrated multiplexer which can allow multiplexed addressing of many more output ports. Even with a modest number of pixels, the spatial resolution of the microimager demonstrated here can be useful in biological studies, for example for in-vivo fluorescent imaging.

9.3 Conclusion

The work presented in this thesis aims to address the outstanding need for high-density flexible photonic neural interfaces to expand the neuroscience tool set. I have presented the design, simulation, fabrication, characterization, and proof-of-concept biological demonstration of two forms of photonic neural interfaces: passive Parylene photonic waveguides and active μLEDs monolithically integrated on a Parylene substrate.

The first major outcome of this work is the development of a new integrated photonic platform: Parylene photonics, based on flexible biocompatible materials Parylene C and PDMS. This fully flexible and biocompatible photonic platform is compelling for use in implantable applications. Furthermore, the high index contrast between the materials enables confined optical modes in extremely small (1 μm × 1 μm) waveguides, which can be densely routed with negligible crosstalk.

A novel microfabrication process is developed and optimized for high-throughput realization of Parylene photonic waveguides. This fabrication process is scalable and many of these Parylene photonic waveguide arrays can be realized in parallel. A novel smoothing technique to reduce propagation losses in the Parylene photonic waveguides due to sidewall scattering by exploiting the conformal deposition characteristics of Parylene C is developed and characterized. Furthermore, a simulation study is undertaken to show that the conformal deposition of Parylene C in a silicon mold would enable the development of fundamentally new etchless waveguide designs. Furthermore, the waveguides are designed to monolithically integrate input/output micromirrors for out-of-plane input/output coupling. The waveguide and system properties including propagation loss, coupling efficiency, and output beam profiles were rigorously characterized using a custom-built automated robotic characterization system.

Parylene photonic waveguide arrays were demonstrated for in-vivo optogenetic stimulation of red-shifted ReaChR opsins. Several practical challenges were addressed to enable this demonstration, including the optimization of input coupling efficiency and also attachment to a rigid shuttle to enable implantation of the flexible neural probe. A sophisticated signal processing pipeline was developed to enable high-throughput spike sorting of data collected from the Parylene photonic neural probes. In all, this work shows that Parylene photonics is a practical platform to be used in neuroscience studies. Furthermore, integrated recording electrodes have been demonstrated in Parylene photonic waveguide neural probes, which paves the way for fully-flexible bi-directional neural interfaces using Parylene photonics.

The second main contribution of this thesis is the development of GaN μLEDs on a flexible Parylene substrate. Using a novel microfabrication process, I was able to fabricate lithographically-defined arrays of μLEDs monolithically encapsulated in a flexible substrate for the first time, bypassing throughput and yield limiting flip-chip bonding steps that have been used in the literature. Additionally, the monolithic integration allows for the development of novel functionalities in this architecture, including simultaneous bidirectional light emission from the top and bottom surfaces of the neural probe by the μLED through the transparent substrate, dense 2D arrays of multiplexed μLEDs, and double-sided (front- and backside) recording electrodes. Additionally, a rigorous optical and thermal simulation study was undertaken to determine safe stimulation regimes using the μLED neural probe to avoid thermal damage to the tissue. Proof of concept ex vivo optogenetic stimulation experiments were also performed to demonstrate the feasibility of optogenetic stimulation using the novel devices.

In summary, the work presented in my thesis represents a complete course of research to address a fundamental need in the development of neuroscience tools and BCIs. This work used a variety of techniques including simulation to understand the underlying properties of a device architecture, microfabrication processes to realize devices in the novel architectures, benchtop characterization to measure the performance, and demonstration in a biological system.

The groundwork laid in this thesis paves the way for new investigations, some of which I have explicitly identified in this chapter. This includes: the application of these novel device architectures to new settings and experimental paradigms, including non-penetrating surface neural interfaces, as well as using the architecture for completely new modalities, such as imaging using Parylene photonic waveguides.

This page intentionally left blank

References

[1] Z. Ahmed, J. Reddy, K. Deshpande, A. Krishnan, P. Venkatesh, S. Kelly, P. Grover, and M. Chamanzar, "Flexible Ultra-resolution Subdermal EEG Probes," in *2018 IEEE Biomedical Circuits and Systems Conference, BioCAS 2018 - Proceedings*. Institute of Electrical and Electronics Engineers Inc., 12 2018. doi: 10.1109/BIOCAS.2018.8584672. ISBN 9781538636039 4, 122

[2] S. Herculano-Houzel, "The human brain in numbers: a linearly scaled-up primate brain," *Frontiers in Human Neuroscience*, vol. 0, no. NOV, p. 31, 11 2009. doi: 10.3389/NEURO.09.031.2009 4

[3] D. Keller, C. Erö, and H. Markram, "Cell Densities in the Mouse Brain: A Systematic Review," *Frontiers in Neuroanatomy*, vol. 0, p. 83, 10 2018. doi: 10.3389/FNANA.2018.00083 4, 175

[4] A. G. Huth, W. A. de Heer, T. L. Griffiths, F. E. Theunissen, and J. L. Gallant, "Natural speech reveals the semantic maps that tile human cerebral cortex," *Nature 2016 532:7600*, vol. 532, no. 7600, pp. 453–458, 4 2016. doi: 10.1038/nature17637. [Online]. Available: https://www.nature.com/articles/nature17637 4

[5] Y. Zhao, S. Inayat, D. A. Dikin, J. H. Singer, R. S. Ruoff, and J. B. Troy, "Patch clamp technique: Review of the current state of the art and potential contributions from nanoengineering:," *http://dx.doi.org/10.1243/17403499JNN149*, vol. 222, no. 1, pp. 1–11, 7 2009. doi: 10.1243/17403499JNN149. [Online]. Available: https://journals.sagepub.com/doi/10.1243/17403499JNN149 4

[6] E. I. Moser, E. Kropff, and M.-B. Moser, "Place Cells, Grid Cells, and the Brain's Spatial Representation System," *http://dx.doi.org/10.1146/annurev.neuro.31.061307.090723*, vol. 31, pp. 69–89, 6 2008. doi: 10.1146/ANNUREV.NEURO.31.061307.090723. [Online]. Available: https://www.annualreviews.org/doi/abs/10.1146/annurev.neuro.31.061307.090723 4

[7] M. M. McGregor and A. B. Nelson, "Circuit Mechanisms of Parkinson's Disease," *Neuron*, vol. 101, no. 6, pp. 1042–1056, 3 2019. doi: 10.1016/J.NEURON.2019.03.004. [Online]. Available: http://www.cell.com/article/S0896627319302119/fulltexthttp://www.cell.com/article/S0896627319302119/abstracthttps://www.cell.com/neuron/abstract/S0896-6273(19)30211-9 4

[8] A. Vázquez-Guardado, Y. Yang, A. J. Bandodkar, and J. A. Rogers, "Recent advances in neurotechnologies with broad potential for neuroscience research," *Nature Neuroscience 2020 23:12*, vol. 23, no. 12, pp. 1522–1536, 11 2020. doi: 10.1038/s41593-020-00739-8. [Online]. Available: https://www.nature.com/articles/s41593-020-00739-8 5

[9] N. Pérez-Prieto and M. Delgado-Restituto, "Recording Strategies for High Channel Count, Densely Spaced Microelectrode Arrays," *Frontiers in Neuroscience*, vol. 0, p. 869, 7 2021. doi: 10.3389/FNINS.2021.681085 5

[10] G. Buzsáki, E. Stark, A. Berényi, D. Khodagholy, D. Kipke, E. Yoon, and K. D. Wise, "Tools for Probing Local Circuits: High-Density Silicon Probes Combined with Optogenetics," *Neuron*, vol. 86, no. 1, pp. 92–105, 4 2015. doi: 10.1016/J.NEURON.2015.01.028. [Online]. Available: https://www.sciencedirect.com/science/article/pii/S0896627315000860 5

[11] G. Buzsáki, "Large-scale recording of neuronal ensembles," *Nature Neuroscience*, vol. 7, no. 5, pp. 446–451, 5 2004. doi: 10.1038/nn1233. [Online]. Available: http://www.nature.com/articles/nn1233 5

[12] I. H. Stevenson and K. P. Kording, "How advances in neural recording affect data analysis," *Nature Neuroscience*, vol. 14, no. 2, pp. 139–142, 2 2011. doi: 10.1038/nn.2731. [Online]. Available: http://www.nature.com/articles/nn.2731 5

[13] T.-M. Fu, G. Hong, T. Zhou, T. G. Schuhmann, R. D. Viveros, and C. M. Lieber, "Stable long-term chronic brain mapping at the single-neuron level," *Nature Methods 2016 13:10*, vol. 13, no. 10, pp. 875–882, 8 2016. doi: 10.1038/nmeth.3969. [Online]. Available: https://www.nature.com/articles/nmeth.3969 5

[14] M. B. Lee, D. R. Kramer, T. Peng, M. F. Barbaro, C. Y. Liu, S. Kellis, and B. Lee, "Clinical neuroprosthetics: Today and tomorrow," *Journal of Clinical Neuroscience*, vol. 68, pp. 13–19, 10 2019. doi: 10.1016/J.JOCN.2019.07.056 5

[15] J. Delbeke, L. Hoffman, K. Mols, D. Braeken, and D. Prodanov, "And Then There Was Light: Perspectives of Optogenetics for Deep Brain Stimulation and Neuromodulation," *Frontiers in Neuroscience*, vol. 11, p. 663, 12 2017. doi: 10.3389/fnins.2017.00663. [Online]. Available: http://journal.frontiersin.org/article/10.3389/fnins.2017.00663/full 6, 8

[16] R. Chen, A. Canales, and P. Anikeeva, "Neural recording and modulation technologies," *Nature Reviews Materials*, vol. 2, no. 2, p. 16093, 1 2017. doi: 10.1038/natrevmats.2016.93. [Online]. Available: http://www.nature.com/articles/natrevmats201693 6

[17] H. Zhao, "Recent Progress of Development of Optogenetic Implantable Neural Probes." *International journal of molecular sciences*, vol. 18, no. 8, 8 2017. doi: 10.3390/ijms18081751. [Online]. Available: http://www.ncbi.nlm.nih.gov/pubmed/28800085http://www.pubmedcentral.nih.gov/articlerender.fcgi?artid=PMC5578141 6

[18] T. Yamaguchi, D. Wei, S. C. Song, B. Lim, N. X. Tritsch, and D. Lin, "Posterior amygdala regulates sexual and aggressive behaviors in male mice," *Nature Neuroscience 2020 23:9*, vol. 23, no. 9, pp. 1111–1124, 7 2020. doi: 10.1038/s41593-020-0675-x. [Online]. Available: https://www.nature.com/articles/s41593-020-0675-x 7

[19] A. H. Gittis and E. A. Yttri, "Translating insights from optogenetics into therapies for Parkinson's disease," *Current Opinion in Biomedical Engineering*, vol. 8, pp. 14–19, 12 2018. doi: 10.1016/J.COBME.2018.08.008 7

[20] K. J. Mastro, K. T. Zitelli, A. M. Willard, K. H. Leblanc, A. V. Kravitz, and A. H. Gittis, "Cell-specific pallidal intervention induces long-lasting motor recovery in dopamine-depleted mice," *Nature Neuroscience 2017 20:6*, vol. 20, no. 6, pp. 815–823, 5 2017. doi: 10.1038/nn.4559. [Online]. Available: https://www.nature.com/articles/nn.4559 8

[21] T. A. Spix, S. Nanivadekar, N. Toong, I. M. Kaplow, B. R. Isett, Y. Goksen, A. R. Pfenning, and A. H. Gittis, "Population-specific neuromodulation prolongs therapeutic benefits of deep brain stimulation," *Science*, vol. 374, no. 6564, pp. 201–206, 10 2021. doi: 10.1126/SCIENCE.ABI7852/SUPPL_FILE/SCIENCE.ABI7852_MOVIES_S1_AND_S2.ZIP. [Online]. Available: https://www.science.org/doi/abs/10.1126/science.abi7852 8

[22] E. Cela and P. J. Sjöström, "Novel Optogenetic Approaches in Epilepsy Research," *Frontiers in Neuroscience*, vol. 13, p. 947, 9 2019. doi: 10.3389/FNINS.2019.00947/BIBTEX 8

[23] E. Krook-Magnuson, C. Armstrong, M. Oijala, and I. Soltesz, "On-demand optogenetic control of spontaneous seizures in temporal lobe epilepsy," *Nature Communications 2013 4:1*, vol. 4, no. 1, pp. 1–8, 1 2013. doi: 10.1038/ncomms2376. [Online]. Available: https://www.nature.com/articles/ncomms2376 8

[24] E. Krook-Magnuson, C. Armstrong, A. Bui, S. Lew, M. Oijala, and I. Soltesz, "In vivo evaluation of the dentate gate theory in epilepsy," *The Journal of Physiology*, vol. 593, no. 10, pp. 2379–2388, 5 2015. doi: 10.1113/JP270056. [Online]. Available: https://onlinelibrary.wiley.com/doi/full/10.1113/JP270056https://onlinelibrary.wiley.com/doi/abs/10.1113/JP270056https://physoc.onlinelibrary.wiley.com/doi/10.1113/JP270056 8

[25] S. I. Osawa, M. Iwasaki, R. Hosaka, Y. Matsuzaka, H. Tomita, T. Ishizuka, E. Sugano, E. Okumura, H. Yawo, N. Nakasato, T. Tominaga, and H. Mushiake, "Optogenetically Induced Seizure and the Longitudinal Hippocampal Network Dynamics," *PLOS ONE*, vol. 8, no. 4, p. e60928, 4 2013. doi: 10.1371/JOURNAL.PONE.0060928. [Online]. Available: https://journals.plos.org/plosone/article?id=10.1371/journal.pone.0060928 8

[26] V. Ntziachristos, "Going deeper than microscopy: the optical imaging frontier in biology," *Nature Methods*, vol. 7, no. 8, pp. 603–614, 8 2010. doi: 10.1038/nmeth.1483. [Online]. Available: http://www.nature.com/articles/nmeth.1483 8

[27] X. Deng and M. Gu, "Penetration depth of single-, two-, and three-photon fluorescence microscopic imaging through human cortex structures: Monte Carlo simulation," *Applied Optics*, vol. 42, no. 16, p. 3321, 6 2003. doi: 10.1364/AO.42.003321. [Online]. Available: https://www.osapublishing.org/abstract.cfm?URI=ao-42-16-3321 8

[28] F. Wu, E. Stark, M. Im, I.-J. Cho, E.-S. Yoon, G. Buzsáki, K. D. Wise, and E. Yoon, "An implantable neural probe with monolithically integrated dielectric waveguide and recording electrodes for optogenetics applications." *Journal of neural engineering*, vol. 10, no. 5, p. 056012, 10 2013. doi: 10.1088/1741-2560/10/5/056012. [Online]. Available: http://www.ncbi.nlm.nih.gov/pubmed/23985803http://www.pubmedcentral.nih.gov/articlerender.fcgi?artid=PMC4056669 9

[29] L. Hoffman, M. Welkenhuysen, A. Andrei, S. Musa, Z. Luo, S. Libbrecht, S. Severi, P. Soussan, V. Baekelandt, S. Haesler, G. Gielen, R. Puers, and D. Braeken, "High-density optrode-electrode neural probe using SixNy photonics for in vivo optogenetics," in *Technical Digest - International Electron Devices Meeting, IEDM*, vol. 2016-Febru, Washington, D.C., 2015. doi: 10.1109/IEDM.2015.7409795. ISSN 01631918 pp. 1–29. [Online]. Available: http://ieeexplore.ieee.org/document/7409795/ 9, 10

[30] M. Schwaerzle, O. Paul, and P. Ruther, "Compact silicon-based optrode with integrated laser diode chips, SU-8 waveguides and platinum electrodes for optogenetic applications," *Journal of Micromechanics and Microengineering*, vol. 27, no. 6, p. 065004, 6 2017. doi: 10.1088/1361-6439/aa6ad4. [Online]. Available: https://iopscience.iop.org/article/10.1088/1361-6439/aa6ad4https://iopscience.iop.org/article/10.1088/1361-6439/aa6ad4/metahttp://stacks.iop.org/0960-1317/27/i=6/a=065004?key=crossref.c283747ea3add17327df5e1a733dec6c 9, 10

[31] H. Zhao, A. Soltan, P. Maaskant, N. Dong, X. Sun, and P. Degenaar, "A Scalable Optoelectronic Neural Probe Architecture With Self-Diagnostic Capability," *IEEE Transactions on Circuits and Systems I: Regular Papers*, pp. 1–12, 2018. doi: 10.1109/TCSI.2018.2792219. [Online]. Available: http://ieeexplore.ieee.org/document/8268676/ 9

[32] N. McAlinden, D. Massoubre, E. Richardson, E. Gu, S. Sakata, M. D. Dawson, and K. Mathieson, "Thermal and optical characterization of micro-LED probes for in vivo optogenetic neural stimulation," *Optics Letters*, vol. 38, no. 6, p. 992, 3 2013. doi: 10.1364/OL.38.000992. [Online]. Available: https://www.osapublishing.org/abstract.cfm?URI=ol-38-6-992 9

[33] K. N. Noh, S. I. Park, R. Qazi, Z. Zou, A. D. Mickle, J. G. Grajales-Reyes, K.-I. Jang, R. W. Gereau, J. Xiao, J. A. Rogers, and J.-W. Jeong, "Miniaturized, Battery-Free Optofluidic Systems with Potential for Wireless Pharmacology and Optogenetics," *Small*, vol. 14, no. 4, p. 1702479, 1 2018. doi: 10.1002/smll.201702479. [Online]. Available: http://doi.wiley.com/10.1002/smll.201702479 9

[34] B. J. Kim, J. T. W. Kuo, S. A. Hara, C. D. Lee, L. Yu, C. A. Gutierrez, T. Q. Hoang, V. Pikov, and E. Meng, "3D Parylene sheath neural probe for chronic recordings," *Journal of Neural Engineering*, vol. 10, no. 4, p. 045002, 8 2013. doi: 10.1088/1741-2560/10/4/045002. [Online]. Available: http://stacks.iop.org/1741-2552/10/i=4/a=045002?key=crossref.fd85b87523c2c29de227e49dfc398369 9

[35] G. Shin, A. M. Gomez, R. Al-Hasani, Y. R. Jeong, J. Kim, Z. Xie, A. Banks, S. M. Lee, S. Y. Han, C. J. Yoo, J.-L. Lee, S. H. Lee, J. Kurniawan, J. Tureb, Z. Guo, J. Yoon, S.-I. Park, S. Y. Bang, Y. Nam, M. C. Walicki, V. K. Samineni, A. D. Mickle, K. Lee, S. Y. Heo, J. G. McCall, T. Pan, L. Wang, X. Feng, T.-i. Kim, J. K. Kim, Y. Li, Y. Huang, R. W. Gereau, J. S. Ha, M. R. Bruchas, and J. A. Rogers, "Flexible Near-Field Wireless Optoelectronics as Subdermal Implants for Broad Applications in Optogenetics," *Neuron*, vol. 93, no. 3, pp. 509–521, 2 2017. doi: 10.1016/J.NEURON.2016.12.031. [Online]. Available: https://www.sciencedirect.com/science/article/pii/S0896627316310042 9

[36] A. N. Zorzos, J. Scholvin, E. S. Boyden, and C. G. Fonstad, "Three-dimensional multiwaveguide probe array for light delivery to distributed brain circuits," *Optics Letters*, vol. 37, no. 23, p. 4841, 12 2012. doi: 10.1364/OL.37.004841. [Online]. Available: https://www.osapublishing.org/abstract.cfm?URI=ol-37-23-4841 9, 10, 26

[37] E. Shim, Y. Chen, S. Masmanidis, and M. Li, "Multisite silicon neural probes with integrated silicon nitride waveguides and gratings for optogenetic applications," *Scientific Reports*, vol. 6, no. 1, p. 22693, 9 2016. doi: 10.1038/srep22693. [Online]. Available: http://www.nature.com/articles/srep22693 9, 78

[38] S. Libbrecht, L. Hoffman, M. Welkenhuysen, C. Van den Haute, V. Baekelandt, D. Braeken, and S. Haesler, "Proximal and distal modulation of neural activity by spatially confined optogenetic activation with an integrated high-density optoelectrode," *Journal of Neurophysiology*, vol. 120, no. 1, pp. 149–161, 7 2018. doi: 10.1152/jn.00888.2017. [Online]. Available: https://www.physiology.org/doi/10.1152/jn.00888.2017 9, 11, 26

[39] S. Park, G. Loke, Y. Fink, and P. Anikeeva, "Flexible fiber-based optoelectronics for neural interfaces," pp. 1826–1852, 3 2019. [Online]. Available: https://pubs.rsc.org/en/content/articlehtml/2019/cs/c8cs00710ahttps://pubs.rsc.org/en/content/articlelanding/2019/cs/c8cs00710a 9

[40] I.-J. Cho, H. W. Baac, and E. Yoon, "A 16-site neural probe integrated with a waveguide for optical stimulation," in *2010 IEEE 23rd International Conference on Micro Electro Mechanical Systems (MEMS)*. IEEE, 1 2010. doi: 10.1109/MEMSYS.2010.5442376. ISBN 978-1-4244-5761-8 pp. 995–998. [Online]. Available: http://ieeexplore.ieee.org/document/5442376/ 10

[41] M. Schwaerzle, J. Nehlich, U. T. Schwarz, O. Paul, and P. Ruther, "Hybrid polymer waveguide characterization for microoptical tools with integrated laser diode chips for optogenetic applications at 430 nm and 650 nm," in *Proc. SPIE 9690, Clinical*

and Translational Neurophotonics; Neural Imaging and Sensing; and Optogenetics and Optical Manipulation, S. J. Madsen, V. X. D. Yang, E. D. Jansen, Q. Luo, S. K. Mohanty, and N. V. Thakor, Eds., vol. 9690. International Society for Optics and Photonics, 3 2016. doi: 10.1117/12.2212554 p. 96902K. [Online]. Available: http://proceedings.spiedigitallibrary.org/proceeding.aspx?doi=10.1117/12.2212554 10

[42] K. Kampasi, I. Ladner, J. Zhou, A. Calónico Soto, J. Hernandez, S. Patra, and R. u. Haque, "POEMS (Polymeric Opto-Electro-Mechanical Systems) for advanced neural interfaces," *Materials Letters*, vol. 285, p. 129015, 2 2021. doi: 10.1016/j.matlet.2020.129015 10

[43] S. Park, H. Yuk, R. Zhao, Y. S. Yim, E. W. Woldeghebriel, J. Kang, A. Canales, Y. Fink, G. B. Choi, X. Zhao, and P. Anikeeva, "Adaptive and multifunctional hydrogel hybrid probes for long-term sensing and modulation of neural activity," *Nature Communications 2021 12:1*, vol. 12, no. 1, pp. 1–12, 6 2021. doi: 10.1038/s41467-021-23802-9. [Online]. Available: https://www.nature.com/articles/s41467-021-23802-9 10

[44] S. Park, Y. Guo, X. Jia, H. K. Choe, B. Grena, J. Kang, J. Park, C. Lu, A. Canales, R. Chen, Y. S. Yim, G. B. Choi, Y. Fink, and P. Anikeeva, "One-step optogenetics with multifunctional flexible polymer fibers," *Nature Neuroscience*, vol. 20, no. 4, pp. 612–619, 3 2017. doi: 10.1038/nn.4510. [Online]. Available: https://pubmed.ncbi.nlm.nih.gov/28218915/https://www.nature.com/articles/nn.4510 10

[45] X. Wen, T. Liu, P. Y. Chiou, Ximiao Wen, Tingyi Liu, and Pei-Yu Chiou, "A hybrid silicon-PDMS multifunctional neural probe," in *2016 International Conference on Optical MEMS and Nanophotonics (OMN)*, vol. 2016-Septe, 2016. doi: 10.1109/OMN.2016.7565849. ISSN 21605041 pp. 1–2. [Online]. Available: http://ieeexplore.ieee.org/document/7565849/ 10

[46] K. Kampasi, E. Stark, J. Seymour, K. Na, H. G. Winful, G. Buzsáki, K. D. Wise, and E. Yoon, "Fiberless multicolor neural optoelectrode for in vivo circuit analysis," *Scientific Reports*, vol. 6, no. 1, p. 30961, 11 2016. doi: 10.1038/srep30961. [Online]. Available: http://www.nature.com/articles/srep30961www.nature.com/scientificreports 10

[47] E. Segev, J. Reimer, L. C. Moreaux, T. M. Fowler, D. Chi, W. D. Sacher, M. Lo, K. D. M.D., A. S. Tolias, A. Faraon, and M. L. Roukes, "Patterned photostimulation via visible-wavelength photonic probes for deep brain optogenetics," *https://doi.org/10.1117/1.NPh.4.1.011002*, vol. 4, no. 1, p. 011002, 12 2016. doi: 10.1117/1.NPH.4.1.011002. [Online]. Available: https://www.spiedigitallibrary.org/journals/neurophotonics/volume-4/issue-1/011002/Patterned-photostimulation-via-visible-wavelength-photonic-probes-for-deep-brain/10.1117/1.NPh.4.1.011002.fullhttps://www.spiedigitallibrary.org/journals/neurophotonics/volume-4/issue-1/011002/Patterned-photostimulation-via-visible-wavelength-photonic-probes-for-deep-brai 10.1117/1.NPh.4.1.011002.short 11

[48] F. Wu, E. Stark, P.-C. Ku, K. D. Wise, G. Buzsáki, and E. Yoon, "Monolithically Integrated μLEDs on Silicon Neural Probes for High-Resolution Optogenetic Studies in Behaving Animals." *Neuron*, vol. 88, no. 6, pp. 1136–1148, 12 2015. doi: 10.1016/j.neuron.2015.10.032. [Online]. Available: http://www.ncbi.nlm.nih.gov/pubmed/26627311http://www.pubmedcentral.nih.gov/articlerender.fcgi?artid=PMC4702503 11, 12, 93, 142, 143, 152, 154

[49] B. Ji, Z. Guo, M. Wang, B. Yang, X. Wang, W. Li, and J. Liu, "Flexible polyimide-based hybrid opto-electric neural interface with 16 channels of micro-LEDs and electrodes," *Microsystems & Nanoengineering*, vol. 4, no. 1, p. 27, 12 2018. doi: 10.1038/s41378-018-0027-0. [Online]. Available: http://www.nature.com/articles/s41378-018-0027-0 11

[50] D. Keppeler, M. Schwaerzle, T. Harczos, L. Jablonski, A. Dieter, B. Wolf, S. Ayub, C. Vogl, C. Wrobel, G. Hoch, K. Abdellatif, M. Jeschke, V. Rankovic, O. Paul, P. Ruther, and T. Moser, "Multichannel optogenetic stimulation of the auditory pathway using microfabricated LED cochlear implants in rodents," *Science Translational Medicine*, vol. 12, no. 553, 7 2020. doi: 10.1126/SCITRANSLMED.ABB8086 11

[51] C. Liu, Y. Zhao, X. Cai, Y. Xie, T. Wang, D. Cheng, L. Li, R. Li, Y. Deng, H. Ding, G. Lv, G. Zhao, L. Liu, G. Zou, M. Feng, Q. Sun, L. Yin, and X. Sheng, "A wireless, implantable optoelectrochemical probe for optogenetic stimulation and dopamine detection," *Microsystems and Nanoengineering*, vol. 6, no. 1, pp. 1–12, 12 2020. doi: 10.1038/s41378-020-0176-9. [Online]. Available: www.nature.com/micronano 11

[52] B. J. Kim, C. A. Gutierrez, G. A. Gerhardt, and E. Meng, "Parylene-based electrochemical-MEMS force sensor array for assessing neural probe insertion mechanics," in *Proceedings of the IEEE International Conference on Micro Electro Mechanical Systems (MEMS)*, 2012. doi: 10.1109/MEMSYS.2012.6170109. ISBN 9781467303248. ISSN 10846999 pp. 124–127. 11

[53] E. Klein, C. Gossler, O. Paul, and P. Ruther, "High-Density μLED-Based Optical Cochlear Implant With Improved Thermomechanical Behavior." *Frontiers in neuroscience*, vol. 12, p. 659, 2018. doi: 10.3389/fnins.2018.00659. [Online]. Available: http://www.ncbi.nlm.nih.gov/pubmed/30327585http://www.pubmedcentral.nih.gov/articlerender.fcgi?artid=PMC6174235 11

[54] A. Dieter, E. Klein, D. Keppeler, L. Jablonski, T. Harczos, G. Hoch, V. Rankovic, O. Paul, M. Jeschke, P. Ruther, and T. Moser, "μLED-based optical cochlear implants for spectrally selective activation of the auditory nerve," *EMBO Molecular Medicine*, vol. 12, no. 8, p. e12387, 8 2020. doi: 10.15252/EMMM.202012387. [Online]. Available: https://onlinelibrary.wiley.com/doi/full/10.15252/emmm.202012387https://onlinelibrary.wiley.com/doi/abs/10.15252/emmm.202012387https://www.embopress.org/doi/abs/10.15252/emmm.202012387 11

[55] W. Yang and R. Yuste, "In vivo imaging of neural activity," *Nature Methods*, vol. 14, no. 4, pp. 349–359, 4 2017. doi: 10.1038/nmeth.4230. [Online]. Available: https://www.nature.com/articles/nmeth.4230http://www.nature.com/articles/nmeth.4230 12

[56] D. Wu, A. C. Sedgwick, T. Gunnlaugsson, E. U. Akkaya, J. Yoon, and T. D. James, "Fluorescent chemosensors: the past, present and future," *Chemical Society Reviews*, vol. 46, no. 23, pp. 7105–7123, 11 2017. doi: 10.1039/C7CS00240H. [Online]. Available: http://xlink.rsc.org/?DOI=C7CS00240H 12

[57] O. M. Carrasco-Zevallos, C. Viehland, B. Keller, M. Draelos, A. N. Kuo, C. A. Toth, and J. A. Izatt, "Review of intraoperative optical coherence tomography: technology and applications [Invited]," *Biomedical Optics Express*, vol. 8, no. 3, p. 1607, 3 2017. doi: 10.1364/BOE.8.001607. [Online]. Available: https://www.osapublishing.org/abstract.cfm?URI=boe-8-3-1607 12

[58] Z. Zhang, L. E. Russell, A. M. Packer, O. M. Gauld, and M. Häusser, "Closed-loop all-optical manipulation of neural circuits in vivo," *Nature methods*, vol. 15, no. 12, p. 1037, 12 2018. doi: 10.1038/S41592-018-0183-Z. [Online]. Available: /pmc/articles/PMC6513754//pmc/articles/PMC6513754/?report=abstracthttps://www.ncbi.nlm.nih.gov/pmc/articles/PMC6513754/ 13

[59] G. Oh, E. Chung, and S. H. Yun, "Optical fibers for high-resolution in vivo microendoscopic fluorescence imaging," *Optical Fiber Technology*, vol. 19, no. 6, pp. 760–771, 12 2013. doi: 10.1016/J.YOFTE.2013.07.008. [Online]. Available: https://www.sciencedirect.com/science/article/pii/S1068520013000886 13

[60] B. A. Flusberg, E. D. Cocker, W. Piyawattanametha, J. C. Jung, E. L. M. Cheung, and M. J. Schnitzer, "Fiber-optic fluorescence imaging," *Nature Methods 2005 2:12*, vol. 2, no. 12, pp. 941–950, 11 2005. doi: 10.1038/nmeth820. [Online]. Available: https://www.nature.com/articles/nmeth820 13

[61] D. Szarowski, M. Andersen, S. Retterer, A. Spence, M. Isaacson, H. Craighead, J. Turner, and W. Shain, "Brain responses to micro-machined silicon devices," *Brain Research*, vol. 983, no. 1-2, pp. 23–35, 9 2003. doi: 10.1016/S0006-8993(03)03023-3 13

[62] T. D. Y. Kozai, A. S. Jaquins-Gerstl, A. L. Vazquez, A. C. Michael, and X. T. Cui, "Brain Tissue Responses to Neural Implants Impact Signal Sensitivity and Intervention Strategies," *ACS Chemical Neuroscience*, vol. 6, no. 1, pp. 48–67, 1 2015. doi: 10.1021/cn500256e. [Online]. Available: http://pubs.acs.org/doi/10.1021/cn500256e 13

[63] P. Moshayedi, G. Ng, J. C. Kwok, G. S. Yeo, C. E. Bryant, J. W. Fawcett, K. Franze, and J. Guck, "The relationship between glial cell mechanosensitivity and foreign body reactions in the central nervous system," *Biomaterials*, vol. 35, no. 13, pp. 3919–3925, 4 2014. doi: 10.1016/J.BIOMATERIALS.2014.01.038. [Online]. Available: https://www.sciencedirect.com/science/article/pii/S0142961214000544 13

[64] W. J. Tyler, "The mechanobiology of brain function," pp. 867–878, 12 2012. [Online]. Available: www.nature.com/reviews/neuro 13

[65] B. J. Black, A. Kanneganti, A. Joshi-Imre, R. Rihani, B. Chakraborty, J. Abbott, J. J. Pancrazio, and S. F. Cogan, "Chronic recording and electrochemical performance of Utah microelectrode arrays implanted in rat motor cortex," *Journal of Neurophysiology*, vol. 120, no. 4, pp. 2083–2090, 10 2018. [Online]. Available: https://journals.physiology.org/doi/abs/10.1152/jn.00181.2018 13

[66] J. W. Salatino, K. A. Ludwig, T. D. Kozai, and E. K. Purcell, "Glial responses to implanted electrodes in the brain," *Nature Biomedical Engineering*, vol. 1, no. 11, pp. 862–877, 11 2017. doi: 10.1038/s41551-017-0154-1 13

[67] A. M. Stiller, B. J. Black, C. Kung, A. Ashok, S. F. Cogan, V. D. Varner, and J. J. Pancrazio, "A meta-analysis of intracortical device stiffness and its correlation with histological outcomes," *Micromachines*, vol. 9, no. 9, 2018. doi: 10.3390/mi9090443 13, 14

[68] A. Weltman, J. Yoo, E. Meng, A. Weltman, J. Yoo, and E. Meng, "Flexible, Penetrating Brain Probes Enabled by Advances in Polymer Microfabrication," *Micromachines*, vol. 7, no. 12, p. 180, 10 2016. doi: 10.3390/mi7100180. [Online]. Available: http://www.mdpi.com/2072-666X/7/10/180 13, 165

[69] M. Polanco, S. Bawab, and H. Yoon, "Computational assessment of neural probe and brain tissue interface under transient motion," *Biosensors*, vol. 6, no. 2, 6 2016. doi: 10.3390/bios6020027. [Online]. Available: https://pubmed.ncbi.nlm.nih.gov/27322338/ 13

[70] A. Gilletti and J. Muthuswamy, "Brain micromotion around implants in the rodent somatosensory cortex," *Journal of Neural Engineering*, vol. 3, no. 3, pp. 189–195, 9 2006. doi: 10.1088/1741-2560/3/3/001. [Online]. Available: http://stacks.iop.org/1741-2552/3/i=3/a=001?key=crossref.0a962fc1b2d9f23f2d6892320eb8201c 13

[71] J. Subbaroyan, D. C. Martin, and D. R. Kipke, "A finite-element model of the mechanical effects of implantable microelectrodes in the cerebral cortex," *Journal of Neural Engineering*, vol. 2, no. 4, pp. 103–113, 12 2005. doi: 10.1088/1741-2560/2/4/006. [Online]. Available: http://stacks.iop.org/1741-2552/2/i=4/a=006?key=crossref.aa9f0b7a9173cfc79eecb56212747f38 13

[72] H. C. Lee, F. Ejserholm, J. Gaire, S. Currlin, J. Schouenborg, L. Wallman, M. Bengtsson, K. Park, and K. J. Otto, "Histological evaluation of flexible neural implants; Flexibility limit for reducing the tissue response?" *Journal of Neural Engineering*, vol. 14, no. 3, 5 2017. doi: 10.1088/1741-2552/aa68f0 14

[73] A. Lecomte, E. Descamps, and C. Bergaud, "A review on mechanical considerations for chronically-implanted neural probes," *Journal of Neural Engineering*, vol. 15, no. 3, p. 031001, 6 2018. doi: 10.1088/1741-2552/aa8b4f. [Online]. Available: https://doi.org/10.1088/1741-2552/aa8b4fhttp://stacks.iop.org/1741-2552/15/i=3/a=031001?key=crossref.79aed9ebdad537879880687b2a219f2d 14, 15

[74] D. Thomson, A. Zilkie, J. E. Bowers, T. Komljenovic, G. T. Reed, L. Vivien, D. Marris-Morini, E. Cassan, L. Virot, J.-M. Fédéli, J.-M. Hartmann, J. H. Schmid, D.-X. Xu, F. Boeuf, P. O'Brien, G. Z. Mashanovich, and M. Nedeljkovic, "Roadmap on silicon photonics," *Journal of Optics*, vol. 18, no. 7, p. 073003, 7 2016. doi: 10.1088/2040-8978/18/7/073003. [Online]. Available: http://stacks.iop.org/2040-8986/18/i=7/a=073003?key=crossref.4a5bbda045e84b8801eba3e3605b6fb2 14, 54

[75] W. Bai, H. Yang, Y. Ma, H. Chen, J. Shin, Y. Liu, Q. Yang, I. Kandela, Z. Liu, S.-K. Kang, C. Wei, C. R. Haney, A. Brikha, X. Ge, X. Feng, P. V. Braun, Y. Huang, W. Zhou, and J. A. Rogers, "Flexible Transient Optical Waveguides and Surface-Wave Biosensors Constructed from Monocrystalline Silicon," *Advanced Materials*, vol. 30, no. 32, p. 1801584, 8 2018. doi: 10.1002/adma.201801584. [Online]. Available: http://doi.wiley.com/10.1002/adma.201801584 15

[76] R. Khilwani, P. J. Gilgunn, T. D. Kozai, X. C. Ong, E. Korkmaz, P. K. Gunalan, X. T. Cui, G. K. Fedder, and O. B. Ozdoganlar, "Ultra-miniature ultra-compliant neural probes with dissolvable delivery needles: design, fabrication and characterization," *Biomedical Microdevices*, 2016. doi: 10.1007/s10544-016-0125-4 15

[77] M. A. Hopcroft, W. D. Nix, and T. W. Kenny, "What is the Young's Modulus of Silicon?" *Journal of Microelectromechanical Systems*, vol. 19, no. 2, pp. 229–238, 4 2010. doi: 10.1109/JMEMS.2009.2039697. [Online]. Available: http://ieeexplore.ieee.org/document/5430873/ 15

[78] A. Khan, J. Philip, and P. Hess, "Young's modulus of silicon nitride used in scanning force microscope cantilevers," *Journal of Applied Physics*, vol. 95, no. 4, pp. 1667–1672, 2 2004. doi: 10.1063/1.1638886. [Online]. Available: http://aip.scitation.org/doi/10.1063/1.1638886 15

[79] C. Hassler, R. P. von Metzen, P. Ruther, and T. Stieglitz, "Characterization of parylene C as an encapsulation material for implanted neural prostheses," *Journal of Biomedical Materials Research Part B: Applied Biomaterials*, vol. 9999B, no. 1, pp. NA–NA, 4 2010. doi: 10.1002/jbm.b.31584. [Online]. Available: http://doi.wiley.com/10.1002/jbm.b.31584 15

[80] I. D. Johnston, D. K. McCluskey, C. K. L. Tan, and M. C. Tracey, "Mechanical characterization of bulk Sylgard 184 for microfluidics and microengineering," *Journal of Micromechanics and Microengineering*, vol. 24, no. 3, p. 035017, 3 2014. doi: 10.1088/0960-1317/24/3/035017. [Online]. Available: http://stacks.iop.org/0960-1317/24/i=3/a=035017?key=crossref.cf83b17be3210f20943ae0e9169fc9b8 15

[81] S. Budday, R. Nay, R. de Rooij, P. Steinmann, T. Wyrobek, T. C. Ovaert, and E. Kuhl, "Mechanical properties of gray and white matter brain tissue by indentation," *Journal of the Mechanical Behavior of Biomedical Materials*, vol. 46, pp. 318–330, 6 2015. doi: 10.1016/J.JMBBM.2015.02.024 15

[82] C. T. McKee, J. A. Last, P. Russell, and C. J. Murphy, "Indentation versus tensile measurements of Young's modulus for soft biological tissues." *Tissue engineering. Part B, Reviews*, vol. 17, no. 3, pp. 155–64, 6 2011. doi: 10.1089/ten.TEB.2010.0520. [Online]. Available: http://www.ncbi.nlm.nih.gov/pubmed/21303220http://www.pubmedcentral.nih.gov/articlerender.fcgi?artid=PMC3099446 15

[83] A. Ersen and M. Sahin, "Polydimethylsiloxane-based optical waveguides for tetherless powering of floating microstimulators," *Journal of Biomedical Optics*, vol. 22, no. 5, p. 055005, 5 2017. doi: 10.1117/1.jbo.22.5.055005 15

[84] F. Rehberger, E. Fiedler, F. Kohler, M. Mueller, A. Seifert, H. Zappe, and T. Siteglitz, "Lichtwellenleiter aus PDMS für biomedizinische Anwendungen," *Biomedical Engineering-Biomedizinische Technik*, vol. 59, pp. S1068–S1071, 2014. doi: 10.1515/bmt-2014-4450 15

[85] X. Wang, A. W. Hirschberg, H. Xu, Z. Slingsby-Smith, A. Lecomte, K. Scholten, D. Song, and E. Meng, "A Parylene Neural Probe Array for Multi-Region Deep Brain Recordings," *Journal of Microelectromechanical Systems*, vol. 29, no. 4, pp. 499–513, 8 2020. doi: 10.1109/JMEMS.2020.3000235 16

[86] L. Luan, X. Wei, Z. Zhao, J. J. Siegel, O. Potnis, C. A. Tuppen, S. Lin, S. Kazmi, R. A. Fowler, S. Holloway, A. K. Dunn, R. A. Chitwood, and C. Xie, "Ultraflexible nanoelectronic probes form reliable, glial scar–free neural integration," *Science Advances*, vol. 3, no. 2, p. e1601966, 2 2017. doi: 10.1126/sciadv.1601966. [Online]. Available: http://advances.sciencemag.org/http://advances.sciencemag.org/lookup/doi/10.1126/sciadv.1601966 16

[87] A. J. Shoffstall, S. Srinivasan, M. Willis, A. M. Stiller, M. Ecker, W. E. Voit, J. J. Pancrazio, and J. R. Capadona, "A Mosquito Inspired Strategy to Implant Microprobes into the Brain," *Scientific Reports*, vol. 8, no. 1, p. 122, 12 2018. doi: 10.1038/s41598-017-18522-4. [Online]. Available: http://www.nature.com/articles/s41598-017-18522-4 16, 100

[88] A. Lecomte, V. Castagnola, E. Descamps, L. Dahan, M. C. Blatché, T. M. Dinis, E. Leclerc, C. Egles, and C. Bergaud, "No Title," *Journal of Micromechanics and Microengineering*, vol. 25, no. 12, p. 125003, 12 2015. doi: 10.1088/0960-1317/25/12/125003. [Online]. Available: http://stacks.iop.org/0960-1317/25/i=12/a=125003?key=crossref.05cf68334bbbd8bb9890ae141beaa739 16

[89] A. Weltman, H. Xu, K. Scholten, T. W. Berger, D. Song, and E. Meng, "Deep brain targeting strategy for bare parylene neural probe arrays," in *2016 Solid-State Sensors, Actuators and Microsystems Workshop, Hilton Head 2016*, 2016. doi: 10.31438/trf.hh2016.82. ISBN 9781940470023 16

[90] S. Rezaei, Y. Xu, and S. W. Pang, "Control of neural probe shank flexibility by fluidic pressure in embedded microchannel using PDMS/PI hybrid substrate," *PLOS ONE*, vol. 14, no. 7, p. e0220258, 7 2019. doi: 10.1371/journal.pone.0220258. [Online]. Available: https://dx.plos.org/10.1371/journal.pone.0220258 16

[91] S. Yagi, S. Yamagiwa, Y. Kubota, H. Sawahata, R. Numano, T. Imashioya, H. Oi, M. Ishida, and T. Kawano, "Dissolvable Base Scaffolds Allow Tissue Penetration of High-Aspect-Ratio Flexible Microneedles," *Advanced Healthcare Materials*, 2015. doi: 10.1002/adhm.201500305 16

[92] J. W. Reddy, M. Lassiter, and M. Chamanzar, "Parylene photonics: a flexible, broadband optical waveguide platform with integrated micromirrors for biointerfaces," *Microsystems and Nanoengineering*, vol. 6, no. 1, pp. 1–14, 12 2020. doi: 10.1038/s41378-020-00186-2. [Online]. Available: www.nature.com/micronano 19, 35, 73, 99

[93] Y. S. Jeong, B. Ratier, A. Moliton, and L. Guyard, "UV-visible and infrared characterization of poly(p-xylylene) films for waveguide applications and OLED encapsulation," in *Synthetic Metals*, vol. 127, no. 1-3, 3 2002. doi: 10.1016/S0379-6779(01)00621-X. ISSN 03796779 pp. 189–193. 20

[94] C. Heo, H. Park, Y. T. Kim, E. Baeg, Y. H. Kim, S. G. Kim, and M. Suh, "A soft, transparent, freely accessible cranial window for chronic imaging and electrophysiology," *Scientific Reports*, vol. 6, 6 2016. doi: 10.1038/srep27818 20

[95] I. R. Minev, P. Musienko, A. Hirsch, Q. Barraud, N. Wenger, E. M. Moraud, J. Gandar, M. Capogrosso, T. Milekovic, L. Asboth, R. F. Torres, N. Vachicouras, Q. Liu, N. Pavlova, S. Duis, A. Larmagnac, J. Vörös, S. Micera, Z. Suo, G. Courtine, and S. P. Lacour, "Electronic dura mater for long-term multimodal neural interfaces," *Science*, vol. 347, no. 6218, pp. 159–163, 1 2015. doi: 10.1126/science.1260318 20

[96] FDA, "21CFR878.3540," 2018. [Online]. Available: https://www.accessdata.fda.gov/scripts/cdrh/cfdocs/cfcfr/cfrsearch.cfm?fr=878.3540 20

[97] N. Stark, "Literature Review: Biological Safety of Parylene C," *Medical Plastics and Biomaterials*, 1996. [Online]. Available: https://www.mddionline.com/literature-review-biological-safety-parylene-c 20

[98] Z. Marjanovic-Balaban and D. Jelic, "Polymeric Biomaterials in Clinical Practice," in *Biomaterials in Clinical Practice*. Cham: Springer International Publishing, 2018, pp. 101–117. [Online]. Available: http://link.springer.com/10.1007/978-3-319-68025-5_4 21

[99] Z. Zhu and T. Brown, "Full-vectorial finite-difference analysis of microstructured optical fibers," *Optics Express*, vol. 10, no. 17, p. 853, 8 2002. doi: 10.1364/oe.10.000853. [Online]. Available: http://www.opticsexpress.org/abstract.cfm?URI=OPEX-9-13-681 21

[100] T. J. Foutz, R. L. Arlow, and C. C. McIntyre, "Theoretical principles underlying optical stimulation of a channelrhodopsin-2 positive pyramidal neuron," *Journal of Neurophysiology*, vol. 107, no. 12, pp. 3235–3245, 6 2012. doi: 10.1152/jn.00501.2011. [Online]. Available: http://www.physiology.org/doi/10.1152/jn.00501.2011 29, 31, 32, 157, 170, 171

[101] J. Y. Lin, "A User's Guide to Channelrhodopsin Variants: Features, Limitations and Future Developments," *Experimental physiology*, vol. 96, no. 1, p. 19, 1 2011. doi: 10.1113/EXPPHYSIOL.2009.051961. [Online]. Available: /pmc/articles/PMC2995811//pmc/articles/PMC2995811/?report=abstracthttps://www.ncbi.nlm.nih.gov/pmc/articles/PMC2995811/ 29

[102] S. I. Al-Juboori, A. Dondzillo, E. A. Stubblefield, G. Felsen, T. C. Lei, and A. Klug, "Light Scattering Properties Vary across Different Regions of the Adult Mouse Brain," *PLoS ONE*, vol. 8, no. 7, p. e67626, 7 2013. doi: 10.1371/journal.pone.0067626. [Online]. Available: http://www.ncbi.nlm.nih.gov/pubmed/23874433http://www.pubmedcentral.nih.gov/articlerender.fcgi?artid=PMC3706487http://dx.plos.org/10.1371/journal.pone.0067626 32, 156, 159

[103] A. N. Yaroslavsky, P. C. Schulze, I. V. Yaroslavsky, R. Schober, F. Ulrich, and H.-J. Schwarzmaier, "Optical properties of selected native and coagulated human brain tissues in vitro in the visible and near infrared spectral range," *Physics in Medicine and Biology*, vol. 47, no. 12, p. 305, 6 2002. doi: 10.1088/0031-9155/47/12/305. [Online]. Available: http://stacks.iop.org/0031-9155/47/i=12/a=305?key=crossref.12561e2d4456e07e7003a552da27ef9f 32, 159

[104] "Cambridge NeuroTech Silicon Neural Probe Catalog | Cambridge NeuroTech." [Online]. Available: https://www.cambridgeneurotech.com/catalog 33

[105] Z. Ahmed, J. W. Reddy, T. Teichert, and M. Chamanzar, "High-density Steeltrodes: A Novel Platform for High Resolution Recording in Primates [*]," in *2019 9th International IEEE/EMBS Conference on Neural Engineering (NER)*. IEEE, 3 2019. doi: 10.1109/NER.2019.8716921. ISBN 978-1-5386-7921-0 pp. 835–838. [Online]. Available: https://ieeexplore.ieee.org/document/8716921/ 33, 122

[106] M. Ochoa, P. Wei, A. J. Wolley, K. J. Otto, and B. Ziaie, "A hybrid PDMS-Parylene subdural multi-electrode array." *Biomedical microdevices*, vol. 15, no. 3, pp. 437–43, 6 2013. doi: 10.1007/s10544-013-9743-2. [Online]. Available: http://www.ncbi.nlm.nih.gov/pubmed/23334754http://www.pubmedcentral.nih.gov/articlerender.fcgi?artid=PMC3651747http://link.springer.com/10.1007/s10544-013-9743-2 33

[107] K. P. Rola, "Anisotropic etching of silicon in KOH + Triton X-100 for 45° micromirror applications," *Microsystem Technologies*, vol. 23, no. 5, pp. 1463–1473, 5 2017. doi: 10.1007/s00542-016-3103-0. [Online]. Available: http://link.springer.com/10.1007/s00542-016-3103-0 36

[108] K. P. Rola and I. Zubel, "Triton Surfactant as an Additive to KOH Silicon Etchant," *Journal of Microelectromechanical Systems*, vol. 22, no. 6, pp. 1373–1382, 12 2013. doi: 10.1109/JMEMS.2013.2262590. [Online]. Available: http://ieeexplore.ieee.org/document/6549174/ 36

[109] A. L. Thangawng, R. S. Ruoff, M. A. Swartz, and M. R. Glucksberg, "An ultra-thin PDMS membrane as a bio/micro–nano interface: fabrication and characterization," *Biomedical Microdevices*, vol. 9, no. 4, pp. 587–595, 7 2007. doi: 10.1007/s10544-007-9070-6. [Online]. Available: http://link.springer.com/10.1007/s10544-007-9070-6 38

[110] D. Meyerhofer, "Characteristics of resist films produced by spinning," *Journal of Applied Physics*, vol. 49, no. 7, p. 3993, 8 2008. doi: 10.1063/1.325357. [Online]. Available: https://aip.scitation.org/doi/abs/10.1063/1.325357 38

[111] M. Tyona, "A theoritical study on spin coating technique," *Advances in materials Research*, vol. 2, no. 4, pp. 195–208, 12 2013. doi: 10.12989/AMR.2013.2.4.195 38

[112] D. E. Haas, J. N. Quijada, S. J. Picone, and D. P. B. III, "Effect of solvent evaporation rate on skin formation during spin coating of complex solutions," *https://doi.org/10.1117/12.384348*, vol. 3943, pp. 280–284, 5 2000. doi: 10.1117/12.384348. [Online]. Available: https://www.spiedigitallibrary.org/conference-proceedings-of-spie/3943/0000/Effect-of-solvent-evaporation-rate-on-skin-formation-during-spin/10.1117/12.384348.fullhttps://www.spiedigitallibrary.org/conference-proceedings-of-spie/3943/0000/Effect-of-solvent-evaporation-rate-on-skin-formation-during-spin/10.1117/12.384348.shorthttps://www.spiedigitallibrary.org/conference-proceedings-of-spie/3943/0000/Effect-of-solvent-evaporation-rate-on-skin-formation-during-spin/.full 38

[113] K. Choonee, R. R. Syms, M. M. Ahmad, and H. Zou, "Post processing of microstructures by PDMS spray deposition," *Sensors and Actuators A: Physical*, vol. 155, no. 2, pp. 253–262, 10 2009. doi: 10.1016/J.SNA.2009.08.029 42

[114] W. Chen, R. H. W. Lam, and J. Fu, "Photolithographic surface micromachining of polydimethylsiloxane (PDMS)." *Lab on a chip*, vol. 12, no. 2, pp. 391–5, 1 2012. doi: 10.1039/c1lc20721k. [Online]. Available: http://www.ncbi.nlm.nih.gov/pubmed/22089984http://www.pubmedcentral.nih.gov/articlerender.fcgi?artid=PMC4120064 43, 51

[115] A. E.-J. Lim, Junfeng Song, Qing Fang, Chao Li, Xiaoguang Tu, Ning Duan, Kok Kiong Chen, R. P.-C. Tern, and Tsung-Yang Liow, "Review of Silicon Photonics Foundry Efforts," *IEEE Journal of Selected Topics in Quantum Electronics*, vol. 20, no. 4, pp. 405–416, 7 2014. doi: 10.1109/JSTQE.2013.2293274. [Online]. Available: http://ieeexplore.ieee.org/document/6676843/ 43, 54

[116] J. T. Kuo, B. J. Kim, S. A. Hara, C. D. Lee, C. A. Gutierrez, T. Q. Hoang, and E. Meng, "Novel flexible Parylene neural probe with 3D sheath structure for enhancing tissue integration," *Lab Chip*, vol. 13, no. 4, pp. 554–561, 1 2013. doi: 10.1039/C2LC40935F. [Online]. Available: http://xlink.rsc.org/?DOI=C2LC40935F 43

[117] G. Hass and J. E. Waylonis, "Optical Constants and Reflectance and Transmittance of Evaporated Aluminum in the Visible and Ultraviolet*," *Journal of the Optical Society of America*, vol. 51, no. 7, p. 719, 7 1961. doi: 10.1364/JOSA.51.000719. [Online]. Available: https://www.osapublishing.org/abstract.cfm?URI=josa-51-7-719 43

[118] H. E. Bennett and J. O. Porteus, "Relation Between Surface Roughness and Specular Reflectance at Normal Incidence," *JOSA, Vol. 51, Issue 2, pp. 123-129*, vol. 51, no. 2, pp. 123–129, 2 1961. doi: 10.1364/JOSA.51.000123. [Online]. Available: https://www.osapublishing.org/viewmedia.cfm?uri=josa-51-2-123&seq=0&html=truehttps://www.osapublishing.org/abstract.cfm?uri=josa-51-2-123https://www.osapublishing.org/josa/abstract.cfm?uri=josa-51-2-123 44

[119] J. Garra, T. Long, J. Currie, T. Schneider, R. White, and M. Paranjape, "Dry etching of polydimethylsiloxane for microfluidic systems," *Journal of Vacuum Science & Technology A: Vacuum, Surfaces, and Films*, vol. 20, no. 3, pp. 975–982, 5 2002. doi: 10.1116/1.1460896. [Online]. Available: http://avs.scitation.org/doi/10.1116/1.1460896 45

[120] J. W. Reddy and M. Chamanzar, "Low-loss flexible Parylene photonic waveguides for optical implants," *Optics Letters*, vol. 43, no. 17, p. 4112, 9 2018. doi: 10.1364/OL.43.004112. [Online]. Available: https://www.osapublishing.org/abstract.cfm?URI=ol-43-17-4112 45

[121] M. Chamanzar, D. J. Denman, T. J. Blanche, and M. M. Maharbiz, "Ultracompact optoflex neural probes for high-resolution electrophysiology and optogenetic stimulation," in *2015 28th IEEE International Conference on Micro Electro Mechanical Systems (MEMS)*. IEEE, 1 2015. doi: 10.1109/MEMSYS.2015.7051049. ISBN 978-1-4799-7955-4 pp. 682–685. [Online]. Available: http://ieeexplore.ieee.org/document/7051049/ 45, 134

[122] R. P. von Metzen and T. Stieglitz, "The effects of annealing on mechanical, chemical, and physical properties and structural stability of Parylene C," *Biomedical Microdevices*, vol. 15, no. 5, pp. 727–735, 10 2013. doi: 10.1007/s10544-013-9758-8. [Online]. Available: http://www.ncbi.nlm.nih.gov/pubmed/23494595http://link.springer.com/10.1007/s10544-013-9758-8 47, 133

[123] J. W. Reddy, S. Nelson, and M. Chamanzar, "2D Optical Confinement in an Etchless Stratified Trench Waveguide," *Manuscript submitted for publication*, 2021. 53

[124] G. A. Porkolab, P. Apiratikul, B. Wang, S. H. Guo, and C. J. K. Richardson, "Low propagation loss AlGaAs waveguides fabricated with plasma-assisted photoresist reflow," *Optics Express*, vol. 22, no. 7, p. 7733, 4 2014. doi: 10.1364/oe.22.007733 54

[125] J. Cardenas, C. B. Poitras, J. T. Robinson, K. Preston, L. Chen, and M. Lipson, "Low loss etchless silicon photonic waveguides," in *Optics InfoBase Conference Papers*, vol. 17, no. 6. Optical Society of America, 3 2009. doi: 10.1364/oe.17.004752. ISBN 9781557528698. ISSN 21622701 pp. 4752–4757. 54

[126] A. Griffith, J. Cardenas, C. B. Poitras, and M. Lipson, "High quality factor and high confinement silicon resonators using etchless process," in *CLEO: Science and Innovations, CLEO_SI 2012*, vol. 20, no. 19. Optical Society of America, 9 2012. doi: 10.1364/oe.20.021341. ISBN 9781557529435. ISSN 1094-4087 pp. 21 341–21 345. 54

[127] L.-W. Luo, G. S. Wiederhecker, J. Cardenas, C. Poitras, and M. Lipson, "High quality factor etchless silicon photonic ring resonators," *Optics Express*, vol. 19, no. 7, p. 6284, 3 2011. doi: 10.1364/oe.19.006284 54

[128] S. Valouch, H. Sieber, S. Kettlitz, C. Eschenbaum, U. Hollenbach, and U. Lemmer, "Direct fabrication of PDMS waveguides via low-cost DUV irradiation for optical sensing," *Optics Express*, vol. 20, no. 27, p. 28855, 12 2012. doi: 10.1364/oe.20.028855. [Online]. Available: https://www.osapublishing.org/viewmedia.cfm?uri=oe-20-27-28855&seq=0&html=truehttps://www.osapublishing.org/abstract.cfm?uri=oe-20-27-28855https://www.osapublishing.org/oe/abstract.cfm?uri=oe-20-27-28855 54

[129] Q. Zhao, Y. Huang, and O. Boyraz, "Optical properties of V-groove silicon nitride trench waveguides," *Journal of the Optical Society of America A*, vol. 33, no. 9, p. 1851, 9 2016. [Online]. Available: https://www.osapublishing.org/abstract.cfm?URI=josaa-33-9-1851 54

[130] Q. Zhao, Y. Huang, R. Torun, S. Rahman, T. C. Atasever, and O. Boyraz, "Numerical investigation of silicon nitride trench waveguide," in *Photonic Fiber and Crystal Devices: Advances in Materials and Innovations in Device Applications IX*, S. Yin and R. Guo, Eds., vol. 9586, no. 26. SPIE, 8 2015. doi: 10.1117/12.2188378 p. 95860O. [Online]. Available: http://proceedings.spiedigitallibrary.org/proceeding.aspx?doi=10.1117/12.2188378 54

[131] Q. Zhao, C. Guclu, Y. Huang, F. Capolino, and O. Boyraz, "Plasmon optical trapping in silicon nitride trench waveguide," in *CLEO: QELS - Fundamental Science, CLEO_QELS 2015*. Optical Society of America (OSA), 5 2015. doi: 10.1364/CLEO_AT.2015.JTu5A.80. ISBN 9781557529688 p. 1551p. [Online]. Available: https://www.osapublishing.org/abstract.cfm?uri=CLEO_QELS-2015-JTu5A.80 54

[132] Y. Huang, Q. Zhao, L. Kamyab, A. Rostami, F. Capolino, and O. Boyraz, "Sub-micron silicon nitride waveguide fabrication using conventional optical lithography," in *Optics InfoBase Conference Papers*, vol. 23, no. 1. Optical Society of American (OSA), 3 2014. doi: 10.1364/oe.23.006780. ISBN 9781557527370. ISSN 21622701 pp. 1678–1687. [Online]. Available: https://www.osapublishing.org/viewmedia.cfm?uri=oe-23-5-6780&seq=0&html=truehttps://www.osapublishing.org/abstract.cfm?uri=oe-23-5-6780https://www.osapublishing.org/oe/abstract.cfm?uri=oe-23-5-6780 54

[133] Y. Huang, Q. Zhao, N. Sharac, R. Ragan, and O. Boyraz, "Highly nonlinear sub-micron silicon nitride trench waveguide coated with gold nanoparticles," in *Nonlinear Optics and Applications IX*, M. Bertolotti, J. W. Haus, and A. M. Zheltikov, Eds., vol. 9503. SPIE, 5 2015. doi: 10.1117/12.2182290. ISBN 9781628416244. ISSN 1996756X p. 95030H. [Online]. Available: http://proceedings.spiedigitallibrary.org/proceeding.aspx?doi=10.1117/12.2182290 54

[134] W.-T. Tsang, C.-C. Tseng, and S. Wang, "Optical Waveguides Fabricated by Preferential Etching," *Applied Optics*, vol. 14, no. 5, p. 1200, 5 1975. doi: 10.1364/ao.14.001200. [Online]. Available: https://www.osapublishing.org/viewmedia.cfm?uri=ao-14-5-1200&seq=0&html=truehttps://www.osapublishing.org/abstract.cfm?uri=ao-14-5-1200https://www.osapublishing.org/ao/abstract.cfm?uri=ao-14-5-1200 54

[135] P. F. Heidrich, J. S. Harper, E. G. Lean, and H. N. Yu, "High density multichannel optical waveguides with integrated couplers," in *1975 International Electron Devices Meeting*. IEEE, 1975. doi: 10.1109/iedm.1975.188957 pp. 602–603. 54

[136] G. Righini, A. Szczurek, J. Krzak, A. Lukowiak, M. Ferrari, S. Varas, and A. Chiasera, "Flexible Photonics: Where Are We Now?" in *220 22nd International Conference on Transparent Optical Netwroks (ICTON)*. Institute of Electrical and Electronics Engineers (IEEE), 9 2020. doi: 10.1109/icton51198.2020.9203092 pp. 1–4. 56

[137] H. Li, Y. Cao, Z. Wang, and X. Feng, "Flexible and stretchable inorganic optoelectronics," *Optical Materials Express*, vol. 9, no. 10, p. 4023, 10 2019. doi: 10.1364/ome.9.004023. [Online]. Available: https://doi.org/10.1364/OME.9.004023 56

[138] W. Peng and H. Wu, "Flexible and Stretchable Photonic Sensors Based on Modulation of Light Transmission," *Advanced Optical Materials*, vol. 7, no. 12, p. 1900329, 6 2019. doi: 10.1002/adom.201900329. [Online]. Available: https://onlinelibrary.wiley.com/doi/abs/10.1002/adom.201900329 56

[139] H. Puliyalil and U. Cvelbar, "Selective plasma etching of polymeric substrates for advanced applications," *Nanomaterials*, vol. 6, no. 6, 6 2016. doi: 10.3390/nano6060108 56

[140] E. Meng, P.-Y. Li, and Y.-C. Tai, "Plasma removal of Parylene C," *IOP PUBLISHING JOURNAL OF MICROMECHANICS AND MICROENGINEERING J. Micromech. Microeng*, vol. 18, p. 13, 2008. doi: 10.1088/0960-1317/18/4/045004 56

[141] S. D. Gedney and B. Zhao, "An auxiliary differential equation formulation for the complex-frequency shifted PML," *IEEE Transactions on Antennas and Propagation*, vol. 58, no. 3, pp. 838–847, 3 2010. doi: 10.1109/TAP.2009.2037765 65

[142] R. Venkateswaran, J. W. Reddy, and M. Chamanzar, "A Semi-Automated System for Wafer-Scale Optical Waveguide Characterization," in *2021 43rd Annual International Conference of the IEEE Engineering in Medicine & Biology Society (EMBC)*. IEEE, 2021. 76, 80

[143] I. P. Kaminow and L. W. Stulz, "Loss in cleaved Ti-diffused LiNbO3 waveguides," *Applied Physics Letters*, vol. 33, no. 1, pp. 62–64, 7 1978. doi: 10.1063/1.90191. [Online]. Available: http://aip.scitation.org/doi/10.1063/1.90191 77

[144] T. Ito and Y. Kokubun, "Nondestructive measurement of propagation loss and coupling efficiency in microring resonator filters using filter responses," *Japanese Journal of Applied Physics*, vol. 43, no. 3, pp. 1002–1005, 3 2004. doi: 10.1143/JJAP.43.1002. [Online]. Available: http://stacks.iop.org/1347-4065/43/1002https://iopscience.iop.org/article/10.1143/JJAP.43.1002https://iopscience.iop.org/article/10.1143/JJAP.43.1002/meta 77

[145] A. N. Zorzos, E. S. Boyden, and C. G. Fonstad, "Multiwaveguide implantable probe for light delivery to sets of distributed brain targets," *Optics Letters*, vol. 35, no. 24, p. 4133, 12 2010. doi: 10.1364/OL.35.004133. [Online]. Available: https://www.osapublishing.org/abstract.cfm?URI=ol-35-24-4133 78

[146] M. A. Fischler and R. C. Bolles, "Random sample consensus: a paradigm for model fitting with applications to image analysis and automated cartography," *Communications of the ACM*, vol. 24, no. 6, pp. 381–395, 6 1981. doi: 10.1145/358669.358692. [Online]. Available: http://portal.acm.org/citation.cfm?doid=358669.358692https://dl.acm.org/doi/10.1145/358669.358692 78

[147] D. Marcuse, "Power Distribution and Radiation Losses in Multimode Dielectric Slab Waveguides," *Bell System Technical Journal*, vol. 51, no. 2, pp. 429–454, 1972. doi: 10.1002/j.1538-7305.1972.tb01928.x 80

[148] P. Andersen and E. I. Moser, "Brain temperature and hippocampal function," *Hippocampus*, vol. 5, no. 6, pp. 491–498, 1995. doi: 10.1002/hipo.450050602. [Online]. Available: http://doi.wiley.com/10.1002/hipo.450050602 94

[149] A. Melikyan and P. Dong, "Adiabatic mode converters for silicon photonics: Power and polarization broadband manipulators," *APL Photonics*, vol. 4, no. 3, p. 030803, 3 2019. doi: 10.1063/1.5080247. [Online]. Available: https://aip.scitation.org/doi/abs/10.1063/1.5080247 94

[150] H. S. Lee, I. Park, K. S. Jeon, and E. H. Lee, "Fabrication of micro-lenses for optical interconnection using micro ink-jetting technique," *Microelectronic Engineering*, vol. 87, no. 5-8, pp. 1447–1450, 5 2010. doi: 10.1016/J.MEE.2009.11.116 94

[151] Y. Yaacob, N. A. Baharudin, S. Ambran, O. Mikami, and C. Fujikawa, "Optical coupling for multi-layered optical printed wiring board using micro lens array," *2016 IEEE 6th International Conference on Photonics, ICP 2016*, 7 2016. doi: 10.1109/ICP.2016.7510038 94

[152] A. Mohanty, Q. Li, M. A. Tadayon, S. P. Roberts, G. R. Bhatt, E. Shim, X. Ji, J. Cardenas, S. A. Miller, A. Kepecs, and M. Lipson, "Reconfigurable nanophotonic silicon probes for sub-millisecond deep-brain optical stimulation," *Nature Biomedical Engineering 2020 4:2*, vol. 4, no. 2, pp. 223–231, 2 2020. doi: 10.1038/s41551-020-0516-y. [Online]. Available: https://www.nature.com/articles/s41551-020-0516-y 96

[153] J. Pas, A. L. Rutz, P. P. Quilichini, A. Slézia, A. Ghestem, A. Kaszas, M. J. Donahue, V. F. Curto, R. P. O'Connor, C. Bernard, A. Williamson, and G. G. Malliaras, "A bilayered PVA/PLGA-bioresorbable shuttle to improve the implantation of flexible neural probes," *Journal of Neural Engineering*, vol. 15, no. 6, p. 065001, 12 2018. doi: 10.1088/1741-2552/aadc1d. [Online]. Available: http://stacks.iop.org/1741-2552/15/i=6/a=065001?key=crossref.1d46ca409f3f33dde0edd4e286c4f19a 100

[154] T. D. Y. Kozai and D. R. Kipke, "Insertion shuttle with carboxyl terminated self-assembled monolayer coatings for implanting flexible polymer neural probes in the brain," *Journal of neuroscience methods*, vol. 184, no. 2, p. 199, 11 2009. doi: 10.1016/J.JNEUMETH.2009.08.002. [Online]. Available: /pmc/articles/PMC3165009//pmc/articles/PMC3165009/?report=abstracthttps://www.ncbi.nlm.nih.gov/pmc/articles/PMC3165009/ 100

[155] Z. Zhao, X. Li, F. He, X. Wei, S. Lin, and C. Xie, "Parallel, minimally-invasive implantation of ultra-flexible neural electrode arrays," *Journal of Neural Engineering*, vol. 16, no. 3, p. 035001, 4 2019. doi: 10.1088/1741-2552/AB05B6. [Online]. Available: https://iopscience.iop.org/article/10.1088/1741-2552/ab05b6https://iopscience.iop.org/article/10.1088/1741-2552/ab05b6/meta 100

[156] K. B. Bjugstad, K. Lampe, D. S. Kern, and M. Mahoney, "Biocompatibility of poly(ethylene glycol)-based hydrogels in the brain: An analysis of the glial response across space and time," *Journal of Biomedical Materials Research Part A*, vol. 95A, no. 1, pp. 79–91, 10 2010. doi: 10.1002/JBM.A.32809. [Online]. Available: https://onlinelibrary.wiley.com/doi/full/10.1002/jbm.a.32809https://onlinelibrary.wiley.com/doi/abs/10.1002/jbm.a.32809https://onlinelibrary.wiley.com/doi/10.1002/jbm.a.32809 100

[157] J. Y. Lin, P. M. Knutsen, A. Muller, D. Kleinfeld, and R. Y. Tsien, "ReaChR: a red-shifted variant of channelrhodopsin enables deep transcranial optogenetic excitation," *Nature Neuroscience*, vol. 16, no. 10, pp. 1499–1508, 10 2013. doi: 10.1038/nn.3502. [Online]. Available: http://www.nature.com/articles/nn.3502 109, 114

[158] J. E. Chung, J. F. Magland, A. H. Barnett, V. M. Tolosa, A. C. Tooker, K. Y. Lee, K. G. Shah, S. H. Felix, L. M. Frank, and L. F. Greengard, "A Fully Automated Approach to Spike Sorting," *Neuron*, vol. 95, no. 6, pp. 1381–1394, 9 2017. doi: 10.1016/j.neuron.2017.08.030 115, 117

[159] C. C. Aggarwal, A. Hinneburg, and D. A. Keim, "On the Surprising Behavior of Distance Metrics in High Dimensional Space," *Lecture Notes in Computer Science (including subseries Lecture Notes in Artificial Intelligence and Lecture Notes in Bioinformatics)*, vol. 1973, pp. 420–434, 2001. doi: 10.1007/3-540-44503-X_27. [Online]. Available: https://link.springer.com/chapter/10.1007/3-540-44503-X_27 116

[160] A. P. Buccino, C. L. Hurwitz, S. Garcia, J. Magland, J. H. Siegle, R. Hurwitz, and M. H. Hennig, "Spikeinterface, a unified framework for spike sorting," *eLife*, vol. 9, pp. 1–24, 10 2020. doi: 10.7554/ELIFE.61834 118

[161] A. D. Rakić, A. B. Djurišić, J. M. Elazar, and M. L. Majewski, "Optical properties of metallic films for vertical-cavity optoelectronic devices," *Applied Optics*, vol. 37, no. 22, p. 5271, 8 1998. doi: 10.1364/AO.37.005271. [Online]. Available: https://www.osapublishing.org/abstract.cfm?URI=ao-37-22-5271 124

[162] J. W. Reddy, I. Kimukin, Z. Ahmed, E. Towe, and M. Chamanzar, "High density, double-sided, flexible optoelectrical neural probes with embedded micro-LEDs," *Frontiers in Neuroscience*, vol. 13, p. 572, 2019. doi: 10.3389/FNINS.2019.00572. [Online]. Available: https://www.frontiersin.org/articles/10.3389/fnins.2019.00572/full 127, 141, 169, 170

[163] L. A. Geddes and R. Roeder, "Criteria for the selection of materials for implanted electrodes." *Annals of biomedical engineering*, vol. 31, no. 7, pp. 879–90, 2003. [Online]. Available: http://www.ncbi.nlm.nih.gov/pubmed/12971619 133

[164] J. J. Jun, N. A. Steinmetz, J. H. Siegle, D. J. Denman, M. Bauza, B. Barbarits, A. K. Lee, C. A. Anastassiou, A. Andrei, C. Aydın, M. Barbic, T. J. Blanche, V. Bonin, J. Couto, B. Dutta, S. L. Gratiy, D. A. Gutnisky, M. Häusser, B. Karsh, P. Ledochowitsch, C. M. Lopez, C. Mitelut, S. Musa, M. Okun, M. Pachitariu, J. Putzeys, P. D. Rich, C. Rossant, W.-l. Sun, K. Svoboda, M. Carandini, K. D. Harris, C. Koch, J. O'Keefe, and T. D. Harris, "Fully integrated silicon probes for high-density recording of neural activity," *Nature*, vol. 551, no. 7679, pp. 232–236, 11 2017. doi: 10.1038/nature24636. [Online]. Available: http://www.nature.com/doifinder/10.1038/nature24636 134

[165] J. L. Shobe, L. D. Claar, S. Parhami, K. I. Bakhurin, and S. C. Masmanidis, "Brain activity mapping at multiple scales with silicon microprobes containing 1,024 electrodes," *Journal of Neurophysiology*, vol. 114, no. 3, pp. 2043–2052, 9 2015. doi: 10.1152/jn.00464.2015. [Online]. Available: http://www.physiology.org/doi/10.1152/jn.00464.2015 134

[166] C. Goßler, C. Bierbrauer, R. Moser, M. Kunzer, K. Holc, W. Pletschen, K. Köhler, J. Wagner, M. Schwaerzle, P. Ruther, O. Paul, J. Neef, D. Keppeler, G. Hoch, T. Moser, and U. T. Schwarz, "GaN-based micro-LED arrays on flexible substrates for optical cochlear implants," *Journal of Physics D: Applied Physics*, vol. 47, no. 20, p. 205401, 5 2014. doi: 10.1088/0022-3727/47/20/205401. [Online]. Available: http://stacks.iop.org/0022-3727/47/i=20/a=205401?key=crossref.1b55f51641ec7f05b53d3d9e44077034 138

[167] A. E. Kelly, J. J. D. McKendry, S. Zhang, D. Massoubre, B. R. Rae, R. P. Green, R. K. Henderson, and M. D. Dawson, "High-speed GaN micro-LED arrays for data communications," in *2012 14th International Conference on Transparent Optical Networks (ICTON)*. IEEE, 7 2012. doi: 10.1109/ICTON.2012.6253883. ISBN 978-1-4673-2229-4 pp. 1–5. [Online]. Available: http://ieeexplore.ieee.org/document/6253883/ 139

[168] J. Urban-Ciecko, J.-S. Jouhanneau, S. E. Myal, J. F. Poulet, and A. L. Barth, "Precisely Timed Nicotinic Activation Drives SST Inhibition in Neocortical Circuits," *Neuron*, vol. 97, no. 3, pp. 611–625, 2 2018. doi: 10.1016/J.NEURON.2018.01.037. [Online]. Available: https://www.sciencedirect.com/science/article/pii/S089662731830062X 148

[169] N. Dong, R. Berlinguer-Palmini, A. Soltan, N. Ponon, A. O'Neil, A. Travelyan, P. Maaskant, P. Degenaar, and X. Sun, "Opto-electro-thermal optimization of photonic probes for optogenetic neural stimulation," *Journal of Biophotonics*, vol. 11, no. 10, p. e201700358, 10 2018. doi: 10.1002/jbio.201700358. [Online]. Available: http://doi.wiley.com/10.1002/jbio.201700358 152, 154

[170] J. G. Bernstein, X. Han, M. A. Henninger, E. Y. Ko, X. Qian, G. Talei Franzesi, J. P. McConnell, P. Stern, R. Desimone, and E. S. Boyden, "Prosthetic systems for therapeutic optical activation and silencing of genetically targeted neurons," in *Proc. SPIE 6854, Optical Interactions with Tissue and Cells XIX*, S. L. Jacques, W. P. Roach, and R. J. Thomas, Eds., vol. 6854. International Society for Optics and Photonics, 2 2008. doi: 10.1117/12.768798 p. 68540H. [Online]. Available: http://proceedings.spiedigitallibrary.org/proceeding.aspx?doi=10.1117/12.768798 156

[171] L. Wang, S. L. Jacques, and L. Zheng, "MCML—Monte Carlo modeling of light transport in multi-layered tissues," *Computer Methods and Programs in Biomedicine*, vol. 47, no. 2, pp. 131–146, 7 1995. doi: 10.1016/0169-2607(95)01640-F. [Online]. Available: https://www.sciencedirect.com/science/article/pii/016926079501640F 156

[172] J. P. Neto, P. Baião, G. Lopes, J. Frazão, J. Nogueira, E. Fortunato, P. Barquinha, and A. R. Kampff, "Does Impedance Matter When Recording Spikes With Polytrodes?" *Frontiers in Neuroscience*, vol. 12, p. 715, 10 2018. doi: 10.3389/fnins.2018.00715. [Online]. Available: https://www.frontiersin.org/article/10.3389/fnins.2018.00715/full 166

[173] A. Ahuja, M. Behrend, J. Whalen, M. Humayun, and J. Weiland, "The Dependence of Spectral Impedance on Disc Microelectrode Radius," *IEEE Transactions on Biomedical Engineering*, vol. 55, no. 4, pp. 1457–1460, 4 2008. doi: 10.1109/TBME.2007.912430. [Online]. Available: http://ieeexplore.ieee.org/document/4384243/ 166

[174] D. Kim, Y. Sung, J. Park, and G. Yeom, "A study of transparent indium tin oxide (ITO) contact to p-GaN," *Thin Solid Films*, vol. 398-399, pp. 87–92, 11 2001. doi: 10.1016/S0040-6090(01)01368-2. [Online]. Available: https://www.sciencedirect.com/science/article/pii/S0040609001013682 166

[175] M. M. Elwassif, Q. Kong, M. Vazquez, and M. Bikson, "Bio-heat transfer model of deep brain stimulation-induced temperature changes," *Journal of Neural Engineering*, vol. 3, no. 4, p. 306, 12 2006. doi: 10.1088/1741-2560/3/4/008. [Online]. Available: https://iopscience.iop.org/article/10.1088/1741-2560/3/4/008https://iopscience.iop.org/article/10.1088/1741-2560/3/4/008/meta 169

[176] A. Berndt, P. Schoenenberger, J. Mattis, K. M. Tye, K. Deisseroth, P. Hegemann, and T. G. Oertner, "High-efficiency channelrhodopsins for fast neuronal stimulation at low light levels," *Proceedings of the National Academy of Sciences of the United States of America*, vol. 108, no. 18, pp. 7595–7600, 5 2011. doi: 10.1073/PNAS.1017210108/-/DCSUPPLEMENTAL. [Online]. Available: https://www.pnas.org/content/108/18/7595https://www.pnas.org/content/108/18/7595.abstract 170

[177] N. C. Klapoetke, Y. Murata, S. S. Kim, S. R. Pulver, A. Birdsey-Benson, Y. K. Cho, T. K. Morimoto, A. S. Chuong, E. J. Carpenter, Z. Tian, J. Wang, Y. Xie, Z. Yan, Y. Zhang, B. Y. Chow, B. Surek, M. Melkonian, V. Jayaraman, M. Constantine-Paton, G. K.-S. Wong, and E. S. Boyden, "Independent optical excitation of distinct neural populations," *Nature Methods*, vol. 11, no. 3, pp. 338–346, 3 2014. doi: 10.1038/nmeth.2836. [Online]. Available: http://www.nature.com/articles/nmeth.2836 171

[178] F. Wu, E. Stark, P. C. Ku, K. D. Wise, G. Buzsáki, and E. Yoon, "Monolithically Integrated μLEDs on Silicon Neural Probes for High-Resolution Optogenetic Studies in Behaving Animals," *Neuron*, vol. 88, no. 6, pp. 1136–1148, 12 2015. doi: 10.1016/J.NEURON.2015.10.032 171

[179] M. Wang, X. Wang, P. Moni, A. Liu, D. H. Kim, W. J. Jo, H. Sojoudi, and K. K. Gleason, "CVD Polymers for Devices and Device Fabrication," *Advanced Materials*, vol. 29, no. 11, p. 1604606, 3 2017. doi: 10.1002/ADMA.201604606. [Online]. Available: https://onlinelibrary.wiley.com/doi/full/10.1002/adma.201604606https://onlinelibrary.wiley.com/doi/abs/10.1002/adma.201604606https://onlinelibrary.wiley.com/doi/10.1002/adma.201604606 171, 176

[180] B. Feng, B. Deng, Y. Fu, L. G. Liu, Z. C. Li, M. X. Feng, H. M. Zhao, and Q. Sun, "Efficiency improvement of GaN-on-silicon thin-film light-emitting diodes with optimized via-like n-electrodes," *Semiconductor Science and Technology*, vol. 32, no. 7, p. 075009, 6 2017. doi: 10.1088/1361-6641/AA7276. [Online]. Available: https://iopscience.iop.org/article/10.1088/1361-6641/aa7276https://iopscience.iop.org/article/10.1088/1361-6641/aa7276/meta 171, 176

[181] P. Tian, J. J. McKendry, Z. Gong, B. Guilhabert, I. M. Watson, E. Gu, Z. Chen, G. Zhang, and M. D. Dawson, "Size-dependent efficiency and efficiency droop of blue InGaN micro-light emitting diodes," *Applied Physics Letters*, vol. 101, no. 23, p. 231110, 12 2012. doi: 10.1063/1.4769835. [Online]. Available: https://aip.scitation.org/doi/abs/10.1063/1.4769835 172

[182] J. Zhu, T. Takahashi, D. Ohori, K. Endo, S. Samukawa, M. Shimizu, and X. L. Wang, "Near-Complete Elimination of Size-Dependent Efficiency Decrease in GaN Micro-Light-Emitting Diodes," *physica status solidi (a)*, vol. 216, no. 22, p. 1900380, 11 2019. doi: 10.1002/PSSA.201900380. [Online]. Available: https://onlinelibrary.wiley.com/doi/full/10.1002/pssa.201900380https://onlinelibrary.wiley.com/doi/abs/10.1002/pssa.201900380https://onlinelibrary.wiley.com/doi/10.1002/pssa.201900380 172

[183] A. Yazdan-Shahmorad, C. Diaz-Botia, T. Hanson, V. Kharazia, P. Ledochowitsch, M. Maharbiz, and P. Sabes, "A Large-Scale Interface for Optogenetic Stimulation and Recording in Nonhuman Primates," *Neuron*, vol. 89, no. 5, pp. 927–939, 3 2016. doi: 10.1016/j.neuron.2016.01.013. [Online]. Available: http://linkinghub.elsevier.com/retrieve/pii/S0896627316000143http://www.ncbi.nlm.nih.gov/pubmed/26875625https://linkinghub.elsevier.com/retrieve/pii/S0896627316000143 178, 179

[184] A. Yazdan-Shahmorad, C. Diaz-Botia, T. Hanson, P. Ledochowitsch, M. M. Maharabiz, and P. N. Sabes, "Demonstration of a setup for chronic optogenetic stimulation and recording across cortical areas in non-human primates," in *Proc. SPIE 9305, Optical Techniques in Neurosurgery, Neurophotonics, and Optogenetics II*, H. Hirschberg, S. J. Madsen, E. D. Jansen, Q. Luo, S. K. Mohanty, and N. V. Thakor, Eds., 3 2015. doi: 10.1117/12.2080405 p. 93052K. [Online]. Available: http://proceedings.spiedigitallibrary.org/proceeding.aspx?doi=10.1117/12.2080405 178, 179

[185] A. Gerits, R. Farivar, B. Rosen, L. Wald, E. Boyden, and W. Vanduffel, "Optogenetically Induced Behavioral and Functional Network Changes in Primates," *Current Biology*, vol. 22, no. 18, pp. 1722–1726, 9 2012. doi: 10.1016/j.cub.2012.07.023. [Online]. Available: http://www.ncbi.nlm.nih.gov/pubmed/22840516http://www.pubmedcentral.nih.gov/articlerender.fcgi?artid=PMC3461112https://linkinghub.elsevier.com/retrieve/pii/S0960982212008147 178

[186] J. Nassi, M. Avery, A. Cetin, A. Roe, and J. Reynolds, "Optogenetic Activation of Normalization in Alert Macaque Visual Cortex," *Neuron*, vol. 86, no. 6, pp. 1504–1517, 6 2015. doi: 10.1016/j.neuron.2015.05.040. [Online]. Available: http://www.ncbi.nlm.nih.gov/pubmed/26087167http://www.pubmedcentral.nih.gov/articlerender.fcgi?artid=PMC4534089https://linkinghub.elsevier.com/retrieve/pii/S0896627315004791 178, 179

[187] R. Portugues, K. E. Severi, C. Wyart, and M. B. Ahrens, "Optogenetics in a transparent animal: circuit function in the larval zebrafish," *Current Opinion in Neurobiology*, vol. 23, no. 1, pp. 119–126, 2 2013. doi: 10.1016/j.conb.2012.11.001. [Online]. Available: http://www.ncbi.nlm.nih.gov/pubmed/23246238https://linkinghub.elsevier.com/retrieve/pii/S0959438812001638 178

[188] T. J. Richner, S. Thongpang, S. K. Brodnick, A. A. Schendel, R. W. Falk, L. A. Krugner-Higby, R. Pashaie, and J. C. Williams, "Optogenetic micro-electrocorticography for modulating and localizing cerebral cortex activity," *Journal of Neural Engineering*, vol. 11, no. 1, p. 016010, 2 2014. doi: 10.1088/1741-2560/11/1/016010. [Online]. Available: http://www.ncbi.nlm.nih.gov/pubmed/24445482http://www.pubmedcentral.nih.gov/articlerender.fcgi?artid=PMC4026187http://stacks.iop.org/1741-2552/11/i=1/a=016010?key=crossref.d4e0e10c6a4ed8dace21f902b635048d 178

[189] P. Anikeeva, A. S. Andalman, I. Witten, M. Warden, I. Goshen, L. Grosenick, L. A. Gunaydin, L. M. Frank, and K. Deisseroth, "Optetrode: a multichannel readout for optogenetic control in freely moving mice," *Nature Neuroscience 2011 15:1*, vol. 15, no. 1, pp. 163–170, 12 2011. doi: 10.1038/nn.2992. [Online]. Available: https://www.nature.com/articles/nn.2992 179

[190] M. Trumpis, C. H. Chiang, A. L. Orsborn, B. Bent, J. Li, J. A. Rogers, B. Pesaran, G. Cogan, and J. Viventi, "Sufficient sampling for kriging prediction of cortical potential in rat, monkey, and human μECoG," *Journal of Neural Engineering*, vol. 18, no. 3, p. 036011, 3 2021. doi: 10.1088/1741-2552/ABD460. [Online]. Available: https://iopscience.iop.org/article/10.1088/1741-2552/abd460https://iopscience.iop.org/article/10.1088/1741-2552/abd460/meta 179

[191] C. H. Chiang, C. Wang, K. Barth, S. Rahimpour, M. Trumpis, S. Duraivel, I. Rachinskiy, A. Dubey, K. E. Wingel, M. Wong, N. S. Witham, T. Odell, V. Woods, B. Bent, W. Doyle, D. Friedman, E. Bihler, C. F. Reiche, D. G. Southwell, M. M. Haglund, A. H. Friedman, S. P. Lad, S. Devore, O. Devinsky, F. Solzbacher, B. Pesaran, G. Cogan, and J. Viventi, "Flexible, high-resolution thin-film electrodes for human and animal neural research," *Journal of Neural Engineering*, vol. 18, no. 4, p. 045009, 6 2021. doi: 10.1088/1741-2552/AC02DC. [Online]. Available: https://iopscience.iop.org/article/10.1088/1741-2552/ac02dchttps://iopscience.iop.org/article/10.1088/1741-2552/ac02dc/meta 179

[192] J. W. Reddy, M. H. Malekoshoaraie, V. Hassanzade, R. Venkateswaran, and M. Chamanzar, "Parylene Photonic Microimager for Implantable Imaging," in *2021 43rd Annual International Conference of the IEEE Engineering in Medicine & Biology Society (EMBC)*. IEEE, 2021. 180

[193] H. Yashiro, I. Nakahara, K. Funabiki, and H. Riquimaroux, "Micro-endoscopic system for functional assessment of neural circuits in deep brain regions: Simultaneous optical and electrical recordings of auditory responses in mouse's inferior colliculus," *Neuroscience Research*, vol. 119, pp. 61–69, 6 2017. doi: 10.1016/J.NEURES.2017.01.002 180

[194] B. T. Laing, J. N. Siemian, S. Sarsfield, and Y. Aponte, "Fluorescence microendoscopy for in vivo deep-brain imaging of neuronal circuits," *Journal of Neuroscience Methods*, vol. 348, p. 109015, 1 2021. doi: 10.1016/J.JNEUMETH.2020.109015 180